Supramolecular injectable
hydrogels for local cardiac therapy

SUPRAMOLECULAR INJECTABLE HYDROGELS FOR LOCAL CARDIAC THERAPY

MAAIKE SCHOTMAN

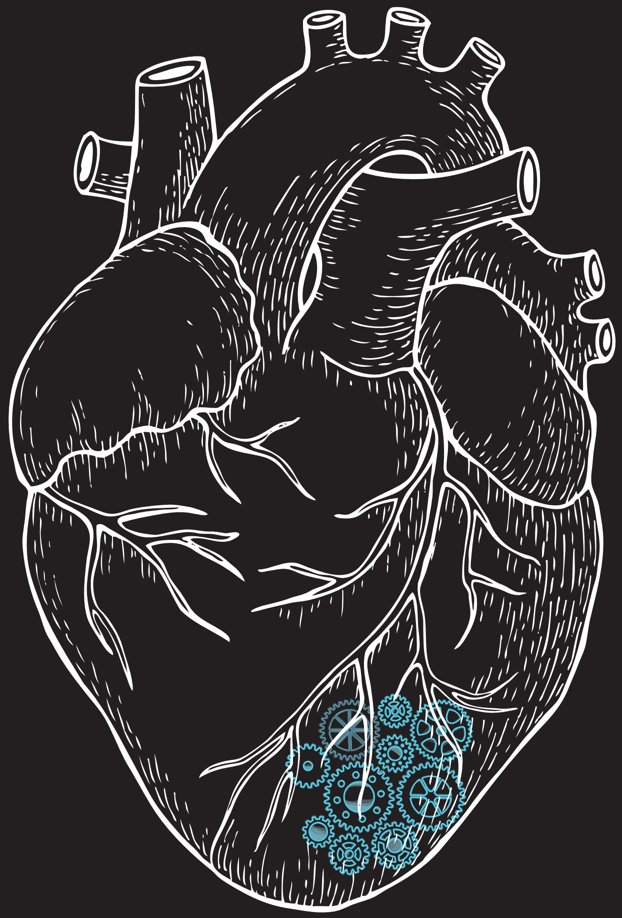

Supramolecular injectable hydrogels for local cardiac therapy

MAAIKE SCHOTMAN

Supramolecular injectable hydrogels for local cardiac therapy

PROEFSCHRIFT

ter verkrijging van de graad van doctor aan de Technische Universiteit
Eindhoven, op gezag van de rector magnificus prof.dr.ir. F.P.T. Baaijens, voor een
commissie aangewezen door het College voor Promoties, in het openbaar te
verdedigen op donderdag 9 december 2021 om 13:30 uur

door

Maaike J. G. Schotman

geboren te Vriezenveen

Dit proefschrift is goedgekeurd door de promotoren en de samenstelling van de promotiecommissie is als volgt:

voorzitter: prof.dr. M. Merkx
promotor: prof.dr.dr P.Y.W. Dankers
copromotor: dr. L.K.E.A. Abdelmohsen
leden: prof.dr. R.P. Sijbesma
prof.dr. C.V.C. Bouten
prof.dr. S.A.J. Chamuleau (Amsterdam Universitair Medisch Centrum)
prof.dr. J.A. Burdick (University of Pennsylvania)
adviseur: dr. A.M. Smits (Leiden Universitair Medisch Centrum)

Het onderzoek of ontwerp dat in dit proefschrift wordt beschreven is uitgevoerd in overeenstemming met de TU/e Gedragscode Wetenschapsbeoefening.

Printed by: Gildeprint, Enschede

Cover design by Karen Wijnen and Rafaël Klein

A catalogue record is available from the Eindhoven University of Technology Library.

ISBN: 978-90-386-5417-1

The research described in this thesis was funded by the Dutch Heart Foundation (CVON2014-27, REMAIN).

Financial support by the Dutch Heart Foundation for the publication of thesis is gratefully acknowledged.

Content

Chapter 1 1
Introduction to this thesis

Chapter 2
Factors influencing retention of injected biomaterials to treat myocardial infarction 13

Chapter 3
Design and investigation of ureido-pyrimidinone based supramolecular polymer hydrogel 41

Chapter 4
Tuning the affinity of amphiphilic guest molecules in a supramolecular transient network 67

Chapter 5
Hydrogel-loaded giant unilamellar vesicles as versatile viscoadaptable platforms 85

Chapter 6
In vivo retention quantification of supramolecular hydrogels engineered for cardiac delivery 101

Chapter 7
Supramolecular hydrogels as RNAi cardiac delivery systems 121

Chapter 8
Epilogue 139

Summary 153

Curriculum Vitae 155

List of Publications 157

Dankwoord 159

1

Introduction to the thesis

Preface

Cardiovascular diseases, including conditions as arrhythmia, strokes, and myocardial infarction among others, represent the most frequently occurring causes of death worldwide. As for most diseases, prevention is better than cure; cardiovascular diseases can be circumvented by e.g. a healthy diet, regular exercise, and limited alcohol consumption. When occurring, the damage that results from cardiovascular diseases can be significant. A heart attack, i. e. myocardial infarction, occurs when the blood flow to the heart muscle is limited or blocked, depleting a part of the heart muscle from oxygen. The amount of damage is dependent on the area size of depletion, with an increasing damage when a larger muscle area is affected, leading to irreversible necrosis of the heart muscle. Current treatments are often palliative and include blood-thinning medication and aspirins, with heart transplantation being the only definitive treatment, however it involves high risks and donors are scarce.

Several studies[1-5] as well as reviews[6-8] showcase the use of stem cells for damaged myocardium regeneration as a state-of-the-art therapy, with stem cells differentiating into cardiac lineages. Moreover, these studies demonstrate the advantages of such stem cell therapies. However, conclusive results are difficult to be determined from these studies, mainly due to the heterogeneity of clinical trials, such as differences in delivery method, group sizes, cell type, and delivery timing. Furthermore, low cellular cardiac retention (<10%) was observed directly after injection[9], and has been frequently reported.[10-13] New therapies with high potential to treat myocardial infarction are based on growth factors[14] and RNA interference (RNAi) drugs[15], though with high washout rates due to the cardiac environment.[16] Drug delivery vehicles are being developed that are proposed to deliver the drugs or cells to the site of interest, i.e. the infarcted region, and increase the retention and therapeutic efficacy. In this chapter, we discuss the possibilities of using a supramolecular biomaterial as drug delivery vehicle to improve the therapeutic efficacy and thereof stimulate the cardiac regeneration.

1. Drug delivery

Drug delivery refers to a method or process in which a pharmaceutical compound is administered to obtain a therapeutic in vivo effect.[17] To prevent adverse cardiac remodeling after myocardial infarction, pharmacological treatments, such as anti-inflammatory agents, RNAi therapeutics, or certain enzyme inhibitors, can be used.[18] However, high concentrations of drugs are needed to reach an effective therapeutic effect, which, in turn, results in unwanted side effects , e.g. toxicity to other organs.[19] Drug delivery systems can be used to carry and transport therapeutic drugs, in which the drug solubility can be increased, as well as the drug efficacy, and reduce possible side-effects.[20]

In the field of nanomedicine, several drug delivery vehicles have been developed for cardiovascular diseases, such as carbon nanostructures, polymeric nanocarriers, and lipid-based nanocarriers.[21] These nanocarriers can be injected systemically or locally, and protect the incorporated drugs from degradation in the biological environment.[22] Nevertheless, systemic injection can lead to a high off-target toxicity, and removal of these particles from the body represents a limitation.[23] Furthermore, many challenges need to be overcome for nanomedicine to reach the clinic, e.g. biocompatibility and safety, large scale manufacturing, low drug-encapsulation efficiency, and cost-effectiveness in comparison to current therapies.

On the other hand, macroscale drug delivery systems, e.g. cardiac patches[24] or injectable hydrogels[25], display larger sizes (with dimensions over 1 mm[26]) in comparison to micro- and nanocarriers and are often delivered by local administration or injection. This facilitates effective treatment at lower therapeutic dosage, which further prevents toxic side-effects.[27] Furthermore, such systems provide an increase in sustained therapeutic release over time, whilst protecting therapeutics from degradation in the biological environment.[26] The therapeutic drug release from these systems can be controlled by different mechanisms, i.e. diffusion, drug-carrier affinity or carrier degradation.[26] Cardiac patches can be introduced to the infarcted area, containing cells to enhance the cellular retention and survival at the target side, as well as other factors such as growth factors or RNAi therapeutics.[24] Hydrogels can be transplanted or injected in a minimal invasive manner for in situ gelation at the targeting site, containing cells or therapeutics to limit the adverse cardiac remodeling. In this thesis, we explore the use of macroscale injectable hydrogels as drug delivery systems for cardiac regenerative applications, with supramolecular biomaterials displaying reversible associations that enable this injectability in a minimally invasive manner.

2. Supramolecular biomaterials

Supramolecular chemistry is defined as chemistry beyond the molecule,[28,29] in which the spatial organization of a system is dependent primarily on the non-covalent crosslinks. These types of dynamic crosslinks are often found in nature, e.g. the cellular interaction with the extracellular matrix, the double helix folding of DNA, or protein-protein interaction, combined by electrostatic forces, hydrogen bonding and hydrophobic interactions. In this regard, a wide array of biomaterials that simulate such natural interactive processes have been developed.[30] Supramolecular biomaterials are crosslinked by these non-covalent interactions (i.e. hydrogen bonding, electrostatic interactions, Van der Waals forces, and pi-pi interactions), offering control over material properties by its reversible, tunable, dynamic and modular nature, capturing the complexity of the native biological environment.[31] Examples of such supramolecular motifs are cyclodextrins[32], alginate and polycations[33], bis-urea[34], peptide-amphiphiles[35], and ureido-pyrimidinone (UPy)[36]. The applications of these biomaterials vary from drug delivery purposes, tissue engineering, to regenerative medicine.[37]

Different morphologies of these supramolecular materials can be developed, depending on the application and design, e.g. particles in solution, elastomeric materials, and hydrogels. An example of such supramolecular motifs in solution are coacervates, that can function as cellular mimics[38], which are crowded vesicles based on electrostatic interactions.[39] By electrostatic interactions between amylose polymer chains, modified with positive quaternary amines or negative carboxymethyl groups, phase-separation and consequent formation of liquid coacervate droplets follows (Figure 1.1A).[40] The bis-urea moiety specifically binds by hydrogen bonding interactions, which can be used in the development of elastomeric supramolecular materials, allowing easy modification by urea-functionalized additives (Figure 1.1B).[41] In a modular fashion, this allows adaptation and introduction of, for example, antifouling additives[42], or bioactive ligands[43] to improve the biocompatibility of supramolecular membranes. Assembly behavior based on host-guest crosslinking, e.g. cyclodextrin-adamantane conjugates, can be used to develop shear thinning injectable hydrogels[44], by functionalization of hyaluronic acid polymers with cyclodextrin and adamantane moieties assembling upon mixing (Figure 1.1C).[45] This guest-host assembly can be broken by shear-force, allowing injection followed by in situ gelation. Furthermore, hydrophobic interactions often play a significant role in the assembly of supramolecular biomaterials in aqueous conditions, as observed in the self-assembly behavior of peptide amphiphiles (PA).[46] Besides a long alkyl tail bearing the hydrophobic character and steering self-assembly, β-sheet formation as well as ionic interactions lead to the assembly of this peptide amphiphile, resulting in a cylindrical micelle (Figure 1.1D). This can give rise to self-assembling hydrogels.

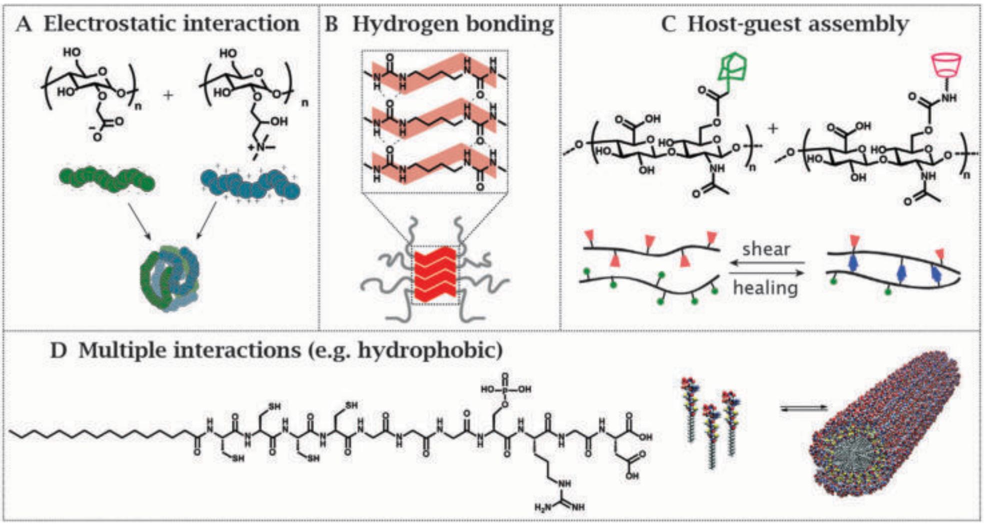

Figure 1.1 Types of supramolecular interactions, showing the assembly of amylose functionalized with a quaternary amine or carboxymethyl group which assemble by electrostatic interaction, image based on ref [39] (A). Bisurea moieties self-complement and stack based on hydrogen bonding (B), host-guest assembly by cyclodextrin and adamantane coupling, functionalized on a hyaluronic acid polymer forming a gel network, which can be disrupted upon shear forces (C). Peptide amphiphiles assemble based on hydrophobic interaction, as well as β-sheet formation and ionic interactions (D).

3. Ureido-pyrimidinone based biomaterials

Similar to the bisurea-based interaction described previously, the UPy moiety forms hydrogen bonds based on self-complementary interactions (Figure 1.2).[36] The UPy-molecule dimerizes by four-fold hydrogen bonding[36,47], with additional urea moieties coupled, protected by alkyl spacers, to the UPy molecules that induce lateral stacking into a fiber formation. The assembly of this system is stabilized by hydrogen bonding, hydrophobic interactions, and pi-pi stacking, bundling into a triplicate fiber formation (Figure 1.2A).[48] UPy-based polymers can be used for the development of supramolecular elastomers[43,48,49], hydrogels[50-52], or assemblies in solution[53,54], displaying dynamic nature due to the reversibility of the UPy-interactions. Hydrogels based on this UPy molecule display pH-responsive behavior, with an increase in pH leading to deprotonation of the enol tautomer, disrupting the four-fold hydrogen bonds (Figure 1.2C).[55] These UPy-based supramolecular polymers are primarily composed of a poly(ethylene glycol) (PEG) backbone for their hydrophilic character, end-functionalized with UPy-moieties. The UPy-PEG hydrogels show pH- and temperature responsive behavior, facilitating injection in the liquid state at a pH > 8.5, and displays fast in situ gelation when in contact with physiological pH.[55] This enables minimally invasive local injection at the target site.

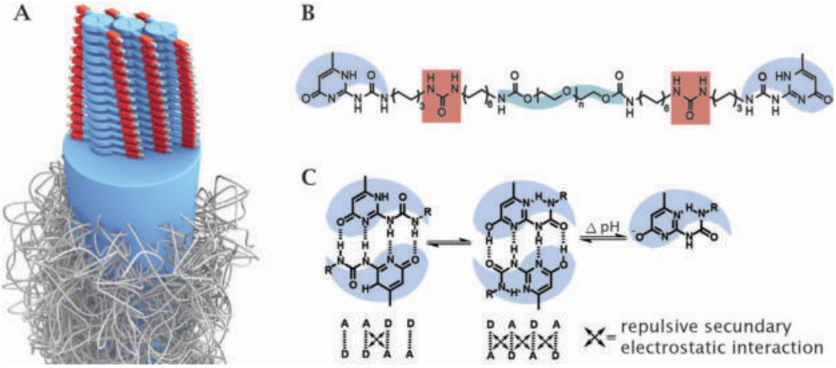

Figure 1.2 An overview of the UPy-molecule, with a schematic overview of the UPy-assembly (A), the bifunctional UPy-PEG molecule (B), and the dimerizing assembling behaviour of the UPy molecule, with the keto-tautomer and the enol-tautomer forming dimers, whereas an increase in pH leads to the formation of the enolate form which leads to a disruption of the four-fold hydrogen bonds (C).

Previous research in our group showed the modularity and applicability of this hydrogel as drug delivery system. A tunable release of RNAi drugs was obtained by cholesterol-functionalization to the RNAi drug, adapting the affinity with the bifunctional UPy-PEG hydrogel (Figure 1.3A).[56] Furthermore, adaptation of the bifunctional UPy-PEG hydrogel by the introduction of a monofunctional UPy-moiety functionalized with an amine group carrying a positive charge (Figure 1.3A'), increased the affinity with negatively charged RNAi drugs, sustaining the drug release. Another study showed the modification of the anticancer drug mitomycin C in a similar modification strategy with cholesterol, increasing the affinity with the bifunctional UPy-PEG hydrogel by hydrophobic interaction (Figure 1.3B).[57] This showed a steady release of the cholesterol-modified mitomycin C from the hydrogel (Figure 1.3B'), as well as cytotoxic effect up to 18 days of release. To enable in vivo visualization, a monofunctional UPy-moiety functionalized with a DOTA molecule chelated with Gadolinium(III) (Figure 1.3C) was introduced to the bifunctional UPy-PEG hydrogel in a modular fashion, enabling visualization of the hydrogel using magnetic resonance imaging (MRI).[58] After catheter-aided intramyocardial injection, the injection sites could be visualized by MRI (Figure 1.3C').

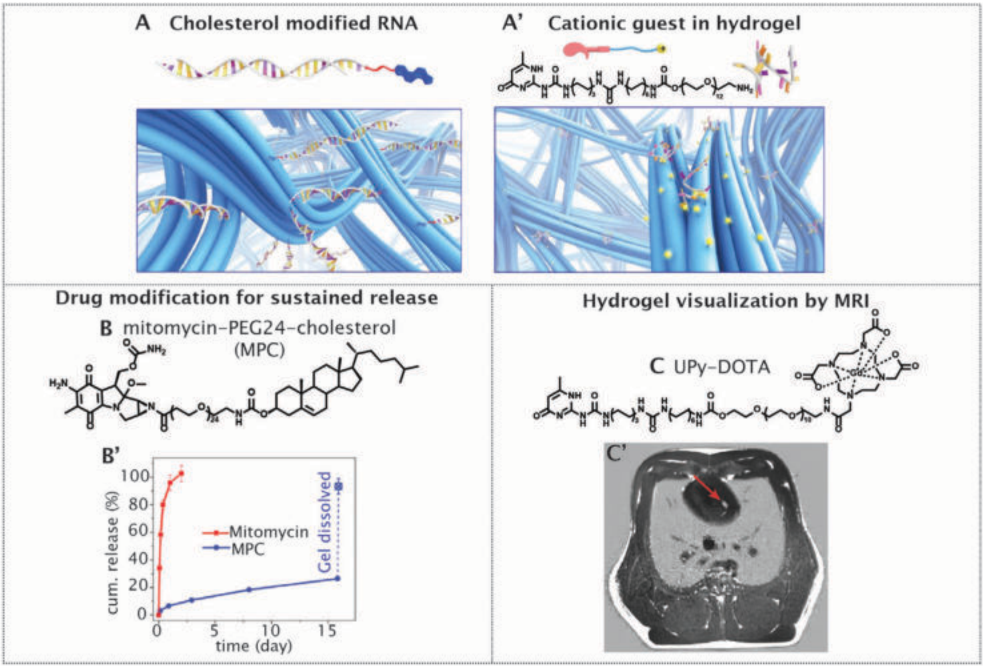

Figure 1.3 The applicability of the bifunctional UPy-PEG hydrogel, the cholesterol-modified RNAi drugs displaying an increased drug affinity with the hydrogel network (A), and implementation of a positively charged monofunctional UPy-amine leads to an increase in affinity with the RNAi molecule due to electrostatic interactions with the negatively-charged RNAi and positively charged hydrogel network (A'). Cholesterol-modification of the anticancer drug mitomycin (B) displays an increased affinity with the hydrogel network and a sustained release from the hydrogel (B'). MRI visualization of the hydrogel was enabled by implementation of a monofunctional UPy-DOTA molecule chelated with the MRI-traceable gadolinium (C) to the bifunctional UPy-PEG hydrogel, visualized in vivo post-injection in a pig heart (C').

When combining the monofunctional UPy-OEG composed of a 517 Da oligo(ethylene glycol) (OEG) chain with the bifunctional UPy-PEG moiety, the ratio between these compounds can have a significant effect in the rigidity of the resulted hydrogels as shown by Kieltyka et al.[59] Interestingly, when small quantities of bifunctional UPy-PEG were added to the monofunctional UPy-OEG (mol ratio of 1 to 11, respectively), strong and rigid hydrogels were obtained, whereas small ratio of monofuntional UPy-OEG to bifunctional UPy-PEG (mol ratio of 1 to 5, respectively) resulted in highly dynamic hydrogel networks. Furthermore, the ethylene glycol chain length in the monofunctional compound showed to have a significant effect on the assembling behavior, with strong rigid networks forming when short ethylene glycol chain length were implemented, whereas this effect disappeared when the ethylene glycol chain length was increased from 517 Da to ~5000 Da. The combination of the bi- and monofunctional UPy molecules was further exploited by examining the dynamic exchange of this monofunctional UPy-compound containing end-functionalized with a glycinamide (UPy-Gly).[50] A high monofunctional UPy-Gly to bifunctional UPy-PEG ratio (molar ratio of 84 to 1, respectively), showed to hinder the exchange dynamics significantly in comparison to lower ratios (i.e. 9 to 1, respectively). Upon addition of bioactive motifs (a monofunctional UPy compound functionalized to a cyclic RGD ligand) an enhanced ligand tethering in the hydrogel (84 to 1 molar ratio) stimulated cellular adhesion and cell spreading behavior.

The combination of pH-responsiveness, modularity, and dynamicity render this hydrogel an ideal drug delivery vehicle. Through tuning in a modular fashion, the functionality, bioactivity, and the release of drug moieties can be adapted.

Aim and outline

The aim of the research described in this thesis is to develop a multi-functional supramolecular, hydrogel-based, drug delivery system that is able to control drug release, achieve retention and allow visualization in the heart after injection (Figure 1.4). Through chemical modifications, and introduction of affinity-based molecules and monofunctional UPy-OEG moieties containing different end-functionalization, the dynamic and bioactive properties of the hydrogel are tuned and the interaction mechanisms between introduced molecules and the hydrogel network are exploited.

In **chapter 2,** we demonstrate the retention of injected biomaterials in the infarcted area for myocardial infarction treatment, and mainly focus on inherent factors influencing such retention, such as cardiac pulsation, time of injection, and mechanical properties of the injected biomaterials. A deeper understanding of the relationship between the material effectiveness and these specific factors is pursued, and a possible focus change is proposed to explore the direct role of the biomaterial and its efficacy in the field of regenerative cardiac therapies, instead of only focusing on cardiac response.

The design and investigation of different UPy-based hydrogels are described in **chapter 3**, in which we show the highly dynamic and tunable properties of these UPy-based systems (Figure 1.4i). A bioactive hydrogel based on a recombinant collagen type 1-based peptide (RCPhC1) functionalized with UPy-moieties is designed, which is combined with a bifunctional UPy-PEG hydrogelator. Furthermore, hydrogels based on monofunctional UPy-moieties are introduced; these hydrogels are functionalized with a single amino acid, in which small quantities of bifunctional UPy-PEG leads to gelation at low weight percentages.

The assembling behavior and dynamicity of several guest molecules are exploited in **chapter 4**, with a monofunctional UPy guest molecules (complementary to the bifunctional host UPy-PEG network based on four-fold hydrogen bonding), a cholesterol guest molecule (highly hydrophobic), and a dodecyl guest molecule (hydrophobic) tethered to the hydrogel network with different affinities (Figure 1.4ii). The behavior of these affinity-tuned molecules is further explored by examination of the diffusive and rheological properties in the hydrogel, as well as morphology and cellular uptake in solution.

In **chapter 5**, a facile strategy is introduced to encapsulate the highly dynamic and pH-responsive bifunctional UPy-PEG into a giant unilamellar vescicle (Figure 1.4iii). An intracellular crowded environment is simulated, the pH-responsive and dynamic behavior and enzymatic inter-lumellar activity is studied. This robust system shows high potential in the fields of synthetic cellular mimics and drug delivery.

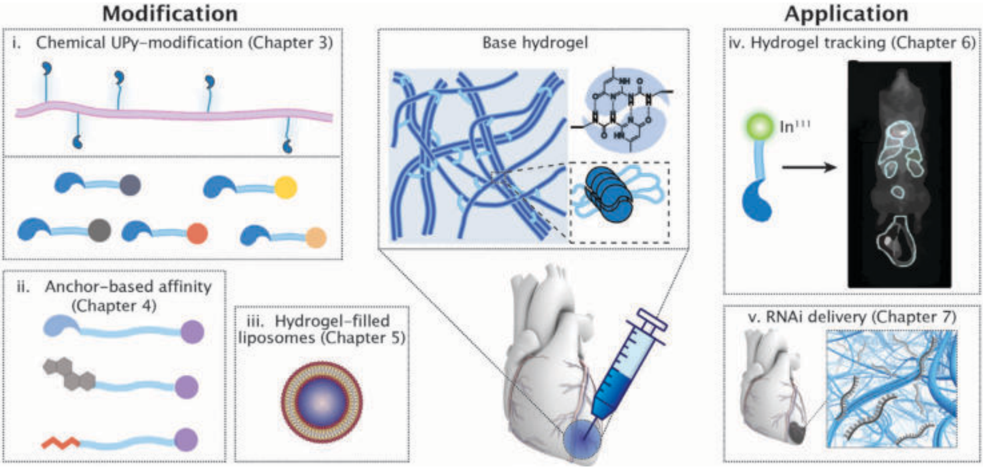

Figure 1.4 An overview of the approaches discussed in this thesis, in which the bifunctional UPy-PEG system is shown as the base hydrogel, chemical modifications on the UPy-hydrogel system are discussed, as well as the implementation of the bifunctional UPy-PEG in a liposome system. Furthermore, applicational research is presented, in which the hydrogel is tracked in vivo after cardiac injection, and the efficacy in combination with an RNAi molecule is examined.

A method to radioactively label the bifunctional UPy-PEG hydrogel in a modular fashion is presented in **chapter 6** (Figure 1.4iv). Our goal was to increase our understanding on the retention and fate of the hydrogel after intramyocardial injection. Furthermore, bioactive and adhesive properties of the UPy-PEG hydrogel were increased by introduction of the UPy-functionalized RCPhC1. Both hydrogels were radioactively labeled and the retention and redistribution were visualized in vivo in a porcine model after cardiac injection in a healthy heart.

The therapeutic efficacy of the hydrogels in combination with RNAi drugs is described in **chapter 7** (Figure 1.4v). To do so, we examined the behavior of bifunctional UPy-PEG in combination with an antimiR drug as well as a bifunctional UPy-PEG in combination with a positively-charged UPy-amine in a rodent. Furthermore, the preparation towards a large animal model (porcine) is described, in which the efficacy of an antimiR encapsulated in the bifunctional UPy-PEG hydrogel in combination with the UPy-functionalized RCPhC1 is examined.

In **chapter 8**, future perspectives considering the supramolecular UPy-based hydrogels are described. The importance of structural assessment of these hydrogels, with methods such as transmission electron microscopy, is discussed.

References

1 G. P. Meyer, K. C. Wollert, J. Lotz, J. Steffens, P. Lippolt, S. Fichtner, H. Hecker, A. Schaefer, L. Arseniev, B. Hertenstein, A. Ganser and H. Drexler, *Circulation*, 2006, **113**, 1287–1294.

2 E. C. Perin, H. F. R. Dohmann, R. Borojevic, S. A. Silva, A. L. S. Sousa, G. V Silva, C. T. Mesquita, L. Belém, W. K. Vaughn, F. O. D. Rangel, J. A. Ri. E. C. and I. 6 and 12 M. A. T. I. of A. B. M. M. C. for I. C. Assad, A. C. Carvalho, R. V. C. Branco, M. I. D. Rossi, H. J. F. Dohmann and J. T. Willerson, *Circulation*, 2004, **110**, II-213–II-218.

3 B. Assmus, J. Honold, V. Schächinger, M. B. Britten, U. Fischer-Rasokat, R. Lehmann, C. Teupe, K. Pistorius, H. Martin, N. D. Abolmaali, T. Tonn, S. Dimmeler and A. M. Zeiher, *N. Engl. J. Med.*, 2006, **355**, 1222–1232.

4 J. G. Rasmussen, O. Frøbert, C. Holst-Hansen, J. Kastrup, U. Baandrup, V. Zachar, T. Fink and U. Simonsen, *Cell Transplant.*, 2014, **23**, 195–206.

5 R. Bolli, A. R. Chugh, D. D'Amario, J. H. Loughran, M. F. Stoddard, S. Ikram, G. M. Beache, S. G. Wagner, A. Leri, T. Hosoda, F. Sanada, J. B. Elmore, P. Goichberg, D. Cappetta, N. K. Solankhi, I. Fahsah, D. G. Rokosh, M. S. Slaughter, J. Kajstura and P. Anversa, *Lancet*, 2011, **378**, 1847–1857.

6 M. Madigan and R. Atoui, *Bioengineering*, 2018, **5**, 28.

7 J. C. George, *Transl. Res.*, 2010, **155**, 10–19.

8 P. P. Zwetsloot, A. M. D. Végh, S. J. Jansen of Lorkeers, G. P. J. van Hout, G. L. Currie, E. S. Sena, H. Gremmels, J. W. Buikema, M.-J. Goumans, M. R. Macleod, P. A. Doevendans, S. A. J. Chamuleau and J. P. G. Sluijter, *Circ. Res.*, 2016, **118**, 1223–1232.

9 D. A. M. Feyen, P. Van Den Hoogen, L. W. Van Laake, E. C. M. Van Eeuwijk, I. Hoefer, G. Pasterkamp, S. A. J. Chamuleau, P. F. Grundeman, P. A. Doevendans and J. P. G. Sluijter, *Eur. Heart J.*, 2017, **38**, 184–186.

10 A. Aicher, W. Brenner, M. Zuhayra, C. Badorff, S. Massoudi, B. Assmus, T. Eckey, E. Henze, A. M. Zeiher and S. Dimmeler, *Circulation*, 2003, **107**, 2134–2139.

11 D. Hou, E. A.-S. Youssef, T. J. Brinton, P. Zhang, P. Rogers, E. T. Price, A. C. Yeung, B. H. Johnstone, P. G. Yock and K. L. March, *Circulation*, 2005, **112**, I-150–I-156.

12 D. Blocklet, M. Toungouz, G. Berkenboom, M. Lambermont, P. Unger, N. Preumont, E. Stoupel, D. Egrise, J.-P. Degaute, M. Goldman and S. Goldman, *Stem Cells*, 2006, **24**, 333–336.

13 M. Hofmann, K. C. Wollert, G. P. Meyer, A. Menke, L. Arseniev, B. Hertenstein, A. Ganser, W. H. Knapp and H. Drexler, *Circulation*, 2005, **111**, 2198–2202.

14 J. de Souza Rebouças, N. S. Santos-Magalhães and F. Rocha Formiga, *Arq. Bras. Cardiol.*, 2016, **107**, 271–275.

15 H. Chu, D. S. Kohane and R. Langer, *Regen. Ther.*, 2016, **4**, 83–91.

16 P. M. Grossman, Z. Han, M. Palasis, J. J. Barry and R. J. Lederman, *Catheter. Cardiovasc. Interv. Off. J. Soc. Card. Angiogr. Interv.*, 2002, **55**, 392–397.

17 G. Tiwari, R. Tiwari, B. Sriwastawa, L. Bhati, S. Pandey, P. Pandey and S. K. Bannerjee, *Int. J. Pharm. Investig.*, 2012, **2**, 2–11.

18 W. Zhao, J. Zhao and J. Rong, *Oxid. Med. Cell. Longev.*, 2020, **2020**, 8815349.

19 P. Mladěnka, L. Applová, J. Patočka, V. M. Costa, F. Remiao, J. Pourová, A. Mladěnka, J. Karlíčková, L. Jahodář, M. Vopršalová, K. J. Varner, M. Štěrba and T.-O. and C. H. K. R. and Collaborators, *Med. Res. Rev.*, 2018, **38**, 1332–1403.

20 C. Li, J. Wang, Y. Wang, H. Gao, G. Wei, Y. Huang, H. Yu, Y. Gan, Y. Wang, L. Mei, H. Chen, H. Hu, Z. Zhang and Y. Jin, *Acta Pharm. Sin. B*, 2019, **9**, 1145–1162.

21 A. Sen Gupta, *Nanomedicine*, 2011, **7**, 763–779.

22 S. Hua and S. Y. Wu, *Front. Pharmacol.*, 2018, **9**, 1397.

23 D. Pretorius, V. Serpooshan and J. Zhang, *Front. Pharmacol.*, 2021, **12**, 163.

24 X. Mei and K. Cheng, *Front. Cardiovasc. Med.*, 2020, **7**, 294.

25 B. Peña, M. Laughter, S. Jett, T. J. Rowland, M. R. G. Taylor, L. Mestroni and D. Park, *Macromol. Biosci.*, 2018, **18**, 1800079.

26 C. J. Kearney and D. J. Mooney, *Nat. Mater.*, 2013, **12**, 1004–1017.

27 P. Huang, X. Wang, X. Liang, J. Yang, C. Zhang, D. Kong and W. Wang, *Acta Biomater.*, 2019, **85**, 1–26.

28 T. Aida, E. W. Meijer and S. I. Stupp, *Science*, 2012, **335**, 813–817.

29 J.-M. Lehn, *Angew. Chemie Int. Ed. English*, 1990, **29**, 1304–1319.

30 P. Y. W. Dankers and E. W. Meijer, *Bull. Chem. Soc. Jpn.*, 2007, **80**, 2047–2073.

31 M. J. Webber, E. A. Appel, E. W. Meijer and R. Langer, *Nat. Mater.*, 2015, **15**, 13–26.

32 G. Liu, Q. Yuan, G. Hollett, W. Zhao, Y. Kang and J. Wu, *Polym. Chem.*, 2018, **9**, 3436–3449.

33 B. Thu, P. Bruheim, T. Espevik, O. Smidsrød, P. Soon-Shiong and G. Skjåk-Braek, *Biomaterials*, 1996, **17**, 1031–1040.

34 R. C. van Gaal, J. F. van Sprang, Z. Borneman and P. Y. W. Dankers, *Macromol. Biosci.*, 2020, **20**, 1900277.

35 M. P. Hendricks, K. Sato, L. C. Palmer and S. I. Stupp, *Acc. Chem. Res.*, 2017, **50**, 2440–2448.

36 R. P. Sijbesma, F. H. Beijer, L. Brunsveld, B. J. B. Folmer, J. H. K. K. Hirschberg, R. F. M. Lange, J. K. L. Lowe and E. W. Meijer, *Science*, 1997, **278**, 1601–1604.

37 M. J. Webber, E. A. Appel, E. W. Meijer and R. Langer, *Nat. Mater.*, 2015, **15**, 13.

38 A. F. Mason and J. C. M. van Hest, *Emerg. Top. Life Sci.*, 2019, **3**, 567–571.

39 M. H. M. E. van Stevendaal, L. Vasiukas, N. A. Yewdall, A. F. Mason and J. C. M. van Hest, *ACS Appl. Mater. & interfaces*, 2021, **13**, 7879–7889.

40 A. F. Mason, B. C. Buddingh', D. S. Williams and J. C. M. van Hest, *J. Am. Chem. Soc.*, 2017, **139**, 17309–17312.

41 R. C. van Gaal, A. F. Vrehen, J. F. van Sprang, P.-P. K. H. Fransen, M. C. van Turnhout and P. Y. W. Dankers, *Biomater. Sci.*, 2021, **9**, 2209–2220.

42 B. D. Ippel, B. Arts, H. M. Keizer and P. Y. W. Dankers, *J. Polym. Sci. Part B Polym. Phys.*, 2019, **57**, 1725–1735.

43 R. C. van Gaal, A. B. C. Buskermolen, B. D. Ippel, P.-P. K. H. Fransen, S. Zaccaria, C. V. C. Bouten and P. Y. W. Dankers, *Biomaterials*, 2019, **224**, 119466.

44 D. N. Tran, D. Colesnic, S. Adam de Beaumais, G. Pembouong, F. Portier, Á. A. Queijo, J. Vázquez Tato, Y. Zhang, M. Ménand, L. Bouteiller and M. Sollogoub, *Org. Chem. Front.*, 2014, **1**, 703–706.

45 C. B. Rodell, A. L. Kaminski and J. A. Burdick, *Biomacromolecules*, 2013, **14**, 4125–4134.

46 J. D. Hartgerink, E. Beniash and S. I. Stupp, *Science*, 2001, **294**, 1684 LP – 1688.

47 F. H. Beijer, R. P. Sijbesma, H. Kooijman, A. L. Spek and E. W. Meijer, *J. Am. Chem. Soc.*, 1998, **120**, 6761–6769.

48 W. P. J. Appel, G. Portale, E. Wisse, P. Y. W. Dankers and E. W. Meijer, *Macromolecules*, 2011, **44**, 6776–6784.

49 R. C. van Gaal, B. D. Ippel, S. Spaans, M. I. Komil and P. Y. W. Dankers, *J. Polym. Sci.*, 2021, **59**, 1253–1266.

50 M. Diba, S. Spaans, S. I. S. Hendrikse, M. M. C. Bastings, M. J. G. Schotman, J. F. van Sprang, D. J. Wu, F. J. M. Hoeben, H. M. Janssen and P. Y. W. Dankers, *Adv. Mater.*, 2021, **33**, 2008111.

51 E. A. Mol, Z. Lei, M. T. Roefs, M. H. Bakker, M.-J. Goumans, P. A. Doevendans, P. Y. W. Dankers, P. Vader and J. P. G. Sluijter, *Adv. Healthc. Mater.*, 2019, **8**, 1900847.

52 M. J. G. Schotman, M. M. C. Peters, G. C. Krijger, I. van Adrichem, R. de Roos, J. L. M. Bemelmans, M. J. Pouderoijen, M. G. T. A. Rutten, K. Neef, S. A. J. Chamuleau and P. Y. W. Dankers, *Adv. Healthc. Mater.*, 2021, **10**, 2001987.

53 M. H. Bakker, R. E. Kieltyka, L. Albertazzi and P. Y. W. Dankers, *RSC Adv.*, 2016, **6**, 110600–110603.

54 M. Putti, O. M. J. A. Stassen, M. J. G. Schotman, C. M. Sahlgren and P. Y. W. Dankers, *ACS Omega*, 2019, **4**, 8178–8187.

55 M. M. C. Bastings, S. Koudstaal, R. E. Kieltyka, Y. Nakano, A. C. H. Pape, D. A. M. Feyen, F. J. van Slochteren, P. A. Doevendans, J. P. G. Sluijter, E. W. Meijer, S. A. J. Chamuleau and P. Y. W. Dankers, *Adv. Healthc. Mater.*, 2014, **3**, 70–78.

56 M. H. Bakker, E. van Rooij and P. Y. W. Dankers, *Chem. – An Asian J.*, 2018, **13**, 3501–3508.

57 M. H. Bakker, M. Grillaud, D. J. Wu, P.-P. K. H. Fransen, I. H. de Hingh and P. Y. W. Dankers, *Macromol. Rapid Commun.*, 2018, **39**, 1800007.

58 M. H. Bakker, C. C. S. Tseng, H. M. Keizer, P. R. Seevinck, H. M. Janssen, F. J. Van Slochteren, S. A. J. Chamuleau and P. Y. W. Dankers, *Adv. Healthc. Mater.*, 2018, **7**, 1–8.

59 R. E. Kieltyka, A. C. H. Pape, L. Albertazzi, Y. Nakano, M. M. C. Bastings, I. K. Voets, P. Y. W. Dankers and E. W. Meijer, *J. Am. Chem. Soc.*, 2013, **135**, 11159–11164.

2

Factors influencing retention of injected biomaterials to treat myocardial infarction

Abstract

Biomaterials that are commonly used for the regenerative treatment of myocardial infarction (MI), often have the capacity to release drugs in a sustained manner, providing strength and stability to the infarcted area, or mimic the extracellular matrix. Retention and redistribution of the injected biomaterials is a factor often overlooked, but plays a significant role in the effectiveness of the treatment. Wash-out of therapeutics from the cardiac area can lead to unwanted side-effects and can therefore add insult to injury. Here, we seek a deeper understanding on the mechanisms that play an important role in the retention of injected therapeutics, being: materials, drugs or a combination thereof. In this chapter, we discuss several factors influencing the therapeutic quantity retained at the target site; being the timing of injection after MI, cardiac pulsation, as well as injectate properties such as volume, mechanical properties, and tissue affinity. We highlight the importance of understanding and taking into account these different parameters. More insight in these parameters can lead to an increase in therapeutic effectiveness, in addition to examination of indirect off-target effects.

This content of this chapter is based on:

M. J. G. Schotman, P. Y. W. Dankers, *Factors influencing retention of injected biomaterials to treat myocardial infarction*, in revision at Advanced Materials Interfaces

1. Introduction

Myocardial infarction (MI) is one of the highest leading causes of death worldwide induced mainly by atherosclerosis, which leads to a reduction or obstruction of blood flow in the coronary circulation.[1] A significant infarction leads to adverse remodeling of the heart, in which fibrosis formation decreases contractile function leading to heart failure.[2]

Current treatments are mostly palliative, focusing on improvement of life quality.[3] New possible drug therapies, e.g. proteins, growth factors, and ribonucleic acid interference (RNAi) drugs, are proposed to stimulate cardiac regeneration.[4-6] These therapies are often injected in or at the border zone of the myocardial infarcted area. However, these injected drugs are rapidly washed away from the pulsatile heart without a delivery system. A wide variety of studies focus on the injection of drugs encapsulated in biomaterials, which can increase the efficacy of encapsulated drugs and improve cardiac function.[7-9]

There are several drug delivery systems that focus on cardiac repair.[10,11] Nano- and microparticles are a class of materials used for targeted therapies aiming to repair the cardiac muscle, in which therapeutics can be encapsulated.[12,13] Other microparticles aim to mimic cellular-like systems, the so-called cell-mimicking microparticles. Poly(-lactic glycolic acid) (PLGA)-based microparticles, carrying similar secreted proteins as cardiac stem cells, were injected to examine their potential to preserve viable myocardium.[8] Microparticles are also being used in the field of theranostics, providing localization in vivo after injection, as well as delivering therapeutics to the site of injection.[14] Other type of microparticles, such as hydrogel microparticles, are used in biomedical applications to deliver cells, drugs, or initiate aggregation at the site of injection to form a microporous scaffold.[15] A high number of studies focus on injectable hydrogels on which the focus will lie mainly in this chapter, which offer the possibility to deliver cells[16-18], drugs[19-22], and mechanical support to the target site[23-25].

To maximize the targeted effect of the drugs encapsulated in hydrogel, the retention at the target site is of high importance. The efficacy of biomaterials (in combination with drugs) is often determined by examining indirect parameters such as the scar thickness, ejection fraction (EF), end-diastolic dimension (EDD), and fractional shortening (FS).[16,26,27] In contrast, only a limited amount of studies focus on the retention of the biomaterial in the heart.[28] It is important to establish a relation between the drug delivery system and cardiac regeneration, which can give more insight in the amount-depending effectiveness of the delivery system. Additionally, examining and possibly increasing the retention of the therapeutic biomaterial at the target site could reduce possible off-target effects (Figure 2.1).

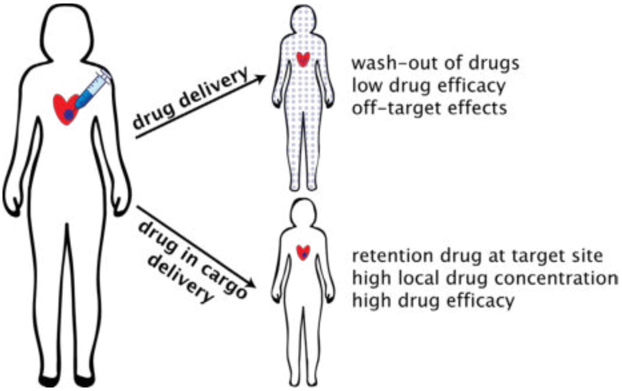

Figure 2.1 Different therapeutic delivery methods are shown in which wash-out of the injected drugs lead to unwanted off-target effects. Drug-containing cargo delivery can increase the effectiveness of the drugs by retention at the target site.

In this review, we specify key parameters which can affect the retention of the delivery system in the cardiac infarcted area, focusing mainly on injectable hydrogels. First, heart inherent characteristics will be described with the focus on injection timing post-MI and cardiac pulsation, followed by characteristics of the hydrogel system such as mechanical properties and tissue affinity (Figure 2.2). Finally, we speculate on the impact of these key parameters on hydrogel retention and focus on the off-target effects that can be induced in case of limited retention. The aim of this chapter is to obtain a deeper understanding on main factors influencing the retention of injectable hydrogels for cardiac repair, which will aid towards improved cardiac regenerative therapies.

2. Cardiac features influencing therapeutic retention

There is a high demand for heart regenerative therapies, due to the incapacity of the heart to regenerate itself post-MI after severe deterioration.[29] One of the major challenges of cardiac disease is improving the efficacy of injected therapeutic agents, with a majority being washed away from the target site due to the continuous movement of the heart.[30] Often, a swift wash-out from the myocardium can be observed *via* the venous drainage, i.e. after intramyocardial cellular injection.[31] Repeated administrations are often necessary to obtain and sustain effective drug levels, which can cause severe side effects depending on the type of drug.[32] This applies mainly to biomolecules with a short half-life, such as RNAi drugs, proteins, and peptides.[33] Improving retention and drug efficacy at the target site will limit the amount of injections necessary for a therapeutic effect. Combinations of hydrogel and therapeutics, as well as the hydrogel alone, which can be injected at the target site, have shown to improve the functional cardiac output when injected post-MI. In this section key parameters known to influence the therapeutic retention by inherent cardiac traits will be discussed, being time of injection and cardiac contraction.

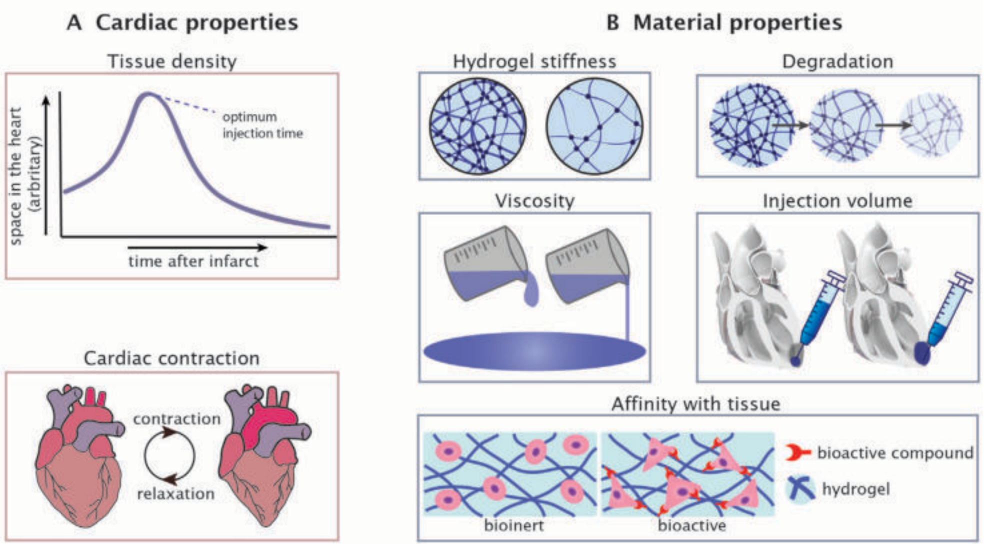

Figure 2.2 The different factors influencing retention of delivery systems; A. inherent cardiac properties such as the timing of injection and cardiac contraction, B. material properties such as the hydrogel stiffness, degradation, viscosity, injection volume and affinity with the tissue.

2.1 Timing of injection therapy

Severe MI leads to a cascade of cellular processes and remodeling events, that result in scar tissue formation to compensate for the loss of cardiomyocytes. The difference between healthy myocardial tissue and myocardial tissue post-infarction is significant, with an extensively higher collagen depletion post-MI.[34] Three main phases post-MI occur; the inflammatory phase, the proliferative phase, and the maturation phase (Figure 2.3).[35] Due to the fast remodeling and progressive pathophysiological process after a cardiac infarct occurs, the timing of therapeutic injection is most likely to have a significant effect on the cardiac outcome[36]. After an infarct occurs, the therapy can be injected early post-MI (during the inflammatory phase), late post-MI (during proliferative phase), or very late post-MI (during or after the healing phase). A greater expression of chemo-attractants and adhesion molecules is hypothesized to be present during the inflammatory phase, which can promote cellular retention.[37,38] However, other studies indicate the harsh conditions of the microenvironment to hamper the cellular viability.[39] When reperfusion in the ischemic myocardium occurred during the first 3 hours after MI, the infarct size was limited significantly and a high number of myocytes were salvaged.[40] An early response directly after MI can therefore lead to a limited remodeling process, but in practice this is challenging to accomplish. Collagenase and gelatinase activity is upregulated during the inflammatory phase, leading to disruption of the collagen network.[41] This can result in an increase of hydrogel degradation during this phase, lowering therapeutic effectiveness. The myocardial interstitium directly post-MI is still preserved, which slowly changes during the inflammatory phase.[42] This forces the hydrogel between fibrillar bundles of the interstices when injected directly post-MI, possibly giving the hydrogel a less bulky character, providing less mechanical support.

Some studies indicate the increased effectiveness in therapy when injected during the proliferating phase, during which the inflammation is resolved and fibroblasts proliferation initiates the formation of collagen-rich scar tissue. Injection during this phase can limit the extracellular matrix (ECM) remodeling and stimulate infarct repair.[43,44] Furthermore, a reduced inflammatory response during this phase can result in lower hydrogel degradation. Subsequently, a higher retention of the injected hydrogel due to limited degradation can be obtained, with a large bulk amount of hydrogel providing myocardial support at the site of injection.

During the healing phase, the scar tissue undergoes a maturation process where the ECM becomes cross-linked and reparative cells are deactivated or go into apoptosis. Myofibroblasts remain, producing collagen and ensuring the ECM remodeling.[43] This process is highly dependent on the size of the infarcted area, with large infarcts inducing this adverse remodeling process.[45] The scar tissue can influence the injectability of the therapeutic carrier, with the stiffness of the collagen changing steadily over time as shown by Fomovsky et al.[46] Myocardial wall thinning can be observed after the healing period[47], due to the increase of ventricular wall stress over time that can dilate the cavity.[48] This extensive wall thinning, which is species independent[49], can lead to a difficulty of injection at the target site, with thin and dense tissue being problematic for injection beyond the healing phase.[41] Furthermore, the delivery of growth factors or other therapeutics can be less effective during the healing phase, when scar maturation is already in a developed stage, limiting regeneration with therapeutics.[39]

Several studies showed the importance of injection timing considering cellular injectates in the infarcted area.[50-55] For hydrogel injection, this timing is also highly important, as shown by Landa et al. who injected a calcium-crosslinked alginate solution in an infarcted rat heart 7 days and 60 days post-myocardial infarction, corresponding to the proliferation and beyond the healing phase, respectively.[56] The cardiac function was examined 60 days after hydrogel injection, with the 7 days post-MI injection showing an increased scar thickness and a reduced left ventricular systolic and diastolic dilation, as well as cardiomyocyte migration to the infarcted area. The 60 days post-MI injection showed beneficial effects as well, but to a lower extent, with an increased scar thickness and improved systolic and diastolic function observed 60 days post-injection. Kadner et al. examined this timing effect after inducing MI in rat heart models, with injection of a poly(ethylene glycol) (PEG)-based hydrogel crosslinked with an enzymatically degradable peptide sequence that was injected immediately and seven days post-MI.[57] Immediate injection post-MI led to no observable improvements, while the delayed delivery led to significant increases in scar thickness, fractional shortening, and reduction in end-systolic diameter against saline controls, examined two and four weeks post-injection.

The timing effect of a thermo-responsive hydrogel was examined by Yoshizumi et al., injecting the biodegradable hydrogel poly(NIPAAm-co-HEMA-co-MAPLA) (NIPAAm: N-isopropylacrylamide methacrylate, HEMA: (hydroxyethyl)methacrylate, MAPLA: methacrylate-polylactic acid)) in a infarcted rat heart.[58] Three different injection time-points were examined, being immediately after MI, three days after MI (3D), and two weeks after MI (2W). Ten weeks post-MI, the 3D and 2W groups showed a beneficial effect over the non-treatment MI control group. The left ventricle wall was thicker, and the 3D group showed the most beneficial effect. Furthermore, the infarction size of the 3D group was smaller in comparison to the control and the 2W group. The hydrogel injection immediately post-MI did not show improved therapeutic effects.

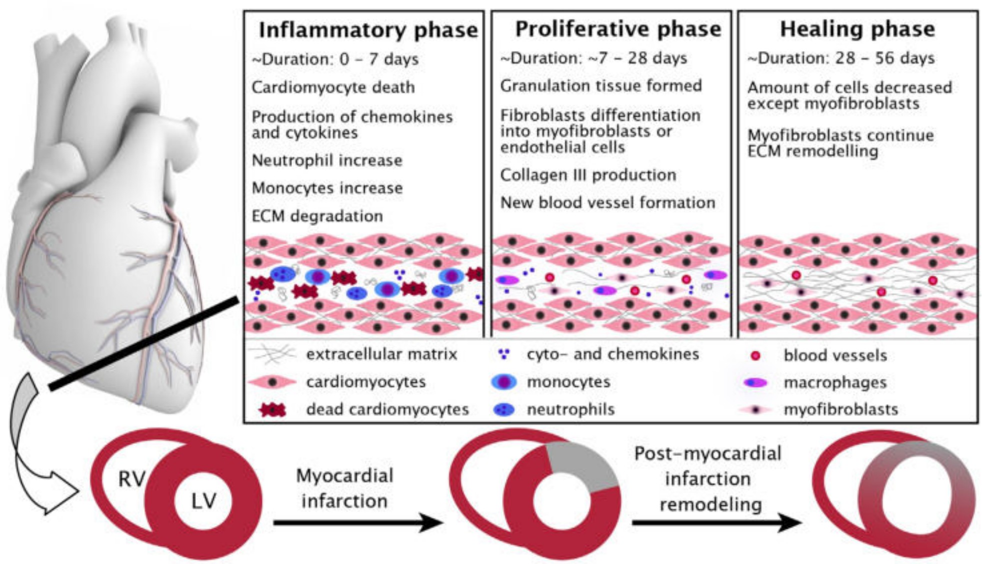

Figure 2.3 Overview of the three stages of cardiac healing post-MI in humans. Directly after MI, oxygen depletion leads to cardiomyocyte death by apoptosis and necrosis. Necrotic cells produce chemokines and cytokines that attract neutrophils and monocytes from the blood. The ECM is degraded, enhancing neutrophils to migrate deep in the tissue (inflammatory phase). Granulation tissue is formed and fibroblasts differentiate into myofibroblasts or endothelial cells, producing ECM consisting mainly of collagen III and blood vessels (proliferative phase). In the final phase, the cell amount is decreased with the exception of myofibroblasts that continue ECM remodeling. Illustrative short axis slices of the heart are shown, representing healthy tissue, tissue shortly after the infract, and tissue after the healing phase.

The timing effect of an injectable hydrogel based on collagen (from rat tail) was examined in an infarcted mouse heart, being injected at 3 hours, 7 days, and 14 days post-MI.[59] The 3 day post-MI injection showed the most beneficial results 4 weeks after therapeutic injection, with the highest left ventricular ejection fraction (LVEF) in comparison to the 7 days, 14 days, and control experiments. This indicated an optimal effect when injecting during the inflammatory phase, whereas a beneficial effect was observed when injected during the proliferation phase (7 day), but to a lower extent. In a follow-up study from the same group, hydrogels based on collagen type III were injected in an infarcted mouse heart at single and multiple time points.[60] The single treatment (3 hours post-MI) showed the highest improvement in LVEF over time compared to the saline controls, which was examined up to 6 weeks. A slight improvement was shown in cardiac function when injecting at three time-points (3 hours, 7 days, and 14 days post-MI), whereas the multiple time point injections at 7 days and 14 days showed a reduction in cardiac function (LVEF) compared to the saline control.

What should be noted is that all of these studies are performed on rodent models, which show differences in cardiac remodeling time of the infarcted area in comparison to humans, with the healing phase of a rat infarction being complete after 3 weeks[61], whereas in humans duration of the healing phase can last around 5 to 6 weeks or more[45]. The inflammatory phase of a rat lasts typically around ~0-5 days post-MI, whereas the proliferation phase occurs after ~5-14 days post-MI.[41] Optimal injection times for rodent models are therefore not directly translatable for human application. An interesting aspect which these studies suggest, is the difference in optimal therapeutic timing between non-bioactive hydrogels (PEG-based and poly(NIPAAm)-based) and bioactive hydrogels (collagen-based). The non-bioactive hydrogels show a trend towards an optimal effect when injected during the proliferation phase, whereas the bioactive hydrogels show a trend towards an optimal effect when injected during the inflammation phase. While the non-bioactive hydrogels are injected to provide mechanical support and therefore stress release to the infarcted tissue, as hypothesized by several studies, injection during the inflammatory phase can possibly lead to a high extent of MMPs and ECM-degrading activity, degrading the non-bioactive hydrogels.[60] During the proliferation phase, these MMPs and ECM-degrading molecules are present in a lower content, slowing down the degradation and not limiting the local gelation. Degradation products of bioactive hydrogels can, in contrast, stimulate signaling cascades leading to cellular adhesion, migration and survival.[62] However, more studies are necessary to truly confirm this effect, as well as the translation towards large animal studies.

While all of these outcomes indicate beneficial cardiac outcomes, to our knowledge the long-term effects of these studies are unknown, with monitoring times not exceeding 3 months.

2.2 Cardiac contraction

In healthy humans the heart pumps approximately 60-100 times per minute with a constant pressure on the ventricles and atria, the force not changing at higher pumping frequencies.[63] A high number of contractile cells are lost post-MI, subsequently leading to lower contractile forces.[64] Injectates are likely to be 'washed away' from this area without any retention, with the pumping function of the heart pushing the injectate out of the target area, e.g. via venous drainage, or squeezed out of the myocardium.[31] The effect of cardiac contraction on injected therapeutics will briefly be described in this section.

The influence of an arrested heart in comparison with a contracting heart is a subject only few studies focus on. A study that does examine this was performed by Terrovitis et al., in which cardiac-derived stem cells were labeled with fluorodeoxyglucose-18 for quantification purpose, and injected in a beating and non-beating MI rat model.[65] Retention of the stem cells in an arrested heart showed to be significantly higher in comparison to the contracting heart, being 75% and 17%, respectively. This indicates that a prominent reason of the cells being washed out of the myocardium of a rat is due to the cardiac contractile function. We hypothesize that hydrogels will respond in a similar manner to the contractile function, but displaying a lower wash-out from the injectate site due to an increased viscosity and lower flow. To our knowledge, no study has thus far has examined the retention of injectable hydrogels in a beating as well as an arrested heart. An increased cellular retention has been observed when encapsulated in an injectable hydrogel.[66-68] Furthermore, many studies have observed an enhanced therapeutic effect when combining the cells with a carrier material.[69,70] Hydrogels itself are also observed to show a functional therapeutic outcome when injected, having mechanical support and therefore elevating wall stress, or mimicking the natural myocardial structure.[71] When hydrogels exhibit rapid gelation, an increase in retention can be obtained, with the gel exhibiting lower flow properties and therefore less wash-out. The contraction can influence the shape of the injected hydrogel, changing its morphology. Self-healing hydrogels are interesting candidates for cardiac delivery, being a hydrogel that has the ability to reversibly repair the damages to itself and recover its functions.[72] For examining the properties of hydrogels, fatigue resistant experiments are often performed on hydrogels, examining the rheological properties of the hydrogel and the ability of the hydrogel to respond to stimuli.[73] In the subsection 'Mechanical biomaterial properties', the mechanical properties of these biomaterials will be discussed more extensively.

3. Biomaterial features influencing therapeutic retention

A high number of natural or synthetic hydrogels, sometimes in combination with therapeutic agents, have been used for cardiac therapies (Figure 2.4). Natural, more bioactive hydrogels (such as decellularized ECM) often induce physiological and chemical signaling mechanisms[24], or improve cell survival and cell motility into the surrounding tissue. Bioinert hydrogels (such as alginate-based hydrogels) are hypothesized to reduce the mean wall stress by the bulking of wall thickness upon hydrogel injection according to Laplace's law, or, as presumed by more recent studies, diminish the stress of cardiomyocytes surrounding the hydrogel on a more cellular level.[24,74,75] Other parameters, such as injection volume, mechanical properties, and injectate retention are of influence on the therapeutic efficacy. These factors will be discussed here.

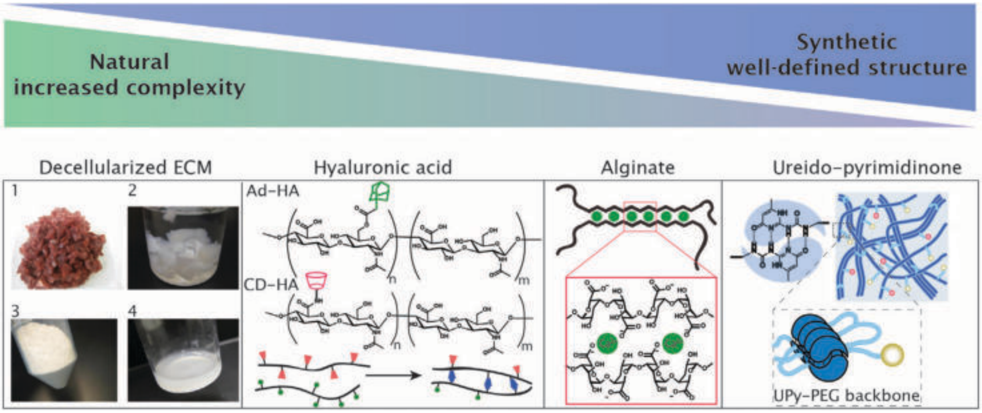

Figure 2.4 Structural properties of supramolecular hydrogels used for cardiac therapy, with a natural hydrogel such as decellularized ECM is prepared by cutting left ventricular porcine tissue into small pieces (1), decellularization (2), lyophilization (3) and the decellularized ECM powder partially digested into an injectable liquid by pepsin (4). Hyaluronic acid can form physical crosslinks by functionalization of cyclodextrin (CD-HA) and adamantane (Ad-HA), which can crosslink by guest-host assembly. Alginate is known to physically cross-link and gelate in the presence of calcium ions. The ureido-pyrimidinone moiety is known to crosslink

based on four-fold hydrogen bonding, which can be disrupted by increasing the pH above 8.5. The natural hydrogels show bio-based high complexity and synthetic hydrogels showing a well-defined structure. Reproduced with permission.[76] Copyright 2016, Elsevier.

3.1 Injection volume

A high number of the cardiomyocytes are lost during an MI, and therefore a number of studies attempted to increase the amount of cells at the infarcted area by injecting viable cells. Different amounts of cells and volumes are often injected, varying with each study and model.[77-84] In human trials, bone marrow-derived stem cells were injected post-infarction, with the total injection volume varying from 10-26 mL.[53,85-87] This indicates no 'golden standard' for the injection volumes, considering these studies.

For injectable hydrogels, to our knowledge, few studies have focused on the volume optimalization in the infarcted myocardium. However, finite element model based studies were performed, in which the optimal volume of the injectate for cardiac therapy was determined. Here, we describe the few studies that did volume optimization experiments, as performed by Wise et al., who developed a finite model of a rat heart and showed the therapeutic benefit between the injection volume of a stiff PEG-based hydrogel and the infarct size.[88] With an infarcted area of 10% of the ventricle wall, 50% volume injection showed to have the largest benefits in comparison to the 25% and 75% volume injection. It was concluded that the injected volume relative to the infarcted area is of influence, and the effectiveness of the injected gel depends on this ratio. Injecting an excessive hydrogel volume could even further decrease the cardiac function. Therefore, the amount of volume injected is of high importance and more caution should be taken on the extensiveness of the infarcted area and the injected hydrogel volume.

The effect of alginate hydrogel injection in an MI swine model was examined during a 60-day follow-up.[89] Three different injection volumes were used, 1, 2 and 4 mL of hydrogel in total. The hydrogel was injected by intracoronary injection, 3 to 4 days post-MI. Favorable effects on the LV remodeling were observed when 2 and 4 mL of hydrogel were injected in the infarcted site, in comparison to 1 mL hydrogel injection. Mild favorable effects were observed for the animals treated with 1 mL hydrogel, preventing little left ventricle diastolic and systolic dilation compared with the control MI model. Hydrogel injections of 2 and 4 mL showed an increase in left ventricle mass, and reversed left ventricle diastolic and systolic dilation.

Table 1. Studies using hydrogel delivery for targeting myocardial infarction since 2017

Hydrogel material (and cell/therapeutic molecules	Model	Injected volume	Time of administration post-MI	Delivery method	End-point after treatment	Functional outcome compared to infarct control	Reference
Hyaluronic acid-based hydrogel with of chol-modified miR-302	Mice	10 µL (with 2 injections)	Directly post-MI	Intramyocardial injection	28 days post-therapy	improved cardiomyocyte proliferation, improved EF and FS, and reduced LVEDV / LVESV, decrease in infarct size	Wang et al.[7]
Laponite® and gelatin type A hydrogel containing secretome of human adipose-derived stem cells	Rat	100 µL (with 5 injections)	Directly post-MI	Intramyocardial injection	21 days post-therapy	Improved EF and FS, decrease in infarct size, increase capillary formation	Waters et al.[93]
Enzymatically degradable PEG-based hydrogel containing heparin and MSC in different cell densities	Rat	100 µL (with 3/4 injections)	30 minutes post-MI	Intramyocardial injection	30 days post-therapy	Improved FS and EF, prevented increase EDD and ESD, prevention anterior wall thinning, reduced scar area	Ciuffreda et al.[16]
Triblock copolymers (PArg-PEG-PArg) and PMNT-PEG-PMNT coupled with poly(acrylic acid)	Mice	50 µL	Directly post-MI	Intramyocardial injection	28 days post-therapy	Improved thickness myocardial tissue, Improved EF and FS, smaller infarction size	Binh Vong et al.[94]
A Mix of mesoporous silica nanoparticles/miR-21 complex combined with aqueous solution of α-cyclodextrin and aldehyde-capped PEG	Pigs	600 µL (with 6 injections)	Directly post-MI	Intramyocardial injection	28 days post-therapy	increase in EF, preserved myocardial wall thickness, small infarct size. Enhanced vascularization	Li et al.[95]
Liposomes based on phosphatidycholine and cholesterol containing VEGF, loaded into a hyaluronic acid-based hydrogel	Rats	100 µL	Directly post-MI	Intramyocardial injection	28 days post-therapy	Increased capillary density, lowest LVDD and LVSD values. Improved EF an FS, thicker ventricle wall	Zhang et al.[96]

Hydrogel material (and cell/therapeutic molecules	Model	Injected volume	Time of administration post-MI	Delivery method	End-point after treatment	Functional outcome compared to infarct control	Reference
N,N-methylenebis(acrylamide) + acrylic acid + core-shell poly(NIPAM) microgels loaded with tissue plasminogen activator (tPA) and small molecule Y-27632	Rats	50 µL	Directly post-MI	Injections in the ventricular cavity with temporary aortic occlusion	28 days post-therapy	Improved EF and FS, decreased scar size, decreased fibrotic markers	Mihalko et al.[97]
Poly(NIPAAm-co-HEMA-co-MAPLA) hydrogel	Rats and pigs	Rat: 100 µL (with 5 injections) Pig: 4 mL (with 20 injections)	Rat: 3 day post-MI Pig: 2 weeks post-MI	Intramyocardial injection for both models	8 weeks post-therapy for both models	Rats: maintained stiffness of LV, Porcine: preserved ESV, improved EF, fractional area change, and cardiac index, smaller infarct size, thicker LV wall.	Matsumura et al.[23]
basic fibroblast growth factor-loaded PVA-TSPBA crosslinked hydrogel	Rats	7.6 mg/kg (estimated ~100 µL)	30 minutes post-MI	Pericardial cavity injection	28 days post-therapy	Smaller scar size, increased EF and FS, reduction in LV hypertrophy	Li et al.[98]
Alginate hydrogel	Swine	3.6 - 4.2 mL (with 12-14 injections)	8 weeks post-MI	Intramyocardial injection	8 weeks post-therapy	Increase in EF, lower pressures at end diastole, reduction of yofiber strains in hydrogel vicinity	Sack et al.[24]
PEG functionalized with UPy-moiety based hydrogel containing VEGF	Mice	20 µL (with 2 injections)	Directly post-MI	Intramyocardial injection	22 days post-therapy	Improved EF and LVESV, improved regional myocardial strain, reduced fibrosis.	Van den Boomen et al. [99]
Alginate hydrogel	Swine	3.6 - 4.2 mL (with 12-14 injections)	8 weeks post-MI	Intramyocardial injection	8 weeks post-therapy	Improved stroke volume, EF, wall thickness, LVESV, reduced myofiber stress	Choy et al.[100]

Hydrogel material (and cell/therapeutic molecules	Model	Injected volume	Time of administration post-MI	Delivery method	End-point after treatment	Functional outcome compared to infarct control	Reference
Alginate hydrogel	Humans	4.6 mL (mean varying per person, 0.3 mL per injections)	Within 30 days post-MI	Intramyocardial injection	6 months post-therapy	Improved exercise capacity, no echocardiographic significant differences	Anker et al. [101]
Extracellular matrix hydrogel	Humans	5.4 mL (maximum amount, varied per person, 0.3 mL injections)	60 days and 3 years post-MI	Percutaneous transendocardial injections	6 months post-therapy	Improvements were showed in the 6-min walk test, no echocardiographic significant differences	Traverse et al.[102]
Hyaluronic acid hydrogel containing rTIMP-3 protein	Pigs	900 µL (with 9 injections)	Directly post-MI	Intramyocardial injection	28 days post-therapy	Improved EF, lower LVEDV and LVESV, reduced LV filling pressure. Reduced fibrillar collagen content.	Purcell et al. [103]
Recombinant human collagen type 1 and type 3.	Mice	50 µL (with 5 injections)	1 week post-MI	Intramyocardial injection	28 days post-therapy	Improved EF. Reduced EDV, restored tensile elasticity of infarcted myocardium, Increased wall thickness for both hydrogels, and reduced scar size.	McLaughlin et al.[104]
Hyaluronic acid hydrogel containing extracellular vesicles	Rats	100 µL (with 5 injections)	Directly post-MI	Intramyocardial injection	28 days post-therapy	Improved EF, increased systolic and diastolic pressure, increased vascular density, increased scar thickness	Chen et al.[68]

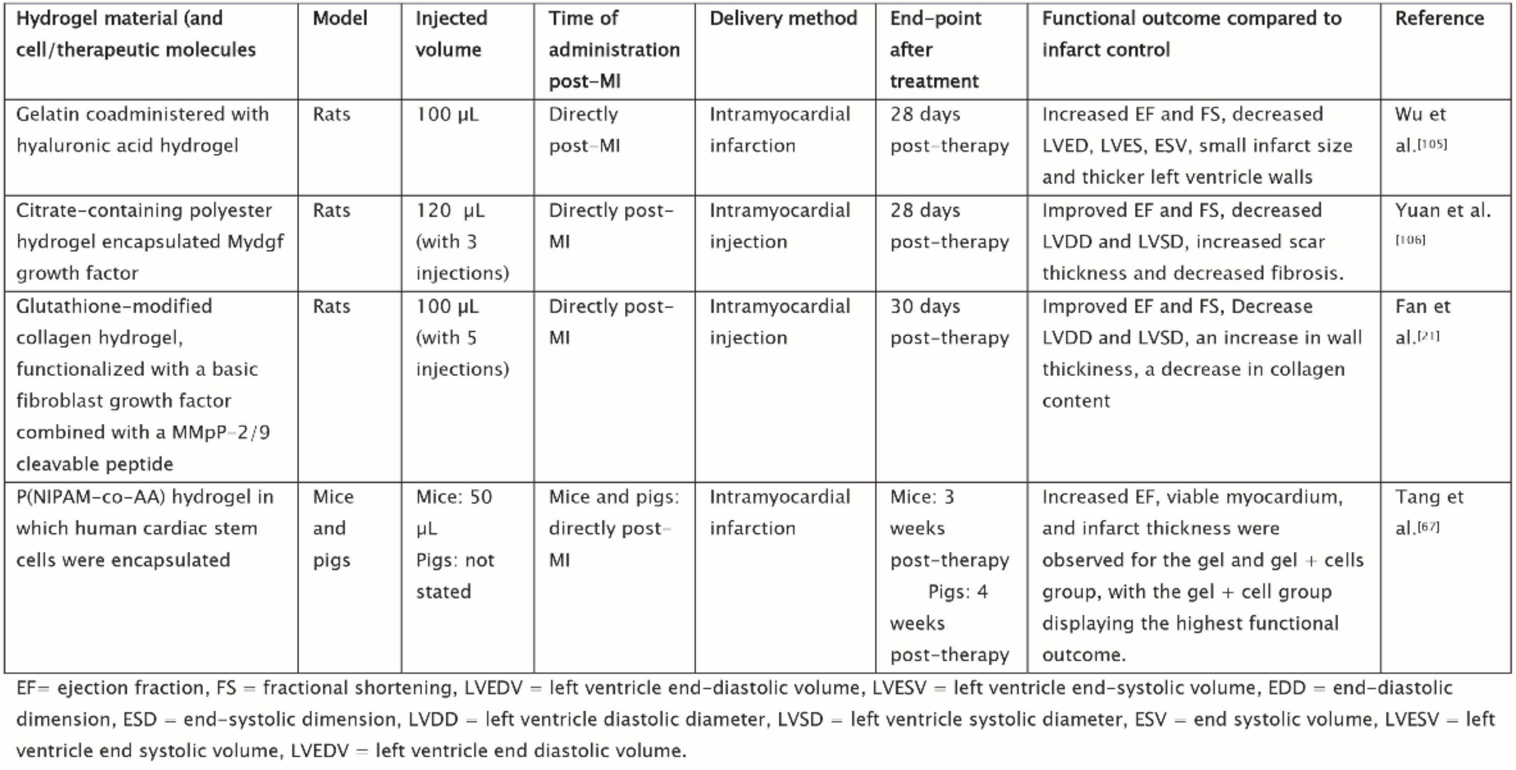

Hydrogel material (and cell/therapeutic molecules	Model	Injected volume	Time of administration post-MI	Delivery method	End-point after treatment	Functional outcome compared to infarct control	Reference
Gelatin coadministered with hyaluronic acid hydrogel	Rats	100 µL	Directly post-MI	Intramyocardial infarction	28 days post-therapy	Increased EF and FS, decreased LVED, LVES, ESV, small infarct size and thicker left ventricle walls	Wu et al.[105]
Citrate-containing polyester hydrogel encapsulated Mydgf growth factor	Rats	120 µL (with 3 injections)	Directly post-MI	Intramyocardial injection	28 days post-therapy	Improved EF and FS, decreased LVDD and LVSD, increased scar thickness and decreased fibrosis.	Yuan et al. [106]
Glutathione-modified collagen hydrogel, functionalized with a basic fibroblast growth factor combined with a MMpP-2/9 cleavable peptide	Rats	100 µL (with 5 injections)	Directly post-MI	Intramyocardial injection	30 days post-therapy	Improved EF and FS, Decrease LVDD and LVSD, an increase in wall thickiness, a decrease in collagen content	Fan et al.[21]
P(NIPAM-co-AA) hydrogel in which human cardiac stem cells were encapsulated	Mice and pigs	Mice: 50 µL Pigs: not stated	Mice and pigs: directly post-MI	Intramyocardial infarction	Mice: 3 weeks post-therapy Pigs: 4 weeks post-therapy	Increased EF, viable myocardium, and infarct thickness were observed for the gel and gel + cells group, with the gel + cell group displaying the highest functional outcome.	Tang et al.[67]

EF= ejection fraction, FS = fractional shortening, LVEDV = left ventricle end-diastolic volume, LVESV = left ventricle end-systolic volume, EDD = end-diastolic dimension, ESD = end-systolic dimension, LVDD = left ventricle diastolic diameter, LVSD = left ventricle systolic diameter, ESV = end systolic volume, LVESV = left ventricle end systolic volume, LVEDV = left ventricle end diastolic volume.

A study by Wang et al. showed the different functional outcomes with finite element models, in which 150 μL and 300 μL of hydrogels with varying stiffness were injected.[90] 150 μL hydrogel injection with a stiffness of 25 kPa reduced the myofibril stress by 18.9% at the epicardium, while 300 μL injection reduced the stress by 31%. Furthermore, 150 μL hydrogel injection with a stiffness of 100 kPa led to myofiber stress reduction of 39.2% at the epicardium, whilst 300 μL injection of the same hydrogel showed a stress reduction of 56.8%. The end diastolic volume decreased more extensively when 300 μL was used compared to the 150 μL injection volume. A finite element model of an ovine left ventricle was exploited by Wall et al., who examined the short-term effects of material injection, comparing a single injection, and multiple injections with changing volumes.[91] Here, decreasing fiber stresses were also observed with increasing volume fraction (examined from 0.5-1.5 mL), in which stiffer materials furthermore improved this reduction. Additionally, the EF and stroke-volume / end-diastolic volume were improved. However, no significant changes were observed in the multiple injection group, in comparison to the infarct control.

Another finite element model examined different factors which are of influence on hydrogel efficacy, being injection volume, hydrogel stiffness, and timing of injection.[92] The hydrogel injection overall showed to reduce the myocardial strain under physiological loading. Three volumes were modelled, being 15, 50, and 170 μL (1.5-17% of the total region volume), of which the local strain was decreased when the hydrogel volume was increased. Furthermore, increasing hydrogel stiffness showed further reduction in myocardial strain, with optimal moduli between 1-25 kPa. Recent studies have hypothesized that bioinert hydrogels can reduce the stress on the myocytes by stimulating fibrotic encapsulation around the surface of the hydrogel, constraining the myocytes to the surface. This can prevent left ventricular dilation, and therefore decreases the stress of the surrounding myocytes.[24,92] Several recent studies have been summarized in a table, with the volume, model, time of administration, delivery method, end-point time after treatment, and functional outcome presented (Table 1). As shown by these studies, the volume of the hydrogel injected at the target site varies highly, with volumes used in porcine models varying from 0.9 mL to ~4 mL. The volumes used in rodent studies seemed to vary from 20 μL to 120 μL, all showing therapeutic beneficial results.

We suggest that future studies need to focus on finding the optimal hydrogel injection volume. A handful of studies presented here show promising work in optimization of hydrogel volumes for cardiac therapy, mainly by using finite element models. Accurate determination of the optimal hydrogel volume follows increased therapeutic. Whether there is a relation between volume amount and cardiac retention is still an open question.

3.2 Mechanical properties of hydrogels

Injectable hydrogels are of great interest for cardiac applications, due to the minimally invasive manner in which they can be delivered to the target area.[107] Stimuli-responsive hydrogels are often used in the cardiac therapy field, with their ability to adapt and gelate in situ based on responses to physical changes such as temperature[108,109], and pH[109,110]. Furthermore, non-inert hydrogels such as fibrin and ECM-derived hydrogels show beneficial results for the treatment of myocardial infarction[111-113]. Often, these hydrogels show a low stiffness (<100 Pa), and their function is mostly dependent on the inherent bioactive compounds inducing a combination of physiological and chemical signaling mechanisms. Therefore, the focus in this subsection lies mostly on inert tunable injectable hydrogels, and their mechanical properties when regarding the therapeutic efficacy.

Hydrogel stiffness

The hydrogel stiffness indicates the rigidity of the hydrogel, and to which extent the hydrogel is able to resist deformation under force. The stiffness of a hydrogel can often be tuned by varying the concentration or cross-linking density. When injected in the myocardium after an infarct, the deformation under the cardiac force is therefore an important parameter to examine. These mechanical properties of the hydrogels, with the focus on moduli, were examined by Ifkovits et al., who injected hyaluronic acid-based hydrogels with differing moduli (~8 and 43 kPa), adapted by a change in the number of reactive methacrylate groups.[114] The hydrogels were injected in an infarcted ovine model 30 minutes post-MI (20 injections of 0.3 mL), and 8 weeks post-MI the functional output was examined. Their findings showed less infarct expansion and reduced LV dilation in the higher modulus group, in comparison to the lower modulus group. An increase in myocardial stabilization was hypothesized, with the high modulus gel reducing the wall stresses in an increased extend in comparison to the low modulus gel. However, only a trend towards functional cardiac improvements was shown in the stiffer hydrogel group, with no significant changes.

These mechanical properties of hyaluronic acid-based hydrogels were further examined by Rodell et al., using a tandem crosslinking approach with the injection of hyaluronic acid hydrogel (<1 kPa), followed by a second injection which stiffened the hydrogel network in situ due to dual-crosslinking (~41 kPa).[115] Infarcted ovine models were used, in which the hydrogels were injected 30 minutes post-MI (16 injections of 0.3 mL). The functional output was examined 8 weeks post-MI. The dual-crosslinked hydrogel showed to have an optimal effect compared to the MI control, with a significant stress reduction, maintaining wall thickness, and improved EF. Some improvements were observed with the lower modulus hydrogel, but less significant as for the dual-crosslinked hydrogel.

The mechanical properties were further explored by finite element models, in which changes of stiffness were varied as well as volumes to examine the therapeutic effect on the cardiac function.[90,91] Both these models show that an increase in material stiffness led to a decrease in myofiber stresses around the injectate site, while the lower stiffness hydrogel showed no significant stress reduction. The stiffness effect showed to recede around 50 kPa.[90] These results indicate the impact of the hydrogel stiffness, having a significant effect on the therapeutic outcome. This was suggested to be mainly due to the fibril stresses around the infarct area being levitated, as well as an improved wall thickness of the infarcted area.

Degradation

The degradation of a material after implantation or injection is an important parameter, which theoretically should match the attenuation or reverse remodeling process. The degradation products should be non-toxic and able to be metabolized and cleared from the body.[116] Hydrogel degradation is an important factor when considered for cardiac therapy, as shown by Dobner et al. who examined the efficacy of a non-degradable hydrogel based on PEG post-MI.[27] The hydrogel was injected with a volume of 100 µL directly after MI, with 2 to 3 injections. The heart size was increased in the saline control due to the MI, but was lower in the PEG hydrogel group after 2 and 4 weeks. However, this effect was lost after 13 weeks, with the ESD and EDD being equivalent for the saline as well as the hydrogel injection. An explanation given for these observations is the delayed buildup of cardiomyocyte stresses, with the PEG hydrogel acting as a buffer initially, but insufficient in reducing the stresses in the myocardium over a longer time span. An ongoing macrophage-based foreign body response was hypothesized to stall this improvement over time. Implementation of peptides which can be degraded by cell driven enzymatic cleavage were introduced to the PEG-based hydrogel in a follow-up study to examine the degradable variant of this hydrogel.[57] This article was briefly mentioned in the 'time of injection' section, in which two time-points were compared, being directly post-MI and one week post-MI after infarction in a rat model. Swift degradation of the hydrogel was observed directly post-MI, with no hydrogel being present four weeks post-injection. The one-week post-MI injection showed little difference in remnants after one and four weeks post-injection, indicating lower degradation rates. The one week post-MI injection showed increases in scar thickness, fractional shortening, and decreases in end-systolic dimensions, but later time-points were not taken into account (as their previous study examined the functional effect of the non-degradable PEG hydrogel 13 weeks post-MI). Whilst these results show beneficial effects of the slowly degradable hydrogel injected one-week post-MI, this study does not elucidate further on the retention and functional outcome of the hydrogel therapy over longer time spans.

Hydrogel degradability and the effect on the functional cardiac output in infarcted ovine models was examined by adaption of hyaluronic acid hydrogels, which were tuned to degrade by enzymatic and hydrolytic degradation.[25] Low (~7 kPa) and high (~35-40 kPa) hydrogel moduli were examined, with both degrading and non-degrading variants being analyzed. All hydrogel groups showed improved cardiac output in comparison to the infarcted control, but no significant differences between the hydrogel groups were observed. For the high hydrogel modulus, the non-degradable variant showed to reduce the LV volume more effectively at 8 weeks post-MI, indicating the importance of wall stabilization over a longer time period.

Natural hydrogels, such as ECM-derived hydrogels, can be modified with an MMP inhibitor such as doxycycline, as shown by Wassenaar et al.[117] The in vivo degradation was examined in rats on healthy myocardial tissue, in which the retention was examined by a fluorescent label attached to the hydrogels two weeks post-injection. This showed a significant increase in fluorescence of the doxycycline modified hydrogels, indicating a lower degradation rate. A prolonged degradation was also observed in similar ECM-based hydrogels which were tuned with genipin, a crosslinking agent extracted from gardenia fruit,[118] reducing the degradation rate in vitro over time.[119] However, this was not tested on an in vivo infarction model.

While all of these studies show that the degradation of the injectable hydrogels can be tuned, so far it is unclear what the optimal degradation rate of the hydrogel should be to reach the optimal functional cardiac output. While non-degradable hydrogels can lead to an adverse in vivo effect over longer time spans, more research needs to be performed to tune the degradation rate with the attenuation or reverse cardiac remodeling process.

Viscosity

One of the key mechanical features when regarding injectable hydrogels is the viscosity, of which the injectability is highly dependent. Determination of the viscosity as a function of shear rate can give insight in the injectability of the hydrogel. For shear-thinning hydrogels the viscosity decreases with increasing shear stress. In some cases, the crosslinks of the hydrogels are broken upon increasing shear, whereas they are reformed once the shear stress has been lifted.[120,121] Furthermore, to inject a hydrogel in a non-invasive manner through a catheter, the Hagen-Poiseuille equation needs to be regarded, which can determine the injectability of a hydrogel (equation 1):

$$\Delta p = \frac{8\mu L Q}{\pi R^4} \qquad (1)$$

Where Δp is the pressure drop through a cylindrical pipe (syringe needle), μ is the dynamic viscosity, L is the length of the pipe, Q is volumetric flow rate, and R is pipe radius. This equation shows the force necessary for injection, dependent on the volumetric flow rate, dynamic viscosity, needle length, needle bore diameter, and syringe plunger area. Higher needle length and dynamic viscosities lead to higher forces necessary for injection, which can limit the injectability of a hydrogel.

Furthermore, the viscosity and gelation time is of importance regarding the in vivo retention after injection. Low viscous solutions, with slow sol-gel transition times, can be easily washed away from the site of injection, which is why swift sol-gel transitions are optimal for proper retention.

For cellular or therapeutic delivery, the mechanical properties of the hydrogel influences the uniform suspension of cells or therapeutics when encapsulated. A problem often occurring when cells or therapeutics are mixed in gels is sedimentation, leading to a concentration gradient of cells or therapeutics. Often, uniform mixes are obtained by vigorous mixing before injection. The sedimentation is dependent on the molecular mass of the therapeutic compound, as well as the frictional coefficient.[122] The viscosity of the hydrogel precursor plays a significant role in this sedimentation process, with an increase of viscosity decreasing the displacement of the cells.[123,124] Na et al. improved the cell suspension of a gelatin-methacrylate based bioink by increasing the viscosity of the solution upon addition of biocompatible silk fibroin particles.[125] They observed the lowest sedimentation values upon addition of 1 w/v% silk fibroin particles, with a viscosity of ~60 Pa.s. While these viscosities were applicable for 3D-bioprinting, these high viscous solutions can be troublesome to inject, depending on the type of syringe, gauge needle and applied force.[73] Still, for minimally invasive injection methods, as well as cell and therapeutic delivery, the viscosity is an important parameter to take into account.

3.3 Biomaterial affinity with the surrounding tissue

The choice of material plays a significant role in how the surrounding tissue responds to this foreign material. Natural biomaterials often show biocompatibility, bioactivity, assist in cellular activities such as cell-cell communication, and potential tissue regenerative properties.[126] Synthetic biomaterials are easily adaptable to obtain high mechanical strength, degradability, and gelation rates. An improved retention can be obtained by introduction of adhesive components to increase the tissue-adhesion between the hydrogel and surrounding tissue at the injectate site.

Increasing the hydrogel adhesion can be realized by introduction of catechol-functionalities, which are known to adhere under wet conditions inspired by the mussel foot proteins.[105,127–129] This was shown by Wu et al., who co-administered a hyaluronic acid hydrogel intramyocardial, whilst a gelatin-dopamine and dopamine-modified polypyrrole was coated on the myocardium surface.[105] The combined therapy showed beneficial effects on the functional output of the heart, displaying the highest wall thickness and lowest infarct size. Furthermore, the combined therapy showed to have the beneficial effects on the cardiac output, with an increased EF and fractional shortening in comparison to the MI control.

The arginine-glycine-aspartic acid (RGD) peptide is a natural ligand peptide, which can interact with integrin receptors to provide cell-cell and cell-ECM interactions.[130] Introduction of the RGD peptide to biomaterials can increase the cell density, cell adhesion and cell migration. Sondermeijer et al. modified an alginate scaffold with cyclo(-RGDfK)-peptide to enhance cellular recruitment in vivo.[131] Moreover, scaffolds were seeded with human mesenchymal precursor cells ($1x10^6$ and $3x10^6$ cells) and patched to the epicardial surface of an infarcted myocardium. Scaffolds with $1x10^6$ cells showed optimal vascularization, while $3x10^6$ cells showed a decrease in vascularization, possibly due to ‘crowding’ of the cells. Scaffolds modified with only cyclo(-RGDfK) were furthermore placed in the abdominal area (abdominal rectus muscles) as a control, which showed robust cellularization and vascularization, in comparison to the patches containing no cyclo(-RGDfK). This shows that materials could be further modified with for example RGD-sequences to further increase cellular retention, cellular recruitment and proliferation.

To increase the cellular adhesion of cardiac stem cells (CSCs), platelet nanovesicles were used to decorate CSCs that increased adhesion properties of the cells.[132] Intracoronary injection of these CSCs with platelet nanovesicles in an infarcted porcine heart showed an increase in cellular retention after 24 hours, in comparison to no platelet nanovesicle decoration.

These studies show that modification of hydrogels with small molecules or peptides can lead to significant increases of adhesion to the surrounding tissue and cellular recruitment. This can furthermore increase the therapeutic effectiveness.

4. Off-target effects

Possible off-target effects of injected materials is a parameter often overlooked. Multiple types of hydrogel systems contain drug cargos, which can be released from the hydrogel in a sustained manner to target the surrounding area. Possible redistribution and complementary side-effects of the injectate material, the cargo, or both is often neglected.

Few studies have focused on the redistribution of cells when injected in the myocardial infarcted area. Bone marrow cells labeled with ^{99m}Tc showed a retention of approximately 17% at the infarct site of rats 24h after injection.[50] Most cells injected were found in the liver (>20%), and less abundantly in the spleen (~8%), and kidneys (~6%). Furthermore, intravenously injected endothelial progenitor cells radioactively labeled ^{111} with indium oxine showed a retention of approximately 1% in a rat heart 96h after injection. Most redistributed cells were found in the spleen and liver (~70%).

A combination of human mesenchymal stem cells and fibrin hydrogel was injected intramyocardially in an infarction model and examined 90 minutes post-injection.[133] The cellular retention was approximately 40% when combined with fibrin hydrogel, with approximately 40% of the cells redistributed to the lungs, whereas cells in saline showed approximately 20% of cardiac retention. The cells in saline showed a redistribution of 40% to the liver, whereas the cells in combination with the fibrin glue showed a redistribution of 20% to the liver. Cellular redistribution for the saline injections was shown in the kidneys (~9%) and spleen (<5%), whereas almost no redistribution was shown in these organs when the cells were encapsulated in the hydrogels. In our group, we showed a ureido-pyrimidinone-based hydrogel that was labeled with a radioactive tracer (^{111}Indium), traceable in vivo.[134] Here, a small pilot showed the redistribution 4 hours after injection in a healthy porcine heart, with 8% of the hydrogel being retained at the inject spot, whereas a high content redistributed to the lungs (29% n=1, 9.5% n=2) and bladder and urine (16% n=1, 22% n=2). When the hydrogel was modified with a recombinant collagen type-1 based material, cardiac retention was around 16% 4 hours post-injection, displaying redistribution of the hydrogel mainly to the lungs (13% n=1, 19% n=2), as well as the bladder and urine (10% n=1, 13% n=2). It should be noted that the injection in a healthy porcine heart could differ from retention in an infarction model.

These studies show possible redistribution of the injectate, and possible corresponding off-target effects. A screening of material redistribution can give a broader comprehension of possible side-effects.

4.1 Retention and Redistribution Evaluation

As mentioned previously, only a limited amount of studies focus on visualizing the retention and redistribution of hydrogels in vivo. Several imaging methods are challenging, with fluorescence imaging having a low penetration depth, Single-photon emission computed tomography (SPECT-CT) imaging often needing a tracer in combination with radiation dosage being received, and magnetic resonance imaging (MRI) being less quantifiable (Figure 2.5).[135] Furthermore, labeling with fluorophores or contrast agents can influence the hydrogel properties.[136]

Hydrogels are often labeled with fluorophores, whereafter the hydrogel content can be visualized ex vivo.[16,57,137-139] While this gives an indication on the injectate remnants and degradation, it is unclear how much of the total injectate volume is retained at the injection site, and how much of the injectate is redistributed to other organs.

Bakker et al. showed a pH-responsive hydrogel, being a viscous liquid at a pH of 9, facilitating injection at basic conditions, whilst gelating under physiological conditions at neutral pH.[140] A DOTA-gadolinium(III) label was added to hydrogel to allow MRI analysis of the gel, which was injected in a healthy porcine heart in vivo with a volume of 0.2 mL. The injected hydrogel was visualized ex vivo and post-injection volume analysis showed matching pre-injection volume, indicating retention of the hydrogel in vivo.

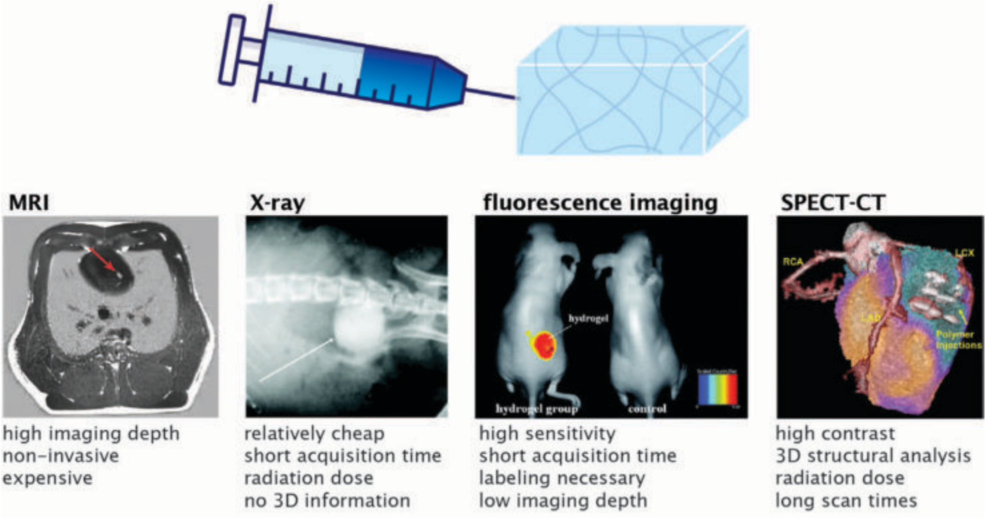

Figure 2.5 Different imaging methods of injectable hydrogels used for cardiac applications, with the pros and cons of the imaging techniques, MRI, energetic high-frequency electromagnetic radiation (X-ray), fluorescence imaging and SPECT-CT. Reproduced with permission.[140] Copyright 2018, Wiley. Reproduced with permission.[143] Copyright 2008 American Chemical Society. Reproduced with permission. Reproduced with permission.[144] Copyright 2015 Royal Society of Chemistry. Reproduced with permission.[141] Copyright 2020 Wiley.

With SPECT-CT a hyaluronic acid-based hydrogel was imaged upon addition of a contrast agent (iohexol) after being injected in an infarcted porcine model.[141] Nine injections of 0.1 mL hydrogel were performed, and directly after injection the location was verified in vivo. The in-vivo degradation rate and hydrogel amount retained at the injection site were unknown, making it challenging to link the hydrogel content in vivo to the therapeutic effect. Redistribution of an alginate type hydrogel was examined by radio-metal indium-111labeling, which enabled non-invasive in-vivo nuclear imaging of the hydrogel.[142] An intra-myocardial injection was performed in mice and imaged over a week, with a volume of 50 μL containing 2% (w/v) alginate hydrogel, imaged over 7 days after injection. At two hours post-injection, the majority of injected alginate was not retained in the heart and was cleared from the body. Redistribution was observed mainly in the kidney and bladder. After seven days, a fraction of approximately 4 to 8% of the material was still observed in the heart, which clarifies the importance of biomaterial tracking in vivo.

The detection of biomaterials post-injection is feasible, but determination of the retention and redistribution of these biomaterials is challenging, with only a handful of studies examining these biomaterial retention and remnants in vivo. These characteristics, however, are of significant importance when linking the therapeutic effect of the biomaterials to the retention post-injection.

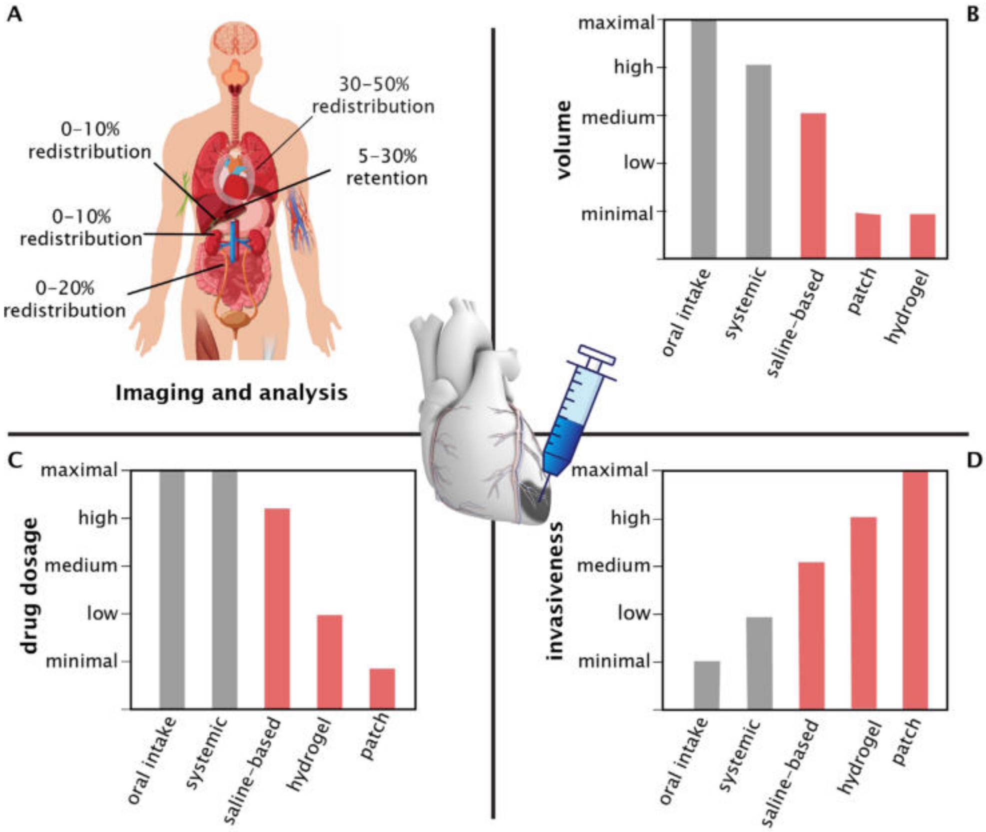

Figure 2.6 The different parameters to consider after in vivo injection of cardiac therapy, with A. the imaging and analysis, providing insight in retention and redistribution of the therapy, and insight in possible side-effects, B. the optimal volume, dependent on the type of therapy and material, C. the drug dosage, dependent on the retention and release from the drug carrier, and D. the invasiveness of the therapy.

5. Conclusion

Scientific development for locally administered cardiac regenerative therapies has shown great progress, with medicine in combination with biomaterials, as well as biomaterials alone showing therapeutic benefits by attenuation ventricular remodeling or stimulating cardiac regeneration. A deeper understanding of the effectiveness of these biomaterials in the cardiac environment could be obtained by considering parameters that influence their retention, such as injection timing, cardiac contraction, and material characteristics at the target site (Figure 2.6).

Thus, while current injectable biomaterials are already demonstrating significant improvements in functional cardiac output, visualization of the biomaterials in vivo illuminates the retention at the target site, from which the optimal biomaterial-dependent injection volume could be determined. Furthermore, the aspect of redistribution should be considered, which can predict possible side-effects. The drug dosage could be adapted to complement the retention of the biomaterial.

We propose a focus change to explore the direct role of the biomaterial in cardiac therapies, instead of investigating indirect parameters considering the cardiac response. Only by creating a deeper understanding of the exact dosing and functioning of the biomaterials in vivo, further innovation in biomaterial design can enhance therapeutic efficacy of the injectate in locally administered medicine after myocardial infarction.

References

1 R. Ross, *Nature*, 1993, **362**, 801–809.

2 Y. Matsui, J. Morimoto and T. Uede, *World J. Biol. Chem.*, 2010, **1**, 69–80.

3 M. Jessup and S. Brozena, *N. Engl. J. Med.*, 2003, **348**, 2007–2018.

4 V. F. M. Segers and R. T. Lee, *J. Cardiovasc. Transl. Res.*, 2010, **3**, 469–477.

5 G. M. Ellison, D. Torella, S. Dellegrottaglie, C. Perez-Martinez, A. Perez de Prado, C. Vicinanza, S. Purushothaman, V. Galuppo, C. Iaconetti, C. D. Waring, A. Smith, M. Torella, C. Cuellas Ramon, J. M. Gonzalo-Orden, V. Agosti, C. Indolfi, M. Galiñanes, F. Fernandez-Vazquez and B. Nadal-Ginard, *J. Am. Coll. Cardiol.*, 2011, **58**, 977–986.

6 E. van Rooij and S. Kauppinen, *EMBO Mol. Med.*, 2014, **6**, 851–864.

7 L. L. Wang, Y. Liu, J. J. Chung, T. Wang, A. C. Gaffey, M. Lu, C. A. Cavanaugh, S. Zhou, R. Kanade, P. Atluri, E. E. Morrisey and J. A. Burdick, *Nat. Biomed. Eng.*, 2017, **1**, 983–992.

8 J. Tang, D. Shen, T. G. Caranasos, Z. Wang, A. C. Vandergriff, T. A. Allen, M. T. Hensley, P. U. Dinh, J. Cores, T. S. Li, J. Zhang, Q. Kan and K. Cheng, *Nat. Commun.*, 2017, **8**, 1–9.

9 Z. Fan, Z. Xu, H. Niu, N. Gao, Y. Guan, C. Li, Y. Dang, X. Cui, X. L. Liu, Y. Duan, H. Li, X. Zhou, P. H. Lin, J. Ma and J. Guan, *Sci. Rep.*, 2018, **8**, 1–22.

10 H. Tan and K. G. Marra, *Materials (Basel)*, 2010, **3**, 1746–1767.

11 L. Saludas, S. Pascual-Gil, F. Prósper, E. Garbayo and M. Blanco-Prieto, *Int. J. Pharm.*, 2017, **523**, 454–475.

12 R. M. N. Kumar, *J. Pharm. Pharm. Sci.*, 2000, **3**, 234–258.

13 C. Voukalis, E. Shantsila and G. Y. H. Lip, *Ann. Med.*, 2019, **51**, 193–223.

14 F. Kiessling, S. Fokong, P. Koczera, W. Lederle and T. Lammers, *J. Nucl. Med.*, 2012, **53**, 345–348.

15 A. C. Daly, L. Riley, T. Segura and J. A. Burdick, *Nat. Rev. Mater.*, 2020, **5**, 20–43.

16 M. C. Ciuffreda, G. Malpasso, C. Chokoza, D. Bezuidenhout, K. P. Goetsch, M. Mura, F. Pisano, N. H. Davies and M. Gnecchi, *Acta Biomater.*, 2018, **70**, 71–83.

17 L. Qiao, Y. Kong, Y. Shi, A. Sun, R. Ji, C. Huang, Y. Li and X. Yang, *Life Sci.*, 2019, **239**, 116891.

18 H. Li, J. Gao, Y. Shang, Y. Hua, M. Ye, Z. Yang, C. Ou and M. Chen, *ACS Appl. Mater. Interfaces*, 2018, **10**, 24459–24468.

19 M. M. C. Bastings, S. Koudstaal, R. E. Kieltyka, Y. Nakano, A. C. H. Pape, D. A. M. Feyen, F. J. van Slochteren, P. A. Doevendans, J. P. G. Sluijter, E. W. Meijer, S. A. J. Chamuleau and P. Y. W. Dankers, *Adv. Healthc. Mater.*, 2014, **3**, 70–78.

20 M. D. Krebs, O. Jeon and E. Alsberg, *J. Am. Chem. Soc.*, 2009, **131**, 9204–9206.

21 C. Fan, J. Shi, Y. Zhuang, L. Zhang, L. Huang, W. Yang, B. Chen, Y. Chen, Z. Xiao, H. Shen, Y. Zhao and J. Dai, *Adv. Mater.*, 2019, **31**, 1902900.

22 Y. Wu, T. Chang, W. Chen, X. Wang, J. Li, Y. Chen, Y. Yu, Z. Shen, Q. Yu and Y. Zhang, *Bioact. Mater.*, 2021, **6**, 520–528.

23 Y. Matsumura, Y. Zhu, H. Jiang, A. D'Amore, S. K. Luketich, V. Charwat, T. Yoshizumi, H. Sato, B. Yang, T. Uchibori, K. E. Healy and W. R. Wagner, *Biomaterials*, 2019, **217**, 119289.

24 K. L. Sack, E. Aliotta, J. S. Choy, D. B. Ennis, N. H. Davies, T. Franz, G. S. Kassab and J. M. Guccione, *Acta Biomater.*, 2020, **111**, 170–180.

25 E. Tous, J. L. Ifkovits, K. J. Koomalsingh, T. Shuto, T. Soeda, N. Kondo, J. H. Gorman, R. C. Gorman and J. A. Burdick, *Biomacromolecules*, 2011, **12**, 4127–4135.

26 R. Waters, P. Alam, S. Pacelli, A. R. Chakravarti, R. P. H. Ahmed and A. Paul, *Acta Biomater.*, 2018, **69**, 95–106.

27 S. Dobner, D. Bezuidenhout, P. Govender, P. Zilla and N. Davies, *J. Card. Fail.*, 2009, **15**, 629–636.

28 C. L. Hastings, E. T. Roche, E. Ruiz-Hernandez, K. Schenke-Layland, C. J. Walsh and G. P. Duffy, *Adv. Drug Deliv. Rev.*, 2015, **84**, 85–106.

29 S. A. Doppler, M. A. Deutsch, R. Lange and M. Krane, *J. Thorac. Dis.*, 2013, **5**, 683–697.

30 H. M. Sherif, S. G. Nekolla, A. Saraste, S. Reder, M. Yu, S. Robinson and M. Schwaiger, *J. Nucl. Med.* , 2011, **52**, 617–624.

31 D. A. M. Feyen, P. Van Den Hoogen, L. W. Van Laake, E. C. M. Van Eeuwijk, I. Hoefer, G. Pasterkamp, S. A. J. Chamuleau, P. F. Grundeman, P. A. Doevendans and J. P. G. Sluijter, *Eur. Heart J.*, 2017, **38**, 184–186.

32 L. Sultatos, in *xPharm: The Comprehensive Pharmacology Reference*, eds. S. J. Enna and D. B. Bylund, Elsevier, New York, 2007, pp. 1–4.

33 Y. Hadas, M. G. Katz, C. R. Bridges and L. Zangi, *Wiley Interdiscip. Rev. Syst. Biol. Med.*, 2017, **9**, 1367.

34 E. N. Marieb and K. Hoehn, *Human Anatomy & Physiology, Global Edition*, Pearson, Harlow, 2015, vol. 10.

35 B. R. Weil and S. Neelamegham, *Front. Immunol.*, 2019, **10**, 300.

36 B. I. Jugdutt, *Can. J. Cardiol.*, 1993, **9**, 103–114.

37 J. Bartunek, W. Wijns, G. R. Heyndrickx and M. Vanderheyden, *Nat. Rev. Cardiol.*, 2006, **3**, S52–S56.

38 M. Kucia, B. Dawn, G. Hunt, Y. Guo, M. Wysoczynski, M. Majka, J. Ratajczak, F. Rezzoug, S. T. Ildstad, R. Bolli and M. Z. Ratajczak, *Circ. Res.*, 2004, **95**, 1191–1199.

39 P. Contessotto and A. Pandit, *Biomaterials*, 2021, **275**, 120906.

40 K. A. Reimer, R. S. V. Heide and V. J. Richard, *Am. J. Cardiol.*, 1993, **72**, G13–G21.

41 J. W. Holmes, T. K. Borg and J. W. Covell, *Annu. Rev. Biomed. Eng.*, 2005, **7**, 223–253.

42 S. R. Eckhouse and F. G. Spinale, *Heart Fail. Clin.*, 2012, **8**, 7–20.

43 S. D. Prabhu and N. G. Frangogiannis, *Circ. Res.*, 2016, **119**, 91–112.

44 M. Dobaczewski, C. Gonzalez-Quesada and N. G. Frangogiannis, *J. Mol. Cell. Cardiol.*, 2010, **48**, 504–511.

45 G. Ertl and S. Frantz, *Cardiovasc. Res.*, 2005, **66**, 22–32.

46 G. M. Fomovsky and J. W. Holmes, *Am. J. Physiol. Heart Circ. Physiol.*, 2010, **298**, H221–H228.

47 D. J. Shah, H. W. Kim, O. James, M. Parker, E. Wu, R. O. Bonow, R. M. Judd and R. J. Kim, *JAMA*, 2013, **309**, 909–918.

48 S. Spaans, N. A. M. Bax, C. V. C. Bouten and P. Y. W. Dankers, in *Synthetic Biology: Volume 2*, The Royal Society of Chemistry, 2018, vol. 2, pp. 155–185.

49 W. J. Richardson, S. A. Clarke, T. A. Quinn and J. W. Holmes, *Compr. Physiol.*, 2015, **5**, 1877–1909.

50 J. S. Nakamuta, M. E. Danoviz, F. L. N. Marques, L. dos Santos, C. Becker, G. A. Gonçalves, P. F. Vassallo, I. T. Schettert, P. J. F. Tucci and J. E. Krieger, *PLoS One*, 2009, **4**, e6005.

51 L. C. Amado, A. P. Saliaris, K. H. Schuleri, M. St John, J.-S. Xie, S. Cattaneo, D. J. Durand, T. Fitton, J. Q. Kuang, G. Stewart, S. Lehrke, W. W. Baumgartner, B. J. Martin, A. W. Heldman and J. M. Hare, *Proc. Natl. Acad. Sci. U. S. A.*, 2005, **102**, 11474–11479.

52 W. Sherman, J. Bartunek, D. Dolatabadi, R. Sanz-Ruiz, B. Beleslin, W. Wojakowski, G. Heyndrickx, J. Z. Kimpalou, S. A. Waldman, G. J. Laarman, A. Seron, A. Behfar, J. P. Latere, A. Terzic and W. Wijns, *JACC Cardiovasc. Interv.*, 2018, **11**, 329–338.

53 J. O. Beitnes, E. Hopp, K. Lunde, S. Solheim, H. Arnesen, J. E. Brinchmann, K. Forfang and S. Aakhus, *Heart*, 2009, **95**, 1983–1989.

54 E. Cambria, F. S. Pasqualini, P. Wolint, J. Günter, J. Steiger, A. Bopp, S. P. Hoerstrup and M. Y. Emmert, *npj Regen. Med.*, 2017, **2**, 17.

55 J. H. Traverse, T. D. Henry, C. J. Pepine, J. T. Willerson, D. X. M. Zhao, S. G. Ellis, J. R. Forder, R. D. Anderson, A. K. Hatzopoulos, M. S. Penn, E. C. Perin, J. Chambers, K. W. Baran, G. Raveendran, C. Lambert, A. Lerman, D. I. Simon, D. E. Vaughan, D. Lai, A. P. Gee, D. A. Taylor, C. R. Cogle, J. D. Thomas, R. E. Olson, S. Bowman, J. Francescon, C. Geither, E. Handberg, C. Kappenman, L. Westbrook, L. B. Piller, L. M. Simpson, S. Baraniuk, C. Loghin, D. Aguilar, S. Richman, C. Zierold, D. B. Spoon, J. Bettencourt, S. L. Sayre, R. W. Vojvodic, S. I. Skarlatos, D. J. Gordon, R. F. Ebert, M. Kwak, L. A. Moyé, and R. D. Simari; CCTRN, *JAMA*, 2012, **308**, 2380–2389.

56 N. Landa, L. Miller, M. S. Feinberg, R. Holbova, M. Shachar, I. Freeman, S. Cohen and J. Leor, *Circulation*, 2008, **117**, 1388–1396.

57 K. Kadner, S. Dobner, T. Franz, D. Bezuidenhout, M. S. Sirry, P. Zilla and N. H. Davies, *Biomaterials*, 2012, **33**, 2060–2066.

58 T. Yoshizumi, Y. Zhu, H. Jiang, A. D'Amore, H. Sakaguchi, J. Tchao, K. Tobita and W. R. Wagner, *Biomaterials*, 2016, **83**, 182–193.

59 N. J. R. Blackburn, T. Sofrenovic, D. Kuraitis, A. Ahmadi, B. McNeill, C. Deng, K. J. Rayner, Z. Zhong, M. Ruel and E. J. Suuronen, *Biomaterials*, 2015, **39**, 182–192.

60 J. Pupkaite, V. Sedlakova, C. Eren Cimenci, M. Bak, S. McLaughlin, M. Ruel, E. I. Alarcon and E. J. Suuronen, *ACS Biomater. Sci. Eng.*, 2020, **6**, 4256–4265.

61 B. I. Jugdutt, *Circulation*, 2003, **108**, 1395–1403.

62 G. E. Davis, K. J. Bayless, M. J. Davis and G. A. Meininger, *Am. J. Pathol.*, 2000, **156**, 1489–1498.

63 P. M. Arvidsson, J. Töger, M. Carlsson, K. Steding-Ehrenborg, G. Pedrizzetti, E. Heiberg and H. Arheden, *Am. J. Physiol. Circ. Physiol.*, 2016, **312**, H314–H328.

64 D. F. Goldspink, J. G. Burniston and L.-B. Tan, *Exp. Physiol.*, 2003, **88**, 447–458.

65 J. Terrovitis, R. Lautamäki, M. Bonios, J. Fox, J. M. Engles, J. Yu, M. K. Leppo, M. G. Pomper, R. L. Wahl, J. Seidel, B. M. Tsui, F. M. Bengel, M. R. Abraham and E. Marbán, *J. Am. Coll. Cardiol.*, 2009, **6**, 247–253.

66 J. Li, Y. Lv, D. Zhu, X. Mei, K. Huang, X. Wang, Z. Li, S. Zhang, S. Hu, K. Popowski, K. Cheng and J. Wang, *Chem. Eng. J.*, 2021, **427**, 131581.

67 J. Tang, X. Cui, T. G. Caranasos, M. T. Hensley, A. C. Vandergriff, Y. Hartanto, D. Shen, H. Zhang, J. Zhang and K. Cheng, *ACS Nano*, 2017, **11**, 9738–9749.

68 C. W. Chen, L. L. Wang, S. Zaman, J. Gordon, M. F. Arisi, C. M. Venkataraman, J. J. Chung, G. Hung, A. C. Gaffey, L. A. Spruce, H. Fazelinia, R. C. Gorman, S. H. Seeholzer, J. A. Burdick and P. Atluri, *Cardiovasc. Res.*, 2018, **114**, 1029–1040.

69 M. Sepantafar, R. Maheronnaghsh, H. Mohammadi, S. Rajabi-Zeleti, N. Annabi, N. Aghdami and H. Baharvand, *Biotechnol. Adv.*, 2016, **34**, 362–379.

70 C. Hoeeg, A. Dolatshahi-Pirouz and B. Follin, *Gels (Basel)*, 2021, **7**, 7

71 Z. Li and J. Guan, *Polym.* , 2011, **3**, 740–761

72 Y. Liu and S. Hsu, *Front. Chem.*, 2018, **6**, 449.

73 M. H. Chen, L. L. Wang, J. J. Chung, Y.-H. Kim, P. Atluri and J. A. Burdick, *ACS Biomater. Sci. Eng.*, 2017, **3**, 3146–3160.

74 H. N. Sabbah, M. Wang, R. C. Gupta, S. Rastogi, I. Ilsar, M. S. Sabbah, S. Kohli, S. Helgerson and R. J. Lee, *JACC. Heart Fail.*, 2013, **1**, 252–258.

75 D. L. Mann, R. J. Lee, A. J. S. Coats, G. Neagoe, D. Dragomir, E. Pusineri, M. Piredda, L. Bettari, B.-A. Kirwan, R. Dowling, M. Volterrani, S. D. Solomon, H. N. Sabbah, A. Hinson and S. D. Anker, *Eur. J. Heart Fail.*, 2016, **18**, 314–325.

76 R. M. Wang and K. L. Christman, *Adv. Drug Deliv. Rev.*, 2016, **96**, 77–82.

77 K. Lunde, S. Solheim, S. Aakhus, H. Arnesen, M. Abdelnoor, T. Egeland, K. Endresen, A. Ilebekk, A. Mangschau, J. G. Fjeld, H. J. Smith, E. Taraldsrud, H. K. Grøgaard, R. Bjørnerheim, M. Brekke, C. Müller, E. Hopp, A. Ragnarsson, J. E. Brinchmann and K. Forfang, *N. Engl. J. Med.*, 2006, **355**, 1199–1209.

78 M. Hao, R. Wang and W. Wang, *Anal. Cell. Pathol. (Amst).*, 2017, **2017**, 9404057.

79 K. C. Wollert, G. P. Meyer, J. Lotz, S. Ringes Lichtenberg, P. Lippolt, C. Breidenbach, S. Fichtner, T. Korte, B. Hornig, D. Messinger, L. Arseniev, B. Hertenstein, A. Ganser and H. Drexler, *Lancet*, 2004, **364**, 141–148.

80 J. M. Hare, J. E. Fishman, G. Gerstenblith, D. L. DiFede Velazquez, J. P. Zambrano, V. Y. Suncion, M. Tracy, E. Ghersin, P. V Johnston, J. A. Brinker, E. Breton, J. Davis-Sproul, I. H. Schulman, J. Byrnes, A. M. Mendizabal, M. H. Lowery, D. Rouy, P. Altman, C. Wong Po Foo, P. Ruiz, A. Amador, J. Da Silva, I. K. McNiece, A. W. Heldman, R. George and A. Lardo, *JAMA*, 2012, **308**, 2369–2379.

81 S. Chen, W. Fang, F. Ye, Y.-H. Liu, J. Qian, S. Shan, J. Zhang, R. Z. Chunhua, L. Liao, S. Lin and J. Sun, *Am. J. Cardiol.*, 2004, **94**, 92–95.

82 T. I. G. van der Spoel, S. J. Jansen of Lorkeers, P. Agostoni, E. van Belle, M. Gyöngyösi, J. P. G. Sluijter, M. J. Cramer, P. A. Doevendans and S. A. J. Chamuleau, *Cardiovasc. Res.*, 2011, **91**, 649–658.

83 J. M. Singelyn, P. Sundaramurthy, T. D. Johnson, P. J. Schup-Magoffin, D. P. Hu, D. M. Faulk, J. Wang, K. M. Mayle, K. Bartels, M. Salvatore, A. M. Kinsey, A. N. DeMaria, N. Dib and K. L. Christman, *J. Am. Coll. Cardiol.*, 2012, **59**, 751–763.

84 R. Mukherjee, J. A. Zavadzkas, S. M. Saunders, J. E. McLean, L. B. Jeffords, C. Beck, R. E. Stroud, A. M. Leone, C. N. Koval, W. T. Rivers, S. Basu, A. Sheehy, G. Michal and F. G. Spinale, *Ann. Thorac. Surg.*, 2008, **86**, 1268–1276.

85 G. P. Meyer, K. C. Wollert, J. Lotz, J. Steffens, P. Lippolt, S. Fichtner, H. Hecker, A. Schaefer, L. Arseniev, B. Hertenstein, A. Ganser and H. Drexler, *Circulation*, 2006, **113**, 1287–1294.

86 D. Sürder, R. Manka, V. Lo Cicero, T. Moccetti, K. Rufibach, S. Soncin, L. Turchetto, M. Radrizzani, G. Astori, J. Schwitter, P. Erne, M. Zuber, C. Auf Der Maur, P. Jamshidi, O. Gaemperli, S. Windecker, A. Moschovitis, A. Wahl, I. Bühler, C. Wyss, S. Kozerke, U. Landmesser, T. F. Lüscher and R. Corti, *Circulation*, 2013, **127**, 1968–1979.

87 R. Huang, K. Yao, A. Sun, J. Qian, L. Ge, Y. Zhang, Y. Niu, K. Wang, Y. Zou and J. Ge, *Stem Cell Res. Ther.*, 2015, **6**, 112.

88 P. Wise, N. H. Davies, M. S. Sirry, J. Kortsmit, L. Dubuis, C.-K. Chai, F. P. T. Baaijens and T. Franz, *Int. j. numer. method. biomed. eng.*, 2016, **32**, e02772.

89 J. Leor, S. Tuvia, V. Guetta, F. Manczur, D. Castel, U. Willenz, Ö. Petneházy, N. Landa, M. S. Feinberg, E. Konen, O. Goitein, O. Tsur-Gang, M. Shaul, L. Klapper and S. Cohen, *J. Am. Coll. Cardiol.*, 2009, **54**, 1014–1023.

90 H. Wang, C. B. Rodell, M. E. Lee, N. N. Dusaj, J. H. Gorman, J. A. Burdick, R. C. Gorman and J. F. Wenk, *J. Biomech.*, 2017, **64**, 231–235.

91 S. T. Wall, J. C. Walker, K. E. Healy, M. B. Ratcliffe and J. M. Guccione, *Circulation*, 2006, **114**, 2627–2635.

92 D. S. Li, R. Avazmohammadi, C. B. Rodell, E. W. Hsu, J. A. Burdick, J. H. Gorman, R. C. Gorman and M. S. Sacks, *Acta Biomater.*, 2020, **114**, 296–306.

93 R. Waters, P. Alam, S. Pacelli, A. R. Chakravarti, R. P. H. Ahmed and A. Paul, *Acta Biomater.*, 2018, **69**, 95–106.

94 L. B. Vong, T. Q. Bui, T. Tomita, H. Sakamoto, Y. Hiramatsu and Y. Nagasaki, *Biomaterials*, 2018, **167**, 143–152.

95 Y. Li, X. Chen, R. Jin, L. Chen, M. Dang, H. Cao, Y. Dong, B. Cai, G. Bai, J. J. Gooding, S. Liu, D. Zou, Z. Zhang and C. Yang, *Sci. Adv.*, 2021, **7**, eabd6740.

96 X. Zhang, Y. Lyu, Y. Liu, R. Yang, B. Liu, J. Li, Z. Xu, Q. Zhang, J. Yang and W. Liu, *Nano Today*, 2021, **39**, 101227.

97 E. Mihalko, K. Huang, E. Sproul, K. Cheng and A. C. Brown, *ACS Nano*, 2018, **12**, 7826–7837.

98 Z. Li, D. Zhu, Q. Hui, J. Bi, B. Yu, Z. Huang, S. Hu, Z. Wang, T. Caranasos, J. Rossi, X. Li, K. Cheng and X. Wang, *Adv. Funct. Mater.*, 2021, **31**, 2004377.

99 M. van den Boomen, H. B. Kause, H. C. van Assen, P. Y. W. Dankers, C. V. C. Bouten and K. Vandoorne, *Sci. Rep.*, 2019, **9**, 19366.

100 J. S. Choy, S. Leng, G. Acevedo-Bolton, S. Shaul, L. Fu, X. Guo, L. Zhong, J. M. Guccione and G. S. Kassab, *Int. J. Cardiol.*, 2018, **255**, 129–135.

101 S. D. Anker, A. J. S. Coats, G. Cristian, D. Dragomir, E. Pusineri, M. Piredda, L. Bettari, R. Dowling, M. Volterrani, B.-A. Kirwan, G. Filippatos, J.-L. Mas, N. Danchin, S. D. Solomon, R. J. Lee, F. Ahmann, A. Hinson, H. N. Sabbah and D. L. Mann, *Eur. Heart J.*, 2015, **36**, 2297–2309.

102 J. H. Traverse, T. D. Henry, N. Dib, A. N. Patel, C. Pepine, G. L. Schaer, J. A. DeQuach, A. M. Kinsey, P. Chamberlin and K. L. Christman, *JACC Basic to Transl. Sci.*, 2019, **4**, 659 LP – 669.

103 B. P. Purcell, S. C. Barlow, P. E. Perreault, L. Freeburg, H. Doviak, J. Jacobs, A. Hoenes, K. N. Zellars, A. Y. Khakoo, T. Lee, J. A. Burdick and F. G. Spinale, *Am. J. Physiol. Circ. Physiol.*, 2018, **315**, H814–H825.

104 S. McLaughlin, B. McNeill, J. Podrebarac, K. Hosoyama, V. Sedlakova, G. Cron, D. Smyth, R. Seymour, K. Goel, W. Liang, K. J. Rayner, M. Ruel, E. J. Suuronen and E. I. Alarcon, *Nat. Commun.*, 2019, **10**, 4866.

105 T. Wu, C. Cui, Y. Huang, Y. Liu, C. Fan, X. Han, Y. Yang, Z. Xu, B. Liu, G. Fan and W. Liu, *ACS Appl. Mater. Interfaces*, 2020, **12**, 2039–2048.

106 Z. Yuan, Y.-H. Tsou, X.-Q. Zhang, S. Huang, Y. Yang, M. Gao, W. Ho, Q. Zhao, X. Ye and X. Xu, *ACS Appl. Mater. Interfaces*, 2019, **11**, 38429–38439.

107 B. Peña, M. Laughter, S. Jett, T. J. Rowland, M. R. G. Taylor, L. Mestroni and D. Park, *Macromol. Biosci.*, 2018, **18**, e1800079.

108 H. Wang, D. Zhu, A. Paul, L. Cai, A. Enejder, F. Yang and S. C. Heilshorn, *Adv. Funct. Mater.*, 2017, **27**, 1605609.

109 X. M. Ma, Y. H. Li and Y. Z. Xia, *Adv. Mat. Res.,* 2012, **430–432**, 154–157.

110 A. C. H. Pape, M. H. Bakker, C. C. S. Tseng, M. M. C. Bastings, S. Koudstaal, P. Agostoni, S. A. J. Chamuleau and P. Y. W. Dankers, *J. Vis. Exp.*, 2015, **100**, 1–8.

111 S. B. Seif-Naraghi, M. A. Salvatore, P. J. Schup-Magoffin, D. P. Hu and K. L. Christman, *Tissue Eng. Part A*, 2010, **16**, 2017–2027.

112 L. Ou, W. Li, Y. Zhang, W. Wang, J. Liu, H. Sorg, D. Furlani, R. Gäbel, P. Mark, C. Klopsch, L. Wang, K. Lützow, A. Lendlein, K. Wagner, D. Klee, A. Liebold, R.-K. Li, D. Kong, G. Steinhoff and N. Ma, *J. Cell. Mol. Med.*, 2011, **15**, 1310–1318.

113 N. F. Huang, J. Yu, R. Sievers, S. Li and R. J. Lee, *Tissue Eng.*, 2005, **11**, 1860–1866.

114 J. L. Ifkovits, E. Tous, M. Minakawa, M. Morita, J. D. Robb, K. J. Koomalsingh, J. H. Gorman, R. C. Gorman and J. A. Burdick, *Proc. Natl. Acad. Sci.*, 2010, **107**, 11507–11512.

115 C. B. Rodell, M. E. Lee, H. Wang, S. Takebayashi, T. Takayama, T. Kawamura, J. S. Arkles, N. N. Dusaj, S. M. Dorsey, W. R. T. Witschey, J. J. Pilla, J. H. Gorman, J. F. Wenk, J. A. Burdick and R. C. Gorman, *Circ. Cardiovasc. Interv.* 2016, **9**, e004058.

116 L. S. Nair and C. T. Laurencin, *Prog. Polym. Sci.*, 2007, **32**, 762–798.

117 J. W. Wassenaar, R. L. Braden, K. G. Osborn and K. L. Christman, *J. Mater. Chem. B*, 2016, **4**, 2794–2802.

118 J. S. Yoo, Y. J. Kim, S. H. Kim and S. H. Choi, *Korean J. Thorac. Cardiovasc. Surg.*, 2011, **44**, 197–207.

119 M. E. Jeffords, J. Wu, M. Shah, Y. Hong and G. Zhang, *ACS Appl. Mater. Interfaces*, 2015, **7**, 11053–11061.

120 A. N. Steele, L. Cai, V. N. Truong, B. B. Edwards, A. B. Goldstone, A. Eskandari, A. C. Mitchell, L. M. Marquardt, A. A. Foster, J. R. Cochran, S. C. Heilshorn and Y. J. Woo, *Biotechnol. Bioeng.*, 2017, **114**, 2379–2389.

121 S. Uman, A. Dhand and J. A. Burdick, *J. Appl. Polym. Sci.*, 2020, **137**, 48668.

122 J. A. Ji, J. Liu, S. J. Shire, T. J. Kamerzell, S. Hong, K. Billeci, Y. Shen and Y. J. Wang, *Pharm. Res.*, 2010, **27**, 644–654.

123 A. K. Grosskopf, G. A. Roth, A. A. A. Smith, E. C. Gale, H. L. Hernandez and E. A. Appel, *Bioeng. Transl. Med.*, 2020, **5**, e10147.

124 K. Dubbin, A. Tabet and S. C. Heilshorn, *Biofabrication*, 2017, **9**, 44102.

125 K. Na, S. Shin, H. Lee, D. Shin, J. Baek, H. Kwak, M. Park, J. Shin and J. Hyun, *J. Ind. Eng. Chem.*, 2018, **61**, 340–347.

126 D. K. Sarkar, Y. Xue and S. Sant, in *The Immune Response to Implanted Materials and Devices*, ed. B. Corradetti, 2017, pp. 81–105.

127 Y. Liu, H. Meng, S. Konst, R. Sarmiento, R. Rajachar and B. P. Lee, *ACS Appl. Mater. Interfaces*, 2014, **6**, 16982–16992.

128 Y. Liang, X. Zhao, T. Hu, Y. Han and B. Guo, *J. Colloid Interface Sci.*, 2019, **556**, 514–528.

129 K. Wei, B. Senturk, M. T. Matter, X. Wu, I. K. Herrmann, M. Rottmar and C. Toncelli, *ACS Appl. Mater. Interfaces*, 2019, **11**, 47707–47719.

130 M. Alipour, M. Baneshi, S. Hosseinkhani, R. Mahmoudi, A. Jabari Arabzadeh, M. Akrami, J. Mehrzad and H. Bardania, *J. Biomed. Mater. Res. Part A*, 2020, **108**, 839–850.

131 H. P. Sondermeijer, P. Witkowski, T. Seki, A. van der Laarse, S. Itescu and M. A. Hardy, *Tissue Eng. Part A*, 2017, **24**, 740.

132 J. Tang, T. Su, K. Huang, P. U. Dinh, Z. Wang, A. Vandergriff, M. T. Hensley, J. Cores, T. Allen, T. Li, E. Sproul, E. Mihalko, L. J. Lobo, L. Ruterbories, A. Lynch, A. Brown, T. G. Caranasos, D. Shen, G. A. Stouffer, Z. Gu, J. Zhang and K. Cheng, *Nat. Biomed. Eng.*, 2018, **2**, 17–26.

133 T. P. Martens, A. F. G. Godier, J. J. Parks, L. Q. Wan, M. S. Koeckert, G. M. Eng, B. I. Hudson, W. Sherman and G. Vunjak-Novakovic, *Cell Transpl.*, 2009, **18**, 297–304.

134 M. J. G. Schotman, M. M. C. Peters, G. C. Krijger, I. van Adrichem, R. de Roos, J. L. M. Bemelmans, M. J. Pouderoijen, M. G. T. A. Rutten, K. Neef, S. A. J. Chamuleau and P. Y. W. Dankers, *Adv. Healthc. Mater.*, 2021, **10**, 2001987.

135 K. Lei, Q. Ma, L. Yu and J. Ding, *J. Mater. Chem. B*, 2016, **4**, 7793–7812.

136 M. P. Ginebra, L. Albuixech, E. Fernández-Barragán, C. Aparicio, F. J. Gil, J. San Román, B. Vázquez and J. A. Planell, *Biomaterials*, 2002, **23**, 1873–1882.

137 R. Chen, C. Zhu, L. Xu, Y. Gu, S. Ren, H. Bai, Q. Zhou, X. Liu, S. Lu, X. Bi, W. Li, X. Jia and Z. Chen, *Biomaterials*, 2021, **274**, 120855.

138 L. L. Wang, Y. Liu, J. J. Chung, T. Wang, A. C. Gaffey, M. Lu, C. A. Cavanaugh, S. Zhou, R. Kanade, P. Atluri, E. E. Morrisey and J. A. Burdick, *Nat. Biomed. Eng.*, 2017, **1**, 983–992.

139 L. B. Vong, T. Q. Bui, T. Tomita, H. Sakamoto, Y. Hiramatsu and Y. Nagasaki, *Biomaterials*, 2018, **167**, 143–152.

140 M. H. Bakker, C. C. S. Tseng, H. M. Keizer, P. R. Seevinck, H. M. Janssen, F. J. Van Slochteren, S. A. J. Chamuleau and P. Y. W. Dankers, *Adv. Healthc. Mater.*, 2018, **7**, 1–8.

141 S. Uman, L. L. Wang, S. L. Thorn, Z. Liu, J. S. Duncan, A. J. Sinusas and J. A. Burdick, *Adv. Healthc. Mater.*, 2020, **9**, 2000294.

142 P. S. Patrick, J. C. Bear, H. E. Fitzke, M. Zaw-Thin, I. P. Parkin, M. F. Lythgoe, T. L. Kalber and D. J. Stuckey, *Biomaterials*, 2020, **243**, 119930.

143 D. Mawad, L. A. Poole-Warren, P. Martens, L. H. Koole, T. L. B. Slots and C. S. J. van Hooy-Corstjens, *Biomacromolecules*, 2008, **9**, 263–268.

144 X. Dong, C. Wei, T. Liu and F. Lv, *RSC Adv.*, 2015, **5**, 96336–96344.

3

Design and investigation of ureido-pyrimidinone based supramolecular polymer hydrogels

Abstract

Supramolecular motifs facilitate the modular incorporation of functionality with corresponding motifs. Herein, we present two supramolecular hydrogels based on the ureido-pyrimidinone (UPy) motif. Firstly, a recombinant peptide based on human collagen type 1 (RCPhC1) is introduced, conjugated with UPy moieties at different degrees of functionalization to increase control over the gelation, bioactivity, and mechanical properties. Circular dichroism displayed random coil formation of each UPy-RCPhC1 moiety in solution. Furthermore, hydrogels were formed by addition of the bifunctional UPy-moiety containing a poly(ethylene glycol) backbone (BF UPy-PEG), described in chapter 1. Rheology displayed softer hydrogels and slower hydrogel formation upon increasing the degree of UPy-RCPhC1. Secondly, a library of monofunctional UPy molecules is introduced, functionalized with single amino acids (UPy-AA). The effect of these simple modifications was explored by visualization of the assembling behavior in solution and the cellular compatibility was examined when the UPy-AA were prepared in a gel-like state in combination with the BF UPy-PEG. While all UPy-AA formed fibers in solution, fiber lengths were different. Furthermore, distinct differences were observed in cellular morphology and cell count, indicating the effect of this simple chemical modification on the cellular differentiation and spreading. In conclusion, two different hydrogel systems were presented composed of UPy units, that provide deeper insights in the adaptability of supramolecular UPy-based hydrogels and its applications.

The content described in this chapter is partly based on:

S. Spaans, P. P. K. H. Fransen, M. J. G. Schotman, R. van der Wulp, R. P. M. Lafleur, S. G. J. M. Kluijtmans and P. Y. W. Dankers, *Biomacromolecules,* **2019**, 20(6), 2360-2371

1. Introduction

Development of novel biomaterials by molecular self-assembly are promising solutions for medical treatment strategies. By obtaining inspiration from supramolecular assembling mechanisms in nature, new self-assembly processes can be exploited and a deeper understanding can be obtained regarding the structure, assembly, and dynamic behavior.[1] In the field of supramolecular chemistry, the focus lies on the specific, directional, tunable, reversible, non-covalent motifs, with highly dynamic properties. Components are held together by intermolecular forces, where complex and functional chemical systems are developed.[2] Using the interesting features of supramolecular chemistry and applying them to hydrogels can simulate the development of dynamic and adaptable hydrogel systems reminiscent to those observed in nature, e.g. the dynamic interaction of cells with the extracellular matrix (ECM).[3]

Supramolecular hydrogels that show these interesting dynamic and adaptable features can be exemplified by the thermo-responsive helical polyisocyanide polymer grafted with oligo-ethylene glycol) side chains.[4] This hydrogel resembles the unique stress-stiffening behavior of the ECM, forming a stable helical backbone, which is further stabilized with β-sheet-like peptide hydrogen bonds along the backbone. Another example is the benzene-1,3,5-tricarboxamide (BTA), which self-assembles into fibrils by threefold hydrogen bonding and π- π stacking.[5] This BTA moiety displays hydrogel formation upon mixing of two BTA moieties decorated with a tetra(ethylene glycol), and a poly(ethylene glycol) telechelically decorated with BTA motifs on both ends.[6] Changing the ratios between these two moieties led to adaptation and tunability of the mechanical properties of these hydrogels.

The strongly dimerizing UPy moiety ($K_{dim} > 10^6$ M^{-1} in $CHCl_3$) has been extensively studied over the last two decades, first published by Sijbesma *et al.*[7] Strong dimerization occurs by dynamic four-fold hydrogen bonding, of which thermal and environmental stimulations control the association, dissociation and strength of the bond, enabling mechanical tunability of the system. Functionalization of these UPy units with urea groups protected by alkyl-spacers stimulating one-dimensional lateral stacking forming micrometer long fibers solutions through π-π stacking, hydrophobic interaction and hydrogen bonding.[8] Telechelic functionalization of a 10 kDa poly(ethyelene glycol) (PEG) polymer with UPy units results in the bifunctional UPy polymer (BF UPy-PEG, Figure 3.1).[9] This UPy units display pH-responsiveness, with deprotonation of the enol-tautomer at elevated pH leading to a disruption of the four-fold hydrogen bonding. This renders interesting hydrogel properties at high concentration, which upon increasing the pH above 8.5 renders a sol state, whereas neutralization of the solution results in gel formation (Figure 3.1C).[10] This facilitates the injection of the hydrogel-precursor in the sol state at basic pH (>8.5), which upon coming in contact with the physiological neutral pH (7.4) the hydrogelator switches to the gel state, making this hydrogel a highly valuable candidate for injectable therapeutics. Furthermore, the hydrogel showed self-healing behavior, highlighting its highly dynamic nature.

In this chapter, we display the versatility of different UPy-based hydrogel systems, in which we introduce two different modifications and adaptations of these. First, we present the modification of a recombinant peptide based on collagen type 1, which was modified with UPy conjugation to its backbone. Several properties are assessed, i.e. assembly properties in solution and gelation. Furthermore, a library of different monofunctional UPy units is screened, to which single amino acids are conjugated. The assembly properties in solution as well as the mechanical and cellular adhesive properties in gel state are explored, elucidating the effect of simple modifications on the architectures of supramolecular assemblies.

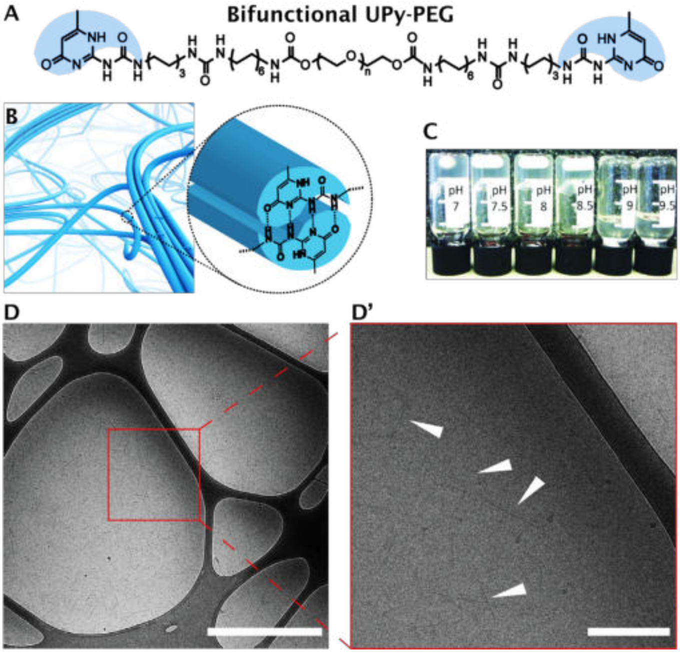

Figure 3.1 An overview of the BF UPy-PEG polymer and its characteristics with the chemical structure (A), the self-complementary dimerization of the ureido-pyrimidinone moiety by four-fold hydrogen bonding, with a schematic hydrogel structure (B), and the pH-responsive gelation, showing the gelation at pH<8.5, whereas at a pH>8.5 a viscous liquid is obtained (C). Cryogenic transmission electron micrographs display the fiber formation of the bifunctional UPy-PEG moiety (10 mg/mL, 890 μM) in neutralized PBS, at magnification 6.5kx, scale bar 1 μm (D) and 24kx, scale bar 200 nm in which the white arrows indicate the fibril structures (D').

2. UPy-modified collagen based peptides

Collagen is the most abundant protein in mammals, with collagen type 1 representing 90% of the total collagen content in the human body that is present in bone, skin, tendons, ligaments, and cornea.[11] The collagen molecule itself forms a triple helix fibril consisting of three polypeptide chains twined around one another, bound together by hydrogen bonds between adjacent peptides (hydrogen bonds between carbonyl and amine groups).[12] The unique characteristics of collagen and its high abundancy in the human body makes it an interesting candidate for biomaterial development. Biomaterial collagen scaffolds can contain cells in their inner structure, replacing native collagen-based extracellular matrix.[13]

Recombinant collagen peptide based on human collagen type 1 (RCPhC1), also known as Cellnest™ (FujiFilm Manufacturing Europe BV), contains multiple repeats of human collagen type

1 fragments and is enriched with arginine-glycine-aspartic acid (RGD) sequences, increasing the cellular adhesive ability.[14] It functions as an integrin-binding site, with the RGD forming a recognition site for the cells which stimulate cellular attachment.[15,16] Mimicking the ECM structure using RCPhC1 would offer similar structural properties as in vivo, of which the degradability can be tuned by the implementation of additional chemical or physical crosslinking.[17] The collagen type 1 recombinant peptide has been used in previous studies concerning cellular adhesion and differentiation of several cell types[18,19], as for wound healing applications[20].

By conjugating UPy-moieties to the RCPhC1 backbone, we aim to achieve control over the hydrogel formation and mechanical properties. The nucleophilic amines of the lysines present in the RCPhC1 backbone were functionalized with a 1,1'-carbonyldiimidazole (CDI)-activated UPy-synthon. A library was created with different degrees of UPy-functionality to the RCPhC1 backbone, i.e. UPy-RCPhC1-2, UPy-RCPhC1-5, UPy-RCPhC1-8, UPy-RCPhC1-12, and UPy-RCPhC1-16 (Figure 3.2). Firstly, the structural properties in solution were examined, mainly focusing on the influence of the grafting density on the RPChC1 backbone. Furthermore, a hybrid network was examined where a grafted UPy-RCPhC1 was introduced to the BF UPy-PEG system, and the gelation and mechanical properties were further elucidated.

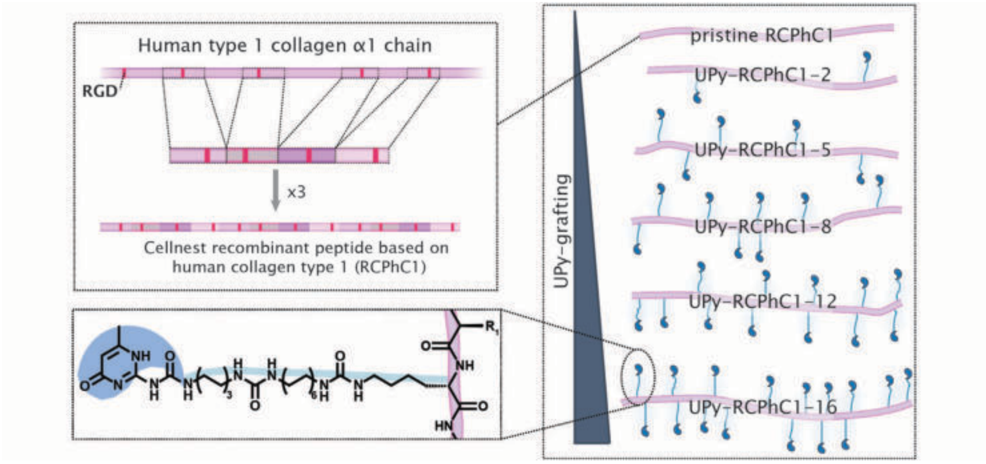

Figure 3.2 An overview of the cellnest recombinant peptide based on human collagen type 1 (RCPhC1), composed of four repeating units present in human type 1 collagen containing the RGD moiety, and the different UPy-grafted RCPhC1 units and the chemical structure.

2.1 Structural elucidation of RCPhC1 derivatives

The structure of RCPhC1 and its UPy-functionalized derivatives were examined in miliQ by circular dichroism (CD), in which the peptide has the spectroscopic signature of a random coil.[21] The random coil formation is also displayed in collagen, where prolines present in the backbone play a significant role in the conformation of this random coil behavior.[22] A change in temperature can lead to conformational changes regarding the secondary structure of collagen.[23] For these reasons, two temperatures were measured, being 5 and 20 °C to examine the secondary structure of this RCPhC1(-functionalized) peptide (Figure 3.3). The pristine

RCPhC1 displayed random coil behavior, with a peak minimum observed at 195 nm and a maximum peak at 220 nm at 20 °C. Upon cooling, collagen often show an increased stability towards a triple helical structure[24-27], which is also shown here with an increase in signal at 5 °C for the peak at 220. A hypothesis to explain this behavior is that the intermolecular forces are increased upon the slower movement of the molecules (decrease of kinetic energy). Therefore, the intermolecular forces present remain largely in the random coil formation, as shown previously.[28] When UPy-moieties were functionalized to the RCPhC1 backbone, small shifts were observed in the minimum of the spectra, with UPy-RCPhC1-2 at 198 nm, UPy-RCPhC1-5 at 200 nm, UPy-RCPhC1-8 at 199 nm, UPy-RCPhC1-12 at 199 nm, and UPy-RCPhC1-16 min 202 (Figure 3.3B-F). The maximum peak at 220 nm did not shift after UPy-moiety functionalization in the spectra. The shift at the minimum peak could indicate a small structural change upon functionalization of the free lysines present in the RPChC1 backbone. All UPy-functionalized RCPhC1 showed an increase in CD signal upon cooling, with significant increases larger in comparison to the pristine RCPhC1 observed for UPy-RCPhC1-2, i.e. -8.24 (20 °C) and 1.27 (5 °C) at 220 nm, UPy-RCPhC1-5 displayed -9.10 (20 °C) and 8.65 (5 °C) at 220 nm, and UPy-RCPhC1-8 displayed -7.13 (20 °C) and 5.14 (5 °C) at 220 nm. This can indicate an additional intermolecular crosslinking effect of the UPy-moieties present on the RCPhC1 backbone, further increasing the stability and aiding towards a triple helical structure by UPy-UPy dimerization. For the remaining functionalized RCPhC1, the ellipticity change was less significant, with UPy-RCPhC1-12 showing a CD signal of -7.27 (20 °C) and -0.79 (5 °C) at 220 nm, and UPy-RCPhC1-16 showed a CD signal of -13.66 (20 °C) and -7.98 (5 °C) at 220 nm.

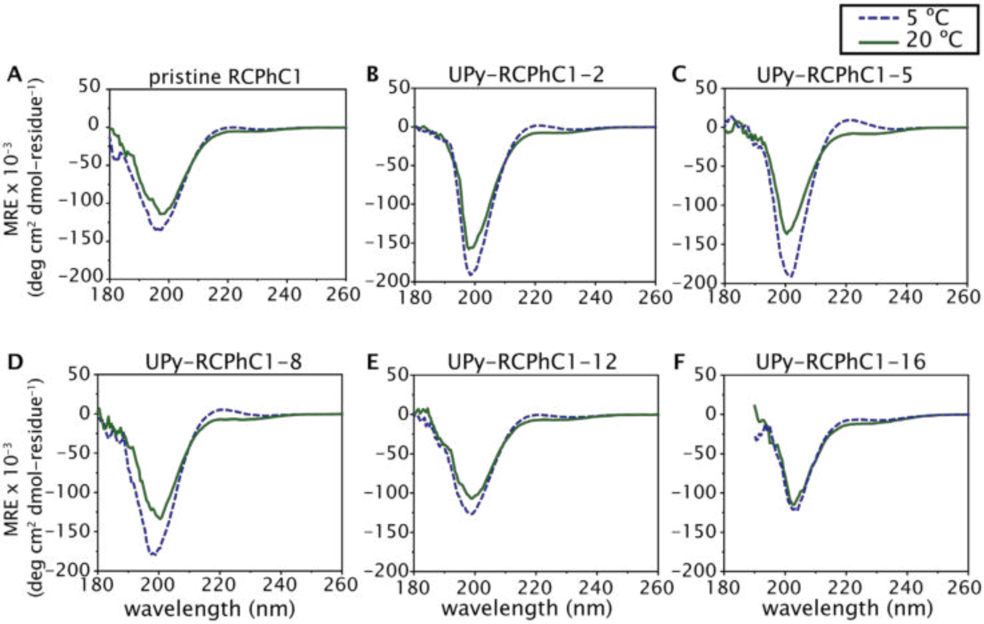

Figure 3.3 Circular dichroism spectra showing the mean residue ellipticity (MRE) of pristine RCPhC1 (A), and the UPy-functionalized RCPhC1 being UPy-RCPhC1-2 (B), UPy-RCPhC1-5 (C), UPy-RCPhC1-8 (D), UPy-RCPhC1-12 (E), and UPy-RCPhC1-16 (F) at a concentration of 0.5 mg/mL in miliQ, at 5 °C and 20 °C.

To further elucidate the structural conformation the UPy-RCPhC1 derivatives, the zeta-potential was measured and dynamic light scattering (DLS) was used to examine the aggregation behavior in solution. A decrease of the zeta-potential was observed with increasing UPy-functionality (Table 3.1). This is expected, as a higher UPy-functionality leads to a lower lysine (positive charge) content on the RCPhC1 backbone. The additional effect of the UPy-moieties functionalized on the RCPhC1 backbone is further explored here by measuring the hydrodynamic radius in 1x PBS solution at two different pH, being ~neutral (5-7) and basic (10-13). The UPy-moiety is known to be pH-dependent, with deprotonation of the enolate anion occurring at a high pH, leading to a disruption of the four-fold hydrogen bonding. Lowering the pH leads to protonation, enabling dimerization.[29] At an elevated pH, the effects of the UPy-UPy interactions is hypothesized to be less observed therefore. The pristine RCPhC1 shows a small change in size from 20 °C basic pH (18±9 nm) to 5 °C (15±7 nm, Figure 3.4A). Subpopulations are shown at 20 °C, basic pH for UPy-RCPhC1-2 (peak 1: 12±2 nm, peak 2: 168±37 nm), UPy-RCPhC1-5 (peak 1: 14±4 nm, peak 2: 190±75 nm), and UPy-RCPhC1-8 (peak 1: 15±6 nm, peak 2: 260±117 nm). An increase in UPy-functionality leads to a decrease of polarity, by introduction of non-polar side-groups. This can lead to the higher extend of subpopulations. No significant change in size was observed when the sample was cooled down to 5 °C (Figure 3.4B-D). Upon decreasing the pH, the subpopulations became more distinctive and broader, indicating that formation of UPy-UPy interactions play a role in the particle aggregation behavior. Pristine RCPhC1 showed an additional subpopulation upon lowering of the pH (623±282 nm), which broadened upon cooling down to 5 °C (Figure 3.4A'). For UPy-RCPhC1-12 and UPy-RCPhC1-16, one population was observed (Figure 3.4E, F), 28±15 nm and 14±6 nm, respectively which showed no changes upon cooling. Lowering the pH resulted in larger aggregate formation of 120±60 nm for UPy-RCPhC1-12 and 379±160 nm for UPy-RCPhC1-16. These results indicate the complex molecular aggregation behavior of these structures, where the RCPhC1-RCPhC1 interactions as well as the UPy-UPy interactions play a significant role and are both dependent on temperature as well as pH changes.

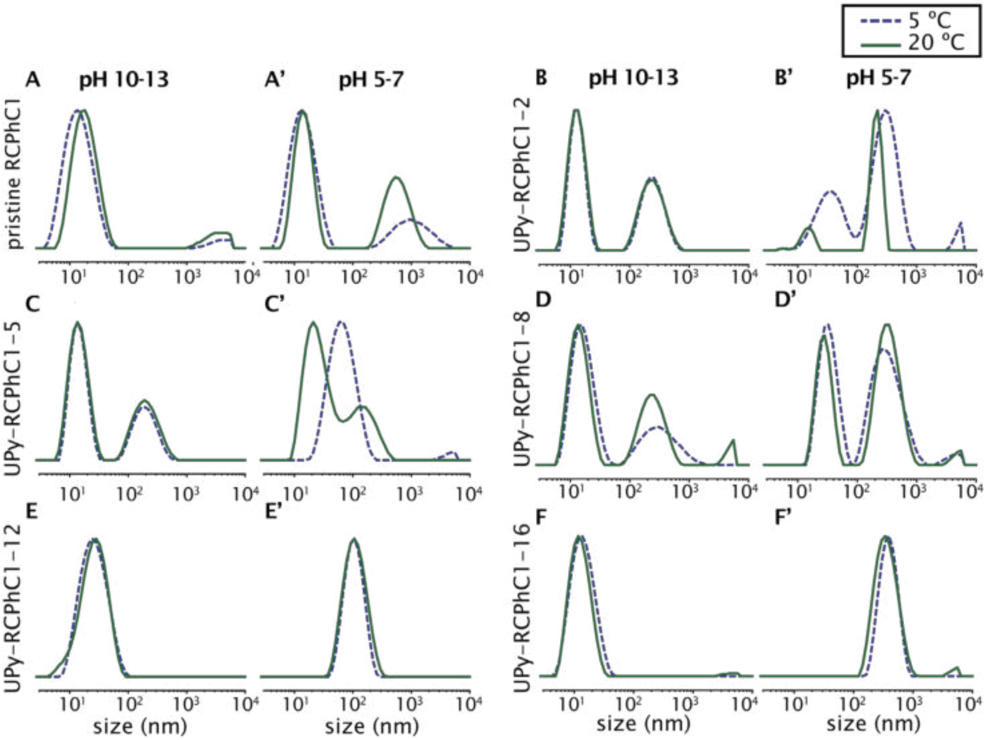

Figure 3.4 Dynamic light scattering measurements of the (UPy-)RCPhC1 derivatives, showing the normalized intensity distribution at neutral pH (5-7) and at elevated pH (10-13), at a temperature of 20 and 5 °C, in 1x PBS at a concentration of 2 mg/mL.

Table 3.1 Overview of the zeta-potential of the RCPhC1 and UPy-RCPhC1 derivatives.

Derivative	**Zeta-potential (mV)**	**Derivative**	**Zeta-potential (mV)**
RCPhC1	-6.1±0.2	UPy-RCPhC1-8	-15.5±0.7
UPy-RCPhC1-2	-6.9±0.1	UPy-RCPhC1-12	-29.0±1.6
UPy-RCPhC1-5	-9.4±0.8	UPy-RCPhC1-16	-34.6±2.0

2.2 Hydrogel formation

The influence of the UPy-RCPhC1 derivative when combined with the BF UPy-PEG-based hydrogel system was examined, where the effect of UPy-RCPhC1 on the aggregation and mechanical properties is examined. UPy-RCPhC1-5 is examined further, due to its high solubility and interesting secondary structure. Cryogenic transmission electron microscopy (cryo-TEM(is performed to analyze the aggregation behavior in solution (Figure 3.5). The particle size of the UPy-RCPhC1-5 in solution is 8.2±2.0 nm, whereas upon introduction of BF UPy-PEG (UPy-RCPhC1-5 : BF UPy-PEG, mol ratio 1:9) a similar size of 8.0±2.7 is observed. This indicates that the addition of BF UPy-PEG does not lead to significant structural changes.

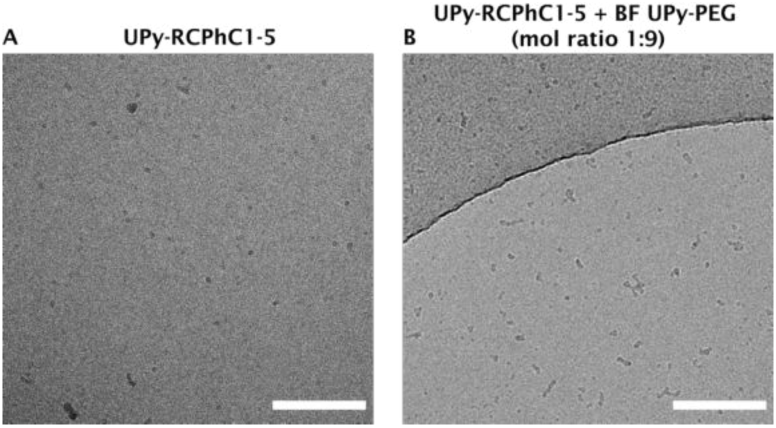

Figure 3.5 Cryogenic transmission electron micrographs of UPy-RCPhC1-5 (A) and UPy-RCPhC1-5 combined with BF UPy-PEG (B, mol ratio 1:9) both dissolved in PBS at a concentration of 0.5 mg/mL (magnification 24kx, scale 200 nm).

The BF UPy-PEG based hydrogel is known to be an inert, pH-responsive, self-healing hydrogel, with a storage modulus around 10 kPa.[10] Addition of a UPy-RCPhC1 derivative could potentially increase the bioactivity of this hydrogel, creating a hybrid bioactive hydrogel. The UPy-groups functionalized to the RCPhC1 backbone were hypothesized to interact with the UPy-moieties of the BF UPy-PEG network. The mechanical properties of several ratios, namely 9:1, 3:1 and 1:1, between BF UPy-PEG and UPy-RCPhC1-5 were examined using rheology. The gelation speed was examined by dissolving the two compounds at differing ratio in basic PBS, resulting in a sol-state at a pH of 9, whereafter a small quantity of acid is added. Two minutes after acid addition, the mechanical properties were measured over a time span of 20 minutes (Figure 3.6). BF UPy-PEG showed direct gelation after acid addition (G'>G'') and a storage modulus of 11 kPa after 20 min. Addition of a small quantity of UPy-RCPhC1-5 (mol ratio 9:1, BF UPy-PEG:UPy-RCPhC1) resulted in a significant decrease in stiffness (~2250 Pa storage modulus after 20 min), but showed direct gelation as well after acid addition. Further increase of UPy-RCPhC1-5 (mol ratio 3:1, BF UPy-PEG:UPy-RCPhC1) showed to further soften the network (670 Pa storage modulus after 20 min), with the network showing direct gelation. The 1:1 molar ratio resulted in the softest hydrogel (120 Pa storage modulus after 20 min), during which the network gelated after ~4 min. These results show a significant effect due to UPy-RCPhC1-5 addition, which decreases the stiffness of the hydrogel significantly. The higher molar ratios (9:1, 3:1) showed swift gelation, whereas the molar ratio 1:1 showed a delayed gelation. Still, all molar ratios showed gelation upon neutralization of the sol-state. The quantity of UPy-moieties is 2 per 11 kDa for BF UPy-PEG, whereas the UPy-RCPhC1-5 contains 5 per 53.5 kDa, decreasing the number of UPy-UPy interactions and therefore crosslink interactions when the UPy-RCPhC1-5 content is increased (Table 3.2), which can lower the stiffness of the hydrogels.

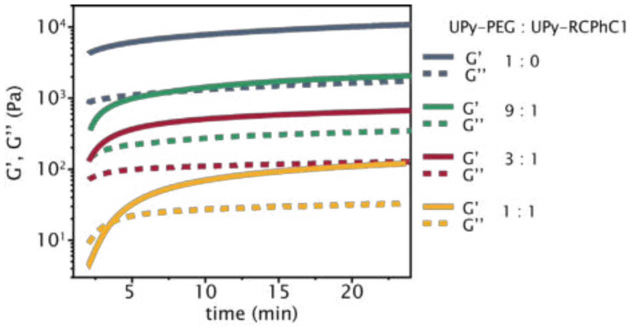

Figure 3.6 Gelation properties of different combinations BF UPy-PEG and UPy-RCPhC1 at mol ratio of 1:0 (blue), 9:1 (green), 3:1 (red), and 1:1 (yellow) at 37 °C, 1 rad/s, 1% strain.

The mechanical properties of the 1:0 and 9:1 molar ratio of BF UPy-PEG to UPy-RCPhC1-5 were further examined using rheology, where both hydrogels show frequency-dependent viscoelastic behavior (Figure 3.7A). For both hydrogels, there is an increase of storage moduli when the frequency is increased, whereas the loss modulus slightly decreases for the 1:0 hydrogel, but an increase of loss modulus is shown for the 9:1 ratio hydrogel. For both hydrogels, the storage moduli is decreased at lower frequencies (i.e. higher measuring time), being 4720 Pa for 1:0 ratio, and 518 Pa for 9:1 ratio. At higher frequencies (i.e. lower measuring time), the storage modulus is increased to 25400 Pa for 1:0 ratio, and 7760 Pa for 9:1 ratio. This indicates the dynamicity of the network at lower frequencies, and the occurrence of structural rearrangement. At higher frequencies both gels act more as solid-like materials.

Table 3.2 Properties of different combination BF UPy-PEG:UPy-RCPhC1, indicating the storage moduli, viscosity, and molarity of the UPy-groups.

Mol ratio UPy-PEG : UPy-RCPhC1	Storage moduli at neutral pH (Pa)	Approximate viscosity at pH 9 (Pa.s)	Theoretical concentration UPy-moieties (mM)
1:0	11000	0.439	0.53
9:1	2250	0.349	0.38
3:1	690	0.238	0.26
1:1	120	0.236	0.17

The strain sweep shows a linear course for the storage modulus from 1 – 20% for the 1:0 ratio (Figure 3.7B), whereas the 9:1 ratio shows a small decrease of storage modulus over the increasing strain (~3700 Pa at 1% strain, ~2500 Pa at 50% strain). The hydrogel disruption for the 9:1 hydrogel occurs at a strain of ~85%, whereas the 1:0 ratio hydrogel disrupts at a strain of ~40%. Both hydrogels show a recovery after the strain-sweep (Figure 3.7C), with the 1:0 ratio gel reaching a storage modulus of 18000 Pa, whereas the 9:1 recovers to a storage modulus of 980 Pa. The addition of UPy-RCPhC1-5 lowers the storage moduli as well as loss modulus in comparison to the pristine BF UPy-PEG hydrogel (ratio 1:0). However, the gelation properties, viscoelastic behavior and recovery properties remain intact.

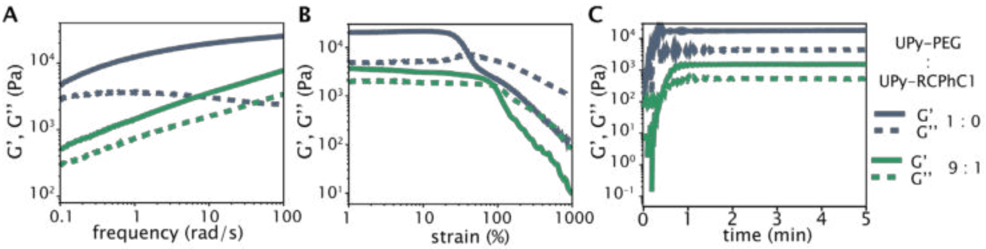

Figure 3.7 Mechanical properties of two hydrogels, being the hydrogel based on solely BF UPy-PEG (blue, mol ratio of 1:0) and the BF UPy-PEG combined with UPy-RCPhC1 (green, mol ratio 9 : 1), with the frequency sweep (A) measured at 1% strain, the strain sweep (B) measured at 1 rad/s, and a recovery curve at 1% strain and 1 rad/s over time (C) measured at 37 °C.

Using scanning electron microscopy (SEM), the lyophilized hydrogel networks were examined (Figure 3.8) For both hydrogels, a porous network was observed where the 1 : 0 ratio showed to have pore sizes of around 7.7±3.7, whereas the 9:1 ratio showed pore size of 9.2±5.6. A larger variation in pore size was observed for the 9:1 ratio, with occasionally small 'spikes' appearing in the lumen. Whether this indicates a drying effect, or presence of insolubilized hydrogel remnants is unknown. These results indicate small structural differences between the two lyophilized hydrogels.

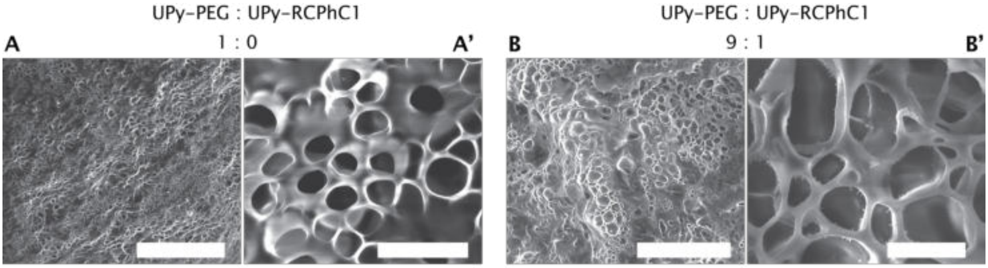

Figure 3.8 Scanning electron micrographs of the morphology of BF UPy-PEG and UPy-RCPhC1 hydrogels after neutralization and lyophilization, with BF UPy-PEG (A, scale 200 μm) and a zoom-in micrograph (A', 20 μm), and UPy-PEG and UPy-RCPhC1 at a ratio of 9 : 1 (B, scale 100 μm) with a zoom-in micrograph (B', 10 μm).

3. UPy-amino acid library

Peptide-based hydrogels show the interesting features of amino acid components with their functional side chains, hierarchical structure, responsiveness, cooperativity and multi-valency.[30] It is known that changing a single amino acid in a peptide-chain can lead to a dysfunctional peptide, changing its folding properties.[31] Development of a semi-synthetic supramolecular protein structure can give more insight in this peptide/protein formation and the influence of single amino acid functionalization on its function. Implementing the unique individual properties of amino acids into supramolecular hydrogels could induce additional functionality and folding properties. As an example, histidine and alanine encourage the formation of A_R-helical structures, whereas cysteine, glycine and proline the formation of extended structure and bends.[32]

Cui et al. synthesized a series of peptide amphiphiles, which by changing the sequence of the amino acid order, a variety of 1D morphologies was obtained, such as nanobelts, single and bundled nanofibers, twisted ribbons, helical ribbons, and nanotubes.[33] Foo *et al.* demonstrated a two component system, which went from a sol to a gel state by simple mixing.[34] In this system, the gelation occurs between specific molecular-recognition interactions, when mixing WW domains, i.e. small proteins which mediates specific interactions with protein ligands containing two tryptophans (thus the name WW), and proline-rich peptide repeating units. This enabled encapsulation of cells without affecting the cell viability and illustrates the high assembling ability of protein and peptide modified domains.

Furthermore, positively and negatively charged hydrogels often show high cellular attachment in comparison to neutral hydrogels.[35,36] The ζ-potential is of high importance when the cellular spreading on a hydrogel is examined, where the optimal ζ-potential values are often dependent on the cell type.[37] Phadke et al. showed that an optimal balance of hydrophobic and hydrophilic interactions at the hydrogel interface containing flexible-pendant side chains could lead to rapid self-healing, which hydrogels only based on proteins often do not exhibit, despite their amide and carboxylic functional groups.[38]

Here, a library of monofunctional UPy units is introduced, which were functionalized with a variety of single amino acids (UPy-AA, Figure 3.9). Previous research has shown that the exchange dynamics of monofunctional UPy units and BF UPy-PEG in solution were highly dependent on the ratio between these two units[39], whereas at higher concentrations gelation and its mechanical and dynamic properties can be tuned by adapting the ratio between monofunctional UPy units and BF UPy-PEG.[29] An increase in brittleness was observed when the fraction of monofunctional UPy moieties in the hydrogels was increased, whereas an increase of the BF UPy-PEG led to an increase in dynamicity and self-healing ability. This adaptive dynamicity was further explored by addition of cell-adhesive functionalities, with the exchange dynamics leading to a significantly altered cell-adhesiveness.[40] The implementation of additional functionality to monofunctional UPy units can induce interesting structural changes in solution using different UPy-AA combination, and possibly increase bioactivity of the UPy-AA based hydrogel. The effect of such small structural changes was elucidated by characterization of the molecular assembly and gelation properties. Furthermore, the relationship between the UPy-AA hydrogels and cellular interaction is exploited, in collaboration with Annika Vrehen. The UPy-AA were subdivided into five different groups, being the UPy-AA with charged positive side chains: UPy-arginine (UPy-Arg), UPy-histidine (UPy-His), and UPy-lysine (UPy-Lys), charged negative side chain: UPy-aspartic acid (UPy-Asp), polar uncharged side chains, UPy-serine (UPy-Ser) and UPy-asparagine (UPy-Asn), special cases: UPy-glycine (UPy-Gly), UPy-cysteine (UPy-Cys), and UPy-proline (UPy-Pro), and hydrophobic side chains: UPy-alanine (UPy-Ala), UPy-valine (UPy-Val), UPy-tyrosine (UPy-Tyr), UPy-isoleucine (UPy-Ile), UPy-leucine (UPy-Leu), and UPy-methionine (UPy-Met). Two UPy-AA were left out of the study due to poor solubility, being a UPy unit containing a phenylalanine, and tryptophan side chain.

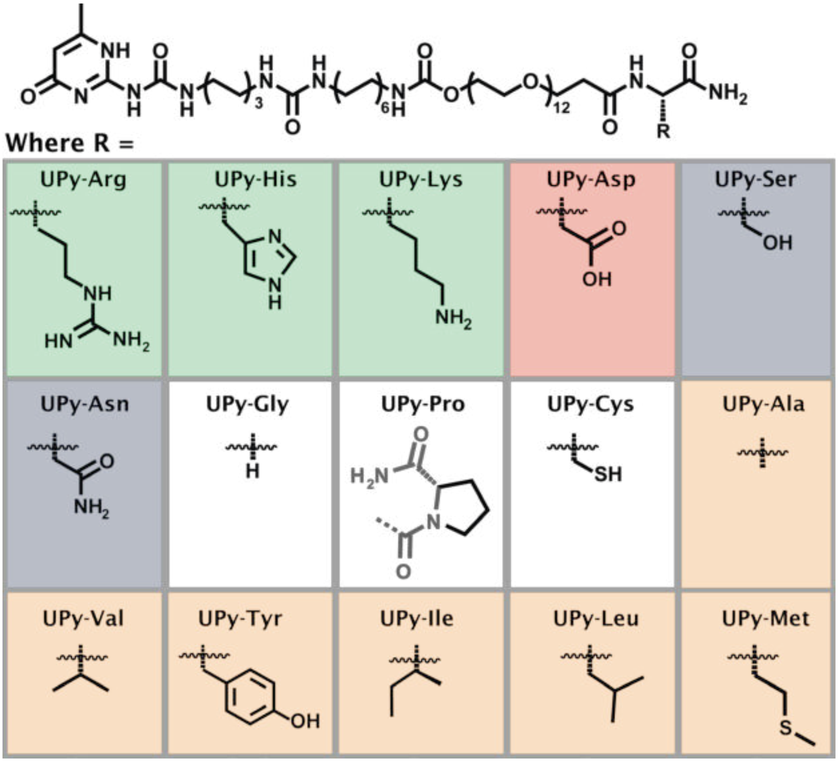

Figure 3.9 Overview of the monofunctional UPy-moieties, with different amino acid functionalities, i.e. positively charged UPy-AA (green), negatively charged UPy-AA (red), polar UPy-AA (blue), special cases (white), and hydrophobic UPy-AA (orange).

3.1 Properties in solution

To explore the effect of the amino acid functionality on the self-assembly of the UPy units, the UPy-AA compounds were dissolved in alkaline PBS (pH ~12) at elevated temperature for optimal solubility. At high pH, the crosslinks are disrupted by deprotonation of the UPy molecule.[10] The samples were neutralized with 1 M HCl and the assembling behavior of the UPy-AA was characterized using cryo-TEM (Figure 3.10), from which the fiber diameter was determined. Furthermore, the zeta-potential was measured (Figure 3.11), determining the net surface charge of the UPy-AA in solution. UPy-Arg (diameter size 5.7±1.8 nm) and UPy-Lys (diameter size 6.7±1.5 nm) show to form long flexible nanofibers that tend to cluster and entangle randomly, both displaying a positive charge, e.g. 37.6±4.1 mV and 39.2±2.4 mV, respectively. Noteworthy is that these are the only UPy-AA that display clustering tendency, as well as being the only UPy-AA containing a positive charged side chain at neutral pH. Part of the lysine side chain could be shielded by the negatively charged phosphates presents in PBS, neutralizing the charge. A hydrophobic nonpolar side chain originates due to this salt shielding, favorable for hydrophobic clusters.[41] Arginine shows similar fibril networks as lysine, both containing a positive charge. Here, cluster formations can also be formed due to the arginine moieties being partly charge shielded. UPy-His (0.20±1.1 mV, diameter size 5.3±1.2 nm) shows long fibril assembly that appear to be bundling with some occasional shorter fibers. UPy-Asp has a short, polar, negatively-charged side group, and is the sole UPy-AA having a negative charge of this group, displaying highly structured fiber bundling assembly along with thick long fibers (-49.6±4.9 mV, diameter size 5.4±0.8 nm). The polar UPy-Ser (diameter size 6.2±1.6 nm) and UPy-Asn (diameter size 6.2±1.1 nm) show long, flexible fiber assembly. Both UPy-Ser and UPy-Asn display negative zeta potentials (-23.6±2.6 mV and -43.6±3.4 mV, respectively), with UPy-Asn having a significantly lower zeta potential. However, the structural appearance differs between UPy-Asn and UPy-Asp, with UPy-Asp forming a higher bundling formation, whereas UPy-Asn shows more thick fibril morphologies. UPy-Gly (diameter size 7.1±1.5 nm) and UPy-Pro (diameter size 6.5±1.4 nm) both show a negative zeta potential (-29.6±2.5 mV and -8.5±1.1 mV, respectively). UPy-Pro differs slightly from UPy-Gly, with the latter one showing long fiber formation, whereas UPy-Pro assembles into long undisrupted fibers along with shorter fibers, ranging from approximately 50 to 400 nm or higher in size, which can indicate some fiber disruption due to the proline side chain. Furthermore, UPy-Cys (-25.1±2.9 mV, diameter size 6.3±1.1 nm) having a negative zeta potential as well, displays short fiber formation, with the cysteine containing side chain shortening the fiber length (varying from 10 to 300 nm). UPy-Ala (fiber diameter 5.2±1.3 nm) and UPy-Val (fiber diameter 7.3±1.8 nm) showed elongated fiber formation, whereas UPy-Tyr (fiber diameter 5.5±1.2 nm) and UPy-Ile (fiber diameter 6.4±1.5 nm) showed short fiber formation. UPy-Tyr and UPy-Ile both appeared to cluster in short bundles, whereas interestingly, UPy-Leu (fiber diameter 6.2±1.1 nm), the isomer of UPy-Ile, showed to form longer fibers. UPy-Met (fiber diameter 5.8±1.4 nm) showed long fiber formation and bundling assembly. The UPy-AA with a hydrophobic amino acid functionality all showed to have slightly negatively charged zeta potentials, with being -16±1.8 mV (UPy-Ala), -8.4±0.4 mV (UPy-Val), -15.6±1.1 mV (UPy-Tyr), -7.1±0.5 mV (UPy-Ile), -12.1±1.1 mV (UPy-Leu), and -15.1±1.1 mV (UPy-Met). These results show structural changes as well as charge density in solution are obtained by changing the end group functionalization of the UPy units with single amino acids, changing fiber bundling assembly, fiber length and fiber diameter. The gel state of the UPy-AA will further explore, examining the influence of the amino acids on the mechanical properties as well as cellular response.

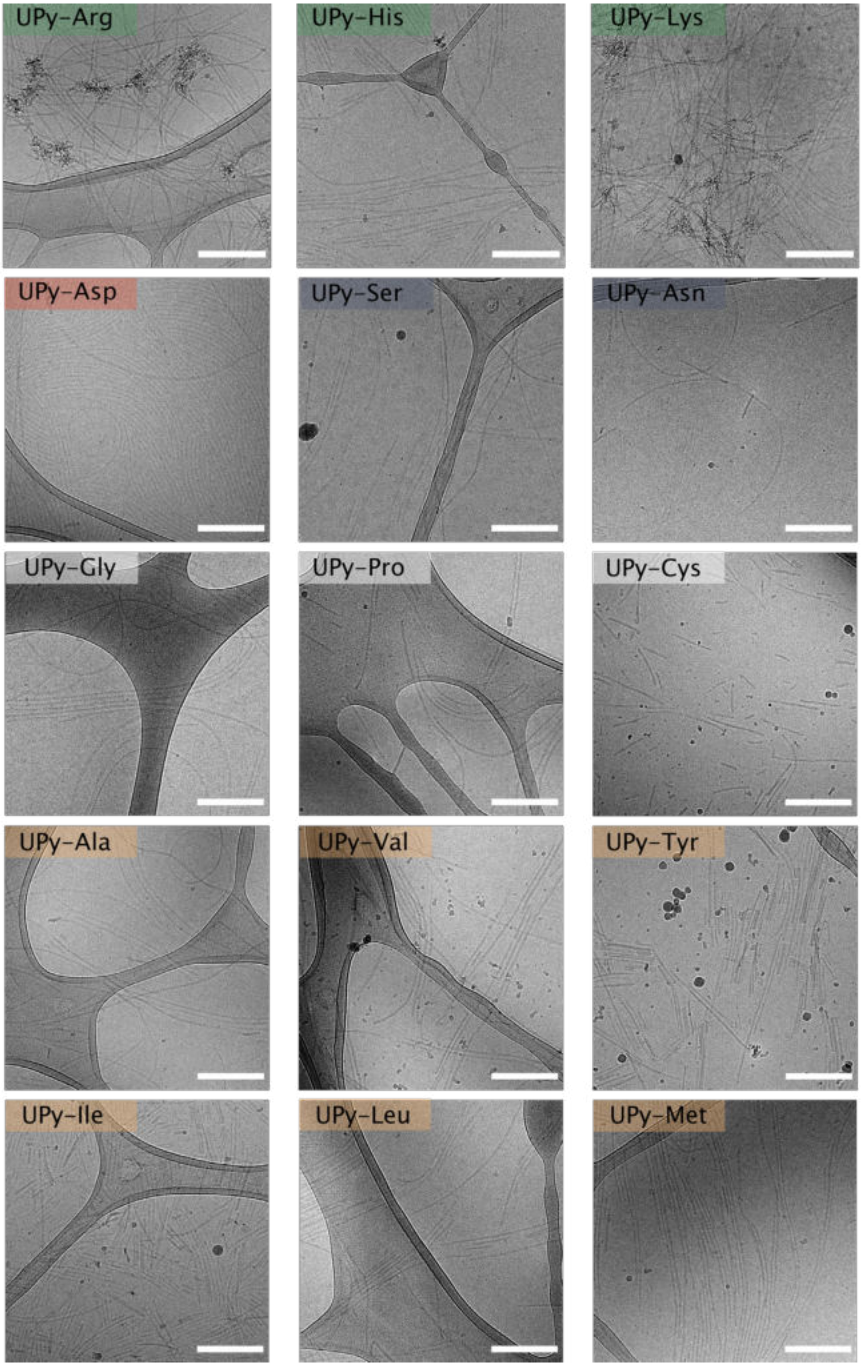

Figure 3.10 Cryogenic transmission electron microscopy images of the diluted UPy-AA (80 μM, ~0.1 mg/mL) in neutralized PBS, at a magnification of 24k, scale bar represents 200 nm.

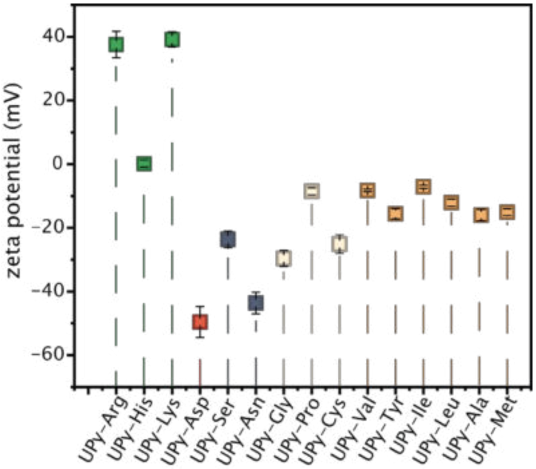

Figure 3.11 Zeta-potential measurements of UPy-amino acids in solution at a concentration of 0.4 mM at a 0.1x PBS concentration.

3.2 Hydrogel formation and rheological properties of the UPy-AA

Low contents of BF UPy-PEG led to formation of solid-like hydrogels, with the BF UPy-PEG acting as a crosslinker between the monofunctional fibers of the UPy-AA.[40] The effect of the UPy-AA at increased concentration (~18.7 mM) crosslinked with BF UPy-PEG (0.23 mM, mol ratio of 80 to 1) was examined by rheology and cellular compatibility. The mechanical properties of these gels were measured, determining the storage modulus (Figure 3.12A) and yield stress (Figure 3.12B). Cells are known to be responsive towards material stiffness, with loss of cytoskeletal tension on soft substrates leading to a rounded morphology, whereas stiff substrates can withstand higher traction forces from the cells, which increase the tensile state of the cytoskeleton leading to a spread-out morphology.[42] This makes the stiffness of hydrogels an important factor to examine. Furthermore, the yield stress of the hydrogels is determined, which correlates with the critical strain and shows when the hydrogel network start to behave more fluid-like (disruption of the network).

The following UPy-AA were left out for the hydrogel studies due to poor solubility at high concentrations, resulting in highly turbid or semi-gelated solutions, i.e. UPy-Cys, UPy-Ile, and UPy-Leu. The storage moduli varied for the UPy-AA hydrogels from 1045±49.5 Pa to 3195±982.9 Pa, with UPy-Val showing the lowest and UPy-Ser showing the highest storage moduli. Positively charged UPy-AA hydrogels showed a somewhat higher storage modulus, with UPy-Arg hydrogel, UPy-His hydrogel, UPy-Lys hydrogels having storage moduli of 2315±92 Pa, 1575±346 Pa, and 3025±856 Pa, respectively. Furthermore, they showed to have similar yield stresses of 12.6±4.0, 9.4±0.2 and 10.8±0.07 Pa, respectively. The UPy-Asn hydrogel showed a similar stiffness to UPy-Ser, with a moduli of 2820±297 Pa. Equal yield stresses were observed for these hydrogels, with a yield stress of 7.6±2.3 Pa (UPy-Ser) and 6.9±0.45 Pa (UPy-Asn). A storage moduli of 1630 Pa was observed for the UPy-Asp, with a yield stress of 7.2±1.3 Pa. UPy-Gly hydrogel and UPy-Pro hydrogel showed storage moduli of 2450±792 Pa and 1905±615 Pa, with yield stresses of 8.9±3.4 Pa and 10.2±0.4 Pa, respectively.

A subtle difference in storage moduli is observed between the different groups, with the hydrophobic UPy-AA (UPy-Ala, UPy-Val, UPy-Tyr, and UPy-Met) displaying a trend towards a lower storage modulus, whereas the positively charged (UPy-Arg, UPy-Lys) and polar (UPy-Ser, UPy-Asn) show a trend towards a higher storage modulus. This effect could be due to the enhanced solubility and mobility of the positively-charged and polar amino acids groups, which stimulates the supramolecular crosslink formation. However, the UPy-Asp hydrogel showed to have a lower stiffness in comparison to its charged and polar counterparts. During hydrogel preparation, the UPy-Asp molecule at high concentration (~18.7 mM in basic PBS) showed to be slightly turbid, indicating partial solubility. However, a hydrogel was formed upon addition of the BF UPy-PEG. This can indicate that the negative side-group of the UPy-Asp molecule has an aggregative effect. The cryo-TEM images of UPy-Asp shows large fiber bundle formations, which can sterically hinder the BF UPy-PEG molecules in some extent to form supramolecular interactions, lowering the supramolecular crosslinks between the UPy-Asp and BF UPy-PEG.

The UPy-Ala, UPy-Val, UPy-Tyr, and UPy-Met hydrogels showed relatively low storage moduli, being 1455±275 Pa, 1045±50 Pa, 1745±276 Pa, and 1202±662 Pa, with yield stresses of 13.2±0.5 Pa, 9.8±3.2 Pa, 2.7±0.5 Pa, and 6.2±1.1 Pa, respectively. The non-polar amino acid group functionalized to the UPy-AA moiety can lead to some hydrophobic interactions between the UPy-AA side-chains. This clustering can limit the mobility of the UPy-moieties, therefore lowering the crosslink density to some extent. What can be concluded from these results is that the UPy-AA hydrogel stiffnesses appear to be in similar ranges regarding the storage moduli, with small differences in mechanical properties being observed.

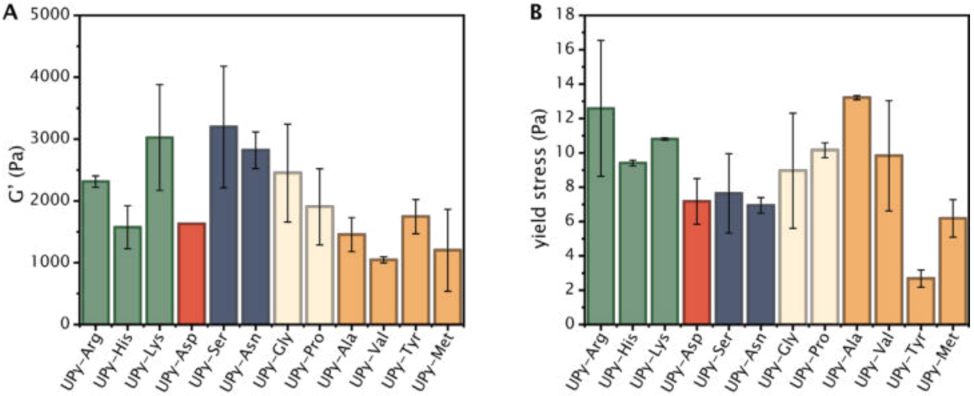

Figure 3.12 The storage modulus (A) and the yield stress (B) of the UPy-AA is shown at a frequency of 1 rad/s, 1% strain, at a concentration of 18.7 mM UPy-AA combined with 0.23 mM BF UPy-PEG in 1x PBS. Data is represented as mean ± SD, n=2.

3.3 Human dermal fibroblasts 2D culture on UPy-AA hydrogels

To examine the cellular compatibility and adhesive properties of the hydrogels, normal human dermal fibroblasts (NHDFs) were cultured in 2D on the hydrogels for three days. A monofunctional UPy-moiety functionalized with an adhesive ligand, UPy-cRGD (1 mM), was added to the hydrogels to enhance cell spreading. The UPy-Arg and UPy-Lys hydrogels show high cell viability, and a clear spread morphology (Figure 3.13), indicating cellular compatibility of these positively charged hydrogels. This was confirmed by nuclei count (Figure 3.14), showing 266±35 and 142±19 cells /mm^2 for UPy-Arg and UPy-Lys, respectively. The UPy-His hydrogels show a similar spread morphology, as high cell viability (307±22 cells/mm^2). Though the histidine contains a neutral charge at neutral pH (confirmed by the zeta-potential measurements), the histidine side-chain shows to have a positive effect regarding the cellular spreading. Similar trends were observed in other studies, in which positive coatings[43] and positively-charged hydrogels[44,45] often show high cellular adhesion This is mediated by the interaction between polyanionic cell surface and polycationic surface or hydrogel. UPy-Asp shows high cellular adhesion with high spread-out cellular morphology, but low nuclei count in comparison to the positively charged hydrogels (98±25 cells/mm^2). Negatively charged surfaces can bind to polar functionalities on the cell membrane and can mediate protein binding, with proteins containing polyelectrolytic charges.[46] Bet et al. stated an improved cellular adhesion due to the polarity of the negative charge influencing the wettability to a level suitable for cell adhesion.[47] This can therefore increase the cellular adhesion between negative charged hydrogels and cell membrane, leading to a spread out cellular morphology. Furthermore, the DAPI stain, which contains two amidine side groups with a positive charge, stained the fibril structure of the UPy-Asp hydrogel network (Figure 3.13, Figure 3.15). Interestingly, the cells appear to align with the fibril network (Figure 3.15), which further strengthens the hypothesis of proteins being absorbed on the UPy-Asp hydrogel. By protein absorption assays, this hypothesis can be affirmed.

High variability was observed for the UPy-Ser hydrogel, showing differing cellular morphologies as well as large variation in the nuclei count (184±162). This was also observed for the metabolic activity (results not shown here) and hydrogel stiffness, which showed a high variability in storage moduli (3195±983 Pa). This can indicate some variation in gelation due to the serine side-chain. The UPy-Asn and UPy-Pro hydrogels show more outstretched cellular morphologies, with a high quantity of cells (267±5 and 256±51 cells/mm^2). UPy-Gly shows similar cell quantity (262±25 cells/mm^2), but the cells appear to show a more clustered morphology. Interestingly, the non-polar UPy-AA hydrogels (UPy-Val, UPy-Tyr, UPy-Leu, and UPy-Met) show highly similar cellular behavior, with small and slightly outstretched single cells or small clusters of cells. Overall, a lower cell count was observed for the non-polar UPy-AA. The exception of this group is the UPy-Ala hydrogel, showing a high cell count (203±7 cells/mm^2) as well as a stretched out morphology. With a single methyl group as side-chain, the hydrophobic character of the UPy-Ala is lower in comparison to the other hydrophobic UPy-AA. UPy-Met displays a similar cell count as UPy-Lys (150±47 cells/mm^2), but shows a less spread out morphology. UPy-Val, UPy-Tyr, and UPy-Leu display a cell count of 80±2, 85±4, and 106±20 cells/mm^2. The somewhat lower stiffness could influence the decrease in spread

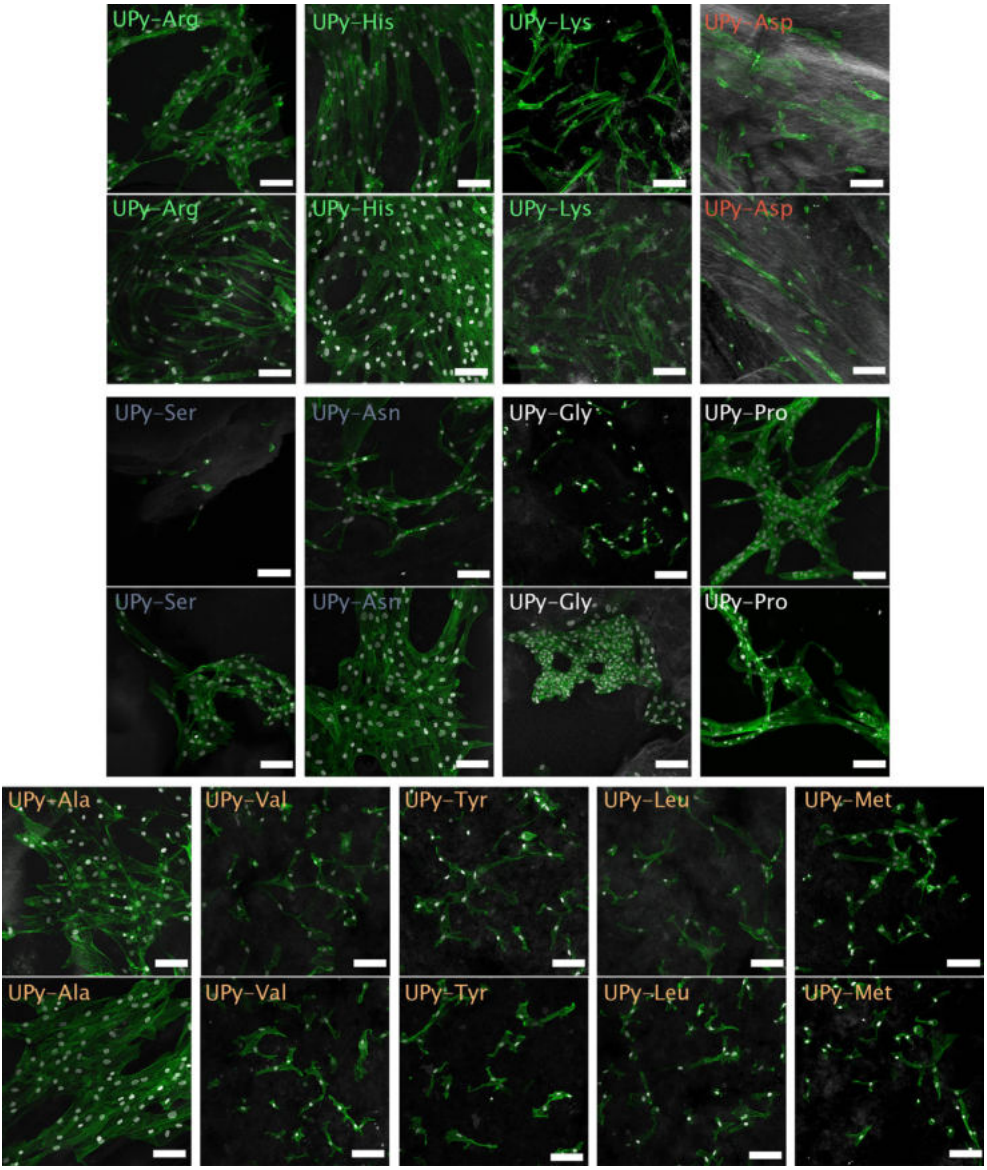

Figure 3.13 Fluorescence micrographs of fixated NHDFs cultured in 2D for three days on the UPy-AA hydrogels containing 1 mM UPy-cRGD. The actin cytoskeleton is presented in green, and the nuclei is presented in white, with each condition visualized in n=2. Scale bars represent 100 µm.

out morphology and nuclei count. Furthermore, the increase in hydrophobic side-chains could lead to a more collapsed state of the side chains, which can entrap the ligand moieties present in the hydrogel, making them less available for cellular attachment. For future experiments, combinations of these UPy-AA can be prepared, which can create synthetic-like supramolecular proteins. This can result in cellular-adhesive ligands in a supramolecular manner, without the necessity of adding additional ligands to the hydrogel.

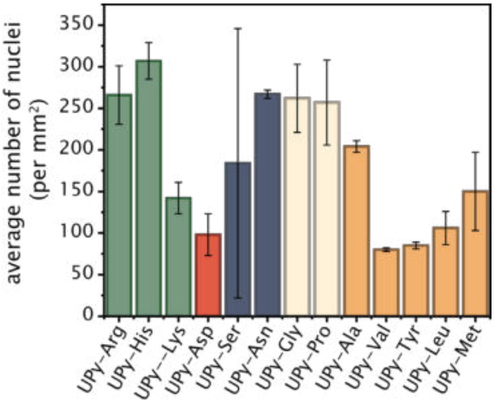

Figure 3.14 Average number of nuclei per mm2 of fixated NHDFs quantification, cultured on the UPy-AA hydrogels, data derived from two replicates, mean ± standard error of the mean presented.

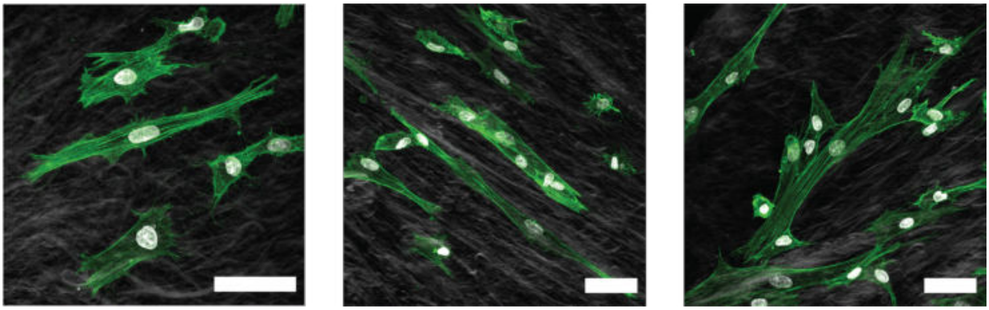

Figure 3.15 Fluorescence micrographs of fixated NHDFs cultured on UPy-Asp hydrogels containing 1 mM UPy-cRGD cultured for three days. The actin cytoskeleton is presented in green and the nuclei is presented in white for better fiber visualization, scale bars represent 50 μm.

4. Conclusion

In this chapter, the versatility of the UPy-based system was exploited, introducing two different modification strategies which manipulated the structural organization of the self-assembly and gelation properties. By adaptation of a collagen-mimicking peptide conjugated with UPy-moieties, the properties in solution demonstrated an adaptation of assembling behavior based on the degree of UPy conjugation of the peptide. In addition, hydrogels were prepared by combining the conjugated peptide moiety with the BF UPy-PEG, resulting in hydrogels with varying gelation properties measured by rheology, dependent on the ratio between conjugated peptide moiety and BF UPy-PEG. Moreover, a UPy-amino acid library was introduced, in which monofunctional UPy units were functionalized with single amino acids. These small modifications in chemical structure displayed large differences in aggregation behavior and gelation properties, with 2D cellular adhesion studies furthermore demonstrating differences in cell-count and morphology. This research provides insight in the assembly behavior and varying hydrogel fabrications methods of the UPy-based systems. The flexibility of the hydrogel design allows for a tunable composition by implementation of different supramolecular motifs. This provides an excellent platform for the development of multi-component hydrogels with highly tunable properties, applicable in the field of tissue engineering (as synthetic extracellular matrices) or drug delivery.

Experimental section

Materials and instrumentation

All reagents, chemical, materials and solvents were obtained from commercial sources and were used as received, unless stated otherwise. The UPy-AA library and the UPy-PEG polymer with $M_{n,PEG}$=10 kg/mol were synthesized by SyMO-Chem BV, Eindhoven, the Netherlands. FujiFilm Manufacturing Europe B.V. kindly provided us the Cellnest, a recombinant peptide based on human collagen type I (RCPhC1), which was used without further purification. MiliQ water was purified on an EMD Milipore Mili-Q integral Water Purification System. 1x Phosphate buffered saline (PBS) was prepared using PBS tablets (Sigma Aldrich), which was filtered before use (MF-milipore Membrane filter, 0.45 μm pore size).

Rheological measurements were performed on an Anton Paar Physica MCR501 rheometer, equipped with a P-PTD 200 evaporation blocker to prevent sample drying. Dynamic light scattering as well as zeta potential were measured on a Malvern instrument Zetasizer, model Nano ZSP. Zetasizer software was used to analyze and process the zeta potential data. Scanning electron microscopy was performed using an FEI Quanta 600 and Xt Microscope Control software. Circular Dichroism (CD) measurements were performed on a JASCO J-815 Spectrometer equipped with a JASCO MPTC-490S temperature control system. Reverse-phase high-performance liquid chromatography-mass spectrometry (RP-HPLC-MS) was performed on a Thermo scientific LCQ fleet spectrometer. Waters Xevo G2 Quadrupole Time of Flight (QToF) Liquid Chromatography-Mass Spectrometry equipped with an Agilent Polaris C18A reverse phase column was used to examine the purity of the RCPhC1 and UPy-RCPhC1 derivatives. ^{1}H-NMR spectra were recorded on a 400 MHz NMR (Varian Mercury Vx or Varian 400 MR) operating at 400 MHz. Cellular visualization was performed on a White Light Laser Confocal Microscope Leica TCS SP8 X, at 20x, 40x and 63x magnification.

RCPhC1 functionalization by Peter-Paul Fransen and Sergio Spaans

The UPy-RCPhC1 library was kindly provided by Peter-Paul Fransen and Sergio Spaans, which was synthesized in a similar manner as described previously by Spaans *et al.*[48] In short, UPy-hexyl-urea-dodecyl-amine was dissolved in DMSO and N,N-diisopropylethylamine was added, whereafter CDI was added. The CDI functionalization was confirmed by RP-HPLC-MS, after which the solution was added to RCPhC1 dissolved in DMSO and left stirring overnight at argon environment. The reaction mixture was precipitated the following day in diethyl ether and centrifuged at 3500 rpm for 5 minutes, whereafter the pellet was dissolved in demi water: ethanol (1:1, v/v). This was dialysed using a membrane (cut-off 3.5 kDa) in 800 mL demi water:ethanol (1:1, v/v) solution for 48 h, which was refreshed 1x. In the final step, the mixture was dialysed against pure demi water for 24h, after which the solution was freeze dried, obtaining a white material. The degree of substitution was determined by ^{1}H-NMR and the purity was determined with a QToF liquid chromatography – mass spectrometry.

Circular dichroism

Circular dichroism (CD) samples were prepared by dissolving 0.5 mg/mL of the compounds in miliQ water and stirring for 30 minutes. The higher functionalized UPy-RCPhC1-12 and UPy-RCPhC1-16 were stirred at 50 °C for 30 minutes. For sample measurement, a scan speed of 100 nm/min was used, with a data pitch of 0.25 nm, a response time of 0.5 s, and a bandwidth of 2 nm. A suprasil® quartz cuvette was used with a pathlength of 1 mm, and a chamber volume of 350 μL (Hellma Analytics). The spectra were measured from 300 to 170 nm, and the temperature was increased to 60 °C and decreased to 5 °C with steps of 1 °C/min. By 'Adjacent-Averaging', the spectra were processed with a 5 points of window. The molar residual ellipticity was determined using the following equation[49]:

$$[\theta] = \frac{\theta * m}{C * l * n_z}$$

Where θ is the ellipticity in millidegrees, m is the molecular weight in g/mol, c is the concentration in mg/mL, l is the path length in cm, and n_z is the number of amino acids in the peptide.

Dynamic light scattering

Samples for DLS measurements were prepared by dissolving 2 mg/mL of the RCPhC1(-functionalized) compounds in PBS annealing for 1 h at 70 °C, whereafter the samples were left to equilibrate to room temperature (RT) for 15 min. The samples were filtered before measurement with a Whatman PDVF filter, 0.45 µm. The samples were measured at two temperatures, initially at 20 °C and it was decreased to 5 °C, equilibrating for 500 seconds before measuring.

Zeta-potential measurements

For the RCPhC1(-functionalized) samples, the samples were dissolved in (4-(2-hydroxyethyl)-1-piperazineethanesulfonic acid) (1 mM, pH=7.6) at a concentration of 0.1 mg/mL and filtered with a 0.45 μm collagen filter. For the UPy-amino acid, the samples were annealed in basic PBS (80 mM NaOH) at a concentration of 4 mM for 30 minutes at 70 °C. After dissolving, the samples were neutralized to pH 7.0-7.1 with 1 M HCl. After neutralization, samples were 5x diluted with MiliQ, resulting in a PBS concentration of 0.1 x, 0.4 mM sample concentration. A DTS1070 cuvette was used for measuring the zeta potential, where the measurement duration was automated and automatic attenuation and voltage was selected. The samples were measured in triplo, at RT, with a 30 s equilibration time.

Preparation UPy-RCPhC1 and BF UPy-PEG hydrogelator

A total amount of 10 mg of the UPy-RCPhC1-5 and BF UPy-PEG was weighted at a molar ratio of 0:1 (10 mg, 0.89 µmol BF UPy-PEG), 1:9 (3.5 mg, 65 nmol UPy-RCPhC-5; 6.5 mg, 580 nmol UPy-PEG), 1:3 (6.1 mg, 115 nmol UPy-RCPhC1-5; 3.9 mg, 345 nmol UPy-PEG), or 1:1 (8.3 mg, 154 nmol UPy-RCPhC1-5; 1.7 mg, 155 nmol UPy-PEG). Basic PBS was added for a final concentration of 10 wt% (90 uL, pH 11.7, adapted with 1 M NaOH) and the compounds were annealed at 70 °C for 1 hour. The samples were left to equilibrate to RT and further adapted to a pH of 9 with 1 M NaOH or 1 M HCl solutions.

Rheology of RCPhC1

Rheological measurements were performed on an Anton Paar Physica MCR501 rheometer, using a P-PTD 200 evaporation blocker to prevent drying of the sample. A cone plate geometry (25 mm, 1°) was used for measuring at a measuring distance of 49 μm. The hydrogel in sol-state was pipetted on the bottom plate and HCl (1 M) was added to the hydrogel to initiate gelation and trimmed accordingly, whereafter the gelation time-sweep was started immediately after acid addition. For the angular frequency, strain, and recovery sweeps the hydrogels were cured for ~30 minutes. The storage and loss moduli were recorded as a function of angular frequency (0.1 – 100 rad/s) at 1% strain, as a function of strain (1-1000%) at 1 rad/s, and recovery at 1% strain, and 1 rad/s. The viscosity at a pH of 9 was determined using the cone plate geometry (25 mm, 1°) at a measuring distance of 49 μm. The different solutions of UPy-RCPhC1 and BF UPy-PEG combinations were pipetted on the plate and the samples were trimmed after lowering the cone plate geometry. The samples were measured at RT, and the viscosity was measured at different strain points, being 100, 150, 200, 300, 500, and 700 s^{-1}, with 100 measuring points per strain. The viscosity of the samples was determined by calculation of the average at each of these points.

SEM by Boris Arts

Hydrogels were prepared as mentioned previously, whereafter the hydrogels were freeze-dried. Samples were mounted on a metal stub by using double sided carbon tape. Visualization of the samples was performed on Quanta 600F scanning electron microscope (FEI, Eindhoven, The Netherlands) under low vacuum with an accelerating voltage of 10 kV and a working distance of 10 mm and a spot size of 3.5 nm.

Cryo-TEM

For the UPy-RCPhC1-5 and combination of UPy-PEG and UPy-RCPhC1-5, samples were dissolved at 0.5 mg/mL at 70 °C for 1 hour. For these samples, Quantifoil grids were used (R 2/2, copper grid, mesh size 200, Quantifoil). For the UPy-AA, samples were prepared by dissolving 80 μM UPy-AA in basic PBS (80 mM NaOH) at 70 °C, after which the samples were neutralized by 1 M HCl. Lacey carbon film grids (Electron Microscopy Sciences, 200 mesh) were used for imaging. Prior to sample addition, grids were surface plasma treated (at 5 mA for 40s) using a Cressington 208 carbon coater. Using an automated vitrification robot (FEI VitrobotTM Mark III), 3 μL sample was applied to the grids and excess sample was removed by blotting using filter paper for 3 s at -3 mm. The thin film formed was vitrified by plunging the grid into liquid ethane just above its freezing point. On a FEI-Titan TEM equipped with a field emission gun operating at 300 kV the samples were examined. Post-GIF (Gatan imaging filter) 2x2 Gatan CCD camera was used for recording of the images. Micrographs were taken at low dose conditions, using a defocus setting of -10 μm at 25k magnification, or defocus setting of -40 μm at 6.5k magnification. The fiber thickness is determined in digital micrograph, where three images are taken at a magnification of 24kx, determining the fiber thickness of 5 fibers per image.

UPy-AA hydrogel preparation

UPy-AA hydrogels were prepared by dissolving the UPy-AA at 37.4 mM and the bifunctional UPy-PEG separately at 0.46 mM in basic PBS (80 mM NaOH) at 70 °C for 1 h. For the cellular adhesion analysis experiments, UPy-cRGD (1 mM) was included and dissolved together with the UPy-AA. Samples were neutralized by addition of HCl (1 M), and left to equilibrate for 15 min, whereafter the dissolved UPy-AA (50 µL of the neutralized solution) and bifunctional UPy-PEG (50 µL of the neutralized solution) were mixed in a cylindrical Teflon mold (diameter 8 mm, 2 mm height) for rheology or 40 µL UPy-AA and 40 µL of UPy-PEG in a 96-well plate (GREINER) for cellular experiments. The samples were left to gelate over night at 37 °C before rheological experiments or cells seeding. Before cellular experiments were performed, the gels were sterilized by 20 minutes of UV exposure, whereafter the hydrogels were washed three times with culture medium.

Rheology of UPy-AA

UPy-AA hydrogels were prepared as stated above. Rheological measurements were performed on an Anton Paar Physica MCR501 rheometer. Hydrogels were measured at 37 °C using a 8 mm plate-plate with a distance of 1 mm. Low viscosity silicon oil (47 V 100m RHODORSIL®) was used to surround the hydrogels to prevent water evaporation. A time sweep was performed, with the storage and loss moduli were recorded for 10 minutes at 1% strain, 1 rad/s, whereafter the angular frequency (100 to 0.1 rad/s, 22 measurement points) at 1% strain and strain sweep (1 to 1000%, 22 measurement points) at 1 rad/s were recorded. The yield stress was determined by measuring the strain-sweep of each UPy-AA hydrogel, from which the cross-over point between the linear regime and a power fit plot for the final 10 points of the curve (strain 145-1000%) was determined, obtaining the yield stress.

Cell culture by Annika Vrehen

Normal human dermal fibroblasts (NHDF; Lonza) were cultured in Dulbecco's Modified Eagle Medium with high glucose and pyruvate (Thermo Fisher Scientific), supplemented with 10% (v/v) fetal bovin serum, 1% (v/v) penicillin and streptomycin and 1% (v/v) glutaMAX under standard culturing conditions at 37°C and 5% CO_2. Harvesting was performed using trypsin/EDTA and cell were used for experiments up to passage 15.

The UPy-AA hydrogels were prepared as stated before. Cells were harvested from the culture flask and seeded at a density of 3500 cells/well (96-well plate) suspended in 200 µL medium.

After three days, the culture medium was removed and the cells were gently washed with phosphate buffered saline (PBS) and fixated with 3.7% (v/v) formaldehyde solution (Merck) + 0.5% (v/v) Triton X-100 v/v (Merck) in PBS for 15 min at RT. The samples were subsequently washed with PBS and stained for the actin cytoskeleton with phalloidin-Atto 488 (Sigma-Aldrich, dilution 1:300) in PBS for 45 min at RT. Subsequently, the samples were washed and stained for the nucleus with 4'-6 diamidino-2-phenylindole (DAPI; 0.1 µg/mL; Sigma Aldrich). After an incubation of DAPI for 10 minutes, samples were washed again with PBS. For visualization, the hydrogels were taken out of the 96-well plate and put on glass microscope slides. Three representative images were acquired per hydrogel to estimate cell distribution over the whole sample. Nuclei were counted with the help of ImageJ 1.53c (national Institutes of Health, USA). Images were acquired with use of a Leica SP8 confocal microscope and LAS x software (Leica). Each gel was measured in duplicate.

References

1 S. Zhang, *Nat. Biotechnol.*, 2003, **21**, 1171–1178.

2 J. M. Lehn, *Chem. Soc. Rev.*, 2007, **36**, 151–160.

3 P. Y. W. Dankers and E. W. Meijer, *Bull. Chem. Soc. Jpn.*, 2007, **80**, 2047–2073.

4 P. H. J. Kouwer, M. Koepf, V. A. A. Le Sage, M. Jaspers, A. M. Van Buul, Z. H. Eksteen-Akeroyd, T. Woltinge, E. Schwartz, H. J. Kitto, R. Hoogenboom, S. J. Picken, R. J. M. Nolte, E. Mendes and A. E. Rowan, *Nature*, 2013, **493**, 651–655.

5 S. Cantekin, T. F. A. de Greef and A. R. A. Palmans, *Chem. Soc. Rev.*, 2012, **41**, 6125–6137.

6 E. Vereroudakis, M. Bantawa, R. P. M. Lafleur, D. Parisi, N. M. Matsumoto, J. W. Peeters, E. Del Gado, E. W. Meijer and D. Vlassopoulos, *ACS Cent. Sci.*, 2020, **6**, 1401–1411.

7 R. P. Sijbesma, F. H. Beijer, L. Brunsveld, B. J. B. Folmer, J. H. K. K. Hirschberg, R. F. M. Lange, J. K. L. Lowe and E. W. Meijer, *Science*, 1997, **278**, 1601–1604.

8 M. M. L. Nieuwenhuizen, T. F. A. De Greef, R. L. J. Van Der Bruggen, J. M. J. Paulusse, W. P. J. Appel, M. M. J. Smulders, R. P. Sijbesma and E. W. Meijer, *Chem. – A Eur. J.*, 2010, **16**, 1601–1612.

9 P. Y. W. Dankers, T. M. Hermans, T. W. Baughman, Y. Kamikawa, R. E. Kieltyka, M. M. C. Bastings, H. M. Janssen, N. A. J. M. Sommerdijk, A. Larsen, M. J. A. Van Luyn, A. W. Bosman, E. R. Popa, G. Fytas and E. W. Meijer, *Adv. Mater.*, 2012, **24**, 2703–2709.

10 M. M. C. Bastings, S. Koudstaal, R. E. Kieltyka, Y. Nakano, A. C. H. Pape, D. A. M. Feyen, F. J. van Slochteren, P. A. Doevendans, J. P. G. Sluijter, E. W. Meijer, S. A. J. Chamuleau and P. Y. W. Dankers, *Adv. Healthc. Mater.*, 2014, **3**, 70–78.

11 R. Parenteau-Bareil, R. Gauvin and F. Berthod, *Materials (Basel).*, 2010, **3**, 1863–1887.

12 R. Khan and M. H. Khan, *J. Indian Soc. Periodontol.*, 2013, **17**, 539–542.

13 L. Cen, W. Liu, L. Cui, W. Zhang and Y. Cao, *Pediatr. Res.*, 2008, **63**, 492–496.

14 A. Tuin, S. G. Kluijtmans, J. B. Bouwstra, M. C. Harmsen and M. J. A. Van Luyn, *Tissue Eng. Part A*, 2010, **16**, 1811–1821.

15 S. L. Bellis, *Biomaterials*, 2011, **32**, 4205–4210.

16 E. Ruoslahti, *Annu. Rev. Cell Dev. Biol.*, 1996, **12**, 697–715.

17 M. Parvizi, J. A. Plantinga, C. A. F. M. van Speuwel-Goossens, E. M. W. M. van Dongen, S. G. J. M. Kluijtmans and M. C. Harmsen, *J. Biomed. Mater. Res. Part A*, 2016, **104**, 503–516.

18 K. Nakamura*, *Curr. Stem Cell Res. Ther.*, 2019, **14**, 52–56.

19 D. Confalonieri, M. La Marca, E. M. W. M. van Dongen, H. Walles and F. Ehlicke, *Tissue Eng. Part A*, 2017, **23**, 946–957.

20 T. Mashiko, H. Takada, S.-H. Wu, K. Kanayama, J. Feng, K. Tashiro, R. Asahi, A. Sunaga, K. Hoshi, A. Kurisaki, T. Takato and K. Yoshimura, *J. Tissue Eng. Regen. Med.*, 2018, **12**, 1186–1194.

21 M. W. T. Werten, G. Eggink, M. A. Cohen Stuart and F. A. de Wolf, *Biotechnol. Adv.*, 2019, **37**, 642–666.

22 R. S. Bhatnagar and C. A. Gough, ed. G. D. Fasman, Springer US, Boston, MA, 1996, pp. 183–199.

23 G. Shanmugam and P. L. Polavarapu, *Chirality*, 2009, **21**, 152–159.

24 R. Wallis, J. M. Shaw, J. Uitdehaag, C.-B. Chen, D. Torgersen and K. Drickamer, *J. Biol. Chem.*, 2004, **279**, 14065–14073.

25 K. Mizuno, T. Hayashi and H. P. Bächinger, *J. Biol. Chem.*, 2003, **278**, 32373–32379.

26 K. E. Drzewiecki, A. S. Parmar, I. D. Gaudet, J. R. Branch, D. H. Pike, V. Nanda and D. I. Shreiber, *Langmuir*, 2014, **30**, 11204–11211.

27 K. E. Drzewiecki, D. R. Grisham, A. S. Parmar, V. Nanda and D. I. Shreiber, *Biophys. J.*, 2016, **111**, 2377–2386.

28 M. W. T. Werten, T. J. van den Bosch, R. D. Wind, H. Mooibroek and F. A. de Wolf, *Yeast*, 1999, **15**, 1087–1096.

29 R. E. Kieltyka, A. C. H. Pape, L. Albertazzi, Y. Nakano, M. M. C. Bastings, I. K. Voets, P. Y. W. Dankers and E. W. Meijer, *J. Am. Chem. Soc.*, 2013, **135**, 11159–11164.

30 N. Singh, M. Kumar, J. F. Miravet, R. V Ulijn and B. Escuder, *Chem. – A Eur. J.*, 2017, **23**, 981–993.

31 A. Safi, K. A. Wallace and L. N. Rusche, *Mol. Cell. Biol.*, 2008, **28**, 2567–2578.

32 S. Rackovsky and D. A. Goldstein, *Biopolymers*, 1987, **26**, 1163–1187.

33 H. Cui, A. G. Cheetham, E. T. Pashuck and S. I. Stupp, *J. Am. Chem. Soc.*, 2014, **136**, 12461–12468.

34 S. C. Wong Po Foo, Cheryl T. S.; Seok Lee, Ji; Mulyasasmita, Widya; Parisi-Amon, Andreina; Heilshorn, *PNAS*, 2009, **106**, 22067–22072.

35 Y. M. Chen, J. J. Yang and J. P. Gong, *J. Adhes.*, 2009, **85**, 839–868.

36 D. Liu, T. Wang, X. Liu and Z. Tong, *Biopolymers*, 2014, **101**, 58–65.

37 M. Gruening, S. Neuber, K. Fricke, C. Helm and B. Nebe, *Am. J. Biomed. Sci. Res.*, , DOI:10.34297.

38 A. Phadke, C. Zhang, B. Arman, C.-C. Hsu, R. A. Mashelkar, A. K. Lele, M. J. Tauber, G. Arya and S. Varghese, *Proc. Natl. Acad. Sci.*, 2012, **109**, 4383 LP – 4388.

39 S. I. S. Hendrikse, S. P. W. Wijnands, R. P. M. Lafleur, M. J. Pouderoijen, H. M. Janssen, P. Y. W. Dankers and E. W. Meijer, *Chem. Commun.*, 2017, **53**, 2279–2282.

40 M. Diba, S. Spaans, S. I. S. Hendrikse, M. M. C. Bastings, M. J. G. Schotman, J. F. van Sprang, D. J. Wu, F. J. M. Hoeben, H. M. Janssen and P. Y. W. Dankers, *Adv. Mater.*, 2021, **37**, 2008111.

41 T. D. Sargeant, C. Aparicio, J. E. Goldberger, H. Cui and S. I. Stupp, *Acta Biomater.*, 2012, **8**, 2456–2465.

42 P. M. Tsimbouri, L. E. McNamara, E. V Alakpa, M. J. Dalby and L.-A. Turner, eds. C. A. Van Blitterswijk and J. De Boer, Academic Press, Oxford, 2014, pp. 217–251.

43 D. Mazia, G. Schatten and W. Sale, *J. Cell Biol.*, 1975, **66**, 198–200.

44 G. B. Schneider, A. English, M. Abraham, R. Zaharias, C. Stanford and J. Keller, *Biomaterials*, 2004, **25**, 3023–3028.

45 A. Hejčl, P. Lesný, M. Přádný, J. Šedý, J. Zámečník, P. Jendelová, J. Michálek and E. Syková, *J. Mater. Sci. Mater. Med.*, 2009, **20**, 1571.

46 G. Camci-Unal, J. W. Nichol, H. Bae, H. Tekin, J. Bischoff and A. Khademhosseini, *J. Tissue Eng. Regen. Med.*, 2013, **7**, 337–347.

47 M. R. Bet, G. Goissis, S. Vargas and H. S. Selistre-de-Araujo, *Biomaterials*, 2003, **24**, 131–137.

48 S. Spaans, P.-P. K. H. Fransen, M. J. G. Schotman, R. van der Wulp, R. P. M. Lafleur, S. G. J. M. Kluijtmans and P. Y. W. Dankers, *Biomacromolecules*, 2019, **20**, 2360–2371.

49 L. E. R. O’Leary, J. A. Fallas, E. L. Bakota, M. K. Kang and J. D. Hartgerink, *Nat. Chem.*, 2011, **3**, 821–828.

4

Tuning the affinity of amphiphilic guest molecules in a supramolecular transient network

Abstract

Dynamicity and adaptability play a central role in biological systems such as the cellular microenvironment. In this chapter, the affinity and dynamics of different guest molecules in a transient supramolecular hydrogel (the host network), a bifunctional ureido-pyrimidinone (UPy) poly(ethylene glycol), is demonstrated. A monofunctional complementary UPy guest is introduced to the system, designed to interact with the host network based on UPy-dimerization. Furthermore, two other guest molecules are introduced to the host network, being cholesterol, dodecyl (c12), designed to interact with the host network based on hydrophobic interactions. Cryogenic transmission electron micrographs showed differences in morphology in solution at nanoscale, with fiber formation displayed by the UPy guest molecule, whereas aggregates were observed for the cholesterol and c12 guests. Cellular uptake studies of cy5-functionalized guests in solution showed no cellular uptake of the UPy guest, whereas the cholesterol guest showed membrane binding and intracellular uptake, and the c12 guest intracellular uptake. Incorporation of the guests molecules to the host network at a molar ratio of 1:100 confirmed no significant changes in rheological properties. By fluorescence recovery after photobleaching, the diffusive properties of the cy5-functionalized guests throughout the host network were elucidated, in which the c12 guest displayed a relatively fast mobility, the UPy guest displayed a decrease in mobility, and the cholesterol guest remained relatively stable in the host network with little mobility. Release curves of cy5-functionalized guests display differences in release, but need further optimization. This chapter demonstrates the tunable dynamic differences of affinity-based interaction between guest molecules and the host-network. The tunability of the host-guest dynamics in transient hydrogels opens the door to various tissue engineering and drug delivery purposes.

This content of this chapter is based on:

M. J. G. Schotman, P. P. K. H. Fransen, J. Song, P. Y. W. Dankers, *Tuning the affinity of amphiphilic guest molecules in a supramolecular transient network*, submitted to RSC Advances

1. Introduction

Biomaterials have increased in complexity and functionality over the last few decades, with many biomaterials being adaptable in degradability[1], bioactivity[2] and drug release[3]. Molecules such as polypeptides and polynucleotides have a diversity of structures and dynamics, displaying many unique properties.[4] Based on reversible noncovalent interactions, e.g. hydrogen bonding, π-π stacking, electrostatic interactions, or hydrophobic interactions, natural systems can execute certain functions by altering their shape in place and time. The field of supramolecular chemistry, based on reversible noncovalent interactions between molecules, takes inspiration from these natural processes attempting to mimic its highly dynamic character. An example of such a supramolecular system is the 1,3,5-tricarboxamide (BTA) molecules, that can be crosslinking by hydrogen bonding and hydrophobic effects.[5] Its function as a dynamic biomaterial in solution and in gel-states has been explored.[6] Furthermore, host-guest based supramolecular interactions display reversible and dynamic properties[7], such as cyclodextrins[8], and curcurbiturils[9]. A supramolecular hydrogel based on this cyclodextrin moiety was shown by Ooi et al., who developed an alginate-based hydrogel functionalized with cyclodextrins (guests), to which different poly(ethylene glycol) (PEG) units functionalized with adamantane groups were added of different valencies.[10] An increase in valency led to a change in dynamics, with an increase in binding affinity, and increase in storage modulus.

In our group we focus on the development of hydrogels based on specific stimuli-responsive supramolecular interactions, i.e. ureido-pyrimidinone (UPy) based hydrogels. These UPy moieties dimerize based on four-fold hydrogen bonding. Conjugation of a urea unit can stabilize lateral stacking by formation of hydrogen bonding. Furthermore, introduction of a hydrophilic poly(ethylene glycol) (PEG) linker results in a bifunctional UPy-PEG hydrogelator (BF UPy-PEG).[11] At elevated concentrations in solution, a hydrogel network can be formed by fiber entanglement and physical crosslinks. The BF UPy-PEG hydrogel displays highly dynamic properties, with swift self-healing recovery, mainly due to the high dimerization constant (K_{dim} $1x10^{7}$ M^{-1} in chloroform saturated with water[12]). Previous work from our group displayed the exchange dynamics in solution to be controlled by mixing different guests, being mono- and bifunctional UPy units to host fibers.[13] The dynamics of a ureido-pyrimidinone (UPy)-based system in gel state was explored by Bastings et al. by encapsulating different monomeric and dimeric UPy-guest molecules in a UPy host hydrogel, displaying a robust interaction between the monomeric and dimeric UPy-guest molecules in the UPy-host network.[14] Work by Bakker et al. described the conjugation strategy of a cholesterol moiety to a chemotherapeutic agent, which enhanced the affinity between the modified drug (guest) and the UPy-based hydrogel (host), resulting in a sustained guest release over time.[15] In another study, the dynamics of a cholesterol-conjugated siRNA moiety (guest) within the UPy-based hydrogel (host) were explored, displaying a relatively slow diffusion in comparison to the siRNA containing no cholesterol-conjugation.[16] This further elucidates the enhanced affinity between the guest (cholesterol modified siRNA) and the host (UPy-based hydrogel).

In this study, we further explore the dynamics between different guests, and a supramolecular BF UPy-PEG host hydrogel. We examined three different guest molecules, hypothesized to have distinctive affinities with the UPy-based host hydrogel (Figure 4.1A). The monofunctional UPy unit functionalized to an oligo(ethylene glycol) (OEG) was presented as an guest molecule (UPy-COOH, Figure 4.1B), interacting with the BF UPy-PEG hydrogel by complementary four-fold hydrogel bonding. A dodecyl molecule and cholesterol molecule were functionalized to an OEG (c12-COOH, and chol-COOH, respectively, Figure 4.1C, D), resulting in two amphiphilic compounds. These two guest molecules are hypothesized to interact with the host BF UPy-PEG based on hydrophobic interactions between the guests and the hydrophobic pockets present in the hydrogel network, created by the lateral stacking of the alkyl spacers induced by the urea moieties (hydrogen bonding) and hydrophobic interaction of the alkyl spacers in the BF UPy-PEG backbone. The unmodified guest molecules were examined (with a carboxylic acid end-group; a stable versatile chemical handle for functionalization) on assembly behavior in solution, and effect on rheological properties upon addition to the hydrogel. The guest assembly in solution was elucidated with cryogenic transmission electron microscopy (cryo-TEM), and functionalization of a fluorophore (cy5) enabled visualization of cellular uptake, diffusivity throughout the hydrogel network using fluorescence recovery after photobleaching (FRAP), and determination of the release from the hydrogel.

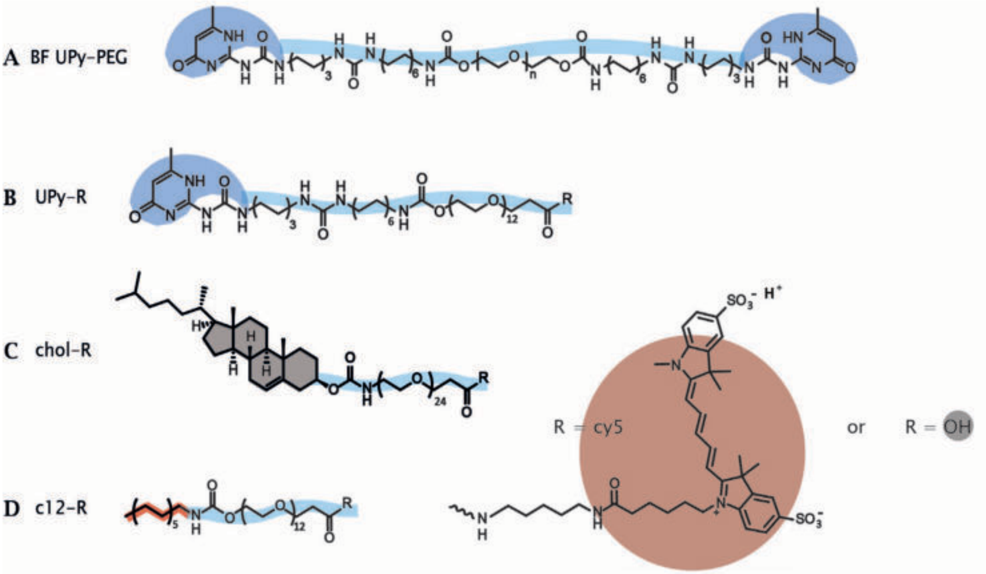

Figure 4.1 Schematic overview of the molecules used in this study. The chemical structure of the hydrogelator BF UPy-PEG (A), the monofunctional UPy guest (B), the cholesterol guest (C), and the dodecyl guest (D), modified with cy5 or unmodified (-OH).

2. System description

To examine the cellular uptake and FRAP of the guest when encapsulated in the host hydrogel, a cy5 fluorophore was coupled to the guest-molecules. Briefly, the cy5-labelling of the three different guests was carried out by reacting the carboxylic acid of the guests to the primary amine present on the cy5 molecule. HATU was used as a coupling reagent in combination with a base to activate the carboxylic acid, subsequently followed by cy5 addition for the carboxamide formation. After purification of the cy5-functionalized guests, the compounds were dissolved in DMSO, and mixed in the desired ratio to the medium (cellular uptake studies) or hydrogelator (FRAP experiments) at basic conditions (pH 9) for proper dissolution. The DMSO content of the final solution was kept below 5%.

3. Guest molecules in solution

To elucidate the assembling behavior in solution, cryo-TEM measurements were performed. Here, the unfunctionalized guest molecules with the carboxylic acid side-group were measured at a concentration of 50 μM. The UPy-COOH displayed single fibers morphology as well as patches of fibers (Figure 4.2A), indicating the clear fibrous self-assembling pattern of UPy-modified molecules. For chol-COOH, small aggregates and micellular formation can be observed (Figure 4.2B). Occasionally, chol-COOH showed to form small fibrils, which are hypothesized to be wormlike micelles. However, larger dispersed aggregates were formed as well, too high in size to be observed in cryo-TEM. Dynamic light scattering showed high polydispersity of the sample in the microscale range (results not shown), further confirming that cryo-TEM does not represent the full structural overview of the particle in solution. For C12-COOH, small spherical aggregates, likely to be micellular formation, were observed (Figure 4.2C). However, complementary structural elucidation techniques, such as small angle light scattering, are required to corroborate these results.

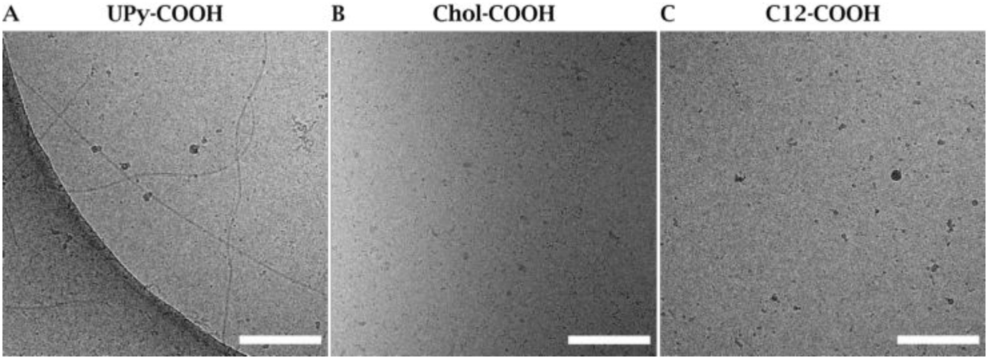

Figure 4.2 transmission electron micrographs of the UPy-COOH (A), chol-COOH (B), and C12-COOH (C) at a concentration of 50 μM in PBS/DMSO (95/5 %v/v), at a magnification of 24,000x (scale bar represents 200 nm).

The cellular uptake of the cy5-functionalized guests was examined on an immortalized proximal tubule epithelial cell line from normal adult human kidney (HK-2). Each guest was added to cell medium at a concentration of 10 μM and incubated for 2 hours with the cells, whereafter the cells were washed, stained and imaged by confocal microscopy (Figure 4.3). Differences in cellular uptake of the guest molecules was observed, with the UPy-cy5 compound

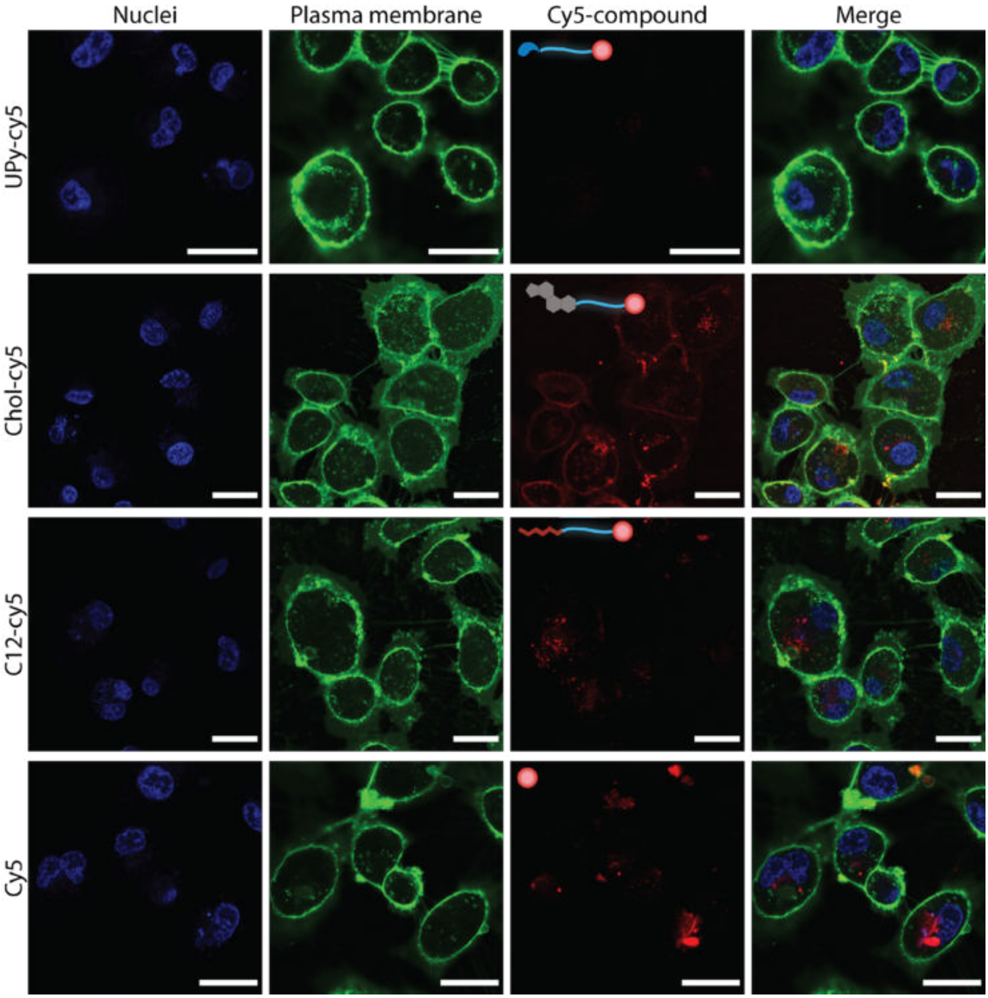

Figure 4.3 Confocal micrographs of HK-2 live cells showing the cy5-labelled guest uptake studies. with the nuclei (blue), plasma membrane (green), cy5 compounds (red), and the merged image shown. The guests were added to medium at a concentration of 10 μM for a time span of 2 hours, whereafter the cells were washed and visualized by live-cell imaging (the scale bar represents 30 μm)

showing a minimum to no cellular uptake. From previous work, presence of cationic charges increased the cellular uptake, whereas neutral charge showed no binding or permeation.[17] The monofunctional UPy-cy5 guest, having no cationic charge present, display cellular inertness. The chol-cy5 is observed to bind to, as well as permeate the membrane, indicating a significant effect of the chol-cy5 guest on the cellular interaction. The chol-cy5 is clearly visible on the membrane, with cholesterol playing a role in the regulation of membrane fluidity, permeability, and hydrophobicity.[18] Furthermore, cholesterol plays an important role as signal transducer and solubilizer of other lipids within the cell.[19] This makes cholesterol-modification interesting in the field of drug delivery, in which cholesterol moieties are often used to enhance the cellular uptake.[15,20,21] C12-cy5 shows intracellular uptake, with clusters c12-cy5 appearing to be present in the cytosol of the cell. Functionalization with alkyl spacers has showed to enhance the cellular transfection, due to its interaction with the cellular membrane.[22-24] The cellular uptake is hypothesized to take place by transmembrane lipid translocation (flip-flop), with diffusion and interaction with the cellular membrane playing a significant role.[25] However, solely cy5 also shows cellular uptake, with large intracellular clusters being visible intracellular, as shown in previous studies[26]. This indicates that the cy5 can have an effect on the cellular uptake of the cy5-bound guests. Still, clear differences are observed within the cy5-labelled guest molecules, with UPy-cy5 showing no uptake, and c12-cy5 and chol-cy5 displaying cellular uptake, with the latter one also displaying membrane binding. In previous work, we showed that using cholesterol or UPy-moieties, the retention of the guest molecules in the gel can be steered, whereafter these moieties can be taken up by the cells (cholesterol), or not taken up by the cell (UPy) after release.[15,27] We further explore the properties of the guest molecules by implementation in a UPy-based hydrogel.

4. Guest molecules in the hydrogel

4.1 Mechanical properties upon guest encapsulation

Hydrogels of the BF UPy-PEG were formed by dissolving the host polymer at basic conditions (pH 11.7 at a final concentration of 10 wt%), which resulted in a viscous liquid. The guest molecules were added from a DMSO stock solution while in the viscous liquid state, and by neutralization a hydrogel was obtained. The mechanical properties of the host hydrogel were examined upon guest encapsulation by rheology (Figure 4.4). The final concentration of the guest molecules in the hydrogel was 100 µM, and a control was measured containing an equal amount of DMSO (5 %v/v) added to the host hydrogel. Frequency and strain sweeps were measured, that displayed an increase in storage moduli with an increase in frequency for all hydrogels. This indicates an increase in elastic properties at higher frequencies, whereas at lower frequencies the viscous properties of the hydrogel were increasing. Upon anchor addition, similar frequency responses were observed, with addition of chol-COOH, c12-COOH, and UPy-COOH displaying a storage modulus of 2540 Pa, 3310 Pa, and 2370 Pa at 0.1 rad/s, respectively. At 10 rad/s, the modulus increases to 11900 Pa, 11700 Pa, and 10600 Pa, respectively. A slow decrease was observed for the loss modulus when the frequency was increased, indicating a less predominant viscous behavior at higher frequencies.

The strain-sweep displayed similar storage and loss moduli for all hydrogels, with the storage moduli showing small variations between each condition in the linear regime (~9500 Pa for the control, ~8400 Pa for UPy-COOH, ~9000 Pa for chol-COOH, and ~9400 for c12-COOH). The determined yield stresses based on the strain sweeps are in similar regimes, with 15.5 Pa, 14.4 Pa, 23.7 Pa, and 9.0 Pa for the control, chol-COOH, c12-COOH, and UPy-COOH, respectively. These results confirm the viscoelastic properties of the hydrogels, with the guest molecule addition not showing significant changes in mechanical properties of the host hydrogel.

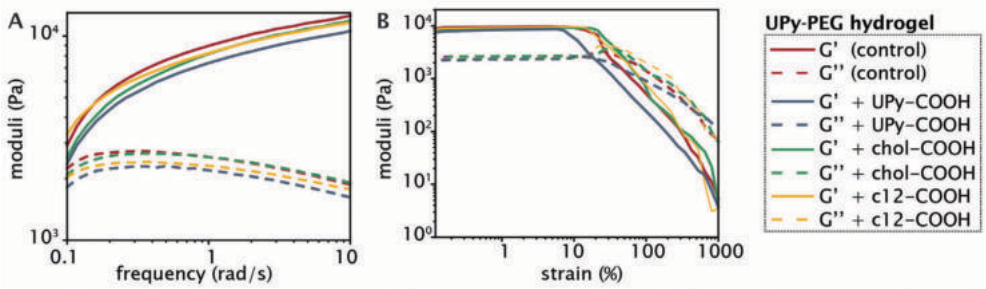

Figure 4.4 Mechanical hydrogel properties of the BF UPy-PEG hydrogel upon anchor addition, with the frequency sweep at 1% strain (A), and the strain sweep at 1 rad/s (B) measured at 37 °C.

The calculated partition coefficient (clogP) values display an indication on the lipophilicity of the compounds. The clogP values for the guests were 2.2 for UPy-COOH, 6.0 for chol-COOH, and 3.6 for c12-COOH. The hydrophilicity of the UPy-COOH guest to be the highest, whereas the chol-COOH guest showed to exhibit a more hydrophobic character. While the chol-COOH guest was well-dissolved in the hydrogel host at a concentration of 100 μM (5% DMSO), similar amounts of chol-COOH in PBS show precipitation and therefore poor solubility. We hypothesize that this is due to the increased affinity with the BF UPy-PEG network, with the hydrophobic pockets present in the host network increasing the solubility of the chol-COOH (Figure 4.6).

4.2 Dynamic properties of guest molecules in host hydrogel

The molecular dynamics of the guest in the host network was examined by FRAP (Figure 4.5). Here, the cy5-labelled guest molecules were bleached by high-intensity illumination at a selected region of 20 μm in diameter. This resulted in a clear dark circular spot, of which the diffusion of the cy5-labelled guest molecules towards the bleached spot was measured over time (Figure 4.5C). Confocal microscopy displayed homogeneous fluorescence of the c12-cy5 guest, as well as the UPy-cy5 guest. The chol-cy5 guest showed an overall homogeneous distribution in the hydrogel, where intermittently small micron-sized aggregates were observed (up to ~3 μm).

The FRAP data indicated a clear difference in diffusive behavior of each guest throughout the hydrogel, of which the swiftest recovery was observed for the c12-cy5 guest, reaching a plateau value after approximately 70 minutes with a mobile fraction of 0.91±0.07. The half time recovery was determined by fitting the data with a single exponential growth model, obtaining a half-time recovery of 4.45±3 min. This indicated that, while the c12-cy5 guest was hypothesized to remain in the hydrophobic pockets of the UPy-PEG hydrogel network, there was a mobility of this guest within the host network, confirmed by measured intensity profiles (Figure 4.5F), that display a restored recovery after 1.5 hours. The cy5 guest was measured as a control, which displayed too swift recovery for measuring (sub-second time scale recovery). The diffusive mobility of UPy-cy5 was observed to be slower, with a plateau reached after approximately 4h, displaying a mobile fraction of 0.56±0.11. After 6 hours, the bleached spot was observed to not be fully recovered (Figure 4.5C). A 100% recovery is not obtained here, which is consistent with previously experiments.[14] The half-time recovery was determined to be

53±20 min. The lowest mobility was observed for chol-cy5, displaying a mobile fraction of 0.26±0.15. This was confirmed by the intensity profile, showing a limited fluorescence recovery even after 6 hours. A single exponential fit could not be performed on this data, due to the low initial recovery leading to an improper fit. From this data, we can conclude that all guest molecules show an affinity with the host hydrogel network, all leading to a slow diffusion (in comparison to the cy5 control). The fastest diffusion in the host network was displayed by the c12-cy5 guest molecule, whereas the chol-cy5 displayed the lowest mobility throughout the network, where a limited recovery was observed even after 12 hours (Figure 4.5C). The UPy-Cy5 guest molecule displayed a lower diffusion in the host network compared to the c12-cy5, indicating a higher affinity with the host network in comparison to the c12-cy5. These results support our hypothesis, that different dynamics are obtained when guest molecules are introduced to a host network, with different affinity based-interactions (hydrogen-bonding and hydrophobic host-guest assembly).

While an interaction between the chol-cy5 guest and the hydrophobic spacers of the host network is hypothesized, the possibility of aggregate formation within the host network remains likely for the high immobile state of the chol-cy5 guest (Figure 4.6B). High polydisperse aggregate formation was observed in PBS by dynamic light scattering (results not shown), and small micron-sized aggregates were observed in the confocal micrographs of the chol-cy5 guest within the host hydrogel network (Figure 4.5C), this can significantly limit the mobility of the guest molecules. An increased association constant for aggregate formation is hypothesized, where dissociated chol-cy5 guests display a slow exchange within the host hydrogel network. As the solubility of the cholesterol guest in the host hydrogel is improved in comparison to PBS, small cholesterol aggregates could possibly interact with the hydrophobic domains present in the host network (Figure 4.6E, F).

A faster exchange was observed between the UPy guest and the host network, with intra and inter-fiber diffusion, as reported in a previous study.[14] The UPy guest shows to form elongated fibers in PBS (Figure 4.2A), as well as micelles.[28] Therefore, the possibility of aggregate or fiber formation of solely the UPy guest molecules, thereby limiting the diffusion remains a possibility (Figure 4.6C). Therefore, whether diffusion of a single UPy guest molecule, or diffusion of the entire fiber containing the fixed guest molecules slows down fluorescent recovery remains unclear.

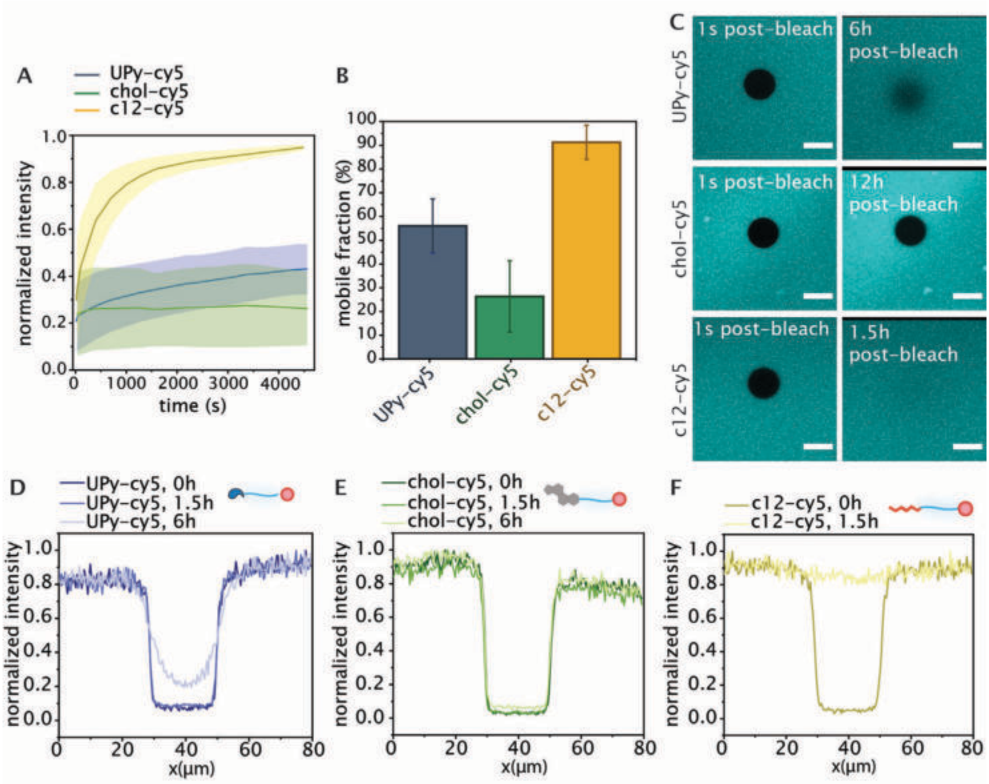

Figure 4.5 Exchange dynamics of the guests in the host hydrogel. The normalized fluorescence intensity of the different cy5 functionalized guests after photobleaching (A), and the fraction of fluorescence intensity that recovers when fluorescence intensity reaches a plateau (B, mobile fraction), Data is represented as ±SD, n=3. The confocal micrographs of the different cy5-labeled guest molecules directly post-bleaching, with the UPy-cy5 visualized 6h post-bleaching, the chol-cy5 visualized 12h post-bleaching, and c12-cy5 visualized 1.5h post-bleaching (C, scale bar represents 20 μm). The measured intensity profile for the bleached spots after 0 hour, 1.5 hour, and 6 hours post-bleaching of D. UPy-cy5, E. chol-cy5, and F. c12-cy5.

The fastest exchange of the three introduced guest molecules was displayed by the c12 guest, which is hypothesized to display fast exchange dynamics with the host network. Due to a short hydrophobic spacer (c12), the guest molecule is hypothesized to have to lowest binding affinity with the host network, remain in the host network only shortly and displaying a fast exchange (Figure 4.6D). Presence of small aggregates based of c12 guests, as displayed in the cryo-TEM images (Figure 4.2C), is possible, which can limit the guest mobility.

Further exploration using fluorescence resonance energy transfer and structural elucidation by super-resolution microscopy can give further insight in the dynamics and aggregation behavior of host-guest interactions. Overall, these results show the complexity of the possible interaction mechanisms and dynamic behavior of guest molecules within the host network.

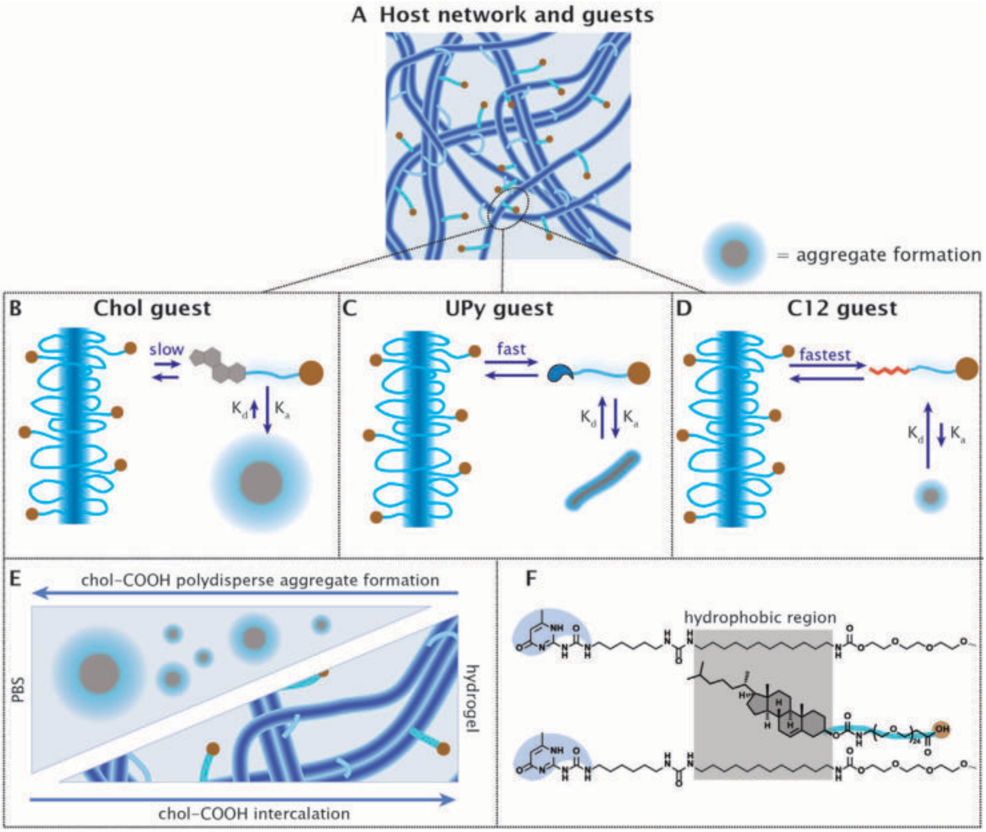

Figure 4.6 Hypothesized interaction mechanism between the host network and guest molecules, displaying the slow equilibrium of intercalating cholesterol guests with the host network, whereas the association constant towards the aggregate formation within the network is high. (A). A faster exchange is hypothesized for the UPy guest molecule and the host network, with the tendency for aggregate (fiber) formation is hypothesized to be equal to the exchange of guest molecules within the host network (C). The fastest exchange is hypothesized to be between the c12 guest and host network, which displays higher mobility and exchange dynamics within the host network (D). The solubility of the cholesterol guests in PBS is poor, resulting in large polydisperse chol-COOH aggregates, whereas the solubility in the BF UPy-PEG hydrogel is increased (E) due to the chol-COOH moiety being retained in the hydrophobic regions of the hydrogel network. A possible interaction of small chol guest aggregates within the hydrophobic domains of the host network is hypothesized. (F).

4.3 Release properties of guest molecules

An immediate burst release is often observed for hydrophilic drugs, occurring when the mesh size of the hydrogel is larger than the encapsulated drug, displaying diffusion dominated release.[29] Furthermore, the release can be adapted by drug-polymer interaction, with conjugation of linkages (covalent or non-covalent), facilitating drug and polymer interaction.[30] There are four main types of non-covalent affinity-based drug release, i.e. hydrophobic interactions, van der Waals forces, hydrogen bonding, and ionic interactions.[31] Here, we examine the release properties of the cy5-labelled guest molecules from the host hydrogel. Previous research observed a correlation between the diffusive behavior of fluorescently-labeled drug moieties in hydrogels determined by FRAP and its release profile.[32] Therefore, we hypothesize the fastest release of the introduced guests molecules to be displayed by c12-cy5. The UPy-cy5 and chol-cy5 guests are hypothesized to display a slower, and the slowest release, respectively.

By addition of cy5-labeled guests to the host hydrogels, the in vitro release in PBS was examined over a time-span of 30 days. After 30 days of release, the gel was dissolved and the remnants of cy5-labelled guest molecules in the gel were examined. A clear difference in release was observed considering the three cy5-labeled guests and the cy5 control (Figure 4.7A). The cy5 displays a burst release diffusion profile, while the other guests display a slower release. The c12-cy5 displays a more retained, slower release in comparison to the chol-cy5 and UPy-cy5, as was expected. Interestingly, none of the guests displays a 100% release over time, with the cy5 accumulating to 61±5.0% release and the c12-cy5 45±6.2%. The total accumulative release of the chol-cy5 and UPy-cy5 displays even lower values of 3.5±1.7% and 8.1±1.0%. We hypothesized quenching of the fluorophores could be leading to this extensively lower signal, as the possibility of the cy5(-labeled guests) to possibly absorb to lab equipment (i.e. pipette tips, wells plate, Eppendorf's). To limit possible adherence to lab equipment and improve dissolution of the cy5-functionalized guests, detergent (0.05 %v/v Tween20) was added in the PBS supernatant solutions, and low-binding lab equipment (with the exception of the wells plate and well inserts) was used. The release of chol-cy5 was examined using this method, displaying a cumulative release of 2.2±0.5% after 14 days (Figure 4.7B). The gel was dissolved after 14 days, and the remnants were examined, in which 33.3±1.5% of the anchor was retained. The ability of the cy5(-guests) molecules to absorb to lab equipment, and the improper dissolution of the cy5(-guests) molecules is hypothesized to therefore play a significant role in the anchor loss. Nevertheless, these results show significant differences in release properties. A high quantity of chol-cy5 guest was still 'lost', which is hypothesized to be due to quenching of the fluorophore. This can be due to collisional quenching, occurring when in contact with other molecules in solution, static quenching, with the complex between a fluorophore and quencher returning to the ground state after light absorption, without emission of a photon, and possibly a combination of these two quenching processes.[33] Previous work by Bakker et al. showed the release of a monofunctional UPy-moiety functionalized to a DOTA moiety from the BF UPy-PEG hydrogel to be 23% over a time-span of 2 weeks. We hypothesize that the optimal release curve of UPy-cy5 will display similar values, showing an increased retained release in comparison to c12-cy5, but increased release in comparison to the chol-cy5. Further evaluation of this is necessary, with exploration of the release by targeted quantitative liquid chromatography-mass spectrometry (LC-MS) to measure the cy5-labeled guests. Additionally, such method allows for quantitative evaluation of anchor-functionalized drug release, thereby moving towards application based systems.

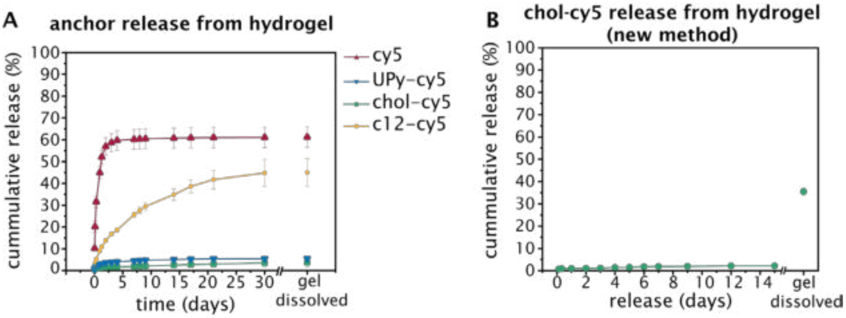

Figure 4.7 Cy5-labeled release studies from BF UPy-PEG hydrogel at a concentration of 100 μM over a time-span of 30 days (A), and the release of the chol-cy5 at a concentration of 100 μM using low-binding equipment and addition of detergent. Data is represented as mean ± SD, n=3.

5. Conclusion

This study demonstrates tunability of dynamics and release within and from a hydrogel using hydrogen-bonding, and hydrophobic affinity-based interactions. Three different guests molecules were explored, which displayed differences in morphology, cellular uptake, dynamicity, and release from the host hydrogel. Hereby insight into tunability of host-guest dynamics and drug release for hydrogel-based systems is provided, with a focus on affinity-based host-guest assembly. Future research into the dynamic adaptivity of implemented bioactive properties can adapt the bioactivity of supramolecular hydrogels, whereas release kinetics of these functionalization modes can enhance drug efficacy. This establishes the basis of a generic 'plug-and-play' system to tune the bioactive properties of hydrogels, and release rate of a wide variety of drug molecules, based on the requirements for the disease in scope.

Experimental section

Materials and instrumentation

All reagents and chemical were obtained from commercial sources and used without purification unless stated otherwise. Phosphate buffered saline (PBS) tablets, 4-methylmorpholine (MMP), N,N-diisopropylethylamine (DIPEA) and 1-[Bis(dimethylamino)methylene]-1H-1,2,3-triazolo[4,5-b]pyridinium 3-oxid hexafluorophosphate (HATU) were purchased from Sigma-Aldrich. Sulfo-Cyanine5 amine was purchased at Lumiprobe. H_2N-PEG_{24}-CO-OtBu was purchased from Iris Biotech. The BF UPy-PEG polymer with $M_{n,PEG}$=10 kg/mol was synthesized by SyMO-Chem BV, Eindhoven. Nunc™ Lab-Tek™ Chambered Coverglass (8-well) were purchased at ThermoFisher Scientific. A Grace Reveleris X2 Flash Chromatography Sytem using Reveleris Silica Flash Cartridges was used for automated column chromatography. Reverse-phase high-performance liquid chromatography-mass spectrometry (RP-HPLC-MS) was performed on a Thermo scientific LCQ fleet spectrometer. Rheological measurements were performed on an Anton Paar Physica MCR501 rheometer. ^{1}H-NMR and ^{19}F-NMR spectra were recorded on a 400 MHz NMR (Varian Mercury Vx or Varian 400 MR) operating at 400 MHz. FRAP measurements were performed on a Leica TCS SP5 inverted confocal laser scanning microscope. The clog P values were determined by Chemdraw. A Tecan Spark 10 M plate reader was used for analysis of the cy5 fluorescence.

Synthetic procedures

Synthesis of c12-COOH: OEG_{12}-tBu (146.6, 0.232 mmol) was dissolved in 2 mL chloroform, which was added dropwise to a solution containing N,N-carbonyldiimidazole (207 mg, 1.27 mmol) in 2 mL chloroform under stirring. This was left stirring overnight at room temperature. After extraction with aqueous citric acid (2 mL), the organic phase was obtained. Analysis with RP-LC-MS revealed complete conversion. Dodecylamine (204.2 mg, 1.01 mmol) dissolved in $CHCl_3$ was added dropwise to the reaction mixture under stirring conditions. The reaction mixture was stirred overnight at 60 °C overnight at reflux. Extraction by aqueous citric acid addition (2 mL) led to a milky solution. Subsequent extraction with brine was performed (3 x 4 mL), resulting in a clear organic layer. The product was further purified by column chromatography using silica, eluting with chloroform containing 5% ethylene glycol dimethacrylate, and a gradient of methanol from 0 to 10%, and a run time of 15 minutes. RP-LC-MS confirmed a pure product. Solvent were removed using a rotary evaporator, after which dichloromethane (DCM) was added to the product (5 mL), to which trifluoroacetic acid (TFA, 5 mL, 1:1 v/v%) was added. This was stirred for 2 hours at room temperature, whereafter DCM was removed by rotary evaporation. TFA was removed from the solution by coevaporation with toluene (3 x 8 mL toluene, 1 x 50 mL toluene) performed by rotary evaporation. This was confirmed with ^{19}F-NMR, yielding a pure product (141.2 mg, 0.17 mol, 73%).

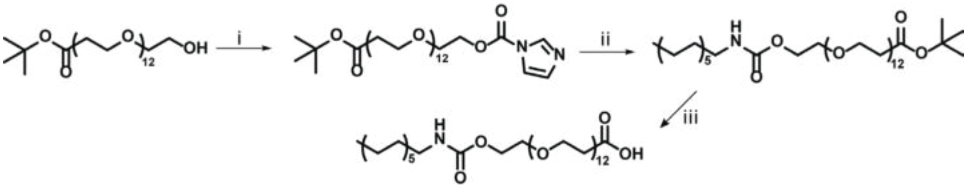

Scheme 4.1 synthesis of C12-COOH. i) CDI, CHCl3, RT, overnight. ii) $C_{12}H_{27}N$, $CHCl_3$, reflux at 60 °C, overnight, iii) TFA, DCM, room temperature, 2 h, 73%.

Synthesis of c12-cy5: C12-COOH (1.7 mg, 0.0021 mmol) was dissolved in DMF (1 mL), and HATU (1.57 mg, 0.004 mmol) was dissolved in DMF (1 mL) whereafter the HATU was added dropwise to the c12-COOH solution. MMP (1.8 µL, 0.017 mmol) was added to the solution, which was stirred for approximately 10 minutes. Sulfo-Cy5-NH_2 (1.9 mg, 0.0027 mmol) was added to the solution dissolved in DMF (3 mL). This was stirred under argon conditions for 4 hours. LC-MS was used to confirm the formation of the reaction product. The crude product was purified by automated reversed-phase C18 silica (4 g), at a flow rate of 18 mL/min. The eluents used were H_2O:ACN (95:5 till 100% of ACN in 15 minutes). Freeze-drying of the collected fractions yielded pure c12-cy5 (1.8 mg, 55% yield). ESI-MS: m/z Calc. for $C_{78}H_{128}N_5O_{22}S_2$: 1550.85; obs. $[M+2H]^{2+}$ 775.33, $[M+H]^{+}$ 1552.00.

Synthesis of chol-cy5: Chol-PEG_{24}-COOH was synthesized as previously reported[15] and kindly provided by Peter-Paul Fransen. Chol-PEG_{24}-COOH (5 mg, 0.0032 mmol) was dissolved in DMF (1 mL) and HATU (2.5 mg, 0.0065 mmol) was added to the mixture. DIPEA (3.5 µL, 0.0201 mmol) was added to the mixture and stirred at room temperature for 15 minutes. Sulfo-Cy5-NH_2 (3.1 mg, 0.0042 mmol) was added dropwise to the mixture and left stirring under argon condition at room temperature overnight. The following day, the reaction mixture was washed with brine two times, after which further purification by automated reversed-phase C18 silica (4 g) gel column chromatography was performed (flow rate 15 mL/min, eluent: H_2O:THF 95:5

until 100% of THF in with reverse chromatography was performed in 15 minutes). Due to further impurities, dialysis was performed using a MWCO of 500-1000 Da for 3 days against demi water. After dialysis, the sample was lyophilized, resulting in a pure blue powder (2.5 mg, 34% yield). HRMS (MALDI-TOF): m/z calculated for $C_{117}H_{196}N_5O_{34}S_2$: 2280.32; found 2280.41$[M+H]^+$.

Synthesis of UPy-cy5: The UPy-OEG_{12}-COOH precursor was synthesized as previously reported[34] and kindly provided by Peter-Paul Fransen. UPy-OEG_{12}-COOH (2.36 mg, 0.00208 µmol) was dissolved in DMF (1 mL) and HATU was added to the mixture (1.58 mg, 0.00416 mmol). N,N-Diisopropylethylamine (2.15 mg, 16.6 µmol) was added and the solution was stirred at room temperature for 15 min. Sulfo-Cy5-NH_2 (2 mg, 27.0 µmol) dissolved in DMF (3 mL) was added to the solution and stirred for 1h at an argon environment. H_2O (containing 0.1 v/v% formic acid, 20 mL) was added to the solution and centrifugated (4 min, 3000 rpm) followed by decantation. Ultrapure water was added (20 mL) and the product was lyophilized. The compound was purified with preparative RP-HPLC using a gradient of 40% ACN in H_2O (both containing 0.1 %v/v formic acid). Lyophilization yielded pure 3 (1.75 mg, 9.4 µmol, 45%) blue solid. ESI-MS: m/z Calc. for $C_{91}H_{149}N_{11}O_{25}S_2$ 1861.37; Obs. $[M+3H]^{3+}$ 621.33, $[M+2H]^{2+}$ 931.17, $[M+H]^+$ 1861.75.

Cryo-TEM measurements

For cryo-TEM measurements quantifoil carbon covered grids were used (Electron Microscopy Sciences, 200 mesh, 50 µ hole size). Prior to sample addition, grids were surface plasma treated (at 5 mA for 40s) using a Cressington 208 carbon coater. Using an automated vitrification robot (FEI Vitrobot™ Mark III), 3 µL sample was applied to the grids and excess sample was removed by blotting using filter paper for 3 s at -3 mm. The thin film formed was vitrified by plunging the grid into liquid ethane just above its freezing point. On an FEI-Titan TEM equipped with a field emission gun operating at 300 kV the samples were examined. Post-GIF (Gatan imaging filter) 2x2 Gatan CCD camera was used for recording of the images. Micrographs were taken at low dose conditions, using a defocus setting of -5 µm at 25k magnification.

Cellular experiments

Human kidney 2 cells (HK-2), immortalized by transduction with human papilloma virus 16 E6/E7 gene, were cultured at 37 °C in 95% air/5% CO2 atmosphere with DMEM (ref. 22320-022) supplemented with 10% FBS and 1% penicillin/streptomycin (P/S). The cells were passed twice a week. For the aggregate uptake studies, HK-2 cells were seeded in an 8-well Thermo Fisher Scientific™ Nunc™ Lab-Tek™ Chamber with #1 borosilicate glass bottom at a density of 2.5×10^4 cells/cm^2 cells per well (n = 4). The guests (UPy-cy5, chol-cy5, c12-cy5) were prepared by adding the necessary amounts from stock solution (5 mg/mL in DMSO) to medium at a concentration of 10 µM. This was left at room temperature while being stirred overnight. The cells were washed three times with PBS after overnight attachment and 0.4 mL of the guests molecules in full culture medium suspension was added to each well. This was incubated for 2 hours, after which the cells were washed with PBS. Subsequentially, cellular nuclei were stained with Hoechst 33342 (Thermofisher Scientific) and cellular membrane was stained with CellMask™ Green plasma membrane stain (Thermofisher Scientific). After staining, the cells were washed three times with PBS, after which Invitrogen™ Live Cell Imaging Solution was added to each well for live imaging. The live imaging was performed under a Leica TCS SP5 inverted confocal laser scanning microscope at 37 °C.

Hydrogel preparation

Hydrogels were prepared with a final concentration of 10 wt% polymer content, where the polymer was firstly dissolved in a basic PBS solution (pH 11.7, adapted with 1M NaOH) at a temperature of 70 °C, being stirred for 1 hour. Subsequently, the guests molecules were added from stock solution with a final concentration of 40 µM for FRAP measurements. For rheological measurements, guests molecules were added from a stock solutions, with a final concentration of 100 µM in the hydrogel. The solutions was mixed for 15 minutes at room temperature, whereafter the sol-state solutions were pipetted in an 8-well Thermo Fisher Scientific™ Nunc™ Lab-Tek™ Chamber for FRAP measurements. For rheological measurements, the hydrogelators (100 µL) were pipetted in a cylindrical Teflon mold (diameter 8 mm, 2 mm height). By pH-induced gelation, the hydrogels were prepared in the wells upon addition of 1 M HCl (1.4 µmol per 100 µL gel solution). This was equilibrated for 1-2 hours before measuring.

Rheology measurements

Hydrogels were measured at 37 °C using a 8 mm plate-plate with a distance of 1 mm on an Anton Paar Physica MCR501 rheometer. Low viscosity silicon oil (47 V 100m RHODORSIL®) was used to surround the hydrogels to prevent water evaporation. A time sweep was performed, with the storage and loss moduli were recorded for 10 minutes at 1% strain, 1 rad/s, whereafter the angular frequency (100 to 0.1 rad/s, 22 measurement points) at 1% strain and strain sweep (1 to 1000%, 22 measurement points) at 1 rad/s were recorded. Each condition is measured in duplicate to confirm reproducibility, whereafter one representative measurement is plotted. The yield stress was determined by measuring the strain-sweep of each UPy-AA hydrogel, from which the cross-over point between the linear regime and a power fit plot for the final 10 points of the curve (strain 145-1000%) was determined.

Fluorescence recovery after photobleaching

A 20x objective (HCX PL APO CS 20.0 x 0.70 DRY UV) was used for imaging and the hydrogels were prepared in an 8-well Thermo Fisher Scientific™ Nunc™ Lab-Tek™ Chamber by pH-induced gelation. Surrounding empty wells were filled with MiliQ to prevent drying of the gels. The sample was placed inside an environmental chamber at 37 °C. The exchange dynamics were examined by illumination of the white laser at 646 nm excitation and 660-700 nm emission with a hybrid detector. The bleached circular area of the hydrogel was kept constant at 20 µm, and illumination at a laser power of 60% was performed for 10 frames (1.3 sec frame^{-1}). Post-bleaching images were taken over a time-span of 2-12 hours, depending on the added anchor. The data was normalized by dividing the average gray values of the bleached area by the average gray values of the total area. Using the FRAPbot software[35], the mobile fraction was determined by single exponential fitting. FRAP measurements were performed in triplicate. Using the imageJ software, the normalized intensity profile of the circular diameter was determined for each anchor condition directly post-bleaching, 1.5 hours post-bleaching, and 6 hours post-bleaching.

Release experiments of the cy5-labeled guests from the hydrogel

The hydrogels were prepared as described in the previous method, with addition of the cy5(-labeled guests) from the DMSO stock after dissolving the polymer at basic conditions.

Cy5(-labeled guests) were added to the dissolved polymers at a concentration of 100 µM, whereafter the solutions were stirred for 30 minutes for homogeneous mixing. 100 µL of the hydrogelator at basic condition (pH 9) was pipetted in Thinserts TC inserts (24 well, 8.0 µm pore size, translucent, Greiner Bio-one®), and placed in a 24 well plate containing 600 µL of PBS (pH 7.2). At set time points the PBS supernatant was refreshed (1, 3, 8, 24, 31 hours, 3, 4, 7, 8, 9, 10, 11, 14, 16, 18, 21, 25, and 30 days) and the supernatants were examined for cy5-fluorophore remnants on a Tecan Spark 10 M plate reader at ex/em of 625/680 with a bandwidth of 20 nm. For proper gel solubility, base (1 M NaOH) was added to switch the gel to the sol-state and enable quantification of the cy5 remnants in the hydrogel. Calibration samples were included of the cy5 fluorophores (cy5, c12-cy5, chol-cy5, UPy-cy5) at the concentrations of 10, 5, 1, 0.5, and 0.1 µM to determine a standard curve. For the new method in which the chol-cy5 was released from the gel, low binding Eppendorfs and pipette tips (BIOplastics ®) were used when handling the cy5-labelled compound. Furthermore, after obtaining the supernatants and the gel remnant in sol-state, Tween20 was added (with a final concentration of 0.05 %v/v) and extensively vortexed, before plate reader analysis.

References

1 L. Yildirimer and A. M. Seifalian, *Biotechnol. Adv.*, 2014, **32**, 984–999.

2 J. A. Hubbell, *Curr. Opin. Biotechnol.*, 1999, **10**, 123–129.

3 O. S. Fenton, K. N. Olafson, P. S. Pillai, M. J. Mitchell and R. Langer, *Adv. Mater.*, 2018, **30**, 1705328.

4 A. V Bryksin, A. C. Brown, M. M. Baksh, M. G. Finn and T. H. Barker, *Acta Biomater.*, 2014, **10**, 1761–1769.

5 S. Cantekin, T. F. A. de Greef and A. R. A. Palmans, *Chem. Soc. Rev.*, 2012, **41**, 6125–6137.

6 S. Varela-Aramburu, G. Morgese, L. Su, S. M. C. Schoenmakers, M. Perrone, L. Leanza, C. Perego, G. M. Pavan, A. R. A. Palmans and E. W. Meijer, *Biomacromolecules*, 2020, **21**, 4105–4115.

7 S. M. Mantooth, B. G. Munoz-Robles and M. J. Webber, *Macromol. Biosci.*, 2019, **19**, 1800281.

8 J. Szejtli, *Chem. Rev.*, 1998, **98**, 1743–1754.

9 C. Márquez, R. R. Hudgins and W. M. Nau, *J. Am. Chem. Soc.*, 2004, **126**, 5806–5816.

10 H. W. Ooi, J. M. M. Kocken, F. L. C. Morgan, A. Malheiro, B. Zoetebier, M. Karperien, P. A. Wieringa, P. J. Dijkstra, L. Moroni and M. B. Baker, *Biomacromolecules*, 2020, **21**, 2208–2217.

11 P. Y. W. Dankers, T. M. Hermans, T. W. Baughman, Y. Kamikawa, R. E. Kieltyka, M. M. C. Bastings, H. M. Janssen, N. A. J. M. Sommerdijk, A. Larsen, M. J. A. Van Luyn, A. W. Bosman, E. R. Popa, G. Fytas and E. W. Meijer, *Adv. Mater.*, 2012, **24**, 2703–2709.

12 S. H. M. Söntjens, R. P. Sijbesma, M. H. P. van Genderen and E. W. Meijer, *J. Am. Chem. Soc.*, 2000, **122**, 7487–7493.

13 S. I. S. Hendrikse, S. P. W. Wijnands, R. P. M. Lafleur, M. J. Pouderoijen, H. M. Janssen, P. Y. W. Dankers and E. W. Meijer, *Chem. Commun.*, 2017, **53**, 2279–2282.

14 M. M. C. Bastings, T. M. Hermans, A. J. H. Spiering, E. W. L. Kemps, L. Albertazzi, E. E. Kurisinkal and P. Y. W. Dankers, *Macromol. Biosci.*, 2019, **19**, 1800296.

15 M. H. Bakker, M. Grillaud, D. J. Wu, P.-P. K. H. Fransen, I. H. de Hingh and P. Y. W. Dankers, *Macromol. Rapid Commun.*, 2018, **39**, 1800007.

16 M. H. Bakker, E. van Rooij and P. Y. W. Dankers, *Chem. - An Asian J.*, 2018, **13**, 3501–3508.

17 M. H. Bakker, R. E. Kieltyka, L. Albertazzi and P. Y. W. Dankers, *RSC Adv.*, 2016, **6**, 110600–110603.

18 W. K. Subczynski, M. Pasenkiewicz-Gierula, J. Widomska, L. Mainali and M. Raguz, *Cell Biochem. Biophys.*, 2017, **75**, 369–385.

19 E. Ikonen, *Nat. Rev. Mol. Cell Biol.*, 2008, **9**, 125–138.

20 L. Zhang, W. F. D. Bennett, T. Zheng, P.-K. Ouyang, X. Ouyang, X. Qiu, A. Luo, M. Karttunen and P. Chen, *J. Phys. Chem. B*, 2016, **120**, 3148–3156.

21 C. F. Bennett and E. E. Swayze, *Annu. Rev. Pharmacol. Toxicol.*, 2010, **50**, 259–293.

22 G. Sanità, B. Carrese and A. Lamberti, *Front. Mol. Biosci.*, 2020, **7**, 381.

23 A. K. Blakney, P. F. McKay, B. I. Yus, Y. Aldon and R. J. Shattock, *Gene Ther.*, 2019, **26**, 363–372.

24 T. Higashi, I. A. Khalil, K. K. Maiti, W. S. Lee, H. Akita, H. Harashima and S.-K. Chung, *J. Control. Release*, 2009, **136**, 140–147.

25 A. A. Gurtovenko and I. Vattulainen, *J. Phys. Chem. B*, 2007, **111**, 13554–13559.

26 H. Takakura, H. Sato, K. Nakajima, M. Suzuki and M. Ogawa, *Cancers*, 2021, **13**, 2245.

27 M. H. Bakker, C. C. S. Tseng, H. M. Keizer, P. R. Seevinck, H. M. Janssen, F. J. Van Slochteren, S. A. J. Chamuleau and P. Y. W. Dankers, *Adv. Healthc. Mater.*, 2018, **7**, 1–8.

28 M. Ramaekers, I. De Feijter, P. H. H. Bomans, N. A. J. M. Sommerdijk, P. Y. W. Dankers and E. W. Meijer, *Macromolecules*, 2014, **47**, 3823–3828.

29 J. Li and D. J. Mooney, *Nat. Rev. Mater.*, 2016, **1**, 16071.

30 S. Bernhard and M. W. Tibbitt, *Adv. Drug Deliv. Rev.*, 2021, **171**, 240–256.

31 N. X. Wang and H. A. von Recum, *Macromol. Biosci.*, 2011, **11**, 321–332.

32 F. Brandl, F. Kastner, R. M. Gschwind, T. Blunk, J. Tessmar and A. Göpferich, *J. Control. Release*, 2010, **142**, 221–228.

33 J. R. Lakowicz, Ed., Springer US, Boston, MA, 2006, pp. 277–330.

34 I. de Feijter, O. J. G. M. Goor, S. I. S. Hendrikse, M. Comellas-Aragonès, S. H. M. Söntjens, S. Zaccaria, P. P. K. H. Fransen, J. W. Peeters, L.-G. Milroy and P. Y. W. Dankers, *Synlett*, 2015, **26**, 2707–2713.

35 R. Kohze, C. E. J. Dieteren, W. J. H. Koopman, R. Brock and S. Schmidt, *Cytometry. A*, 2017, **91**, 810–814.

5

Hydrogel-loaded giant unilamellar vesicles as versatile viscoadaptable platforms

Abstract

Giant unilamellar vesicles (GUVs) have emerged as synthetic cellular platforms, with their confined space, size and unilamellar membrane structure mimicking the natural cells. However, a shortfall of this system is the lack of the highly crowded macromolecular intracellular structure, having influence on many biomacromolecular interactions and enzymatic processes. Here, we introduce a synthetic life-like system, of which the crowded macromolecular intracellular environment is mimicked by hydrogel encapsulation in the GUVs. The hydrogel displays pH-responsive behavior, which, upon basification, exhibits viscous liquid-like behavior. This facilitates easy loading of the hydrogelator at basic conditions in the GUVs by the inverted emulsion method. Neutralization by addition of acid to the outer phase resulted in an increase in viscosity of the encapsulated hydrogelator (gel-state), resulting in the hydrogel-loaded GUVs (HL-GUVs). This viscoadaptable behavior of the encapsulated hydrogelator was confirmed using fluorescence recovery after photobleaching, displaying low dynamicity in the acidic state (pH<5), and high dynamicity at basic state (pH>9). Incorporation of pH-regulating enzymes showed to respond to sensing molecular cues by encapsulation of urease in the HL-GUVs. Furthermore, the enzymatic activity could be modulated by encapsulation of esterase in the HL-GUVs, displaying a significant difference in activity: at neutral pH, product formation was slowed down due to the increased viscosity, as compared to activity at basic conditions (pH 9). Addition of α-hemolysin (pore forming protein) allows the efflux of small molecules from the interior of the GUVs, which was monitored using the small molecule calcein. Empty GUVs displayed a swift release within 25 minutes, whereas HL-GUVs showed a sustained release over a time-span of 145 minutes. Altogether, by introduction of the hydrogelator in the GUVs a complex, yet viscoadaptable synthetic cellular platform was established, serving great potential in the field of synthetic biology.

The content described in this chapter is based on:

M. J. G. Schotman‡, A. Llopis Lorente‡, J. C. M. van Hest, L. K. E. A. Abdelmohsen, P. Y. W. Dankers, *Hydrogel-loaded giant unilamellar vesicles as versatile viscoadaptable platforms*, In preparation, ‡Contributed equally

1. Introduction

In the past decennia, the field of protocells have increased in interest, in which cell mimicry holds manifold potential applications ranging from deepening our understanding of biological mechanisms governing living systems to the design of new materials for applications in biomedicine, sensing, and biotechnology, among others.[1] At a structural level, several bottom-up strategies have been developed for the creation of artificial cell-mimics, such as the assembly of polymeric vesicles (polymersomes),[2] lipid vesicles (liposomes),[3] coacervate droplets,[4] and protein conjugates (proteinosomes).[5] The spatial organization of cells have been harnessed in such synthetic replicas by embedding membrane and lumen proteins, and by encapsulating internal nano-organelles.[6]

Among different artificial cell platforms, giant unilamellar vesicles (GUVs) are of special interest, as they are reminiscent to natural cells by having a phospholipid bilayer membrane and cell-like size; yet GUVs have a diluted aqueous lumen. It is well known that cells adapt their viscosity, metabolic status, and growth according to the mobility and the number (concentration) of signaling molecules (e.g., hormones) available.[7,8] In order to address this issue, Mann´s group presented a new artificial cell model based on GUVs containing an inner coacervate (condensed) phased.[10] Furthermore, a recent study showed that yeast cells modulate intracellular viscosity in response to temperature and energy availability.[9] In previous research, a strategy was presented to spatially organize protein fragments inside GUVs through pH-reversible interactions with the membrane, inducing a biochemical response.[11] Indeed, research into the design of artificial cells able to dynamically respond to external stimulus resulting in adaptive behavior is still very limited – in part, progress is hampered by the lack of versatile strategies for integrating structural responsive elements and self-regulation pathways in one artificial compartment.

Supramolecular hydrogels are an interesting class of drug-delivery systems, that display physiochemical properties, can undergo reversible gel-sol transition due to the noncovalent crosslinking, and show great promise as therapeutic delivery systems. The development of a macrosized hydrogel-containing core-shell capsules was shown as a therapeutic drug carrier,[12] with the core containing the bifunctional ureido pyrimidinone (UPy) moiety in combination with calcium chloride, which was coated by drop-wise addition in an alginate solution. Furthermore, adaptable hydrogels have showed great promise as cell carrier platforms, mimicking the dynamic and biomimetic viscoelastic properties of the extracellular matrix.[13] The applicability of UPy-based hydrogels as synthetic ECM was shown recently[14], in which the dynamic behaviour of the hydrogels could be tuned by implementation of slow and fast exchanging molecules self-assembling into fibers, having a significant effect on the cell-adhesive functionalities. By lowering the size of these hydrogels to microscale, they can function as intracellular matrix as well as drug-encapsulated system, displaying facile injectability, enabling local drug-delivery in a non-invasive manner.[15] Furthermore, smaller hydrogels increase the surface-to-volume ratio, promoting substrate and product transfer, as well as increase drug release.[16]

In this chapter, we explore both of these systems in a hybrid hydrogel-loaded GUV (HL-GUV). This enables the preparation of the hybrid system closely mimicking the intracellular environment of synthetic cells, as well as functioning as a drug-release platform. The inner compartment consists of a UPy-based hydrogel, which can crosslink by fourfold hydrogen bonding UPy-UPy interactions, coupled via alkyl-urea spacers to 10 kDa poly(ethylene glycol) (BF UPy-PEG). A viscous liquid (sol-state) is obtained at basic conditions, whilst at neutral conditions swiftly changes to the gel-state.[17] The vesicles were made of a mix of amphiphiles, showing consistent production and low fusogenicity (Figure 5.1).[18] In different sets of experiments, we examine the reversible viscoadaptability of this system in response to pH, the incorporation of a pH-regulating enzyme, and the regulation of a model enzymatic reaction according to the gel state. Furthermore, a proof-of-concept release study is shown. This opens new possibilities for the design of adaptive cell-like microreactors as well as the use for drug delivery platforms.

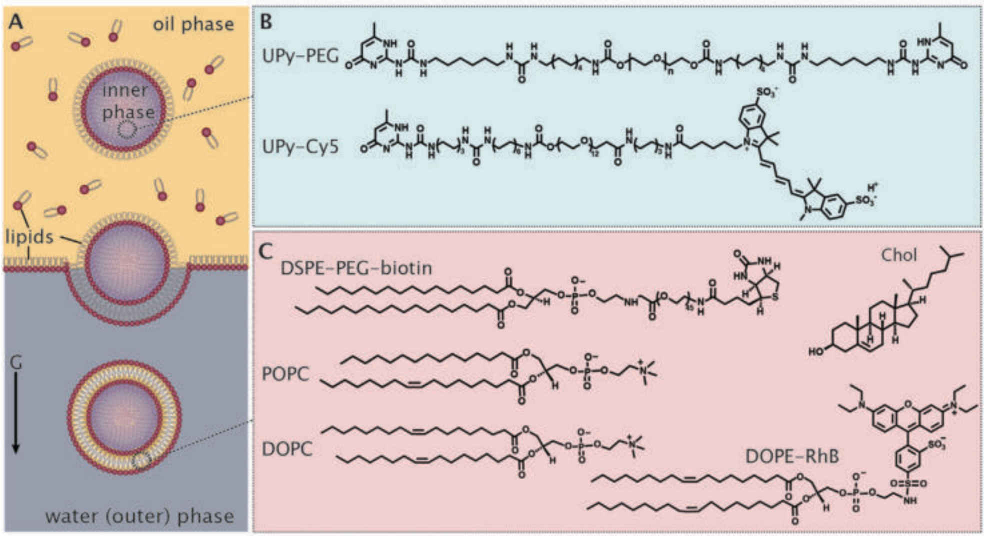

Figure 5.1 Schematic representation of the preparation and the chemical components present in the HL-GUVs, with the preparation method of the HL-GUVs by the inverted emulsion method (A), containing the BF UPy-PEG and UPy-cy5 at basic pH (B). The membrane consists of several lipids, being DSPE-PEG-biotin, POPC, DOPC, DOPE-RhB, and Cholesterol (chol) (C).

2. HL-GUV preparation and dynamic pH-responsive viscoadaptation

The HL-GUVs were prepared using the inverted emulsion method without the need of sophisticated equipment, with stable vesicles and high encapsulation efficiency being obtained.[19] Water-in-oil emulsion was used to prepare the HL-GUVs in which hydrogel (sol-state, high pH) was added to the water phase and subsequently the phospholipids in the oil phase. By centrifugation of the droplets, the vesicles were formed by passing through a water/oil interface covered by phospholipids (Figure 5.1A). Efficient encapsulation was showed by confocal microscopy, with similar vesicle size distributions for (empty) GUVs in basic conditions. Furthermore, the HL-GUVs remained stable upon acidification, showing similar sizes (Figure 5.2). By bright field, the formation of spherical vesicles was observed. Confocal microscopy enabled visualization of the lipid layer of the HL-GUVs (by incorporation of a rhodamine B dye in the lipid membrane), whereas the hydrogel encapsulation was confirmed by visualization of the hydrogel present in the inner lumen, visualization was enabled by addition of a small percentage of cy5-labelled fluorophore encapsulated in the hydrogel (UPy-Cy5). Furthermore, 3D micrographs displayed a uniform lipid layer, furthermore confirming encapsulation of the hydrogelator. This shows an easy and efficient assembly of both supramolecular compounds, with the hydrogel encapsulation not interfering with the vesicle formation.

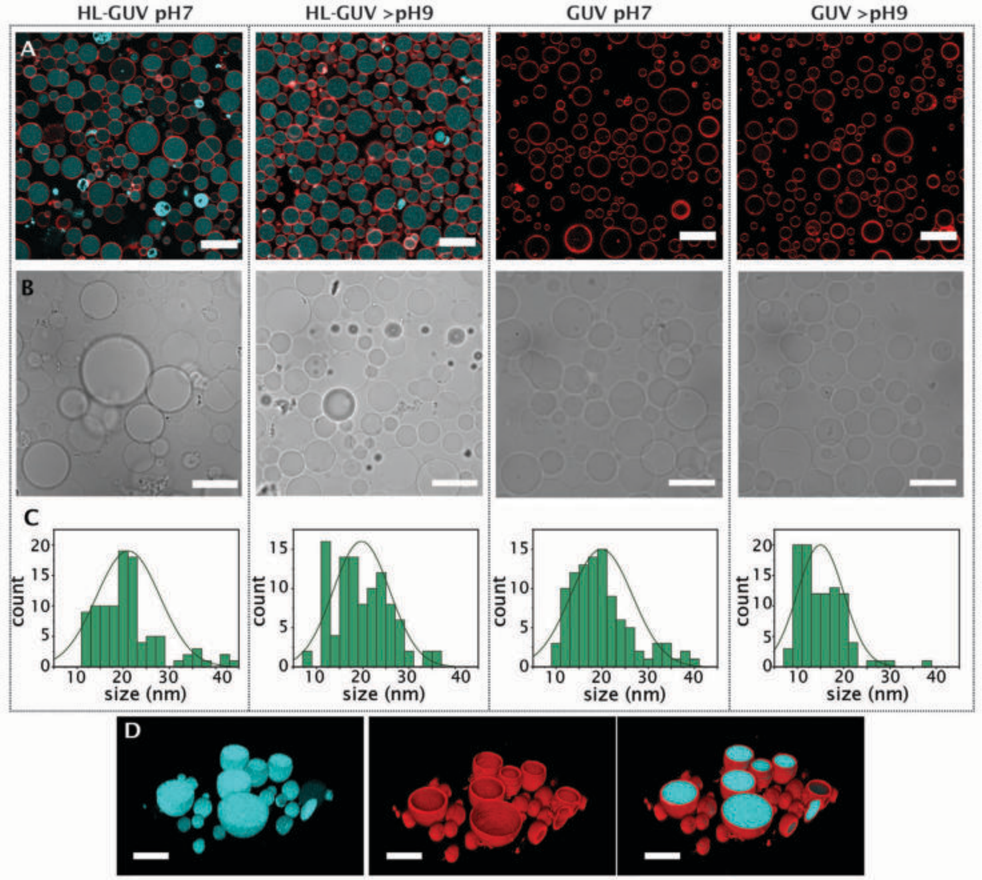

Figure 5.2 Overview of the hydrogel-loaded unilamellar vesicles (HL-GUVs) as well as the giant unilamellar vesicles (GUVs) in 1x PBS, showing the fluorescence micrographs of HL-GUVs and GUVs at pH 7, and >pH 9. The hydrogel contains UPy-Cy5 for visualization (blue), whereas the lipid membrane is stained with rhodamine B (red) (A). The bright field micrographs (B), and size distribution histograms (n=100) (C) of the HL-GUVs and GUVs are shown, and 3D micrograph of the HL-GUVs (D). Scale bar represents 30 μm.

Confocal and bright field microscopy showed the formation of spherical droplets, displaying sizes of 16.3±5.3 μm and 14.8±3.8 μm for the HL-GUVs at pH 9 and 7, respectively, and 16.5±4.6 μm and 18.7±6.9 μm in size for the GUVs at pH 9 and pH 7, respectively (Figure 5.2C). These results show the efficient encapsulation of the hydrogel in the GUVs, indicating similar sizes and morphologies. In addition, no significant changes in morphologies and sizes were observed between neutral and basic state of the HL-GUVs and the GUVs.

The fluidity of the hydrogel in the sol-state and gel-state was examined after preparation, using fluorescence recovery after photobleaching (FRAP). The encapsulated monofunctional UPy-cy5 dye was bleached by increasing the laser intensity to 100% in a circular region of 3 µm in diameter within the HL-GUVs, whereafter the recovery was examined. Directly after preparation at basic conditions FRAP measurements were performed (start, basic), subsequently followed by addition of acid (to the outer medium), followed by another FRAP measurement (cycle 1, acidic). After FRAP measurements, base was added whereafter FRAP was measured (cycle 1, basic). Addition of acid was repeated once more (cycle 2), with a final measurement at acidic conditions (Figure 5.3).

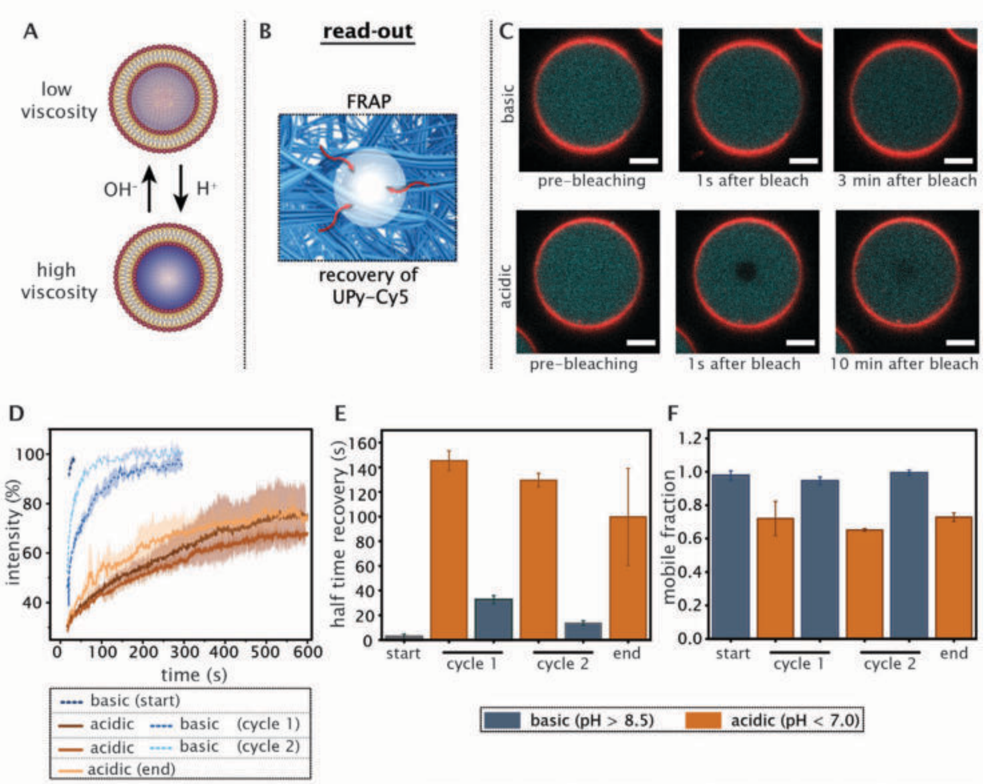

Figure 5.3 Analysis of the viscoadaptation of the encapsulated hydrogelator upon acidification and basification by FRAP, with a schematic overview of the set-up of the experiment (A) and an image of the read-out of this experiment (B), the pre-bleach and post-bleach micrograph images at basic conditions (start), and at acidic conditions (cycle 1) at three different time points, with the pre-bleached image, 1s post-bleaching, and several minutes post-bleaching time-points. The cy5 intensity of each imaged was increased for better visualization, the scale bar represents 5 µm (C). The raw FRAP curves of all three cycles at basic and acidic conditions (D), and the corresponding half time recovery (E) and mobile fraction (F) 600 seconds post-bleaching. Data is represented as ±SD, n=3.

Photobleaching a small section of the sol-state hydrogel at a pH of approximately 10 after preparation gave rise to a fast recovery, with the bleached area recovered to 100% in a time-span of a few seconds. The half-time recovery ($t_{1/2}$) and mobile fraction was determined by fitting the data with a single exponential growth model. Upon acidification of the external environment (cycle 1), a relatively slow recovery was obtained at a pH of approximately 5, showing a mobile fraction of 0.72 ± 0.1 after 600 seconds and a $t_{1/2}$of 145±8 seconds. Subsequent addition of base (cycle 1) to the external environment led to a decrease in $t_{1/2}$, being 33±3 seconds and a mobile fraction of 0.95±0.02. Subsequent acidification (cycle 2) showed a $t_{1/2}$ of 129±5 seconds, with a mobile fraction of 0.65±0.01, whereas basification showed again a decrease in $t_{1/2}$ (14±2 seconds) and an increase in mobile fraction (0.99±0.02). The final FRAP measurements after acid addition, displayed the $t_{1/2}$ to be increased again to 100±39 seconds, with a mobile fraction of 0.73±0.03. This indicates the mobility of the fluorescent probe being significantly limited at acidic/neutral condition, whereas the mobility after base addition was increased. What should be noted is that measuring times did not exceed 600 seconds. Longer measuring times can influence the $t_{1/2}$ and mobile fraction to some extent, however due to time limitation and photobleaching of the cy5 dye over long time-spans, the measuring times were kept constant at 600 seconds for the acidic conditions, allowing impartial comparison. These results indicate the adaptation of the viscosity in the inner lumen, by changing the external pH in the outer medium. Interestingly, this system shows reversibility after several cycles, maintaining its viscoadaptive properties.

3. Enzymatic regulation of viscosity

Previous work showed spatial and structural organization of life-like entities upon enzyme incorporation.[11] Cells are known to respond to external stimuli i.e. changes in pH can show differences in enzyme activity.[20] As proof of principle, urease was encapsulated in the HL-GUVs, which was hypothesized to increase the pH of the inner lumen by the production of ammonia due to urea hydrolysis. By co-encapsulation of pyranine, a water-soluble membrane impermeable pH-responsive fluorophore[21], the pH in the inner lumen was determined. The ratio of pyranine at two excitation wavelength is determined, with the excitation at approximately 460 nm being pH-dependent and based on the 8-hydroxyl group present in the pyranine fluorophore that exhibit a pK_a of approximately 7.3, indicating the level of unprotonated ionized pyranine (Figure 5.4A). Excitation at 415 nm indicates the total pyranine amount in the system, which is independent of pH-changes. The 460/415 nm ratio therefore measures the pyranine ionization level.[22] Here, we observed that 488/405 nm ratio was sufficient to determine the inner lumen pH. The preparation of the HL-GUVs was perfomed whilst the hydrogelator was in the sol-state, i.e. at basic conditions. FRAP experiments were performed to observe the change of sol-state to gel-state of the encapsulated hydrogel. A high pyranine 488/405 ratio (3.0 ± 0.2, start) after preparation indicated basic lumen conditions (Figure 5.4B, C), whereafter subsequent addition of acid (HCl, 0.1M, cycle 1) shows to decrease the ratio ratio to 0.004. Addition of urea shows increase of the ratio (ratio 2.9 ± 0.5, cycle 1). Subsequent acid addition led to a lower ratio (0.01±0.01, cycle 2), whereafter urea addition led to an increase in ratio (2.1

± 0.1, cycle 2). This confirms the urease activity present in the inner lumen of the HL-GUVs, which is shown to increase the pH upon addition of urea. To confirm the sol/gel state of the hydrogelator in the lumen, and the ability of the system to self-regulate its viscosity. FRAP measurements were performed after each addition of acid and urea, displaying a $t_{1/2}$ of 0.82±0.9 seconds with a mobile fraction of 1.03±0.03 after preparation (start), whereas acidification (cycle 1, acidic) increased the $t_{1/2}$ to 148.4±24.3 seconds, with a mobile fraction of 0.7±0.07. Urea addition (cycle 1, basic) led to a decrease in $t_{1/2}$ and an increase in mobile fraction, showing a $t_{1/2}$ of 39.4±31 seconds and a mobile fraction of 0.94±0.07. Acid addition (cycle 2, acidic) increased the $t_{1/2}$ to 78.7±28.9 seconds, whereas the mobile fraction decreased to 0.77±0.02 after 600 seconds measuring time. External addition of urea (cycle 2, basic) led once more to a decrease in $t_{1/2}$ (2.16±1.2 seconds), and an increase in mobile fraction (1.03±0.2). These results show the transition of the gel to sol state can be obtained by external addition of urea, displaying a self-regulating viscoadaptive system. Whilst these results are promising, the pyranine 488/405 ratio appears to decrease slightly as the cycle number increases. It is difficult to state whether this is hydrogel-dependent, dye-dependent, or enzyme dependent. No significant decreases were observed for the fluorescence intensity of pyranine at the 405 nm excitation, indicating no effect of photobleaching. We hypothesize that the hydrogelator appears to stabilize slightly over time, with the fiber disruption being less significant over multiple cycles. This can increase the entrapment of the urease in the network, which could lead to a small decrease in basification, and therefore a decrease in pyranine intensity at excitation 488 nm. A decrease in enzymatic activity due to the accumulation of reaction products can furthermore lead to the pyranine intensity decrease. Lastly, it could be a random factor, where small differences in the urease encapsulation and urea absorption lead to small differences in fluorescence intensity outcome. Taken together, these results show the viscoadaptable properties of the HL-GUVs upon encapsulation of urease, where external stimuli can result in a large change of viscosity of the encapsulated hydrogelator.

4. HL-GUVs as adaptive microreactors

To highlight the cellular mimicking nature of these HL-GUVs, the semipermeable membrane and internal molecular crowding was exploited. Calcein AM is a dye used as a marker to study cellular viability.[23-25] The nonfluorescent calcein AM was used to examine the uptake through the semi-permeable membrane, with conversion to the green-fluorescent calcein after acetoxymethyl ester hydrolysis by (HL-)GUVs encapsulated esterase's. Esterase activity is shown to be pH dependent, with the optimal esterase activity showed to be between pH 6-9.[26] Furthermore, the viscosity of the intracellular environment is known to be of importance when considering the metabolic intracellular activity.[27] Regarding previous experiments, the encapsulated hydrogelator of the HL-GUVs was shown to increase in viscosity with a pH above 8.5 (sol-state), whilst a pH of 7 or lower appeared to decrease the viscosity (gel-state). Therefore, esterase activity was examined at two pH conditions, being 7 and 9. This will give further insight in the esterase activity, whilst tuning the viscosity of the crowded inner-lumen environment. Esterase from porcine liver was loaded in the HL-GUVs, whereafter calcein AM was able to diffuse across the (HL-)GUVs membrane when added to the external environment (Figure 5.5A).

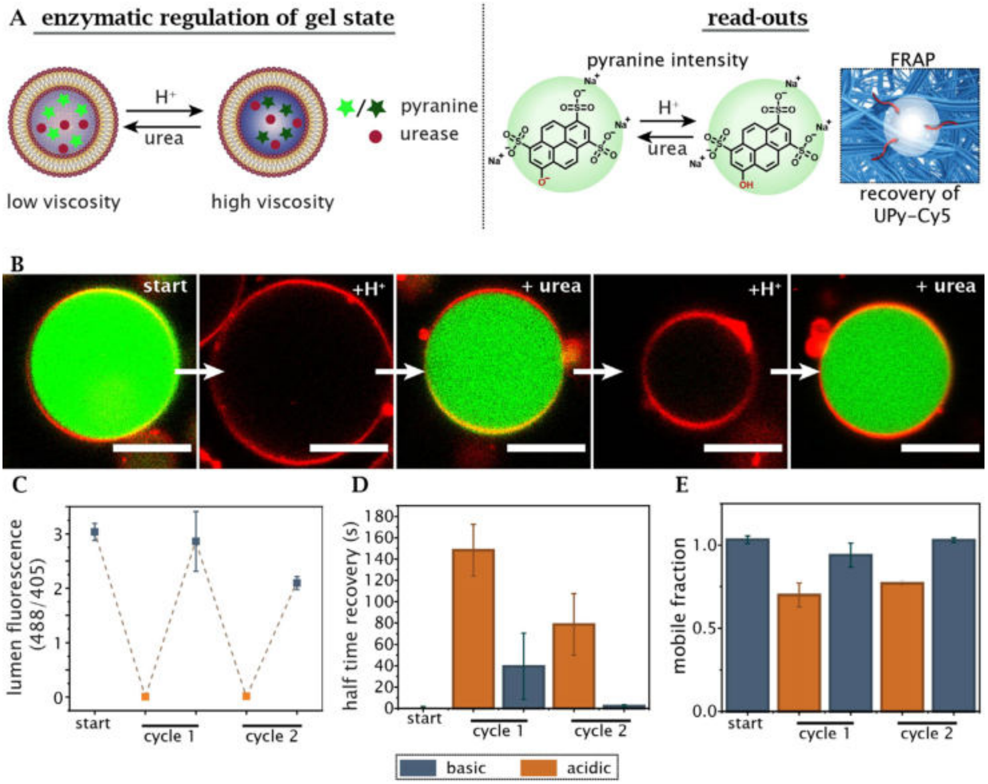

Figure 5.4 Enzymatic regulation of the gel state. Encapsulation of urease and pyranine was performed to adapt and follow pH-fluctuations, with a schematic overview of the encapsulates and cycles performed on the HL-GUVs, with the main read-outs being the pyranine intensity as well as FRAP (A). The confocal micrographs of the HL-GUVs at the start and after acid and urea addition (for two cycles) with the membrane visualized in red (rhodamine B) and the inner lumen in green (pyranine), scale bar represents 10 μm (B). The 488/405 ratio of pyranine during the cycles (after acid and urea addition) (C), as well as the half time recovery (D) and the mobile fraction (E) measured with FRAP. Data is represented as mean ±SD, n=3.

For each condition, a steady increase in calcein fluorescence over time was observed (Figure 5.5B). For the GUVs, the increase in calcein intensity showed small differences at a pH of 7 and 9, with a relative activity of 0.43±0.1 min^{-1} at pH 7, and 0.33±0.06 min^{-1} at pH 9 (Figure 5.5E). For the HL-GUVs, a difference in calcein intensity increase was observed, with the neutral pH showing a relatively lower activity in comparison to the high pH condition (0.14±0.17 and 0.41±0.2 min^{-1}, respectively). These results indicate that the esterase activity is altered when encapsulated in the HL-GUVs, predominantly at neutral pH which is ascribed to the hydrogelator encapsulated having a higher viscosity as showed earlier. This showed to lower the average activity of the esterase, but furthermore increase the deviation in activity. The increase in deviation was also observed for the HL-GUVs at a pH of 9, which suggests an effect of the co-encapsulation of hydrogelator and esterase in the HL-GUVs. However, the average esterase activity of the HL-GUVs at pH 9 displayed a similar activity as for the GUVs at pH 7. This shows the adaptivity of the system, with the gel-state regulating the esterase activity. The large deviation observed for the enzyme activity in the HL-GUVs could indicate particle variation, which could be affected by some heterogeneity in hydrogelator or enzyme encapsulation. Nonetheless, the results demonstrate that HL-GUVs are able to adapt the esterase activity, illustrating the effect of the viscoadaptation on the enzymatic activity.

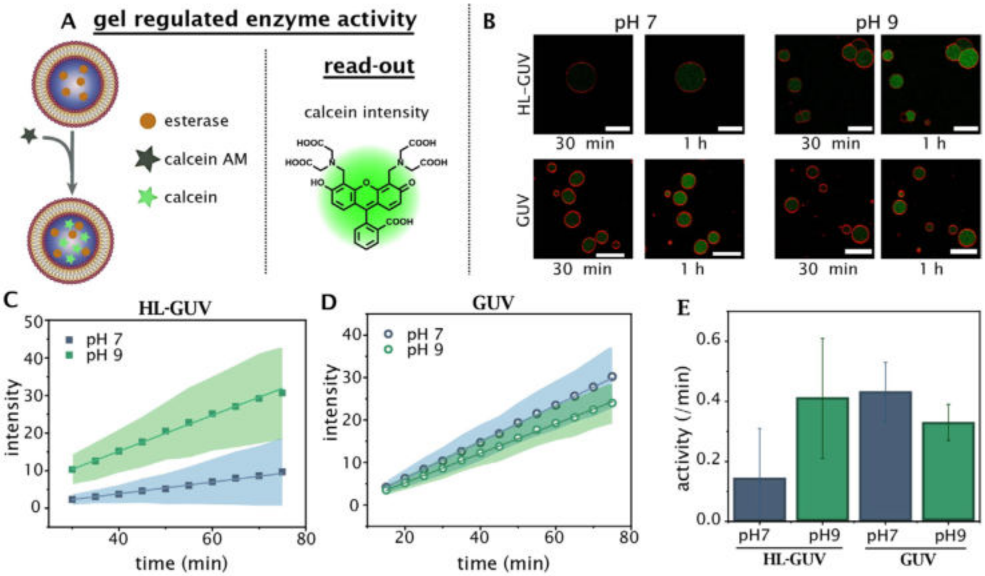

Figure 5.5 Esterase encapsulation in HL-GUVs and GUVs and external addition of calcein AM, with a schematic overview of the experiment and the read-out method measuring calcein intensity (A). Confocal micrographs show the fluorescence intensity of calcein after 30 min and 1h for the HL-GUVs, as well as GUVs at pH 7 and 9, in which the calcein intensity brightness of each imaged being increased with the same ratio for better visualization (B). The intensity increase of HL-GUVs plotted over time (C), as well as the GUVs (D). The relative esterase activity is plotted at two different pHs for the HL-GUVs and GUVs (E). Data is represented as mean ±SD, n>8.

5. HL-GUVs as drug release systems

Liposome particles are of interest as drug and gene delivery systems, decreasing the toxic effects of encapsulated drugs, and protecting the drugs from the external environment.[28] A challenge with this system is the controlled release of drugs or genes from the liposome, with a high drug clearance when the membrane of the liposome is disrupted. A sustained release profile from the liposomes can be obtained by the encapsulation of hydrogels in combination with the drugs.[29-31] In the HL-GUVs, drugs can be easily encapsulated at an increased pH, with the hydrogelator being in the sol-state, whereafter neutralization of the particles leads to a drug-encapsulated gel-state of the HL-GUVs as described before. This shows facile hydrogel and drug encapsulation, without the need of covalent cross-linking mechanisms such as UV-treatment[32,33], that can possibly modify the drug encapsulate.

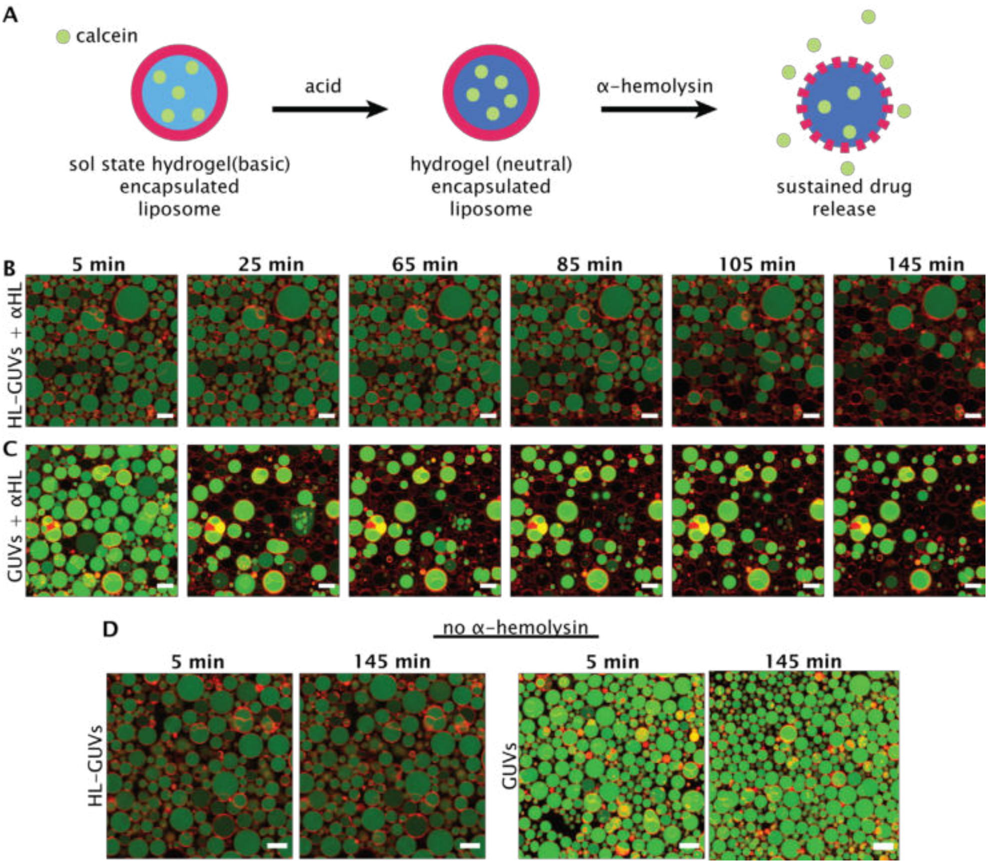

Figure 5.6 Calcein release after α-hemolysin (αHL) addition at pH 7, with a schematic experimental overview (A), fluorescence micrographs of calcein (green) and the HL-GUV membrane colored with rhodamine (red) over a time span of 145 minutes after αHL addition to the HL-GUVs (B) as well as to the GUVs (C). The controls are shown when no αHL was added (D).

We show a proof-of-concept experiment in which calcein is used as a drug model compound and encapsulated in the HL-GUVs as well as the GUVs. After neutralization, α-hemolysin was added, which is a cytotoxic protein that forms pores by generating small cation-permeable channels in the membrane of cells (Figure 5.6).[34] We hypothesize that an increase in sustained release can be obtained by encapsulation of the BF UPy-PEG hydrogel, slowing down the calcein release from the HL-GUVs. The HL-GUVs and GUVs were visualized after addition of α-hemolysin, as well as a control visualizing the particles without α-hemolysin addition. After α-hemolysin addition the calcein is shown to be released from the HL-GUVs after approximately 85 minutes, and slowly increasing in release over 145 minutes. Addition of α-hemolysin to the GUVs leads to a faster calcein release, which occurs swiftly after 25 minutes. However, some of the particles still contain calcein after 145 minutes, in the GUVs as well as in the HL-GUVs. The presence of double layered membranes could lead to less extensive penetration of the α-hemolysin to the inner membrane. Furthermore, the calcein intensity is observed to be higher when encapsulated in the GUVs in comparison to the HL-GUVs. This can indicate a lower encapsulation efficacy when the two encapsulates (BF UPy-PEG and calcein) are combined. Overall, these results show that there is a difference in release kinetics of the model drug calcein from the HL-GUVs in comparison to GUVs. Quantitative analysis is necessary to examine if this difference is significant, but promising results are shown. Adaptations to the encapsulated hydrogelator can be performed to introduce charges to increase the drug-hydrogel affinity, e.g. a positively charged hydrogel can increase the affinity between RNAi therapeutics (negatively-charged) to provide an increase in sustained release. Furthermore, anchor-functionalized drugs (as shown in Chapter 4), can be introduced to furthermore sustain the drug release from the HL-GUVs.

6. Conclusion

In this chapter, two fully synthetic supramolecular systems were assembled into a hybrid micron-sized platform. Encapsulation of a dynamic, pH-sensitive hydrogelator in GUVs showed to display pH-responsive viscoadaptability. Facile encapsulation of urease as a model pH-regulating enzyme allowed for adaptation of the viscosity upon addition of an external molecular stimulus (i.e, urea). In addition, HL-GUVs were exploited as adaptive microreactors, using the esterase/calcein-AM model reaction, in which the internal viscosity regulates the rate of product formation. This shows vast potential of this system in the field of synthetic cells, with the crowded cellular environment being mimicked as well as the viscoadaptive cellular properties being displayed. Furthermore, a proof-of-concept showing calcein release from the HL-GUVs highlights the potential use of the HL-GUVs as a sustained drug release system. This expands the scope of using synthetic cells for studying intracellular biochemical processes in viscoadaptable crowded environments. In addition, the use of this platform as a sustained micron-sized therapeutic delivery system could be further explored.

Experimental section

Materials and reagents

The lipids used in this study were obtained from Avanti Polar Lipids, with the exception of cholesterol, which was obtained from Sigma-Aldrich. Esterase from porcine liver was also obtained by Sigma-Aldrich. Paraffin oil (0.86 g/cm^3 at 20 °C) was obtained from JT Baker. The hydrogelator BF UPy-PEG with M_n PEG = 10 kg mol^{-1} was synthesized by SyMO-Chem BV, Eindhoven, the Netherlands.[35] The monofunctional UPy-Cy5 was synthesized as described previously.[36] Ultrapure water (miliQ) was purified on an EMD Milipore miliQ integral Water Purification system. 1x and 5x Phosphate buffered saline (PBS) was prepared using PBS tablets (Sigma Aldrich), which was filtered before use (MF-milipore Membrane filter, 0.45 µm pore size). MQuant® pH-indicator paper was obtained from Merck.

Lipids used for this study: 1,2-dioleoyl-sn-glycero-3-phosphocholine (DOPC), 1-palmitoyl-2-oleoyl-sn-glycero-3-phosphocholine (POPC), 1,2-dioleoyl-sn-glycero-3-phosphoethanolamine-N-(lissamine rhodamine B sulfonyl) (DOPE-LRB), 1,2-distearoyl-sn-glycero-3-phosphoethanolamine-N-[biotinyl(polyethylene glycol)- 2000] (DSPE-PEG).

Instrumental and characterization

Bulk fluorescence measurements were obtained using the Spark 10 M multimode plate reader. Visualization, FRAP measurements, urea/urease controlled viscosity measurements, and esterase activity measurements were performed on a Leica TCS SP8 inverted confocal microscope (Leica microsystems) equipped with a 63x objective (water or glycerin immersion objective). 8-well or 18-well glass-bottom chamber slides (ibidi GmbH) were used for vesicle visualization, which were treated with 1 mg/mL BSA in miliQ for >30 min, followed by washing with miliQ.

Hydrogel precursor preparation

The hydrogel precursor was prepared by dissolving UPy-PEG (20 mM, 20 wt%) in basic miliQ (pH ~11 adjusted with 1M NaOH) at 70 °C for 1h. After dissolving, the pH was adjusted to 10 – 10.5 with 1M HCl or 1M NaOH. For visualization purposes, monofunctional UPy-Cy5 was added from a stock (5 mg/mL in DMSO) to the dissolved hydrogelator at a concentration of 100 µM. Hydrogelator solutions were prepared fresh and used no longer than 5 hours before encapsulation in the HL-GUVs.

Assembly of hydrogel-loaded giant unilamellar vesicles

HL-GUVs were prepared using the inverted emulsion method. All lipids were prepared in stock solutions in chloroform, from which they were added to the paraffin oil. The molar ratios of the lipids added were as followed: DOPC/Chol/DOPE-LRB/POPC/DSPE-PEG 35/30/0.6/35/1, with a total concentration of 2 µM. This was heated to 80 °C for approximately 30 minutes to evaporate the chloroform, which was vortexed after approximately 10 minutes and 20 minutes. Inner phase solutions for the HL-GUVs were prepared containing 200 mM sucrose, 10 µM of hydrogel precursor solution. When required, 0.1 mM pyranine, esterase (3.5 mg/mL, 21 µM), and/or urease (3.5 mg/mL, ~6.4 µM) were added. For the esterase encapsulation experiments, 5X PBS (pH 10.5, adapted with 1 M NaOH) was added to the inner phase, with a final PBS concentration of 1x. 20 µL of the inner phase was added to the paraffin oil suspension and vortexed for 25 seconds while turning the tube to prevent sedimentation. The entire suspension was taken and layered on top of an outer phase solution in a tube, containing 200 mM glucose in basic miliQ water (pH ~10), and for the esterase experiments 5X PBS (pH 10.5, adapted with 1 M NaOH), resulting in a final PBS concentration of 1X PBS. Subsequently, this was centrifuged at 3,300 g for 20 minutes at room temperature. The HL-GUVs were obtained by puncturing the tube and obtaining the aqueous layer. The HL-GUVs were purified by carefully washing with outer phase and centrifuging for 2 minutes at 1,500 g, removing the supernatant. This was performed two times. Preparation of GUVs containing no hydrogel were performed in a similar manner, with the hydrogel precursor being replaced by basic MiliQ water (pH ~10.5).

Fluorescence recovery after photobleaching

Recovery experiments of the UPy-Cy5 were performed by sample illumination using a white laser at 646/660-700 nm ex/em. A circular area of 3 µm was photo-bleached at 100% laser power for 10 frames (1 frame/s). Post-bleaching was performed for 10 min (1 frame/s) at laser power 0.5%. Images were processed using the Leica Las X software. The fluorescence intensity was normalized by the prebleach steady state fluorescence intensity, correcting for background fluorescence. $t_{1/2}$ and mobile fraction were determined by using the FrapBot software using a single exponential fitting.[37] Two series of samples were prepared, being HL-GUVs loaded with hydrogelator, urease, and pyranine dye, FRAP was performed at basic condition after preparation, after which the external pH of the outer phase was adapted to ~4-5 upon acid addition (0.1M HCl). Subsequently, the external pH was adapted (using 0.1 M NaOH) to approximately ~10, whereafter FRAP was performed. This was repeated for two more cycles.

Urea triggered viscosity reaction

Urease (3.5 mg/mL) and pyranine (1 uL, final concentration 0.1 mM) were co-encapsulated in the HL-GUVs and GUVs. By confocal measurements, the GHLVs and GUVs were visualized. The external pH of the outer phase was adapted to approximately 5 (0.1 M HCl), examined using pH-indicator paper, after which urea (final concentration 25 mM) was added to the outer phase. 5 minutes post-urea addition, the GHLVs were visualized by confocal measurements. One cycle of acid addition and urea addition was performed, where, after each addition, the particles were visualized and the pyranine intensity was examined, at ex/em 488/510, as well as ex/em 405/440. The ratio between the intensity at ex/em 488/510 and ex/em 405/440 was determined, illuminating the inner pH of the HL-GUVs. FRAP measurements were performed as described previously, with each condition was measured in triplicate with the exception of the first acidic condition, which was measured in duplicate.

Esterase triggered calcein AM conversion

Esterase (3.5 mg/mL) was co-encapsulated in the HL-GUVs and GUVs, and prepared as described previously. Subsequently, the prepared HL-GUVs and GUVs were placed in the wells at the corresponding pH (7 or 9) in 1x PBS, adapted with 1 M NaOH. Calcein AM (400 nM) was added to the outer phase, whereafter the HL-GUVs and GUVs were imaged by fluorescence imaging recorded using confocal microscopy. 20 minutes post-calcein AM addition, a time-lapse of the particles was taken, during which every 5 minutes an image was taken at several spots containing HL-GUVs and GUVs. The calcein intensity was examined over a time-span of 1 hour (ex: 488, em: 520), with micrographs being taken every 5 minutes.

α-hemolysin triggered calcein release

Calcein (1 uL, 0.1 nmol from a 100 μM DMSO stock) was co-encapsulated in the HL-GUVs and GUVs. After purification, 10 μL of the liposome stock is added to a 16-well chamber slide (Thermo Scientific™ Nunc™ Lab-Tek™) to a 140 μL outer phase at 1X PBS, pH 7. The HL-GUVs as well as GUVs were visualized using confocal microscopy. α-hemolysin was added to the wells (5 μg, 0.15 nmol per well), whereafter micrographs were taken 5 minutes post-addition. Hereafter, the particles were visualized every 20 minutes post-α-hemolysin addition. No α-hemolysin was added for control experiments.

References

1 S. F. Jordan, H. Rammu, I. N. Zheludev, A. M. Hartley, A. Maréchal and N. Lane, *Nat. Ecol. Evol.*, 2019, **3**, 1705–1714.

2 P. L. W. Welzen, S. W. Martinez Ciriano, S. Cao, A. F. Mason, I. A. B. Welzen-Pijpers and J. C. M. van Hest, *J. Polym. Sci.*, 2021, **59**, 1241–1252.

3 T. Trantidou, M. Friddin, Y. Elani, N. J. Brooks, R. V Law, J. M. Seddon and O. Ces, *ACS Nano*, 2017, **11**, 6549–6565.

4 A. F. Mason, W. J. Altenburg, S. Song, M. van Stevendaal and J. C. M. van Hest, in *Liquid-Liquid Phase Coexistence and Membraneless Organelles*, ed. C. D. Keating, Academic Press, 2021, vol. 646, pp. 51–82.

5 X. Huang, M. Li, D. C. Green, D. S. Williams, A. J. Patil and S. Mann, *Nat. Commun.*, 2013, **4**, 2239.

6 A. F. Mason, N. A. Yewdall, P. L. W. Welzen, J. Shao, M. van Stevendaal, J. C. M. van Hest, D. S. Williams and L. K. E. A. Abdelmohsen, *ACS Cent. Sci.*, 2019, **5**, 1360–1365.

7 O. Chaudhuri, J. Cooper-White, P. A. Janmey, D. J. Mooney and V. B. Shenoy, *Nature*, 2020, **584**, 535–546.

8 R. L. Smith, M. R. Soeters, R. C. I. Wüst and R. H. Houtkooper, *Endocr. Rev.*, 2018, **39**, 489–517.

9 L. B. Persson, V. S. Ambati and O. Brandman, *Cell*, 2020, **183**, 1572–1585.e16.

10 Y. Zhang, Y. Chen, X. Yang, X. He, M. Li, S. Liu, K. Wang, J. Liu and S. Mann, *J. Am. Chem. Soc.*,2021, **143**, 2866–2874.

11 B. C. Buddingh', A. Llopis-Lorente, L. K. E. A. Abdelmohsen and J. C. M. van Hest, *Chem. Sci.*,2020, **11**, 12829–1283.

12 M. Guo, X. Cao, E. W. Meijer and P. Y. W. Dankers, *Macromol. Biosci.*, 2013, **13**, 77–83.

13 H. Wang and S. C. Heilshorn, *Adv. Mater.*, 2015, **27**, 3717–3736.

14 M. Diba, S. Spaans, S. I. S. Hendrikse, M. M. C. Bastings, M. J. G. Schotman, J. F. van Sprang, D. J. Wu, F. J. M. Hoeben, H. M. Janssen and P. Y. W. Dankers, *Adv. Mater.*, 2021, **33**, 2008111.

15 D. S. Kohane, *Biotechnol. Bioeng.*, 2007, **96**, 203–209.

16 J.-Y. Leong, W.-H. Lam, K.-W. Ho, W.-P. Voo, M. F.-X. Lee, H.-P. Lim, S.-L. Lim, B.-T. Tey, D. Poncelet and E.-S. Chan, *Particuology*, 2016, **24**, 44–60.

17 M. M. C. Bastings, S. Koudstaal, R. E. Kieltyka, Y. Nakano, A. C. H. Pape, D. A. M. Feyen, F. J. van Slochteren, P. A. Doevendans, J. P. G. Sluijter, E. W. Meijer, S. A. J. Chamuleau and P. Y. W. Dankers, *Adv. Healthc. Mater.*, 2014, **3**, 70–78.

18 B. C. Buddingh', Technische Universiteit Eindhoven, 2020.

19 S. Pautot, B. J. Frisken and D. A. Weitz, *Langmuir*, 2003, **19**, 2870–2879.

20 C. Claaßen, T. Gerlach and D. Rother, *Adv. Synth. Catal.*, 2019, **361**, 2387–2401.

21 K. Kano and J. H. Fendler, *Biochim. Biophys. Acta - Biomembr.*, 1978, **509**, 289–299.

22 Y. Avnir and Y. Barenholz, *Anal. Biochem.*, 2005, **347**, 34–41.

23 D. Bratosin, L. Mitrofan, C. Palii, J. Estaquier and J. Montreuil, *Cytom. Part A*, 2005, **66**, 78–84.

24 S. A. Weston and C. R. Parish, *Cytometry*, 1992, **13**, 739–749.

25 P. Decherchi, P. Cochard and P. Gauthier, *J. Neurosci. Methods*, 1997, **71**, 205–213.

26 J. Su, Y. Zhou, Q. Lai, X. Li, P. Dong, X. Yang, B. Zhang, J. Zhang, X. Zheng, Y. Tian and T. Zheng, *Int. J. Syst. Evol. Microbiol.*, 2013, **63**, 2095–2100.

27 E. Puchkov, *Biochem. Suppl. Ser. A Membr. Cell Biol.*,2013, **7**, 270–279.

28 T. M. Allen and P. R. Cullis, *Adv. Drug Deliv. Rev.*, 2013, **65**, 36–48.

29 L. Liu, Y. Xiang, Z. Wang, X. Yang, X. Yu, Y. Lu, L. Deng and W. Cui, *NPG Asia Mater.*, 2019, **11**, 81.

30 J. Park, S. H. Wrzesinski, E. Stern, M. Look, J. Criscione, R. Ragheb, S. M. Jay, S. L. Demento, A. Agawu, P. Licona Limon, A. F. Ferrandino, D. Gonzalez, A. Habermann, R. A. Flavell and T. M. Fahmy, *Nat. Mater.*, 2012, **11**, 895–905.

31 E. Yamamoto, M. Kitahara, T. Tsumura and K. Kuroda, *Chem. Mater.*, 2014, **26**, 2927–2933.

32 J. S. Hong, S. M. Stavis, S. H. DePaoli Lacerda, L. E. Locascio, S. R. Raghavan and M. Gaitan, *Langmuir*, 2010, **26**, 11581–11588.

33 Y. Wang, S. Tu, A. N. Pinchuk and M. P. Xiong, *J. Colloid Interface Sci.*, 2013, **406**, 247–255.

34 M. Silbergleit, A. A. Vasquez, C. J. Miller, J. Sun and I. Kato, in *The Microbiome in Health and Disease*, ed. J.. Sun, Academic Press, 2020, vol. 171, pp. 131–193.

35 I. de Feijter, O. J. G. M. Goor, S. I. S. Hendrikse, M. Comellas-Aragonès, S. H. M. Söntjens, S. Zaccaria, P. P. K. H. Fransen, J. W. Peeters, L.-G. Milroy and P. Y. W. Dankers, *Synlett*, 2015, **26**, 2707–2713.

36 M. J. G. Schotman, M. M. C. Peters, G. C. Krijger, I. van Adrichem, R. de Roos, J. L. M. Bemelmans, M. J. Pouderoijen, M. G. T. A. Rutten, K. Neef, S. A. J. Chamuleau and P. Y. W. Dankers, *Adv. Healthc. Mater.*, 2021, **10**, 2001987.

37 R. Kohze, C. E. J. Dieteren, W. J. H. Koopman, R. Brock and S. Schmidt, *Cytometry. A*, 2017, **91**, 810–814.

6

In vivo retention quantification of supramolecular hydrogels engineered for cardiac delivery

Abstract

Recent advances in the field of cardiac regeneration show great potential in the use of injectable hydrogels to reduce immediate flush-out of injected factors, thereby increasing the effectiveness of the encapsulated drugs. To establish a relation between cardiac function and retention of the drug-encapsulating hydrogel, a quantitative in vivo imaging method is required. Here, we develop our supramolecular ureido-pyrimidinone modified poly(ethylene glycol) (UPy-PEG) material into a bioactive hydrogel for radioactive imaging in a large animal model. As radioactive label we synthesized a monofunctional UPy-DOTA complexed with the radioactive isotope indium-111 (UPy-DOTA-^{111}In) being mixed with the hydrogel. Additionally, bioactive and adhesive properties of the UPy-PEG hydrogel were increased by supramolecular introduction of a UPy-functionalized recombinant collagen type 1-based material (UPy-PEG-RCPhC1). This method enabled in vivo tracking of the non-bioactive and bioactive supramolecular hydrogels and quantification of hydrogel retention in a porcine heart. In a small pilot, cardiac retention values of 8% for UPy-PEG and 16% for UPy-PEG-RCPhC1 hydrogel were observed 4 hours post injection. This work highlights the importance of retention quantification of hydrogels *in vivo*, where elucidation of hydrogel quantity at the target site is proposed to strongly influence efficacy of the intended therapy.

The content described in this chapter is based on:

M. J. G. Schotman‡, M. M. C. Peters‡, G. C. Krijger, I. van Adrichem, R. de Roos, J. L. M. Bemelmans, M. J. Pouderoijen, M. G. T. A. Rutten, K. Neef, S. A. J. Chamuleau, P. Y. W. Dankers, *Adv. Health. Mat.* **2021**, 10, 2001987. ‡ Contributed equally

1. Introduction

Ischemic heart disease is responsible for over 9 million deaths per year worldwide as a result of blood flow deficiency in the infarcted area and through resulting adverse ventricular remodeling and contractile dysfunction.[1] This adverse remodeling is caused by the inability of the heart to replace cardiomyocytes lost by ischemic damage to the myocardium. Therapeutic methods to stimulate cardiac repair remain ineffective as potential reparative drugs injected into the heart immediately flush-out through the venous microvasculature of the heart and the injection needle tract.[2] A carrier system to protect and localize regenerative factors at the injection site, and enable sustained, slow therapeutic release might provide a solution to this delivery issue. Biomaterials are increasingly studied in the field of cardiac regeneration, where patches or injectable hydrogels are applied to aid retention and provide sustained release of drug molecules at the target site.[3],[4]

Visualization of these biomaterials after injection or implantation is of high importance to assess the retention and degradation at the target site. Quantification of retention would enable correlation of drug efficacy to presence and availability at the target site, as well as monitoring the fate and distribution of the material in vivo. Based on this, volumes of injection or implantation could be tuned for an optimal drug release effect. Moreover, unwanted side effects at potential off-target sites could be brought to light and prevented by obtaining an enhanced understanding of the distribution.

For retaining drugs at the site of injection, hydrogels are considered good candidates as biocompatible, easily injectable carrier systems for cardiac repair and regeneration.[5] Previously, it was shown that the release of miR-302 from a hyaluronic-based hydrogel promoted cardiomyocyte proliferation and regeneration after myocardial infarction (MI) in a porcine heart.[6] Furthermore, injection of a hydrogel based on decellularized extracellular matrix (ECM) in a rat MI model reduced cardiomyocyte apoptosis and neovascularization.[7] Moreover, efficacy was established in a porcine infarction model[8] and currently, this decellularized ECM-based gel is in its first human-trial to examine the safety and feasibility post MI.[9] Delivery of these hydrogels is primarily performed via a minimally invasive catheter based injection technique, where gelation occurs at the target site triggered by temperature increase.[10] While studying the beneficial effect of hydrogel-mediated delivery of therapeutic factors, primarily indirect parameters and the functional effect of the drugs (e.g. scar thickness, ejection fraction, and end-diastolic volume) were examined.[11-13] Only a few studies examined the degree of hydrogel retention after injection and the potential off-target distribution of the gel, mainly in small animal models.[14-16] A collagen matrix delivery in a mouse model with MI was assessed on its retention and distribution by PET imaging, where the hydrogel was labelled with hexadecyl-4-[(18)F]fluorobenzoate ((18)F-HFB).[17] A more recent study showed in vivo nuclear imaging of an alginate hydrogel in which the nuclear imaging radio-metal indium-111 (^{111}In) was incorporated.[16] Intra-myocardial injection in mice was performed, where a low retention was observed after one week (2-4%). To our knowledge, no study has provided quantitative numbers on the amount of cardiac retention and distribution of a supramolecular hydrogel in a large animal model.

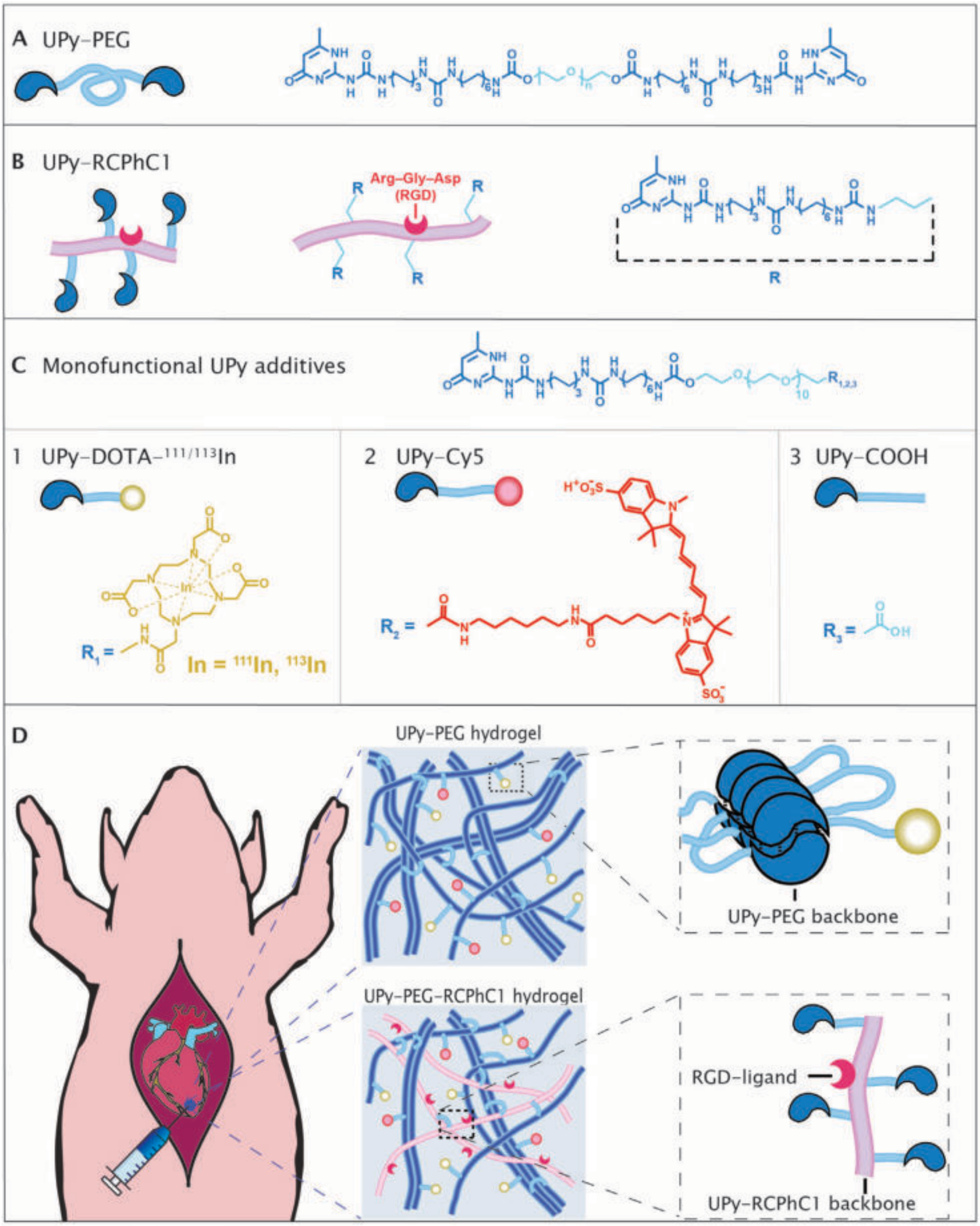

Figure 6.1 Hydrogel formulation and overview of this study. A, B. The chemical structure and schematic overview of hydrogelators UPy-PEG (A) and UPy-PEG-RCPhC1 (B). C. The monofunctional UPy-additives used during this study with the (non-)radioactive label UPy-$^{111/113}$In (1), the fluorescently-labelled UPy-Cy5 (2), and the non-fluorescent label mimic UPy-COOH (3). D. The epicardial hydrogel injection in a porcine model, and the concept of the two different hydrogels used in this study, UPy-PEG and UPy-PEG-RCPhC1.

Here, we show a first approach in performing a quantitative retention study by implementation of a radioactive tracer in our injectable pH- and temperature-responsive supramolecular poly(ethylene glycol) (PEG) hydrogel functionalized at each end with ureido-pyrimidinone (UPy) units (Figure 6.1A).[18] This UPy-PEG hydrogelator is an injectable viscous liquid at a pH > 8.5 and rapidly forms a hydrogel once exposed to physiological pH.[19] To increase tissue adhesiveness, a UPy-functionalized recombinant peptide based on human collagen type 1 is introduced to the hydrogel (RCPhC1, Figure 6.1B), enriched with repeating amino acid sequences based on the integrin-binding peptide RGD (introduced in Chapter 3). Supramolecular labelling of the hydrogel is performed using monofunctional UPy-labels, either for radioactive or for fluorescent visualization. The hydrogel is radioactively labelled using a 1,4,7,10-tetraazacyclododecanetetraacetic acid (DOTA) chelated with radioactive isotope ^{111}In, covalently bound to a monofunctional UPy-moiety, allowing for in vivo radioactive detection. In addition, a fluorescent UPy-Cy5 label was synthesized and used for ex vivo histological fluorescence analysis (Figure 6.1C). Comparative visualisation and quantification of hydrogel retention and distribution was performed for epicardial injections of UPy-PEG and UPy-PEG-RCPhC1 hydrogels in a porcine model (Figure 6.1D).

2. Molecules

The UPy-DOTA was chelated with the radioactive ^{111}In label (Figure 6.2A). A separation and detection of radioactive compound by high-performance liquid chromatography (radio-HPLC) (Figure 6.2B) as well as by instant-thin layer chromatography (iTLC) (Figure 6.2C, D) showed an optimal chelation after approximately 1 hour (with a varying range of 93-98%). The chelation remained stable at basic pH (Figure 6.2B) for approximately 24 hours. As a reference, a non-radioactive isotope indium-113 (^{113}In) was chelated to the UPy-DOTA moiety (UPy-DOTA-^{113}In) for *in vitro* measurements. A monofunctional UPy-moiety functionalized with the fluorescent probe cyanine-5-amine (UPy-Cy5), allowed histological staining after injection, where an unfunctionalized monofunctional UPy-moiety (UPy-COOH) was used as a non-fluorescent reference. To introduce bioactivity and potential adhesion to the cardiac tissue UPy-RCPhC1 was added synthesized by modification of pristine RCPhC1 with UPy-units. ^{1}H-NMR spectroscopy showed an average number of six UPy-moieties grafted on the RCPhC1 backbone (Figure 6.3).

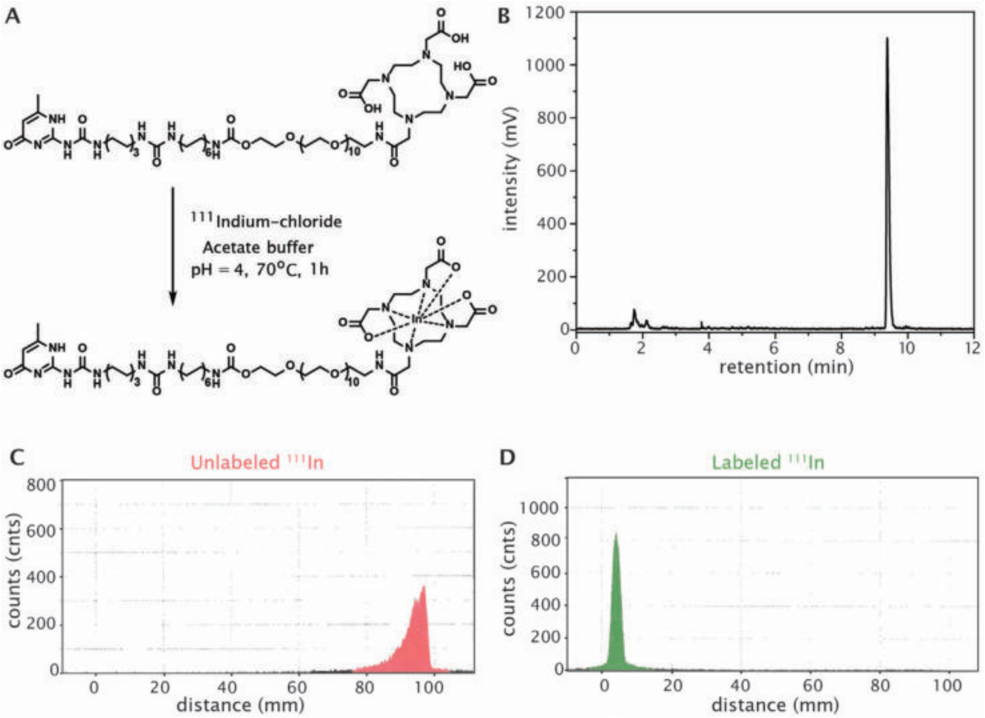

Figure 6.2 Chelation of the ^{111}In with the UPy-DOTA label, with the labelling method (A), and radio-HPLC after chelation of UPy-DOTA-^{111}In at basic pH (>9) (B), with loose ^{111}In at a retention time of 1.8-2.2 minutes and labelled UPy-DOTA-^{111}In at 9.2-9.7 minutes, showing a chelation efficiency of 97%. iTLC of the chelation efficiency of the UPy-DOTA where (C) shows the unchelated loose ^{111}In depicted in red, and (D) the chelated UPy-DOTA-^{111}In depicted in green, showing a chelation efficiency of approximately 99%.

3. Mechanical properties of the hydrogels

The hydrogels were prepared in a simple mix-and-match manner, where the hydrogel precursors were dissolved at high pH PBS (either UPy-PEG, or UPy-PEG in combination with UPy-RCPhC1). Additives were introduced after the hydrogel precursors were fully dissolved. The molar ratio of the UPy-PEG hydrogel for UPy-PEG:UPy-DOTA:UPy-Cy5 or UPy-COOH was set at 10:0.35:0.01. The additive ratio for UPy-PEG-RCPhC1 was identical, containing a 9:1 ratio of UPy-PEG and UPy-RCPhC1. The pH of the hydrogel precursor was adjusted to 9 or 8.8±0.1 for UPy-PEG and UPy-PEG-RCPhC1, respectively. The UPy-PEG-RCPhC1 hydrogelator shows similar viscosities at pH 8.8 to the UPy-PEG hydrogelator at pH 9 (Figure 6.4E), which was desired to keep the flow properties similar.

The myocardium shows viscoelastic characteristics, which is due to a combination of cardiac cells and ECM proteins. During heart failure, collagen accumulation can affect the viscoelasticity of the myocardium significantly.[20] A hydrogel showing viscoelastic properties and accommodating the pulsating behavior of the heart is desired. To examine the mechanical properties of the hydrogels used in this study, UPy-DOTA was chelated in acetate buffer with non-radioactive isotope ^{113}In, where an optimal chelation efficiency was confirmed by RP LC-MS (>95%). A previous study reported that the release of a UPy-DOTA label complexed with Gadolinium(III) from the UPy-PEG hydrogel is in line with the rate of erosion of the hydrogel itself.[21] Rheology was used to examine the influence of the additives (UPy-DOTA-^{113}In and UPy-COOH, Figure 6.1C.3) on the mechanical properties of the hydrogels.

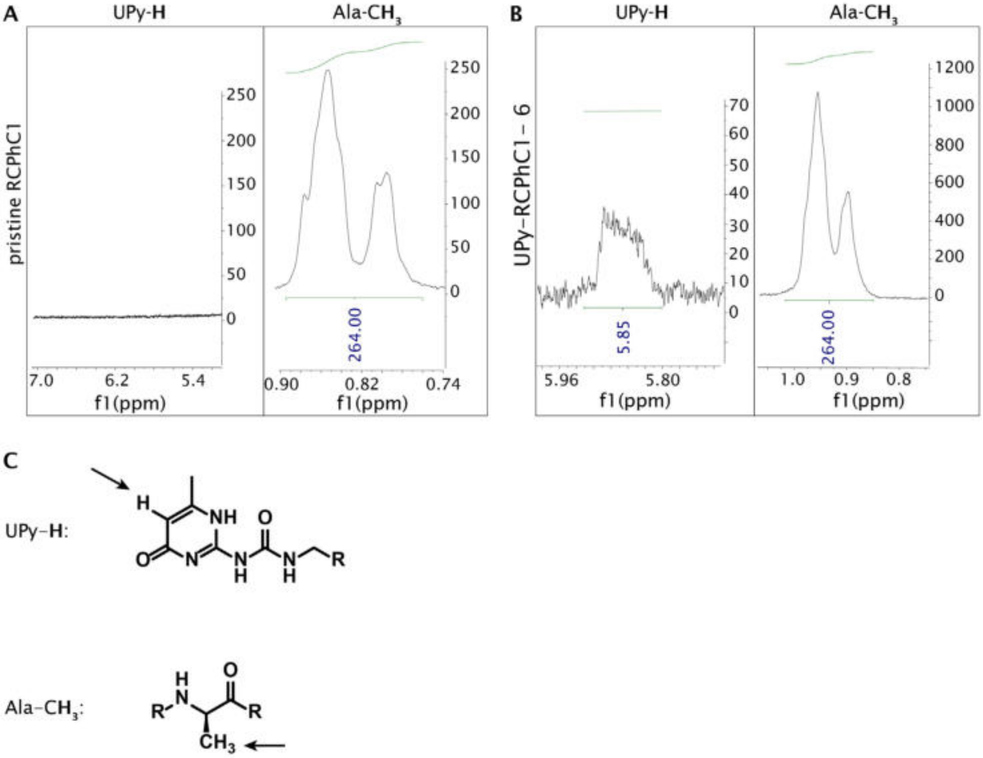

Figure 6.3 Analysis of pristine recombinant collagen peptide derivative, modified with UPy-moieties. (A) ^{1}H NMR graph of RCPhC1 showing the protons of the alanine residues (δ-shift = 0.7 – 1.0), used as a reference, and the absent peaks of the alkylidene proton of the UPy-moiety (δ-shift = 5.8 – 5.9) for RCPhC1 and (B) UPy-RCPhC1 functionalized with an average of six UPy-moieties. (C) Schematic representation of the protons used to determine UPy-functionalization, with the alkylidene proton of the UPy-moiety and the methyl group on the alanine.

After pH neutralization, the UPy-PEG as well as the UPy-PEG-RCPhC1 hydrogels show frequency-depended viscoelastic behaviour, i.e. an increase of G' while frequency was increased, while G'' remains stable or decreases (Figure 6.4A). This behavior is reflected in the tan δ (G''/G') (Figure 6.4B), that showed a decrease for both hydrogels by a factor of 7, 5.3, 3.8, and 1.2 over the tested frequency range for the UPy-PEG, UPy-PEG with additives, UPy-PEG-RCPhC1, and UPy-PEG-RCPhC1 with additives, respectively. This indicates that the solid properties are getting more distinctive as the frequency is increased, whereas at lower frequencies more liquid-like properties are observed. This suggests that at lower frequencies (longer measuring time) there is more time for structural rearrangement, i. e. characteristic interactions in the material can relax and the material starts to flow. At high frequencies (shorter measuring time) there is less time for rearrangement, i. e. all interactions remain present in the structure and have no time to relax, therefore displaying a less dynamic and more solid structure. For the UPy-PEG hydrogel, the additives resulted in a weaker gel, at lower frequencies (with a G' of 9.1 kPa vs. 4.4 kPa at 0.1 rad/s, respectively), as well as higher frequencies (with a G' of 27 kPa vs. 17 kPa at 100 rad/s, respectively, Figure 6.4A, blue). In a previous study, addition of monofunctional UPy-molecules to the bifunctional UPy-PEG molecule showed to decrease the dynamics of the network, influencing the stiffness of this mixture.[22] Addition of UPy-DOTA and UPy-COOH showed to decrease the stiffness, where the latter is added from a stock solution in DMSO, which caused a decrease in stiffness of the hydrogel. However, addition of the monofunctional UPy-molecules show to increase the stiffness of the hydrogel as shown in previous studies, in comparison to solely DMSO addition to the hydrogel. Both UPy-PEG hydrogels showed similar frequency dependent behavior, with increased stiffness at higher frequencies, and the same viscoelastic properties.

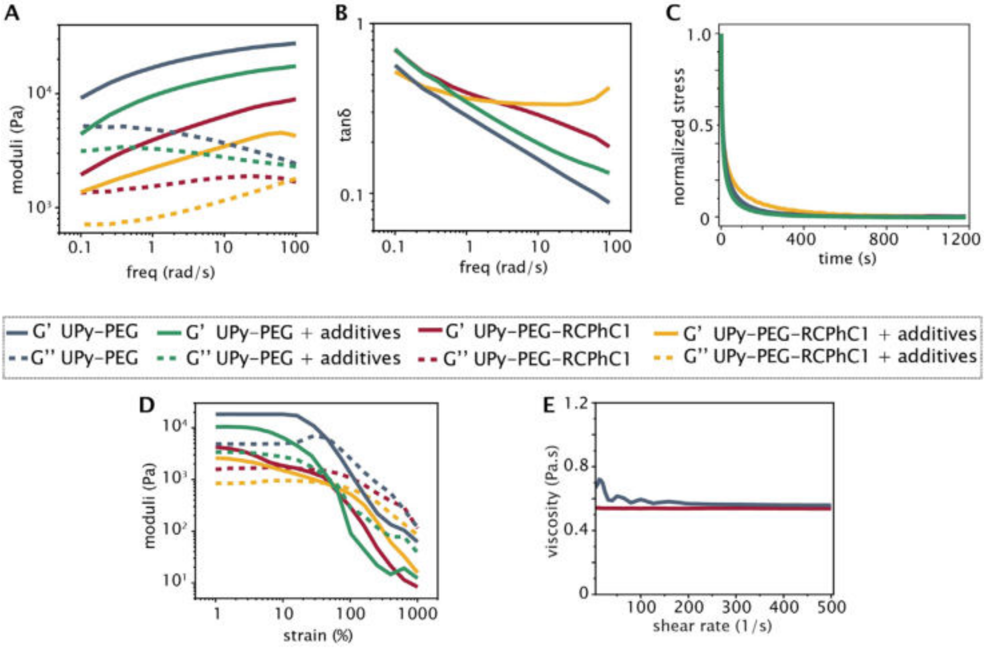

Figure 6.4 The mechanical properties of the hydrogels, showing the frequency sweep (A) and the corresponding tan δ (B) at 1% strain with frequencies between 0.1 and 100 rad/s (A), the stress-relaxation at 1% strain, measured over a time span of 500 seconds (C), and the strain-sweep at 1 rad/s with strains varying from 1 to 1000% (D), showing viscoelastic properties of the UPy-PEG, and the UPy-RCPhC1 hydrogel, measured at 37 °C. The viscosity of UPy-PEG-RCPhC1 and UPy-PEG at a pH of 8.75 (red) and 9.0 (blue), respectively, showing similar viscosities at the different pH (E).

A significant decrease in moduli is observed for the UPy-PEG-RCPhC1 hydrogel, where the UPy-PEG hydrogel showed to be a stiffer gel (2-3 times stiffer in comparison to the UPy-PEG hydrogel). This could be explained by the lower number of UPy-moieties in this hydrogel, lowering the supramolecular cross-linking ability and therefore the stiffness of the hydrogel. Comparison of UPy-PEG-RCPhC1 with and without additives showed small differences in moduli (Figure 6.4A, red). The hydrogel with additives displayed lower storage modulus (with a G' of 1.9 kPa vs. 1.3 kPa at 0.1 rad/s) and loss modulus (with a G'' of 1.4 kPa vs. 0.7 kPa at 0.1 rad/s), indicating that the additives have an influence on the mechanical properties of the hydrogels. However, similar to the UPy-PEG hydrogel, the frequency dependent viscoelastic behaviour of both hydrogels is comparable. The stress-relaxation measurements show similar relaxation curves for the UPy-PEG hydrogel with and without additives, where 50% relaxation was achieved at 6.2 vs. 8 seconds, respectively (Figure 6.4C, blue). For the UPy-PEG-RCPhC1 hydrogels with and without additives, only small differences can be observed, with a time of 6.8 vs. 6.2 seconds at a 50% relaxation, respectively (Figure 6.4C, red). This indicates a minimum to no difference that is observed considering relaxation times. The UPy-PEG hydrogel without additives shows a linear course for storage as well as loss moduli until a minimum of 25% deformation, whereas the UPy-PEG hydrogel with additives shows a slight decrease in G' and G'' after a strain of approximately 5%, whilst still retaining its hydrogel properties. The hydrogels with and without additives are disrupted at 45 and 65% strain, respectively (Figure 6.4D, blue). A similar trend as the UPy-PEG with additives is observed for the UPy-PEG-RCPhC1 hydrogels with and without additives, where a small decrease in G' and G'' is observed after a strain of 6%. Here, disruption of the hydrogels with and without additives occur at approximately 25 and 40% strain, respectively (Figure 6.4D, red). UPy-PEG-RCPhC1 hydrogels with and without additives showed small variability regarding the strain and frequency sweep, where differences in stiffness were observed. This marks the variability of the UPy-functionalized RCPhC1, introduced to the system.

Overall, minor differences in mechanical properties of hydrogel variants were observed between absolute moduli and stiffness of the hydrogels, which should not affect usability in envisioned applications.

4. In vivo Injection in Pig Heart and Scintigraphy

For the porcine experiments, one day prior to in vivo injection the additives (UPy-DOTA-^{111}In and UPy-Cy5) were added to the dissolved hydrogel precursors. Per injection of 200 µL the obtained activity was 5-10 MBq. Detailed hydrogel formation can be found in the experimental section. Hydrogels (UPy-PEG or UPy-PEG-RCPhC1) were injected epicardially (6 x 200 µL) after thoracotomy into the left ventricular wall of beating porcine hearts (*n*=2). Scintigraphic total body scans were performed 1, 2, 3 and 4 hours after injections and biodistribution of the hydrogel was quantified as percentage of radioactive signal in each organ from total whole body radioactive signal to exclude remaining radioactive signal in the dead volume of the syringes.

Areas with high radioactive signal are identified by bright red coloration and areas with low radioactivity are identified by blue coloration.

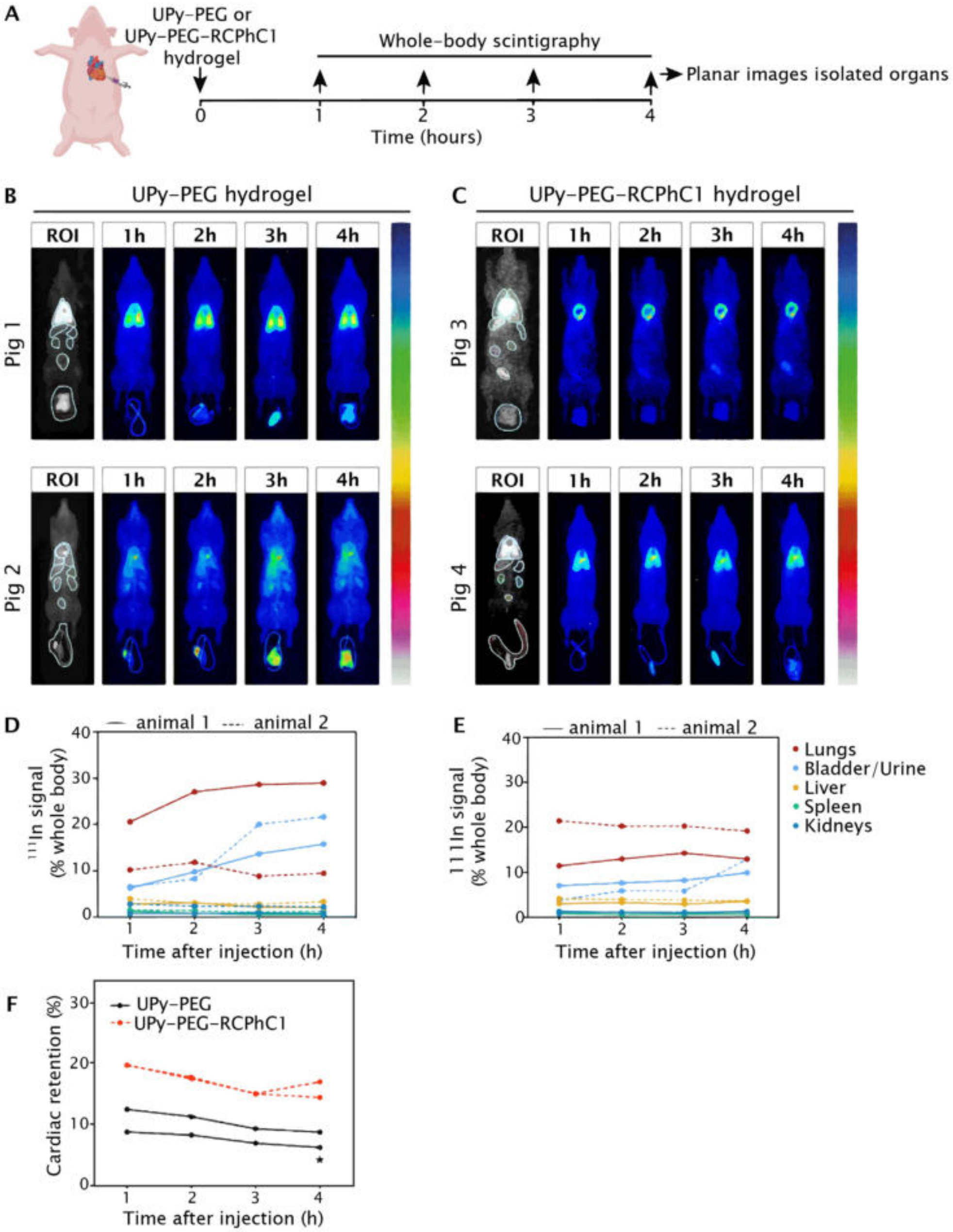

Figure 6.5 Scintigraphy imaging shows biodistribution of supramolecular hydrogels after epicardial injection. A. Experimental protocol. B, C. Whole-body scintigraphy scans 1 to 4 hours after injection of UPy-PEG (B) or UPy-PEG-RCPhC1 (C) hydrogel. Areas with high radioactive signal are identified by bright red colouration and areas with low radioactivity are identified by blue colouration D, E. Quantification of distribution in indicated

remote organs after epicardial injection of UPy-PEG (D) or UPy-PEG-RCPhC1 (E) hydrogel. F. Quantification of cardiac retention. Data are individual animals (*n*=2 per hydrogel). Differences were evaluated using paired students-t-test. * represents $P<0.05$. 4

The total body scans showed that the injections of the UPy-PEG led to a cardiac retention of 6.2% and 8.7% after 4 hours (Figures 6.5B, F). The remaining gel distributed to the lungs (29% and 9.5%), bladder and urine (15.8% and 21.6%), liver (2.0 and 3.4%), kidneys (0.8% and 2.2%), and spleen (0.56 and 1.28%) (Figure 6.5D). The residual activity was distributed evenly across the body without the presence of an increased and localized radioactive signal (“hotspots”).

Injection of UPy-PEG-RCPhC1 showed a cardiac retention of 16.9% and 14.3% after 4 hours (Figure 6.5C, F). The remaining activity was distributed to the lungs (13.0% and 19.2%), bladder and urine (9.9% and 12.9%), liver (3.5% and 3.6%), kidneys (1.3% and 1.2%), and spleen (1.2% and 0.66%) (Figure 6.5C, E). Also, for the UPy-PEG-RCPhC1 the residual activity did not lead to hotspots. When comparing the cardiac retention of the two hydrogels at the 4 time points after injection, UPy-PEG-RCPhC1 injection showed increased retention ($P<0.05$, $n=4$). The ^{111}In signal in the lungs stabilized between 2 and 3 hours after injection of the UPy-PEG hydrogel in both pigs while the ^{111}In signal in the bladder and urine increased till 4 hours after injection indicating secretion (Figure 6.5D). The UPy-PEG-RCPhC1-hydrogel showed no increased in off-target distribution after 1 hour post-injection except for the ^{111}In signal in the bladder and urine (Figure 6.5E). When comparing the off-target biodistribution at the 4 timepoints after injection, no significant difference was found between the two hydrogels for lung biodistribution ($P>0.05$, $\alpha = 0.19$, $n=2$) or bladder/urine biodistribution ($P>0.05$, $\alpha=0.09$, $n=2$).

During scintigraphic whole body scans, the measurement of radioactive signal from organs can be influenced by degree of tissue penetration and scattering, and by signals from overlapping organs. Therefore, 4 hours after injection, organs were isolated and scanned individually. Scanning of the explanted, isolated organs (heart, lungs, bladder/urine, liver, kidneys, spleen) indicated the retained radioactive signal in the heart was 14.8% and 18.9% for UPy-PEG and 22.1% and 31.7% for UPy-PEG-RCPhC1 as a percentage of the total combined signal in the isolated organs (Figure 6.7A,B). Furthermore, scintigraphy showed localised UPy-PEG-RCPhC1 at the individual injection sites with five to six radioactive hotspots (Figure 6.6A), corresponding to the individual injection sites. The UPy-PEG injected pig hearts showed three to four more diffuse and merged injection sites. One UPy-PEG injected heart showed increased radioactive signal at the base of the heart remote from the injection area (Figure 6.6).

It is important to note only a small sample size of merely two animals per group was used to analyze in vivo hydrogel biodistribution. Therefore, no significant conclusions can be drawn on the difference between the two hydrogels in the in vivo experiments. However, the current study does give insights into the potential use of ^{111}In labeling of injectable hydrogels for in vivo hydrogel retention quantification and comparison of retention and off-target distribution of multiple hydrogels. When comparing the cardiac retention of UPy-PEG and UPy-PEG-RCPhC1 in the four pigs we see a trend towards increased retention in the pigs injected with UPy-PEG-RCPhC1. This increase is likely to be caused by an increase in the adhesion of the gel to the extracellular matrix at the site of injection due to the integrin-based recombinant peptide

RCPhC1. Earlier studies using biomaterials to augment factor delivery, focused on the retention of delivered cells or compounds[12],[18] or effects on functional parameters, rather than retention of the biomaterial.[19],[20] Even though these studies gave insight into the potential benefits of hydrogel mediated delivery, so far no knowledge has been generated on the biodistribution of hydrogels in a large animal model after injection or quantitative approaches to determine the degree of retained hydrogel at the site of injection.

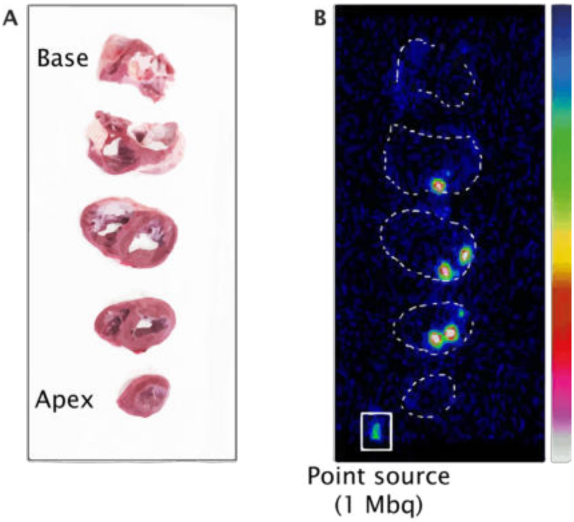

Figure 6.6 Cardiac slices, with (A) brightfield photograph of cardiac slices to identify exact sites of radioactive signal. (B) Scintigraphic scan of cardiac slices shown in A. A 1 Mbq point source was used to localize the exact part of tissue containing the ^{111}In signal.

To verify presence of the gel at the sites with high radioactive signal in the heart, histological analysis was performed. The heart was sliced into five slices from apex to base and individual slices were scanned to identify sites of high ^{111}In signal using a 1 Mbq point source (Figure 6.6). These revealed intense Cy5 signal in sections of tissue with high radioactivity signal, showing deposits of seemingly condensed gel in larger interstitial spaces and strings of gel in the smaller interstitial spaces between individual cardiomyocytes (Figure 6.7C). This was further confirmed by immunofluorescent staining for cardiac alpha actinin (Figure 6.7D). During the washing steps of the staining procedure, the gel in the larger interstitial space dissolved, while the gel surrounding the cardiomyocytes was retained. At the areas remote from the radioactive high intensity regions, no Cy5 signal was found (Figure 6.7D). This pattern of distribution of the gel within the myocardium is hypothesized to be due to the flexibility of the gel to distribute and adhere to the myocardium and the extracellular matrix.

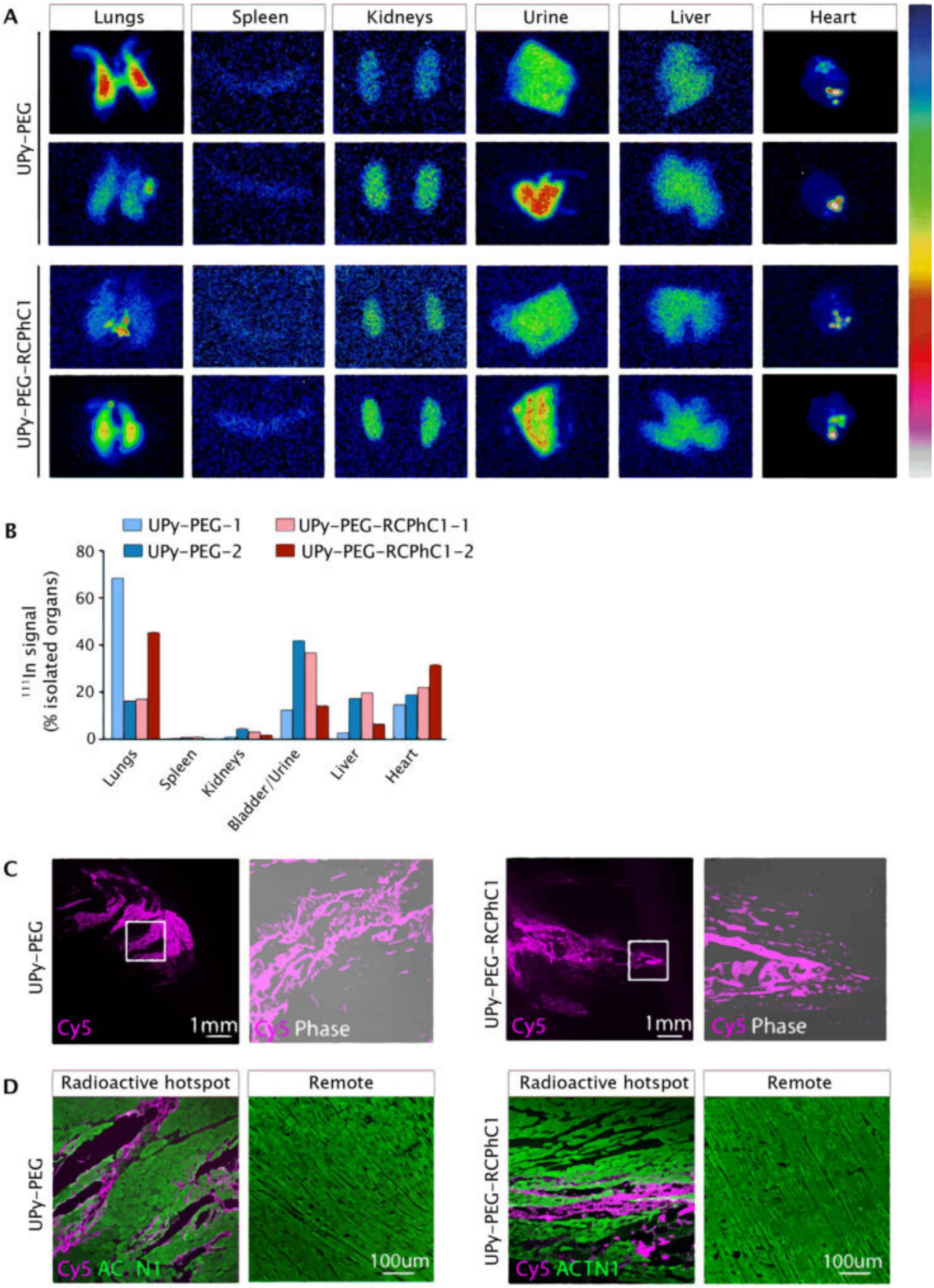

Figure 6.7 Scanning of isolated organs shows organ distribution of supramolecular hydrogels. A, B. Scintigraphic scans of individually isolated organs 4 hours after epicardial injection of supramolecular hydrogels (A) and quantification of radioactive signal as a percentage of total signal in the isolated main organs (B). Areas with high radioactive signal are identified by bright red colouration and areas with low

radioactivity are identified by blue colouration C. Histology representative images of hydrogels by supramolecular bound fluorescent signal UPy-Cy5 in the radioactive high intensity regions of the heart. D. Immunofluorescent staining of myocardium in radioactive hotspots and remote of radioactive hotspot. ACTN1, cardiac alpha actinin. Data is based on individual animals (*n*=2 per hydrogel). Differences were evaluated using a paired students t-test

As a highly vascularized organ, it is likely this accumulation of ^{111}In signal reflects dissolved UPy-polymers that enter the lungs via the coronary veins or the central circulation. Previously, we have shown that the UPy-polymers do not affect biocompatibility or induce toxicity.[16] Further investigation into the effect of pulmonary biodistribution of intracardiac injected hydrogels is needed. The distribution of the hydrogels to the lungs did not increase within 4 hours after injection, considering the UPy-PEG-RCPhC1 hydrogel. The remaining off-target distribution of the hydrogels to the bladder indicated clearance of the hydrogel through the secretory tract which limits the risk of extracardiac accumulation.

As the main cause of limited cardiac retention has been suggested to be the immediate clearing via the dense venous microvasculature and the needle track[25], we tracked the hydrogel biodistribution up to 4 hours after injection. The limited changes within the presence of ^{111}In signal in all organs within these 4 hours is in line with previous studies on the importance to improve acute cardiac retention rather than chronic engraftment.[27,28] Even though the UPy-based hydrogel gelates in physiological pH of the myocardium and shows increased retention compared to previously reported values, the presence of strong cardiac contractions and the needle track remains a challenge to maintain maximal cardiac retention of hydrogels. The achieved cardiac retention of ~30% of UPy-PEG-RCPhC1 hydrogel is likely to increase effectiveness of regenerative therapies compared to non-hydrogel mediated delivery.

With the method described, we were able to quantitatively compare the retention of two supramolecular hydrogels and show these hydrogels appear to be safe on short term follow-up of 4 hours.

5. Conclusion

Quantitative imaging and distribution tracking after intramyocardial injection in a large animal model was achieved via modification of a pH-switchable supramolecular hydrogel. In a simple mix-and-match manner, two types of hydrogels were radioactively labelled in a modular approach, with limited influence on the gelation properties. This ensured radioactive imaging of the hydrogels in a porcine heart in vivo to quantify and compare the retention of these supramolecular hydrogels. Introduction of RCPhC1 to the hydrogel implied to increase hydrogel retention in the heart with defined deposits of hydrogel at the injection sites still visible after 4 hours. Furthermore, the distribution of the hydrogels to other organs was reduced by addition of integrin-based recombinant peptide RCPhC1.

Finally, our method allows for dose quantification, increasing understanding of dose optimization and therefore drug effectiveness, which is of great importance in the translation towards cardiac regenerative therapy. Additionally, this method enables direct visualization of potential off-target localization which can be used for efficient risk-analysis of new therapies.

Acknowledgements

The following people are gratefully thanked for their contributions and for their technical assistance with the animal experiments: Marlijn Janssen, Joyce Visser, Martijn van Nieuwburg, Evelyn Velema, Ingrid Boots, Monique Jacobs, Anke Wassink, and Jeannette Wolfswinkel.

Experimental section

Materials

All starting materials and reagents were obtained from commercial sources and used as received, unless stated otherwise. Solvents from Sigma Aldrich were of p.a. quality. Deuterated chloroform and deuterium oxide were purchased at Cambridge Isotope Laboratories. Sulfo-Cyanine5 amine was purchased at Lumiprobe. FujiFilm Manufacturing Europe B.V. kindly provided us the Cellnest, a recombinant peptide based on human collagen type I (RCPhC1), which was used without further purification.

Instrumentation

^{1}H-NMR spectra were recorded on a 400 MHz NMR operating at 400 MHz for functionalization analysis. Reversed-phase high-performance liquid chromatography-mass spectrometry (RP-HPLC-MS) was performed on a Thermo scientific LCQ fleet spectrometer. The purity of UPy-RCPhC1hC1 was determined with Waters Xevo G2 Quadrupole Time-of-Flight liquid chromatography-mass spectrometry equipped with an Agilent Polaris C18A reverse-phase column (ID 2.0 mm, length 100 mm). Derivatives were dissolved in H_2O (1 mg/mL) and flowed (0.3 mL/min) over the column using a 15-75% water/acetonitrile gradient with 0.1% formic acid prior to analysis in the positive mode in the mass spectrometer. Purification of UPy-Cy5 was performed on a prep-RP-HPLC (using gradients of acetonitrile in water, with addition of 0.1 vol% trifluoroacetic acid), where collected fractions were freeze-dried and analyzed by RP-HPLC-MS. Chelation efficiency was analyzed with two methods: instant thin layer chromatography with a glass microfiber chromatography paper impregnated with a silica gel stationary phase (Agilent Technologies) and sodium chloride 0.9% as a mobile phase, and high performance liquid chromatography (Thermo Scientific Dionex UltiMate 3000), both with NaI(Tl) detector for gamma rays (Canberra). A relatively geometry independent dose calibrator (VDC-404, Veenstra Instruments, the Netherlands) was used to quantify the activity pre-injection.

Synthetic procedures

Synthesis of UPy-DOTA: The precursors UPy-C_6-U-C_{12}-C-OEG_{12}-NH_2 and N-hydroxysuccinimide activated DOTA (DOTA-NHS-xTFA) were synthesized as described elsewhere.[29] UPy-C_6-U-C_{12}-C-OEG_{12}-NH_2 (280 mg, 0.26 mmol) was dissolved in dimethylformamide (DMF, 5 mL) and DOTA-NHS-xTFA (383 mg, 0.53 mmol) and DiPEA (0.62 mL, 3.57 mmol) were added. The reaction mixture was stirred overnight and subsequently the solvent was removed under vacuum and twice co-evaporated with toluene. Eluting over reversed phase C18 column with a gradient ACN/water of 5/95 to 80/20 afforded the intermediate UPy-DOTA (360 mg, 94%) as a white powder after freeze-drying.

^{1}H NMR (400 MHz, CDCl3/CD3OD) δ 5.86 (s, 1H), 4.19 (t, J = 4.7 Hz, 2H), 3.65 (s, 44H), 3.53 (dt, J = 13.3, 6.0 Hz, 7H), 3.43-3.18 (m, 14H), 3.11 (q, J = 7.0 Hz, 13H), 2.25 (s, 3H), 1.58 (p, J = 6.8 Hz, 2H), 1.48 (p, J = 7.2 Hz, 6H), 1.37 (q, J = 5.9, 3.7 Hz, 4H), 1.34–1.17 (m, 16H) ppm. ^{13}C NMR (101 MHz, D_2O-NaOD) δ 179.94, 179.72, 175.39, 173.12, 168.35, 162.77, 159.58, 157.85, 157.34, 156.42, 104.28, 71.99, 69.80, 69.52, 69.32, 68.98, 68.83, 63.74, 58.71, 58.37, 57.16, 50.45, 40.62, 39.78, 39.25, 38.69, 30.21, 30.06, 29.66, 29.48, 29.39, 29.17, 26.89, 26.72, 26.42, 22.64 ppm.

LC-MS (ESI) Rt = 5.75 min, m/z calc for $C_{66}H_{122}N_{12}O_{23}$, 1451.8 Da; found 484.83 $[M+3H]^{3+}$, 726.6 $[M+2H]^{2+}$, 737.5 $[M+Na+H]^{2+}$, 1452.4 $[M+H]^{+}$, 1473.9 $[M+Na]^{+}$.

Synthesis of UPy-cy5: The synthesis of the UPy-COOH has been described previously[29], UPy-COOH (2.36 mg, 2.08 µmol) was dissolved in DMF (2 mL). 1-[Bis(dimethylamino)methylene]-1H-1,2,3-triazolo[4,5-b]pyridinium 3-oxide hexafluorophosphate (HATU, 1.58 mg, 0.00416 mmol) is dissolved in DMF (1 mL) and added dropwise to the UPy-PEG$_{12}$-COOH solution. N,N-Diisopropylethylamine (2.15 mg, 16.6 µmol) was added and the solution was stirred at room temperature for 15 min. Sulfo-Cy5-NH$_2$ (2 mg, 27.0 µmol) dissolved in DMF (3 mL) was added to the solution and stirred for 1 hour at argon environment. H_2O (containing 0.1 v/v% formic acid, 20 mL) was added to the solution and centrifugated (4 min, 3000 rpm) followed by decantation. Ultrapure water was added (20 mL) and the product was lyophilized. The compound was purified with preparative RP-HPLC using a gradient of 40% ACN in H_2O (both containing 0.1 v/v% formic acid). Lyophilization yielded pure UPy-Cy5 (1.75 mg, 9.4 µmol, 45%) as a blue solid. This was dissolved in DMSO at 1 mg/mL and used from this stock solution.

ESI-MS: m/z Calc. for $C_{91}H_{149}N_{11}O_{25}S_2$ 1861.37; Obs. $[M+3H]^{3+}$ 621.33, $[M+2H]^{2+}$ 931.17, $[M+H]^{+}$ 1861.75.

Synthesis of Hydrogelators UPy-PEG and UPy-RCPhC1: The hydrogelator UPy-PEG with M_n,PEG = 10 kg/mol, was synthesized by SyMO-Chem BV, Eindhoven, The Netherlands.[19] Briefly, the PEG was added to 1,1'-carbonyldiimidazole (CDI) in dichloromethane, after which excess of CDI was removed by precipitation in diethyl ether. This was coupled to 1,10-diaminodecane, followed by precipitation in diethyl ether. Solid UPy-isocyanate was added to a solution of diamine terminated-PEG in a mixture of 1:1 dichloromethane and chloroform. The UPy-RCPhC1 was synthesized in a similar manner as described previously by Spaans *et al.*[30] In short, UPy-hexyl-urea-dodecyl-amine was dissolved in DMSO and N,N-diisopropylethylamine was added, whereafter CDI was added. The CDI functionalization was confirmed by RP-HPLC-MS, after which the solution was added to RCPhC1 dissolved in DMSO and left stirring overnight at argon environment.

Preparation of radioactively labelled hydrogel precursor

Two days prior to in vivo injection 20 wt% hydrogel precursors were prepared by dissolving UPy-PEG (36 µmol, 400 mg), or UPy-RCPhC1 (2.53 µmol, 140 mg) and UPy-PEG (23.2 µmol, 260 mg) in 1.6 mL basic PBS (pH 11.7, adjusted with 1 M NaOH) at 70 °C until fully dissolved after approximately 1h. After dissolving, the pH was adjusted to 9 and stored in the fridge until the following day. The following day, UPy-DOTA compound (1.7 µmol, 2.5 mg) was dissolved at 2 mg/mL in acetate buffer (pH 4 - 5) at 50 °C for 30 min. The radioactive isotope indium-111-chloride (107 MBq, Curium, Petten, the Netherlands) was added to the UPy-DOTA dissolved in acetate buffer. This was kept at 70 °C for 1h, after which the chelation efficiency was examined. The chelation efficiency varied from 97 – 99%, determined by radio-HPLC and iTLC. After chelation, the pH was adjusted to 9 using a 5 M, 1 M NaOH solution. This was then added to the hydrogel precursor solutions, where fluorescently labelled UPy-Cy5 (25 nmol, 47 µg) from a DMSO stock solution (1 mg/mL) was added .The weight percentage was adjusted to 10wt% using basic PBS (pH 9). This was stored overnight in the fridge in the dark until injection the following morning. After loading of the six syringes (approximately 200 µL each), the exact activity per syringe was quantified using the dose calibrator.

Preparation of non-radioactively labelled hydrogel

One day prior to measuring, the hydrogel precursor solutions were prepared by dissolving UPy-PEG (40 mg, 3.6 µmol), or (14 mg, 0.25 µmol) and UPy-PEG (26 mg, 2.3 µmol) at 20 wt% in basic PBS (pH 11.7) at 70 °C until fully dissolved after approximately 1h. UPy-DOTA compound (0.25 mg, 0.17 µmol) was dissolved in acetate buffer (2 mg/mL, pH 4 – 5) at 50 °C for 30 min, after which indium-^{113}-chloride (37.3 µg, 0.17 µmol) was added to the acetate buffer and kept at 70 °C for 1h. The chelation was confirmed by reversed-column LC-MS. After chelation, the pH was adjusted to 9 using 5M NaOH and 1м NaOH solutions. This was added to the hydrogel precursor solution, where UPy-COOH (4.7 µg, 2.5 nmol), the non-fluorescent reference of UPy-Cy5, was added from a DMSO stock solution (1 mg/mL). The hydrogel precursor solution was adjusted to pH 9, at a final weight percentage of 11wt%. As control, UPy-PEG (40 mg, 3.6 µmol), or (14 mg, 0.25 µmol) and UPy-PEG (26 mg, 2.3 µmol) were dissolved in basic PBS (pH 11.7) at 70 °C until fully dissolved. The pH was adjusted to 9, and the final weight percentage was 11wt%. This was stored in the fridge until used the following morning. For the rheological measurements, hydrogel disks were made in cylindrical Teflon molds (diameter of 8 mm, height of 2 mm). Precursor gels (100 µL, pH 9) were pipetted in the molds, and of acidic PBS (10 µL, 13 mM HCl) was added, resulting in a final weight percentage of 10wt%. This was left to equilibrate for approximately 1.5h before measuring.

Rheological measurements

Rheological characterization of the hydrogels was performed on a discovery hybrid rheometer (DHR-3, TA Instruments), using a flat stainless-steel geometry with a diameter of 8 mm, with gap heights varying from 500 – 1000 µm. Low viscosity silicon oil (47 V 100, RHODORSIL®) was used around the hydrogel to limit evaporation during measurements at 37 °C. Frequency sweep measurements were performed at $\omega = 0.1$ rad/s to 100 rad/s, at a strain of $\gamma = 1\%$. Stress-relaxation was performed at a strain of $\gamma = 1\%$, over a time span of 500s, where the first 1s of measurement time was disregarded. This data was normalized using the highest stress generated from this point onwards. Strain-sweep measurements were performed at strains between $\gamma = 1$ and $\gamma = 1000\%$, with a frequency of $\omega = 1$ rad/s. Time sweeps of 60 s were performed in between measurements (data not shown), with a strain of $\gamma = 1\%$ and a frequency of $\omega = 1$ rad/s.

Animals and surgical procedure

Four Topigs Norsvin pigs (age ~ six months, weight 60-65 kg) received care in accordance with the guide for the care and use of laboratory pigs prepared by the Institute of Laboratory Animals. Experiments were approved by the Animal Experimentation Committee of the Medicine Faculty of the Utrecht University, the Netherlands. Sedation was mediated by intramuscular infusion of ketamine (10 mg/kg), midazolam (0.4 mg/kg), atropine (0.05 mg/kg), and intravenous injection of thiopental (4 mg/kg) via the cannulated ear vein. General anaesthesia was maintained by continuous infusion of cist-atracurium (0.1 mg/kg.hr), midazolam (0.4 mg./kg.hr), and sufentanil (2.5 μg./kg.hr) via the cannulated ear vein. A thoracotomy was performed to gain access to the epicardium and the apex was loosely fixed with a Starfish Cardiac Positioner (Medtronic, Minneapolis, MN, USA). Six hydrogel injections, with a total volume of 1.2 mL, were performed through a 25-gauge needle. The thorax was closed prior to the first scintigraphic scan.

Short-term in vivo tracking and quantification

To detect the ^{111}In label serial anterior and posterior total body scans were performed with a full field of view gamma scintillation camera with a medium energy general purpose (MEGP) collimator (Philips Skylight Gamma Camera System Dual SPECT with Philips JETStream Workplace R3.0). Photopeak windows of 20% were set at 174-274 keV. With a scan speed of 10 cm/min total body scans were made with a matrix of 512x1024. For static scans of the isolated organs a scan time of 300 seconds per scan were used and a matrix of 256x256. The images were quantified by identifying the heart, lungs, liver, spleen, kidneys and bladder in the anterior and posterior cumulative 174 and 274 keV images as 2D regions of interest (ROI) and determining the total number of counts and pixels per ROI. The square root of the total number of counts from the ROI obtained from the anterior total body scan and the ROI obtained from the posterior total body scan determined the geometric mean of the counts as described by Stratton et al.[31] The geometric mean of the total body ROI was identified as the 100% value to determine the % uptake of the ^{111}In signal in each organ.

Histological analysis

For immunostaining, hearts were snap frozen and cut into 10 μm sections. Fixation of the tissue was mediated by incubation in 100% Acetone for 10 minutes at 4 °C for 10 minutes before permeabilization for 10 min in 1% Triton X-100 in PBS. Heart tissue was then blocked for 1 hour in 10% normal whole goat serum (Vector laboratories S-1000-20) in PBS. Sections were stained overnight at 4 °C with sarcomeric α-actinin (Sigma Aldrich A7811) after which 1 hour incubation with secondary antibody conjugated with Alexa Fluor 488 in combination with nuclear marker Hoechst (Life Technologies 33342) was performed. Sections were then mounted in Fluoromount-GTM (ThermoFischer Scientific 00-4958-02) before imaging with SP8x Leica confocal microscope.

Statistical analysis

The in vivo data are expressed as individual animals as the sample size was $n=2$ per group. Statistical analysis was performed per group in which the individual datapoints per scan were compared and evaluated with a paired students t-test to compare the biodistribution values at the different timepoints past injection per hydrogel. Data analysis was performed using GraphPad Prism version 8.0.0 for Mac OS X, GraphPad Software, San Diego, California USA, www.graphpad.com. $P<0.05$ was considered statistically significant.

References

1 Y. Matsui, J. Morimoto and T. Uede, *World J. Biol. Chem.*, 2010, **1**, 69–80.

2 D. A. M. Feyen, P. Van Den Hoogen, L. W. Van Laake, E. C. M. Van Eeuwijk, I. Hoefer, G. Pasterkamp, S. A. J. Chamuleau, P. F. Grundeman, P. A. Doevendans and J. P. G. Sluijter, *Eur. Heart J.*, 2017, **38**, 184–186.

3 A. Hasan, A. Khattab, M. A. Islam, K. A. Hweij, J. Zeitouny, R. Waters, M. Sayegh, M. M. Hossain and A. Paul, *Adv. Sci.*, 2015, **2**, 1500122.

4 L. M. Stapleton, A. N. Steele, H. Wang, H. Lopez Hernandez, A. C. Yu, M. J. Paulsen, A. A. A. Smith, G. A. Roth, A. D. Thakore, H. J. Lucian, K. P. Totherow, S. W. Baker, Y. Tada, J. M. Farry, A. Eskandari, C. E. Hironaka, K. J. Jaatinen, K. M. Williams, H. Bergamasco, C. Marschel, B. Chadwick, F. Grady, M. Ma, E. A. Appel and Y. J. Woo, *Nat. Biomed. Eng.*, 2019, **3**, 611–620.

5 J. Li and D. J. Mooney, *Designing hydrogels for controlled drug delivery*, 2016, vol. 1.

6 L. L. Wang, Y. Liu, J. J. Chung, T. Wang, A. C. Gaffey, M. Lu, C. A. Cavanaugh, S. Zhou, R. Kanade, P. Atluri, E. E. Morrisey and J. A. Burdick, *Nat. Biomed. Eng.*, 2017, **1**, 983–992.

7 J. W. Wassenaar, R. Gaetani, J. J. Garcia, R. L. Braden, C. G. Luo, D. Huang, A. N. DeMaria, J. H. Omens and K. L. Christman, *J. Am. Coll. Cardiol.*, 2016, **67**, 1074–1086.

8 S. B. Seif-Naraghi, J. M. Singelyn, M. A. Salvatore, K. G. Osborn, J. J. Wang, U. Sampat, O. L. Kwan, G. M. Strachan, J. Wong, P. J. Schup-Magoffin, R. L. Braden, K. Bartels, J. A. DeQuach, M. Preul, A. M. Kinsey, A. N. DeMaria, N. Dib and K. L. Christman, *Sci. Transl. Med.*, 2013, **6**, 247–253.

9 J. H. Traverse, T. D. Henry, N. Dib, A. N. Patel, C. Pepine, G. L. Schaer, J. A. DeQuach, A. M. Kinsey, P. Chamberlin and K. L. Christman, *JACC Basic to Transl. Sci.*, 2019, **4**, 659 LP – 669.

10 A. S. Carlini, R. Gaetani, R. L. Braden, C. Luo, K. L. Christman and N. C. Gianneschi, *Nat. Commun.*, 2019, **10**, 1735.

11 S. Dobner, D. Bezuidenhout, P. Govender, P. Zilla and N. Davies, *J. Card. Fail.*, 2009, **15**, 629–636.

12 M. C. Ciuffreda, G. Malpasso, C. Chokoza, D. Bezuidenhout, K. P. Goetsch, M. Mura, F. Pisano, N. H. Davies and M. Gnecchi, *Acta Biomater.*, 2018, **70**, 71–83.

13 R. Waters, P. Alam, S. Pacelli, A. R. Chakravarti, R. P. H. Ahmed and A. Paul, *Acta Biomater.*, 2018, **69**, 95–106.

14 E. T. Roche, C. L. Hastings, S. A. Lewin, D. E. Shvartsman, Y. Brudno, N. V Vasilyev, F. J. O'Brien, C. J. Walsh, G. P. Duffy and D. J. Mooney, *Biomaterials*, 2014, **35**, 6850–6858.

15 C. L. Hastings, E. T. Roche, E. Ruiz-Hernandez, K. Schenke-Layland, C. J. Walsh and G. P. Duffy, *Adv. Drug Deliv. Rev.*, 2015, **84**, 85–106.

16 P. S. Patrick, J. C. Bear, H. E. Fitzke, M. Zaw-Thin, I. P. Parkin, M. F. Lythgoe, T. L. Kalber and D. J. Stuckey, *Biomaterials*, 2020, **243**, 119930.

17 A. Ahmadi, S. L. Thorn, E. I. Alarcon, M. Kordos, D. T. Padavan, T. Hadizad, G. O. Cron, R. S. Beanlands, J. N. DaSilva, M. Ruel, R. A. deKemp and E. J. Suuronen, *Biomaterials*, 2015, **49**, 18–26.

18 M. M. C. Bastings, S. Koudstaal, R. E. Kieltyka, Y. Nakano, A. C. H. Pape, D. A. M. Feyen, F. J. van Slochteren, P. A. Doevendans, J. P. G. Sluijter, E. W. Meijer, S. A. J. Chamuleau and P. Y. W. Dankers, *Adv. Healthc. Mater.*, 2014, **3**, 70–78.

19 P. Y. W. Dankers, T. M. Hermans, T. W. Baughman, Y. Kamikawa, R. E. Kieltyka, M. M. C. Bastings, H. M. Janssen, N. A. J. M. Sommerdijk, A. Larsen, M. J. A. Van Luyn, A. W. Bosman, E. R. Popa, G. Fytas and E. W. Meijer, *Adv. Mater.*, 2012, **24**, 2703–2709.

20 N. C. C. Zhijie Wang, Mark J. Golob, in *Viscoelastic and Viscoplastic Materials*, 2016.

21 M. H. Bakker, C. C. S. Tseng, H. M. Keizer, P. R. Seevinck, H. M. Janssen, F. J. Van Slochteren, S. A. J. Chamuleau and P. Y. W. Dankers, *Adv. Healthc. Mater.*, 2018, **7**, 1–8.

22 S. I. S. Hendrikse, S. P. W. Wijnands, R. P. M. Lafleur, M. J. Pouderoijen, H. M. Janssen, P. Y. W. Dankers and E. W. Meijer, *Chem. Commun.*, 2017, **53**, 2279–2282.

23 J. C. Garbern, E. Minami, P. S. Stayton and C. E. Murry, *Biomaterials*, 2011, **32**, 2407–2416.

24 C.-H. Chen, M.-Y. Chang, S.-S. Wang and P. C. H. Hsieh, *Am. J. Physiol. Circ. Physiol.*, 2014, **306**, H1078–H1086.

25 M. Bonios, J. Terrovitis, C. Y. Chang, J. M. Engles, T. Higuchi, R. Lautamäki, J. Yu, J. Fox, M. Pomper, R. L. Wahl, B. M. Tsui, B. O'Rourke, F. M. Bengel, E. Marbán and M. Roselle Abraham, *J. Nucl. Cardiol.*, 2011, **18**, 443.

26 S.-H. Li, T. Y. Y. Lai, Z. Sun, M. Han, E. Moriyama, B. Wilson, S. Fazel, R. D. Weisel, T. Yau, J. C. Wu and R.-K. Li, *J. Thorac. Cardiovasc. Surg.*, 2009, **137**, 1225–1233.

27 H. Dongming, Y. E. Al-Shaykh, B. T. J., Z. Ping, R. Pamela, E. T.Price, A. C. Yueng, B. H. Johnstone, P. G. Yock and K. L. March, *Circulation*, 2005, **112**, I-150–I-156.

28 P. Menasche, *Nat. Rev. Cardiol.*, 2018, **15**, 659–671.

29 I. de Feijter, O. J. G. M. Goor, S. I. S. Hendrikse, M. Comellas-Aragonès, S. H. M. Söntjens, S. Zaccaria, P. P. K. H. Fransen, J. W. Peeters, L.-G. Milroy and P. Y. W. Dankers, *Synlett*, 2015, **26**, 2707–2713.

30 S. Spaans, P.-P. K. H. Fransen, M. J. G. Schotman, R. van der Wulp, R. P. M. Lafleur, S. G. J. M. Kluijtmans and P. Y. W. Dankers, *Biomacromolecules*, 2019, **20**, 2360–2371.

31 J. R. Stratton, P. J. Ballem, T. Gernsheimer, M. Cerqueira and S. J. Slichter, *J. Nucl. Med.*, 1989, **30**, 629–637.

7

Supramolecular hydrogels as RNAi cardiac delivery systems

Abstract

MircoRNAs (miRNAs) are often dysregulated in human diseases, as is known for myocardial infarction (MI). The miRNA-15 family is, among others, highly upregulated during MI. Inhibition by complementary base pairing (antimiR complementation) can lead to reduction of infarct size, inhibiting cardiac remodeling, and enhancing cardiac function. Local delivery, to obtain high efficiency and limited side-effects, can be achieved using delivery systems, such as injectable hydrogels containing these RNAi therapeutics. The injectable ureido-pyrimidinone (UPy) based hydrogels were used as cardiac delivery vehicle of antimiRs. The bifunctional UPy-poly(ethyelene glycol) (BF UPy-PEG) and a cationic charged UPy-PEG were tested as antimiR delivery vehicles in a mouse model. The BF UPy-PEG containing the antimiR showed an enhanced cardiac derepression after an induced MI. Therefore, we proceeded towards a large animal model (porcine), displaying a high degree of similarities to the human myocardium, to examine the therapeutic effectiveness of the hydrogel in combination with the antimiR. The bifunctional UPy-PEG was combined with a human collagen type-1 based peptide, conjugated with UPy units, which was explored as an antimiR delivery system. This study unveils the efficacy of a UPy-based hydrogel as an RNAi delivery vehicle, revealing the clinical relevance of the hydrogel system in the field of cardiac therapy.

The content described in this chapter is partly based on:

J. E. C. Eding, M. Vigil-Garcia, M. Vink, C. Demkes, D. Versteeg, L. Kooijman, M. H. Bakker, M. J. G. Schotman, P. Y. W. Dankers, E. van Rooij, *Hydrogel-based delivery of antimiR-195 improves cardiac efficacy after ischemic injury*, in preparation

A. Cervera i Barea, M. J. G. Schotman, K. Neef, E. van Rooij, P. Y. W. Dankers, J. P. G. Sluijter, *A hydrogel-based RNAi delivery system to improve cardiac efficacy after myocardial infarction,* in preparation

1. Introduction

RNA interference (RNAi) is a natural occurring process with small RNA molecules inducing inhibition of target gene expression or protein translation by complementary binding.[1] Small non-coding RNAs (20-30 nt), microRNAs (miRNAs) or small interfering RNAs (siRNAs), assemble into RNA-induced silencing complexes (RISCs), that can bind to target transcripts and repress the target or trigger their degradation.[2] About two decades ago this was shown for the first time in mammalian cells by Elbashir et al., using an exogenous siRNA that could specifically suppress genes in different mammalian cells.[3]

miRNAs can regulate multiple target genes by specific sequence hybridization of messenger RNAs (mRNAs), which do not require perfect complementarity.[4] A single miRNA can therefore regulate multiple mRNAs. Dysregulation of these miRNAs can be found in numerous diseases, making them interesting candidates for therapeutic use or targets of therapeutics.[5]

Van Rooij et al. found that dysregulation of certain miRNA expression contributes to heart disease.[6] During cardiac hypertrophy, certain miRNAs families were upregulated, leading to cardiac failure.[7][8][9] Manipulation of miR-208 expression could potentially enhance cardiac function, which has a significant influence on the cardiac stress response and regulation of several miRNAs in the diseased heart.[10]

However, these small non-coding RNAs are unstable in serum due to the high degradation rate by serum nucleases, resulting in a short half-live in vivo.[11] Chemical modification of the small RNAs can lead to a significant increase in stability, e.g. by introducing locked nucleic acid (LNA) modification, a phosphorothioate backbone linkage at the 3' end for exonuclease resistance, or increasing the endonuclease resistance by 2' modification.[11] Furthermore, an RNA-modified complex containing the 4'-thioribose modification showed a stability of 600 times greater than natural RNA.[12]

A miRNA family is a group of miRNAs derived from a common ancestor, often showing similar physiological functions.[13] One miRNA family that is upregulated in the ischemic region during ischemic damage is the miR-15 family (containing the same seed sequence), i.e. miR-15a, miR-15b, miR-16-1, miR-16-2, miR-195, and miR-497.[14][15] Inhibition of these miRNA can be performed by chemically modified antisense oligonucleotides, complementary to the miRNA (antimiRs). This can inhibit the miRNA by complementary binding.[16] Using an LNA/DNA-mixmer complementary base-pairing antimiR (antimiR-195, Figure 7.1), miR-16 and miR-195 can be inhibited in ischemic hearts, reducing infarct size, inhibiting cardiac remodeling, and enhancing cardiac function.[14]

Cholesterol-conjugation to a small RNA molecule can increase the cellular internalization, due to its biological role supporting the cellular membrane structure and fluidity.[17] To increase the local delivery of RNAi therapeutics, lipid vesicles[18], as well as hydrogels[19] are often used. Bakker et al. showed that the ureido-pyrimidinone (UPy)-based hydrogel is applicable as an RNAi delivery system, with a cholesterol-modified RNAi moiety showing a sustained release, as well as increasing the positive-charge density of the hydrogel.[20] Furthermore, Wang et al. showed a miRNA-release system based on a hyaluronic acid hydrogel, modified with β-cyclodextrin and adamantane which initiates gelation based on host-guest interactions.[21]

MiR-302, known to promote cardiomyocyte proliferation after myocardial infarction, was modified with a cholesterol group, to improve cellular uptake as well as sustain the release. Injection in an infarcted mouse hart led to an increase in cardiomyocyte proliferation, in comparison to injection of the miR-302 without the hydrogel carrier.

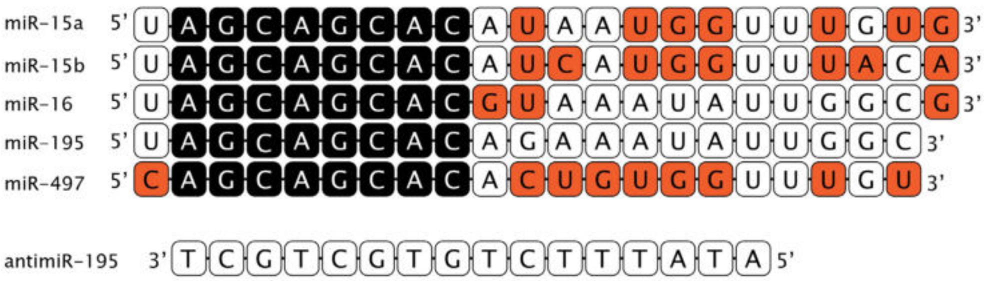

Figure 7.1 An overview of the miR-15 family, sharing a similar seed-sequence, and the antimiR-195. Image obtained from [22].

In this chapter, the compatibility of UPy-based hydrogels as RNAi delivery systems are explored (Figure 7.2). Efficacy of these systems was examined in an in vivo rodent model using two strategies, i.e. RNAi combined with either the pristine or cationic UPy-based hydrogel. The pristine hydrogel is composed of a poly(ethylene glycol) (PEG) chain, end-functionalized with two pH-responsive UPy units (BF UPy-PEG). By self-complementary four-fold hydrogen bonding, these UPy units dimerize in water. Alkyl-spacers between the UPy and PEG shields the UPy units from water, and additional urea moieties induce later stacking of this polymer into fibers. At gel concentration, the fibers crosslink and assemble, forming a dynamic network due to the reversibility of the interaction crosslinks. In a modular fashion, molecules containing UPy units can be introduced to the network, which can intercalate with the UPy-fibers of the BF UPy-PEG network.[20] Easy injection is facilitated by the pH-responsiveness of this system, with the four-fold hydrogen bonds being disrupted at basic conditions. This enables injection as basic conditions (pH >8.5), whereas gelation is initiated when the system in neutralized (in physiological conditions). The cationic UPy-based hydrogel is composed of the BF UPy-PEG in combination with a cationic UPy-additive (UPy-amine), which facilitates interaction of the encapsulated antimiR within the hydrogel network by electrostatic interactions. This leads to a sustained release of the animiR from the hydrogel. The safety of both hydrogels was tested by examining certain stress markers after in vivo cardiac injections in a mouse model. Furthermore, the efficacy of the BF UPy-PEG as antimiR-195 containing delivery system was explored by quantification of the target miR-16 and miR-195, as well as complementary gene targets. Moving towards a more representative clinical model, we describe the use of a bioactive variant of the UPy-based hydrogel, which is used as an RNAi delivery vehicle in a large animal model (porcine). The antimiR-195 therapy was encapsulated in a hydrogel based on the BF UPy-PEG, in combination with a collagen type-1 based hydrogel (RCPhC1) conjugated with UPy-moieties (described in chapter 3 and Chapter 6). The set-up of the porcine study is described, and several hydrogel properties are determined, i.e. rheological properties, release of the antimiR-195 from the hydrogel, and the effect of sterilization.

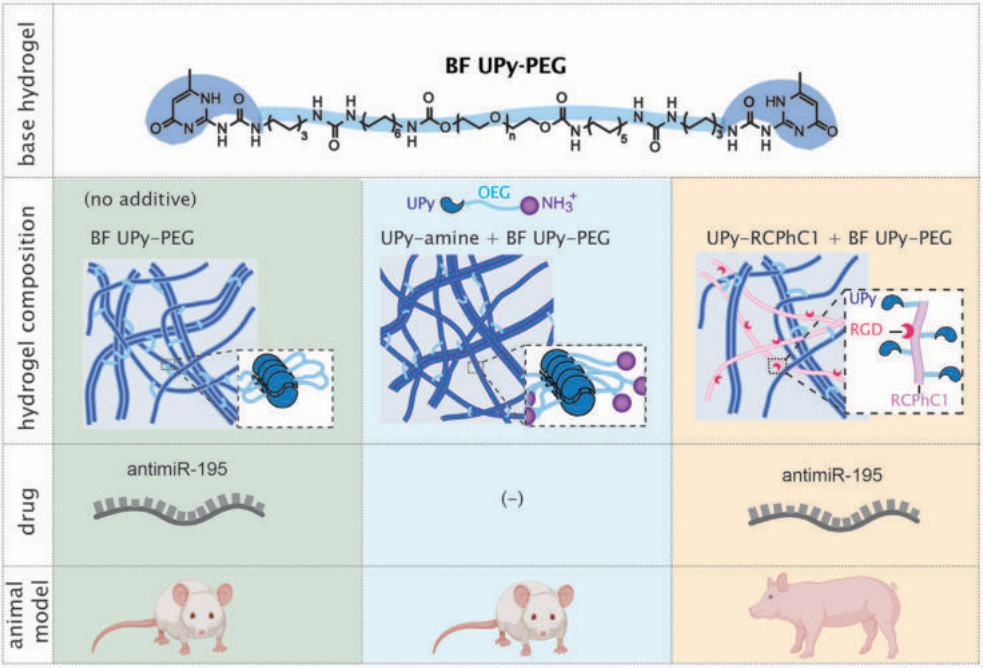

Figure 7.2 The in vivo injectates of the UPy-based hydrogels, with the BF UPy-PEG base hydrogel and the different hydrogel compositions, being cationic adapted UPy-based hydrogel, and the UPy-RCPhC1 hydrogel in combination with the BF UPy-PEG, with and without RNAi therapeutics. The type of animal model these were tested on is furthermore showed.

2. In vivo safety and efficacy in rodents

2.1 Study design

Two types of hydrogels were used in this study, being the pristine BF UPy-PEG hydrogel and a cationic charged UPy-based hydrogel (UPy-Cat), composed of the BF UPy-PEG and a UPy-amine. An increase in affinity between the antimiR-195 was proposed for the latter hydrogel, due to the electrostatic interactions between the anionic charged antimiR-195 and the cationic charged hydrogel.[20] Both hydrogels were first injected in healthy mice hearts (2 x 10 μL) to examine the safety (Figure 7.3A), containing no RNAi therapeutics. By echocardiography and tissue collection, fractional shortening and thickness of the anterior or posterior left ventricular wall (LVAW or LVPW) were determined 3 days and 7 days post-injection. The efficacy of antimiR-195 encapsulated in BF UPy-PEG was examined after the mice were subjected to 60 minutes of left anterior descending artery ligation, whereafter during reperfusion 2 intramyocardial injections (10 μL each) of PBS or BF UPy-PEG (pristine or antimiR-195 leaded) were given. By reverse transcription polymerase chain reaction (RT-PCR), target miRNAs and target genes were quantified.

2.2 Safety study

The safety of both hydrogels were tested by subjecting the mice to intramyocardial injections of the hydrogels, containing no RNAi therapeutics. No significant effects were shown upon injection of BF UPy-PEG, considering the echocardiographic results and the cardiac stress-and fibrosis markers. The UPy-Cat hydrogel caused an increase in thickness of left ventricular anterior wall and left ventricular posterior wall, as well as an increase in cardiac stress- and fibrosis markers (Figure 7.3B). A brief inflammatory response was observed after BF UPy-PEG injection, determined by RNA-sequencing (results not shown). This indicated a small transverse effect of the BF UPy-PEG, which can be caused by the difficulty of injecting in a fast-beating heart of the mouse, with the viscous fluid being troublesome to inject in such a small moving space. Due to the high increase of cardiac stress- and fibrosis markers observed after injection of the UPy-Cat, it was decided to continue the therapeutic efficacy studies with the BF UPy-PEG hydrogel.

2.3 Therapeutic efficacy study

The efficacy of the combined therapeutic delivery system (antimiR-195 and BF UPy-PEG hydrogel) was tested on mice after MI induction. PBS or BF UPy-PEG was injected directly after MI, either pristine or loaded with antimiR-195, with a total volume of 20 µL (2 times 10 µL, Figure 7.3C). AntimiR-195 injection (in PBS or BF UPy-PEG) showed a strong reduction of miR-16 and miR-195 levels (Figure 7.3D). The target cyclin D1 (Ccnd1) and vascular endothelial growth factor A (Vegfa) both showed upregulation for the antimiR in combination with PBS and BF UPy-PEG in combination with the antimiR group (Figure 7.3E). Proliferating cell nuclear antigen (PCNA) and Ki67 both show upregulation with the antimiR dissolved in PBS as well as in combination with the BF UPy-PEG, indicating cardiomyocyte proliferation (Figure 7.3F). This shows that the hydrogel-based delivery after MI enhances the effect of target inhibition and increases cardiomyocyte proliferation. However, the effect is not extensive, which could be due to the low in vivo retention of the BF UPy-PEG hydrogel, with no hydrogel remnants being observed in the cardiac area after 24 hours (Figure 7.3G). The dense myocardial tissue and high heart rate of the mice can play a significant role here. Furthermore, small animal models have higher basal metabolic rates and different physiology in comparison to humans.[23] Therefore, we proceeded towards a large animal model (porcine), displaying a high degree of similarities to the human cardiovascular physiology[24], to examine the therapeutic effectiveness of this carrier system.

3. Translation to large animal model

Findings in small animal models often do not translate into human clinical applications.[25] Zwetsloot et al. showed that treatment with cardiac stem cells led to a significant difference in the therapeutic effect post-MI between large and small animal models. Significant improvement of ejection fraction in both groups was observed, but there was a large reduction in the magnitude of the effect in large animals compared to small animal models.[26] This confirms the necessity of testing the efficacy on larger animals, with similar heart sizes, cardiac function, as well as coronary circulation when compared to humans.[27] The efficacy of antimiR-195 in combination with a hydrogel was therefore tested on porcine models. For the porcine animal studies, the BF UPy-PEG in combination with the UPy-RCPhC1 (UPy-PEG-RCPhC1) was used, which showed a retention of approximately 16% observed after 4h, whereas BF UPy-PEG showed a retention of 8% (Chapter 6). The introduction of UPy-RCPhC1 to the system is hypothesized to increase the bioactive properties of the hydrogel, therefore possibly increasing the retention after injection in the cardiac area due to tissue-adhering motifs. Thus, to examine the efficacy of an injectable hydrogel system in combination with the antimiR-195, the UPy-PEG-RCPhC1 was used.

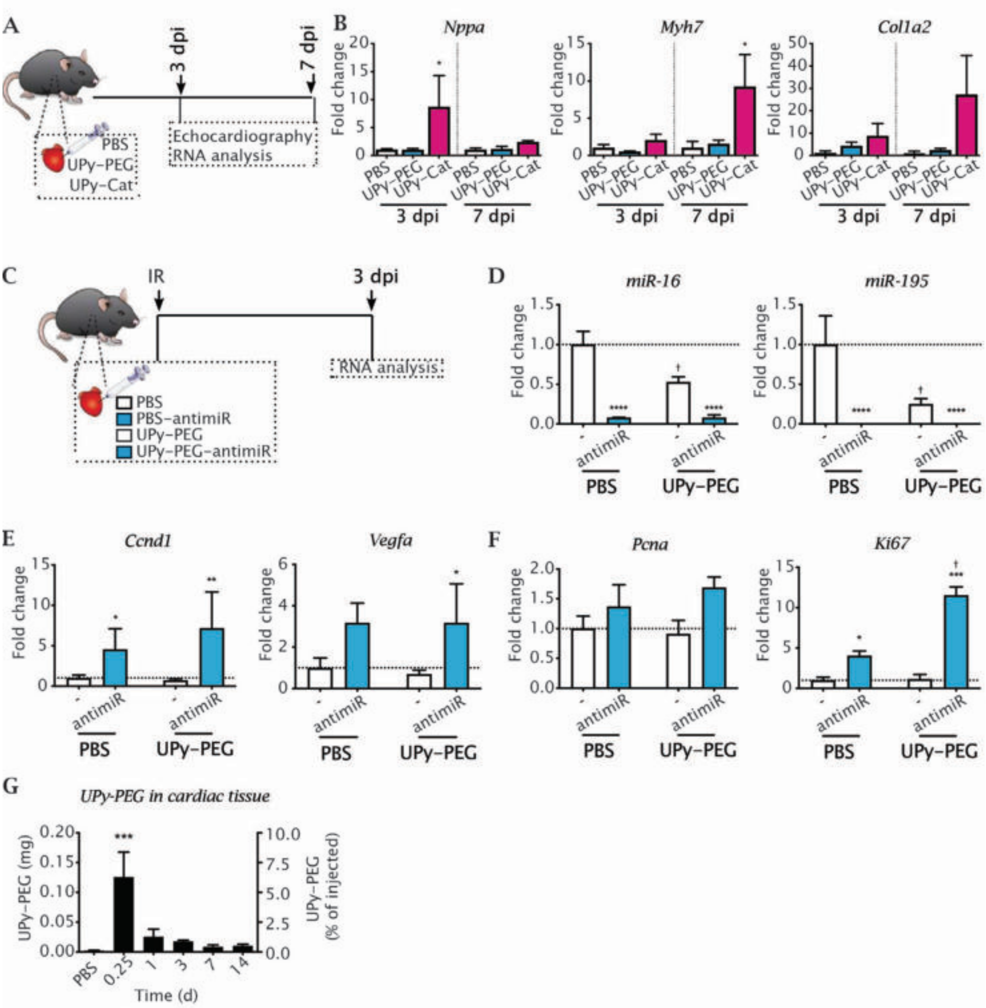

Figure 7.3 Intramyocardial injection of BF UPy-PEG and UPy-Cat with the schematic overview (A), the stress markers Nppa, Myh7, and fibrosis marker Colla2 determined by RT-PCR (B). A schematic overview of intramyocardial injection of PBS or BF UPy-PEG without or in combination with antimiR-195 (C), miR-16 and miR-195 quantification by RT-PCR (D), Ccnd1 and vegfa (E) and Pcna and Ki67 (F) quantification by RT-PCR,

and UPy-PEG determination in cardiac tissue after intramyocardial injection in a healthy mice heart over 14 days determined by anti-PEG ELISA quantification (G). Adapted from 22.

3.1 Study set-up

To assess the effect of the hydrogel in combination with antimiR, the therapy was injected in an acute MI model. In a pilot, pigs received either hydrogel, PBS in combination with antimiR, or hydrogel in combination with antimiR (n=3 for each condition). The selected therapy was injected after induction of a reperfusion injury (I/R injury), during which an artery branch of the left anterior descending was occluded for 75 minutes followed by 30 minutes of reperfusion (Figure 7.4). A total of 5 injection, 200 μL per injection, were delivered around the boarderzone of the infarcted area. Cardiac function was analyzed by echocardiography, determining factors such as the ejection fraction, fractional shortening, left ventricular end diastolic volume, left ventricular end systolic volume, among others. Furthermore, a heart monitor was placed (Reveal LINQ™), which continuously monitored the cardiac function. 28 days post-injection, the animals were terminated and further analysis was performed, e.g. histology of the infarcted area and RT-PCR quantification of selected target genes. The animal procedures and functional cardiac analysis were performed by blinded investigators.

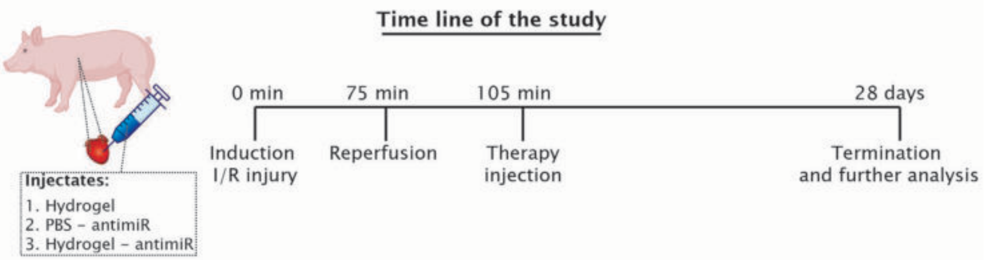

Figure 7.4 Time line and injectates used in the porcine study, where three different injectates were examined, being the hydrogel, PBS in combination with antimiR, and the hydrogel in combination with the antimiR. The I/R injury was induced at time 0 for 75 minutes, whereafter reperfusion took place for 30 minutes. After the reperfusion, the therapy was injected in the border zone of the infarcted area. 28 days post-injection, the porcine was terminated and the effectiveness of the therapy was examined by a variety of methods.

3.2 Rheological properties of UPy-PEG-RCPhC1 combined with antimiR-195

To examine the mechanical properties of the hydrogels upon addition of antimiR, rheology was performed. A frequency sweep and amplitude sweep were performed, which showed no significant differences in strength upon addition of antimiR. The frequency sweep showed gelation at a broad range of frequencies, with a G' (storage modulus) of approximately 3 kPa at low frequencies, which increased upon increasing frequencies, up to ~20 kDa at 100 rad/s (Figure 7.5A). An amplitude sweep showed a linear course of G' and G'' (loss modulus) until approximately 100% strain, whereafter the crossover point indicates the disruption of both hydrogels (Figure 7.5B). Altogether, the mechanical properties did not vary upon addition of antimiR to the UPy-PEG-RCPhC1 hydrogel, indicating that addition of antimiR showed to have no significant effect on the gelation properties of the hydrogel.

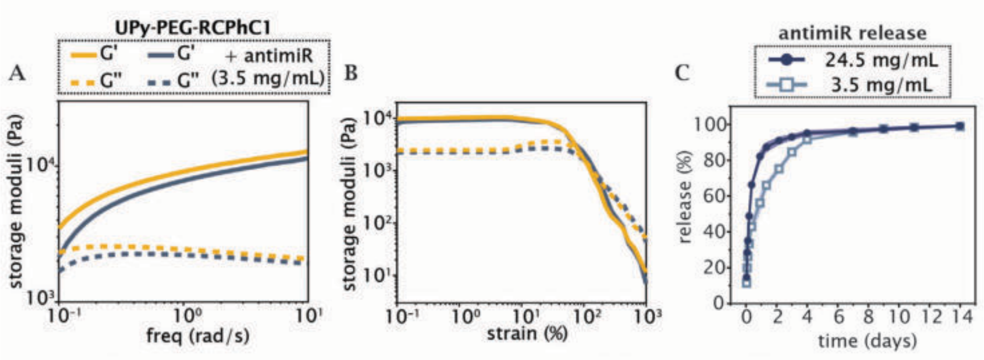

Figure 7.5 Mechanical properties of UPy-PEG-RCPhC1 hydrogels with and without the addition of anitmiR-195 (3.5 mg/mL), with the frequency sweep (A), the strain sweep (B) and the antimiR-195 release from the hydrogel at two different concentrations, being 3.5 and 24.5 mg/mL (C).

3.3 Release profile of antimiR-195 from the UPy-PEG-RCPhC1

Whilst RNAi therapeutics have been widely used for myocardial regeneration, the concentrations used varies widely with a range from approximately 1-30 mg per animal.[28-30] Extrapolation of the results obtained by van Rooij and co-workers can give insight in the optimal concentration regarding porcine studies. The most effective antimiR-195 dosage in the BF UPy-PEG hydrogel (with limited side-effects) was 70 µg, injected in a rodent. Conversion of dosages based on body surface have been shown to increase clinical trial safety by resulting in a conventional starting dose.[31] The factors that influence the scaling between animals are lower metabolic rates for larger animals, as well as slower physiological processes. This suggests that large animals require smaller drug dose based on weight.[32]

To further explore the properties of the hydrogel in which antimiR-195 is encapsulated, the release profile of the antimiR-195 from the hydrogel is examined in vitro. Two different concentrations of antimiR-195 are encapsulated that fall within the concentration range found in literature, being 3.5 mg/mL and 24.5 mg/mL, to clarify possible concentration dependency.

The hydrogel precursor (pH ~8.7) containing the antimiR was added in inserts with a semi-permeable membrane, which were put in a well containing PBS (pH 7.4) to be left to equilibrate to a neutral pH. The accumulative release was determined by refreshing the PBS solution at several predetermined time points. A molecular beacon was used for precise concentration determination of the antimiR. Here, a stem is designed with 5 complementary base pairs, functionalized with a fluorescent probe (6-FAM) and a quencher. The loop sequence is designed complementary to the antimiR-195 sequence, which will lead a disruption of the stem sequence and an enhanced fluorescent signal. The release was examined over a time span of 14 days, whereafter the hydrogel was dissolved and examined on antimiR remnants. A burst release of antimiR is observed for both concentrations, where a 50% release is obtained after approximately 5 and 15 hours for the 24.5 and 3.5 mg/mL, respectively (Figure 7.5C). There are many potential explanations for this burst release. The transition from the sol-state to the gel-state (pH 8.7 to neutral pH) is not instant, allowing the antimiR to move more freely in the viscous liquid. This increases the antimiR release when still in the sol-state. The swelling of the hydrogel can increase the pore-size, and therefore enhance mobility and release of the antimiR. Furthermore, the antimiR is highly water-soluble and is hypothesized to have a low affinity with the hydrogel network, as it is not anchored to the network by complementary binding. During the first days, a slightly slower release is observed at the lower concentration. These results indicate that, independent of concentration, a burst release will occur, and only small differences can be observed regarding the release of the two tested antimiR concentrations from the hydrogel.

Based on these findings as well as previous results obtained from the rodent studies, a similar concentration to the rodent study was selected (3.5 mg/mL, 1 mL total), being furthermore within the observed range found in literature.

3.4 Polymer sterilization

The hydrogel precursors (BF UPy-PEG as well as UPy-RCPhC1) were sterilized by ethylene oxide (EO), carried out by STERIS (Venlo, the Netherlands). ^{1}H-NMR spectra did not show significant differences between the BF UPy-PEG polymer before and after sterilization, with no additional peaks being observed after sterilization (Figure 7.8). Furthermore, the chromatogram did not show significant differences, indicating a molecular weight (M_n) of 2155 before, and 2031 after sterilization, showing no sign of degradation (Figure 7.6A). For the UPy-RCPhC1 polymer, the ^{1}H-NMR spectra showed no additional peaks after the sterilization process (Figure 7.9). The Qtof spectra showed similar chromatograms for the UPy-RCPhC1 polymer before and after sterilization (Figure 7.6B). Lastly, hydrogel precursors were prepared by mixing both polymers in basic PBS, with a final pH of approximately 8.7. The viscosity of the sterilized and non-sterilized hydrogels were examined, with viscosities of 0.58 Pa.s and 0.52 Pa.s on average for the non-sterile and the sterile hydrogel, respectively (Figure 7.6C). This shows no significant difference between both groups. These results indicate that the EO sterilization process has no adverse effect on the polymers and they remain stable.

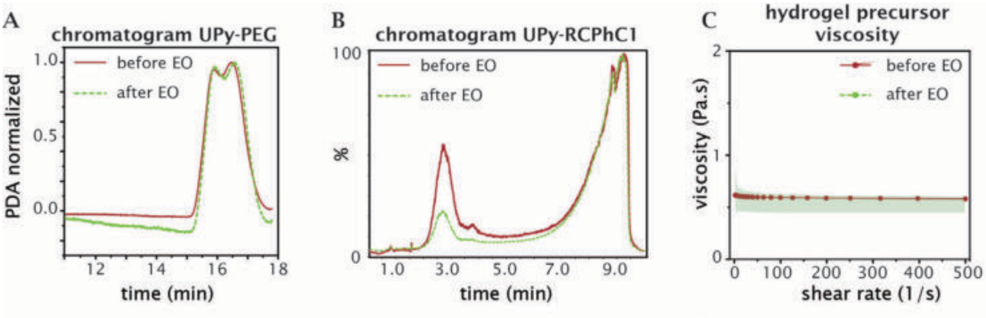

Figure 7.6 Characterization of BF UPy-PEG and UPy-RCPhC1 after sterilization, with an overlay of the chromatograms of BF UPy-PEG before (red) and after EO (green) (A), an overlay of the chromatogram of UPy-RCPhC1 before (red) and after EO (green) (B), and overlay of the viscosities at a pH of ~8.7 of the hydrogel precursors before (red) and after EO (green) (C), data is represented as ±SD, n=2.

3.5 Viscosity change after preparation

The viscosity of the UPy-PEG-RCPhC1 hydrogel is of great importance for the injectability and handling of the hydrogel, with higher viscosity leading to a more troublesome syringe loading and injection (due to a higher resistance of the hydrogel). Therefore, the viscosity as well as the pH (known to be of influence on the viscosity), is examined after preparation of the hydrogel over a time span of several days. The viscosity of the hydrogel increases significantly over time (Figure 7.7), with a viscosity of approximately 0.65 Pa.s at shear rate of 50 s^{-1} at day one, whereas after three days the viscosity is approximately 0.79 Pa.s at a shear rate of 50 s^{-1}. At five and eight days after preparation, the viscosity is further increased to 0.92 Pa.s and 1.35 Pa.s at a shear rate of 50 s^{-1}, respectively. The pH remains relatively stable over time. The frequency sweep and relaxation time show that the hydrogel network displays dynamic properties. This can indicate structural rearrangement over time, with a higher crosslink density being obtained due to continuous rearrangement. These results show the importance of the duration between preparation and injection, with the viscosity of the hydrogel increasing steadily over time. Therefore, for further experiments the time between preparation and injection is kept constant.

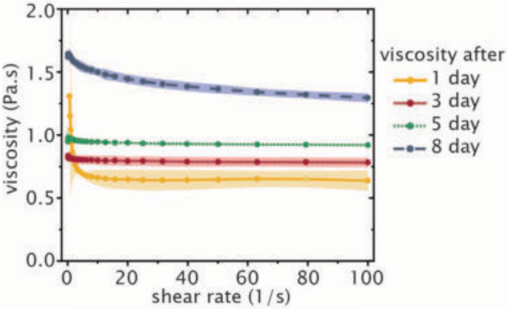

Figure 7.7 Viscosity measurements of UPy-PEG-RCPhC1 in the sol-state prepared at a pH of ~8.7, with the time-points of examination being 1, 3, 5, and 8 days after preparation.

4. General discussion

This study demonstrates the design and applicability of supramolecular hydrogels as RNAi drug carriers in the field of cardiac regeneration. The safety and efficacy of two types of UPy-based hydrogels were examined in a rodent model, being the BF UPy-PEG and the UPy-Cat hydrogel. Rodents are easy in handling, and have low maintenance costs in comparison to larger animals. The in vivo response to injectate therapeutics can therefore be screened in rodent models as a first step towards clinical applications.[24] The UPy-Cat hydrogel displayed a sustained release of the RNAi therapy due to electrostatic interactions between the cationic charges present in the hydrogel, and anionic charges of the RNAi drug.[20] This hydrogel displayed adverse cardiac response in a healthy mouse heart, revealing the side-effect of introducing a positively-charged system in an in vivo model. The BF UPy-PEG hydrogel in combination with the antimiR-195 displayed a small enhancing effect on target inhibition and increase of cardiomyocyte proliferation. This model enabled an initial screening of the safety and efficacy of the hydrogel, taking a step towards clinical translation. While numerous of studies describe the efficacy of a drug encapsulated in a hydrogel tested on a rodent model[33-35], the effects it will have on a large animal or human heart is difficult to predict.

Large animal models display a high degree of similarities in comparison to the human myocardium, as shown in porcine models. A porcine coronary model is often used for studying cardiovascular diseases, with similar coronary artery system to human coronary arteries, as well as similar diagnostic and interventional equipment being utilized.[36] Therefore, there is a necessity in examining the hydrogel in larger animal models.

Further efficacy of the UPy-based hydrogel and RNAi therapy was performed on porcine models. Here, the BF UPy-PEG in combination with the UPy-RCPhC1 (UPy-PEG-RCPhC1) was used as a therapeutic RNAi carrier. This hydrogel showed an approximate cardiac retention of 16% after injection in a healthy porcine heart (Chapter 6). The introduction of UPy-RCPhC1 to the system was hypothesized to increase the retention after injection, due to tissue-adhering motifs present in the peptide backbone. The retention of the UPy-PEG-RCPhC1 hydrogel in combination with the RNAi therapeutics, after injection in an infarcted cardiac porcine model, is hypothesized to be similar as displayed in a healthy porcine heart.

The timing of therapeutic injection after MI is clinically relevant, which was examined by several studies.[37-39] Here, the therapeutic injections take place directly after MI induction. This increases the animal welfare, with the number of necessary anesthesia being lower in comparison to delayed therapy. However, this excludes the examination of deferred therapy, in which days or weeks post-infarction, therapy is administered. Injection during the inflammatory phase (~0-7 days post-infarction) is hypothesized to increase the hydrogel degradation, due to the collagenase and gelatinase activity being highly upregulated.[40] Furthermore, at the early stages of the inflammatory phase, the myocardial interstitial is still well preserved, which modifies further over time.[41] The myocardium is therefore still quite dense, which upon injection is hypothesized to give the hydrogel a more spread-out character between these fibrillar bundles of interstices.[38] Injection during the proliferating phase (~7-28 days) can limit the ECM remodeling and stimulate the infarct repair, before extensive scar thinning and non-reversible dilation occurs.[42,43] Furthermore, after an acute infarct the border zone of the infarct is less facile to locate, with only slight differences in color between healthy and infarcted tissue. During the studies, experienced technicians could frequently locate the infarcted area by eye. The extent of the infarct was intermittently difficult to observe, with the therapeutic injections being placed in the border zone, which is the optimum location for therapeutic injection for contact with viable myocardium.[44]

Many reports in literature further describe the high cellular redistribution accumulating in the lungs after cardiac injection, due to the high microvasculature and capillary system[45,46] (as also shown in Chapter 6). Possible side-effects that can result from myocardium injectate therapy should be taken into account, with the therapy content redistributing to the microvasculature of the lungs causing off-target effects.

Other studies report varying concentrations of RNAi therapeutics, with concentrations ranging from 1 to 30 mg per animal.[28-30] An additional study to optimize the concentration applicable for a porcine model could give further insight in the effectiveness considering RNAi therapeutics. However, due to restrictions in time and the extensiveness of the study, a concentration was used, which was translated from the mice study. This concentration falls in the range found in literature.

While the current study was performed by injecting the hydrogels transepicardial at 5 different locations, after a thoracotomy, for future studies a less invasive manner of injection is aspired, i. e. by catheter in a transendocardial manner. By actively tracked real-time magnetic resonance (MR) guidance, the catheter location from tracking coils present in the tip of the catheter can be visualized in vivo, and a high resolution 3D anatomical 'roadmap' scan can place the catheter tip in this roadmap.[47] This enables accurate transendocardial injections to be placed in the myocardium, which was shown to be feasible with the BF UPy-PEG based hydrogel. A supramolecular label was added to the hydrogel with a gadolinium-moiety to enable MR visualization in vivo after injection.[48] This shows the applicability of minimal invasive delivery of the UPy-based hydrogel.

5. Conclusion

In this work, we showed the applicability of UPy-based supramolecular hydrogels as RNAi delivery systems for cardiac therapy. In mice, a small increase in functional output with an enhanced effect of target inhibition and increase of cardiomyocyte proliferation was observed for the BF UPy-PEG combined with RNAi, upon injection in an infarct. Translation towards large animal studies are important to further elucidate the efficacy of the UPy-based hydrogels as RNAi delivery system. Here, a more bioactive variant of the supramolecular hydrogel, being UPy-RCPhC1 in combination with the BF UPy-PEG, was tested as an RNAi therapeutic delivery vehicle in a porcine heart, which is hypothesized to increase the functional cardiac output in comparison to only the RNAi therapeutics. This supramolecular delivery system is envisioned to display advantages over current cardiac therapeutics, i.e. displaying increased functional cardiac output, with only one surgical procedure necessary, and a less invasive potential use by delivery through a catheter.

Experimental section

Materials

All reagents, chemical, materials and solvents were obtained from commercial sources and were used as received. FujiFilm Manufacturing Europe B.V. kindly provided us the Cellnest, a recombinant peptide based on human collagen type I (RCPhC1), which was used without further purification. The antimiR-195 was kindly provided by prof. dr. Eva van Rooij. Molecular beacon was ordered (IDT, USA) with the following structure: 56-FAM/CAT GCA GCA GCA CAG AAA TAT GCA TG/3IABkFQ. The molecular beacon (MB) was aliquoted and stored at -30 °C in 10 mM Tris-HCl, 1 mM EDTA (MB) buffer prepared with nuclease free water (Sigma Aldrich), pH 8 at a concentration of 100 μM. The molecular beacon solution was thawed before used. For dilution of the supernatant release solution to determine the antimiR quantity, a magnesium (Mg) buffer was prepared, containing 10 mM Tris-HCl 11.5 mM $MgCl_2$, prepared with nuclease free water.

Instrumentation

MiliQ water was purified on an EMD Milipore Mili-Q integral Water Purification System. Reverse-phase high-performance liquid chromatography-mass spectrometry (RP-HPLC-MS) was performed on a Thermo scientific LCQ fleet spectrometer. ^{1}H-NMR spectra were recorded on a Varian Mercury Vx 400 MHz or Varian 400MR 400 MHz spectrometers. Gel permeation chromatography (GPC) was performed on a Shimadzu Prominence-I GPC system, equipped with a differential refractive index detector, equipped with a PL gel 5 µm mixed D column (Polymer Laboratories) and THF as an eluent at a flow rate of 1 mL/min to examine the purity of the BF UPy-PEG moiety before and after sterilization. Waters Xevo G2 Quadrupole Time of Flight (QToF) Liquid Chromatography - Mass Spectrometry equipped with an Agilent Polaris C18A reverse phase column was used to examine the purity of the UPy-RCPhC1 derivative before and after sterilization. Rheological measurements were performed on an Anton Paar Physica MCR501 rheometer, equipped with a P-PTD 200 evaporation blocker to prevent sample drying to examine the gelation as well as the viscosity of the gel state UPy-PEG-RCPhC1 solution before and after sterilization. Fluorescence measurements of the molecular beacon was performed on a Spark M10 multimode plate reader.

Hydrogel preparation

The BF UPy-PEG with M_n,PEG = 10 kg/mol, was synthesized by SyMO-Chem BV, Eindhoven, The Netherlands. Brief synthetic procedures of BF UPy-PEG and UPy-RCPhc1 can be found in Chapter 6. A total amount of 30 mg of the UPy-RCPhC1-5 and UPy-PEG were weighted at a molar ratio of 1 : 9 (10.5 mg, 195 nmol UPy-RCPhC-5; 19.5 mg, 1740 nmol UPy-PEG). Basic PBS was added at 11 wt% (243 µL, pH 12, adapted with 1 M NaOH) and the compounds are dissolved at 70 °C for 1 hour. For rheological measurements, hydrogel disks were made in cylindrical Teflon molds (diameter of 8 mm, height of 2 mm). Precursor gels (100 µL) were pipetted in the molds, and acidic PBS (10, µL 13 mM HCl) was added, resulting in a final weight percentage of 10wt%. This was left to equilibrate for approximately 1.5h before measuring. A plate-plate geometry was used (8 mm diameter), using a gap distance of 1mm.

Rheological measurements

A plate-plate geometry (PP08, 8 mm diameter) was used for to measure the UPy-PEG-RCPhC1 hydrogels with a gap size of 1 mm. The storage and loss moduli were recorded as a function of angular frequency (0.1 - 100 rad/s), of which 0.1 - 10 rad/s was plotted in a graph at 1% strain, as a function of strain (1-1000%) at 1 rad/s, and recovery at 1% strain, and 1 rad/s. Measurements were performed in duplicate, of which one measurement was plotted. The viscosity was determined using the cone plate geometry (25 mm, 1°) at a measuring distance of 49 µm. The UPy-PEG-RCPhC1 in sol state was pipetted on the plate and the sample was trimmed after lowering the cone plate geometry. The samples were measured at room temperature, and the viscosity was measured at different strain points, with an increasing logarithmic strain slope of 0.1 to 100 s^{-1}. The viscosity was measured 1, 3, 5, and 8 days after preparation. After preparation and in between measurements, the hydrogelator was stored in the fridge at a temperature of 7 °C. Measurements were performed in duplicate.

AntimiR release measurements

The desired quantities of antimiR was pipetted into the viscous liquid precursor UPy-PEG-RCPhC1 solution (pH ~8.7), that was adjusted to a final wt% of 10. This was stirred for an additional 15 minutes after antimiR addition. The hydrogel precursors were then pipetted with a volume of 100 µL in Millicell plate inserts (for 24-well plate, 8 µm pore size), and put in a 24-well plate with neutral PBS (600 µL). Empty wells were filled with miliQ to prevent the gels from drying out and the plate was sealed off with parafilm and put in an oven at 37 °C. At set time points, the PBS was refreshed analyzed for antimiR content. The antimiR concentration was determined by taking the supernatant PBS solution and diluting it 10 and 25x (with Mg buffer) for the 3.5 and 24.5 mg/mL, respectively. The molecular beacon was added to the supernatant dilution (1 µM concentrations in MB buffer) at a 1:1 v/v ratio. The concentrations were determined by predetermined calibration curves, and each condition was performed in triplicate.

Sterilization

Sterilization of the polymers was performed by STERIS (Venlo, the Netherlands). The polymers were placed in 12 mL glass vials in predetermined weight, so that weighing after sterilization was not necessary. The vials were placed in sterilisation pouches, with the cap on loosely, so that the gas can infiltrate the polymer. After sterilisation, intactness of the polymers is examined by ^{1}H-NMR spectroscopy, GPC, quadrupole time-of-flight LC/MS (Qtof), and rheology for viscosity examination.

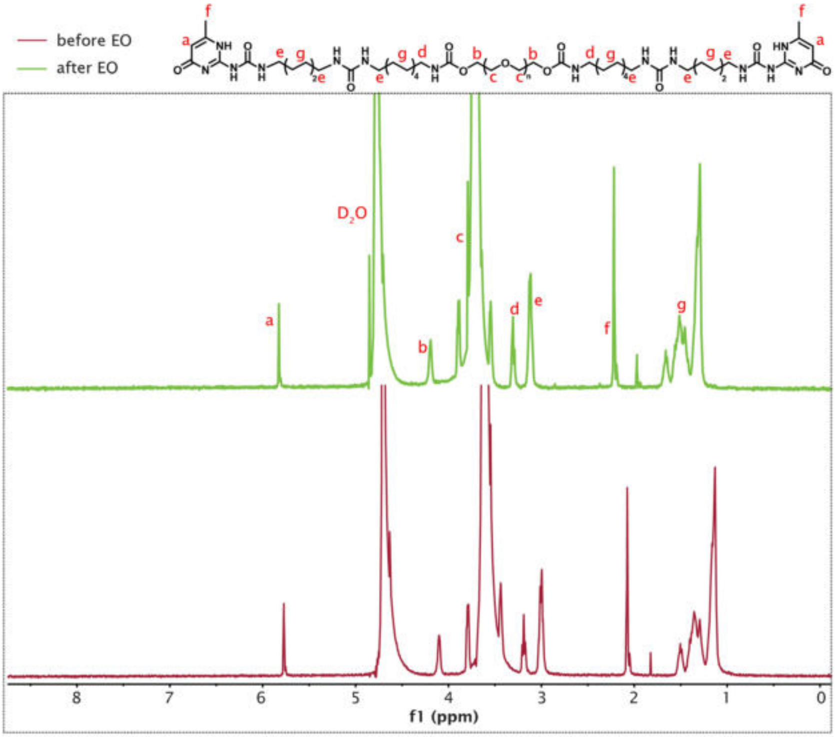

Figure 7.8 ^{1}H-NMR characterization of UPy-PEG before (red) and after (green) sterilization.

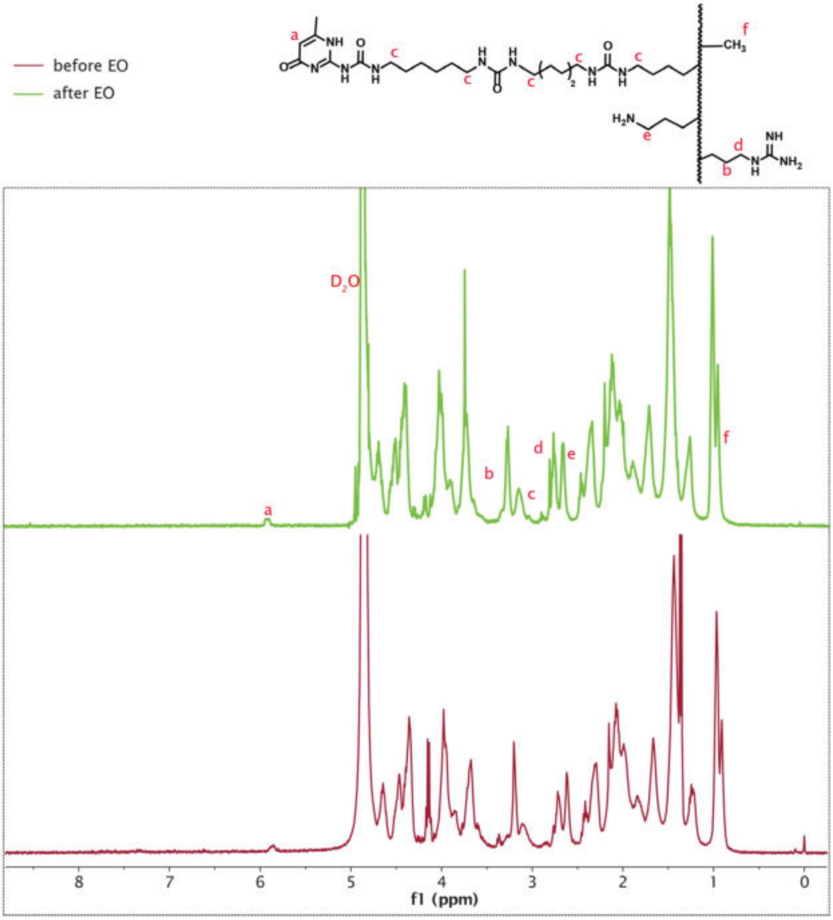

Figure 7.9 ^{1}H-NMR characterization of UPy-RCPhC1 before (red) and after (green) sterilization.

References

1 X. Chen, L. S. Mangala, C. Rodriguez-Aguayo, X. Kong, G. Lopez-Berestein and A. K. Sood, *Cancer Metastasis Rev.*, 2018, **37**, 107–124.

2 D. G. Sashital and J. A. Doudna, *Curr. Opin. Struct. Biol.*, 2010, **20**, 90–97.

3 S. M. Elbashir, J. Harborth, W. Lendeckel, A. Yalcin, K. Weber and T. Tuschl, *Nature*, 2001, **411**, 494–498.

4 A. F. Christopher, R. P. Kaur, G. Kaur, A. Kaur, V. Gupta and P. Bansal, *Perspect. Clin. Res.*, 2016, **7**, 68–74.

5 R. Rupaimoole and F. J. Slack, *Nat. Rev. Drug Discov.*, 2017, **16**, 203–222.

6 E. van Rooij, L. B. Sutherland, N. Liu, A. H. Williams, J. McAnally, R. D. Gerard, J. A. Richardson and E. N. Olson, *Proc. Natl. Acad. Sci.*, 2006, **103**, 18255–18260.

7 G. C. van Almen, W. Verhesen, R. E. W. van Leeuwen, M. van de Vrie, C. Eurlings, M. W. M. Schellings, M. Swinnen, J. P. M. Cleutjens, M. A. M. J. van Zandvoort, S. Heymans and B. Schroen, *Aging Cell*, 2011, **10**, 769–779.

8 T. Thum, P. Galuppo, C. Wolf, J. Fiedler, S. Kneitz, L. W. van Laake, P. A. Doevendans, C. L. Mummery, J. Borlak, A. Haverich, C. Gross, S. Engelhardt, G. Ertl and J. Bauersachs, *Circulation*, 2007, **116**, 258–267.

9 E. van Rooij and S. Kauppinen, *EMBO Mol. Med.*, 2014, **6**, 851–864.

10 E. van Rooij, L. B. Sutherland, X. Qi, J. A. Richardson, J. Hill and E. N. Olson, *Science*, 2007, **316**, 575–579.

11 D. Bumcrot, M. Manoharan, V. Koteliansky and D. W. Y. Sah, *Nat. Chem. Biol.*, 2006, **2**, 711–719.

12 S. Hoshika, N. Minakawa and A. Matsuda, *Nucleic Acids Res.*, 2004, **32**, 3815–3825.

13 Q. Zou, Y. Mao, L. Hu, Y. Wu and Z. Ji, *Comput. Biol. Med.*, 2014, **45**, 157–160.

14 T. G. Hullinger, R. L. Montgomery, A. G. Seto, B. A. Dickinson, H. M. Semus, J. M. Lynch, C. M. Dalby, K. Robinson, C. Stack, P. A. Latimer, J. M. Hare, E. N. Olson and E. van Rooij, *Circ. Res.*, 2012, **110**, 71–81.

15 E. M. Small, R. J. A. Frost and E. N. Olson, *Circulation*, 2010, **121**, 1022–1032.

16 J. Stenvang, A. Petri, M. Lindow, S. Obad and S. Kauppinen, *Silence*, 2012, **3**, 1.

17 M. F. Osborn and A. Khvorova, *Nucleic Acid Ther.*, 2018, **28**, 128–136.

18 A. A. Barba, S. Bochicchio, A. Dalmoro and G. Lamberti, *Pharmaceutics*, 2019, **11**, 360.

19 L. L. Wang and J. A. Burdick, *Adv. Healthc. Mater.*, 2017, **6**, 201601041.

20 M. H. Bakker, E. van Rooij and P. Y. W. Dankers, *Chem. – An Asian J.*, 2018, **13**, 3501–3508.

21 L. L. Wang, Y. Liu, J. J. Chung, T. Wang, A. C. Gaffey, M. Lu, C. A. Cavanaugh, S. Zhou, R. Kanade, P. Atluri, E. E. Morrisey and J. A. Burdick, *Nat. Biomed. Eng.*, 2017, **1**, 983–992.

22 J. E. C. Eding, Universiteit Utrecht, 2020.

23 A. Spannbauer, D. Traxler, K. Zlabinger, A. Gugerell, J. Winkler, J. Mester-Tonczar, D. Lukovic, C. Müller, M. Riesenhuber, N. Pavo and M. Gyöngyösi, *Front. Cardiovasc. Med.*, 2019, **6**, 117.

24 N. Milani-Nejad and P. M. L. Janssen, *Pharmacol. Ther.*, 2014, **141**, 235–249.

25 I. Ribitsch, P. M. Baptista, A. Lange-Consiglio, L. Melotti, M. Patruno, F. Jenner, E. Schnabl-Feichter, L. C. Dutton, D. J. Connolly, F. G. van Steenbeek, J. Dudhia and L. C. Penning, *Front. Bioeng. Biotechnol.,* 2020, **8**, 972.

26 P. P. Zwetsloot, A. M. D. Végh, S. J. Jansen of Lorkeers, G. P. J. van Hout, G. L. Currie, E. S. Sena, H. Gremmels, J. W. Buikema, M.-J. Goumans, M. R. Macleod, P. A. Doevendans, S. A. J. Chamuleau and J. P. G. Sluijter, *Circ. Res.*, 2016, **118**, 1223–1232.

27 P. P. Zwetsloot, A. M. D. Végh, S. J. Jansen of Lorkeers, G. P. J. van Hout, G. L. Currie, E. S. Sena, H. Gremmels, J. W. Buikema, M.-J. Goumans, M. R. Macleod, P. A. Doevendans, S. A. J. Chamuleau and

J. P. G. Sluijter, *Circ. Res.*, 2016, **118**, 1223–1232.

28 Y. Liu, L. Li, Q. Su, T. Liu, Z. Ma and H. Yang, *Echocardiography*, 2015, **32**, 1407–1416.

29 L. L. Wang, Y. Liu, J. J. Chung, T. Wang, A. C. Gaffey, M. Lu, C. A. Cavanaugh, S. Zhou, R. Kanade, P. Atluri, E. E. Morrisey and J. A. Burdick, *Nat. Biomed. Eng.*, 2017, **1**, 983–992.

30 H. Rabea, P. Daniela, Z. Stefanie, F. Ariane, H. Wira, X. Quan-Fu, B. Elisabeth, van R. Eva, Z. A. M., K. Christian and D. Stefanie, *Circulation*, 2013, **128**, 1066–1075.

31 U. S. Department of Health and Human Services and Food and Drug Administration, *Estimating the Maximum Safe Starting Dose in Initial Clinical Trials for Therapeutics in Adult Healthy Volunteers*, july 2005.

32 A. B. Nair and S. Jacob, *J. basic Clin. Pharm.*, 2016, **7**, 27–31.

33 P. Kanda, E. I. Alarcon, T. Yeuchyk, S. Parent, R. A. De Kemp, F. Variola, D. Courtman, D. J. Stewart and D. R. Davis, *ACS Nano*, 2018, **12**, 4338–4350.

34 A. J. Rufaihah, S. R. Vaibavi, M. Plotkin, J. Shen, V. Nithya, J. Wang, D. Seliktar and T. Kofidis, *Biomaterials*, 2013, **34**, 8195–8202.

35 S. Abdalla, G. Makhoul, M. Duong, R. C. J. Chiu and R. Cecere, *Interact. Cardiovasc. Thorac. Surg.*, 2013, **17**, 767–772.

36 Y. Suzuki, A. C. Yeung and F. Ikeno, *J. Biomed. Biotechnol.*, 2011, **2011**, 195483.

37 N. Landa, L. Miller, M. S. Feinberg, R. Holbova, M. Shachar, I. Freeman, S. Cohen and J. Leor, *Circulation*, 2008, **117**, 1388–1396.

38 K. Kadner, S. Dobner, T. Franz, D. Bezuidenhout, M. S. Sirry, P. Zilla and N. H. Davies, *Biomaterials*, 2012, **33**, 2060–2066.

39 T. Yoshizumi, Y. Zhu, H. Jiang, A. D'Amore, H. Sakaguchi, J. Tchao, K. Tobita and W. R. Wagner, *Biomaterials*, 2016, **83**, 182–193.

40 J. W. Holmes, T. K. Borg and J. W. Covell, *Annu. Rev. Biomed. Eng.*, 2005, **7**, 223–253.

41 S. R. Eckhouse and F. G. Spinale, *Heart Fail. Clin.*, 2012, **8**, 7–20.

42 S. D. Prabhu and N. G. Frangogiannis, *Circ. Res.*, 2016, **119**, 91–112.

43 M. Dobaczewski, C. Gonzalez-Quesada and N. G. Frangogiannis, *J. Mol. Cell. Cardiol.*, 2010, **48**, 504–511.

44 J. M. Duran, S. Taghavi, R. M. Berretta, C. A. Makarewich, T. Sharp III, T. Starosta, F. Udeshi, J. C. George, H. Kubo and S. R. Houser, *Clin. Transl. Sci.*, 2012, **5**, 416–421.

45 J. Li, S. Hu, D. Zhu, K. Huang, X. Mei, B. López de Juan Abad and K. Cheng, *J. Am. Heart Assoc.*, 2021, **10**, e020402.

46 M. L. Moreira, P. da Costa Medeiros, S. A. L. de Souza, B. Gutfilen and P. H. Rosado-de-Castro, *Stem Cells Int.*, 2016, **2016**, 3140120.

47 S. Hilbert, P. Sommer, M. Gutberlet, T. Gaspar, B. Foldyna, C. Piorkowski, S. Weiss, T. Lloyd, B. Schnackenburg, S. Krueger, C. Fleiter, I. Paetsch, C. Jahnke, G. Hindricks and M. Grothoff, *Europace,* 2016, **18**, 572–577.

48 C. C. S. Tseng, S. Wenker, M. H. Bakker, A. O. Kraaijeveld, P. Y. W. Dankers, P. R. Seevinck, J. Smink, S. Kimmel, F. J. van Slochteren and S. A. J. Chamuleau, *EuroIntervention*, 2019, **15**, e336–e339.

49 S. Spaans, P.-P. K. H. Fransen, M. J. G. Schotman, R. van der Wulp, R. P. M. Lafleur, S. G. J. M. Kluijtmans and P. Y. W. Dankers, *Biomacromolecules*, 2019, **20**, 2360–2371.

8

Epilogue

1. Introduction

Hydrogels have shown to be a powerful tool in the cardiac regenerative field, due to their easy tunable chemical, physical and mechanical properties; all of which can provide structural support, increase the cellular retention, drug efficacy, or stimulate cellular infiltration in the effected cardiac environment.[1-4] The field of cardiac therapy demands biomaterials that offer biocompatibility, easy injectability to minimize invasiveness, and withstand the harsh and complex response of the cardiac environment. Supramolecular hydrogels show to be ideal candidates, displaying easy modification ability and often high dynamicity and reversible cross-link ability.[5] These highly adaptable hydrogels display exceptionally versatility, offering to key-tools to develop regenerative solution in the field of cardiac regeneration. In this epilogue, the approaches examined in this thesis are summarized, and are put into context in the field of cardiac regeneration. Future directions and further adaptation strategies are given, considering the supramolecular ureido-pyrimidinone (UPy) based hydrogels. A cardiac patch is introduced, which can be applied onto the heart using an adhesive UPy-based hydrogel. Furthermore, motivated by Chapter 5, the development of a nanosized delivery system is discussed, in which a UPy-based hydrogel can be encapsulated to provide an increased sustained release. Lastly, the importance of structural elucidation by cryogenic transmission electron microscopy is highlighted.

Main achievements

In this thesis, the modification and applications of supramolecular hydrogels based on ureido-pyrimidinone (UPy) materials have been described. Research on UPy-based hydrogels showed their applicability as drug delivery candidates[6-8], extracellular matrix mimicking structure[9,10], and for in vivo visualization[11]. Development of novel hydrogels by molecular self-assembly, which properties can be adapted and fine-tuned, show promising solutions for cardiac regenerative therapies. Implementation of bioactive moieties in hydrogels can facilitate cellular encapsulation and protection from the external environment for optimal cardiac delivery of viable cells[12], whereas mechanical properties of hydrogels (e.g. stiffness and viscosity) are of great importance for the effectiveness of the injected therapy.[13-16] Careful considerations regarding the material design need to be made, to obtain an optimal therapeutic effect. Different design strategies of UPy-based hydrogels are introduced (Chapter 3, Figure 8.1i), in which a collagen based peptide conjugated with UPy moieties displayed highly tunable hydrogel properties when combined with a bifunctional UPy unit. Furthermore, a UPy-based library was introduced, where monofunctional UPy units were conjugated with single amino acids, which displayed large differences in aggregation behavior and gelation properties, to which cellular adhesion studies elucidated differences in cell-count and morphology. This chapter provided insight in the assembling behavior of the hydrogels, and displayed the flexibility of the hydrogel design. In the context of previous research, these findings displayed the large influence of small synthetic modifications leading to extensive differences in assembly and structural behavior.

In nature, dynamicity and adaptability play a key role in biological systems. Previous research displayed the dynamicity of material-ligand dynamics in the UPy-based hydrogels.[9,17,18] Here, the dynamicity based on differing types of interaction is further explored, with the analysis of three host molecules (Chapter 4, Figure 8.1ii), designed to interact with the host network based on the bifunctional UPy units. A complementary UPy guest molecule, and two guests based on hydrophobic interactions, i.e. cholesterol and dodecyl, were introduced to the host network. These guest molecules in solution displayed significant differences in cellular absorption and membrane interaction, whereas dynamics of the guest molecules within the host network displayed differences furthermore, indicating a varying binding affinity of each guest to the host network. The interaction mechanisms between the guests and host network still requires elucidation. This paves the way for the development of a generic 'mix and match' approach, adapting the bioactive properties, and release rate for a variety of drug molecules, dependent on the necessity for the envisioned disease.

The versatility of the UPy based hydrogel is demonstrated by encapsulation of the hydrogel in giant unilamellar vesicles, mimicking the crowded marcomolecular intracellular structure (Chapter 5, Figure 8.1iii). This resulted in a synthetic cellular platform, of which the encapsulated hydrogel displayed viscoadaptive behavior by pH-adaptation. While the intracellular crowded environment was mimicked in a fully synthetic cellular approach in previous studies[19,20], here the proposed system displays a complex but easy tunable viscoadaptable platform allowing investigation of different intracellular biochemical processes, serving great potential in the field of synthetic biology.

While a high number of injectable hydrogels are used in cardiac regenerative therapy[21-24], to our knowledge, the fate of the hydrogel after cardiac injection is a factor which is overlooked. A supramolecular labeling method was developed (Chapter 6, Figure 8.1iv), where a monofunctional UPy unit, complexed with a radioactive tracer was combined with the bifunctional UPy-based hydrogel. Furthermore, the bioactive and adhesive properties of the hydrogel were increased by implementation of a collagen based peptide conjugated with UPy moieties (UPy-RCPhC1). This enabled in vivo visualization of the hydrogel retained at the site of injection, and redistribution of the hydrogel. In a healthy porcine heart, a retention of 8% was observed for the bifunctional UPy-based hydrogel over a time span of 4 hours, whereas addition of the UPy-RCPhC1 displayed a retention of 16% over time. This highlights the importance of retention elucidation at the target side, which can greatly influence the efficacy of the injected therapy. The applicability of the UPy based hydrogels as an RNA interference delivery system is exploited (Chapter 7, Figure 8.1v), in which injection of the UPy-based hydrogel in combination with RNAi in an infarcted rodent heart displayed promising. Further efficacy examination in a infarcted porcine study, injecting the RNAi therapeutics encapsulated in a bifunctional UPy-based hydrogel in combination with the UPy-RCPhC1, will elucidate the relevance of the UPy-based hydrogel system as a drug delivery platform in the field of cardiac regeneration.

Myocardial infarction is one of the main causes of death worldwide[25], which is why the demand for cardiac regenerative therapies is so high. When designing materials for cardiac regeneration, a high number of studies focus on regarding only the indirect cardiac parameters when injecting therapeutics in the myocardial infarct site.[26-28] While these parameters are of great importance to examine the cardiac output, an enhanced therapeutic efficacy can be obtained when a deeper understanding is created on the necessary quantity and material properties for an enhanced therapeutic effect. Inherent cardiac factors such as cardiac pulsation and myocardial infarct regeneration greatly affect the retention of materials, but inherent material properties, such as hydrogel stiffness, regeneration, viscosity, injection volume, and affinity with the tissue play a significant role in the therapeutic efficacy as well (Chapter 2). While hydrogel stiffness[13-15,29], and optimal volume determination[15,29-32] are factors studied in previous research, further elucidation on quantitative retention after cardiac injection is necessary to determine the absolute volume necessary for cardiac functional outcome. Furthermore, this can give insight in finding the optimal dosage for drug-carrier systems. As showed in Chapter 6, high redistribution of the injected hydrogel in the myocardium can occur, which enhanced the change of possible unwanted side-effects. This study furthermore demonstrates the necessity of understanding the factors which influence the material retention.

Altogether, our results indicate that UPy-PEG hydrogel is highly tunable and versatile, allowing for visualization in vivo, and providing a valuable delivery platform in the field of cardiac regeneration.

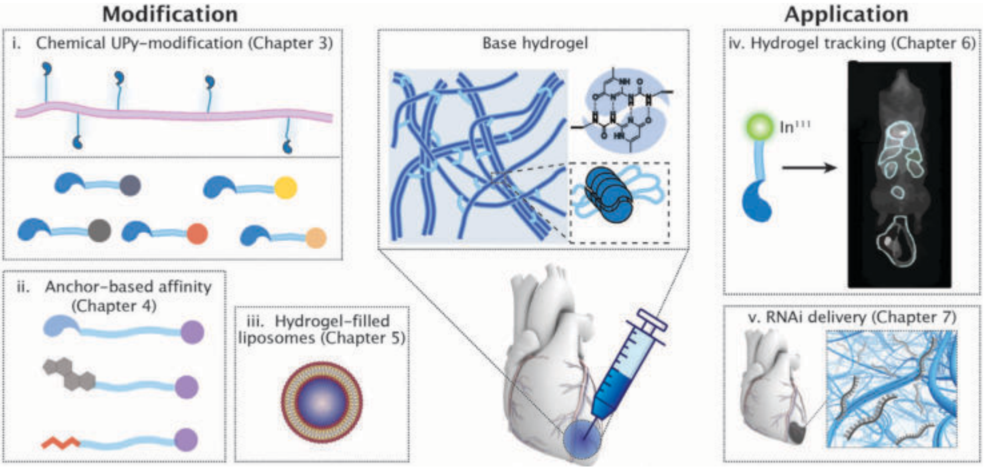

Figure 8.1 Overview of the approaches presented in this thesis, with the BF UPy-PEG as a base material, with several chemical modifications and adaptations of the UPy-based system presented, as well as applicational focuses, being hydrogel tracking and RNAi encapsulated in hydrogel delivery.

2. Further adaptation strategies

2.1 Adhesive hydrogel loaded patch

In chapter 6, the retention of the pristine UPy-PEG as well as the RCPhC1 modified UPy-PEG was shown in a pilot, which was approximately 10 and 20%, respectively. Even though these results were promising, a high amount of hydrogel flush-out from the site of injection was observed which can cause off-target effects. In chapter 2, the factors that could influence this hydrogel/drug retention are discussed in great detail, with several factors including the cardiac pulsation, tissue density, and hydrogel properties could be of influence on these retentive properties. Adaptation to the material is the most straight-forward method for enhancing the retention of the hydrogels. Catechol-modification could possibly lead to an enhancement of adhesion, with the catechol unit functioning as an additional crosslinking moiety and increasing the cohesion and adhesion of the polymer.[33] These catechol groups show to have great promise in the field of bio-inspired adhesives or coatings, with high adhesion properties in wet conditions.[34] The interaction that catechol-groups establish are non-covalent as well as covalent, with a high tendency to form hydrogen bonds, π-π interactions, as well as covalent attachment most likely based on Michael-type addition, however, a clear understanding on the reaction mechanism is still lacking.[35] Oxidation of catechol's promote crosslinking reactions that stimulates the cohesive properties[36], with the chemical oxidant sodium periodate mediating the oxidation process.[37] This makes the catechol moiety an interesting molecule for the fabrication of adhesive hydrogels, as stated in several studies.[38-45] The multiblock PEG-based copolymer, with the UPy-moieties being contained in the backbone (chain-extended UPy-PEG), revealed to obtain strong hydrogels with high strength recovery at large deformation.[46] By end-functionalization of these polymers with catechol-groups, adhesive and cohesive properties were introduced to the polymer (Figure 8.2A).

Cardiac patches have shown great potential for cardiac regenerative therapy[47], but often these patches are sutured to the myocardium, inducing additional damage to the infarcted area.[48,49] A biocompatible adhesive hydrogel layer could be introduced to a patch, avoiding this additional cardiac damage. The CE UPy-PEG-Catechol polymer was dissolved in slightly basic PBS (~pH 8) and subsequent addition of sodium periodate led to the formation of a strong hydrogel. The adhesion of this hydrogel was examined by addition of this precursor hydrogel solution to an electrospun supramolecular patch, composed of chain extended UPy-poly(hexamethylene carbonate) (CE UPy-PC, Figure 8.2B) providing mechanical strength. A small amount of sodium periodate was added to the patch, whereafter addition of the CE UPy-PEG-Catechol was added. The hydrogel containing patch was added to an ex vivo pre-wetted mouse heart after subsequent addition of sodium periodate to the gel-layer for adhesion examination (Figure 8.2C). After 15 minutes, the hybrid patch showed to adhere to the prewetted mouse heart. These preliminary results show the applicability of this hydrogel system to adhere to wet tissue, functioning as an adhesion barrier. Furthermore, therapeutics can be introduced to this hydrogel, therefore serving as a multicomponent system.

However, oxidation of the catechol-groups can lead to additional reactions taking place between amines, amino acids, and proteins.[50] Pre-addition of amine-containing, amino-acids or protein-based therapeutics pre-gelation could therefore lead to covalently cross-linked therapeutics in the hydrogel network, significantly limiting the release of the therapeutics from the hydrogel. Therapeutic introduction to the hydrogel can take place post-gelation, but this previously showed a rather low encapsulation efficiency. Furthermore, the chemical crosslinking mechanism using chemical oxidant sodium periodate occurs relatively fast (sub-minute range), limiting the time of injectability as well as the inherent dynamic nature of the pristine chain extended UPy-PEG polymer.

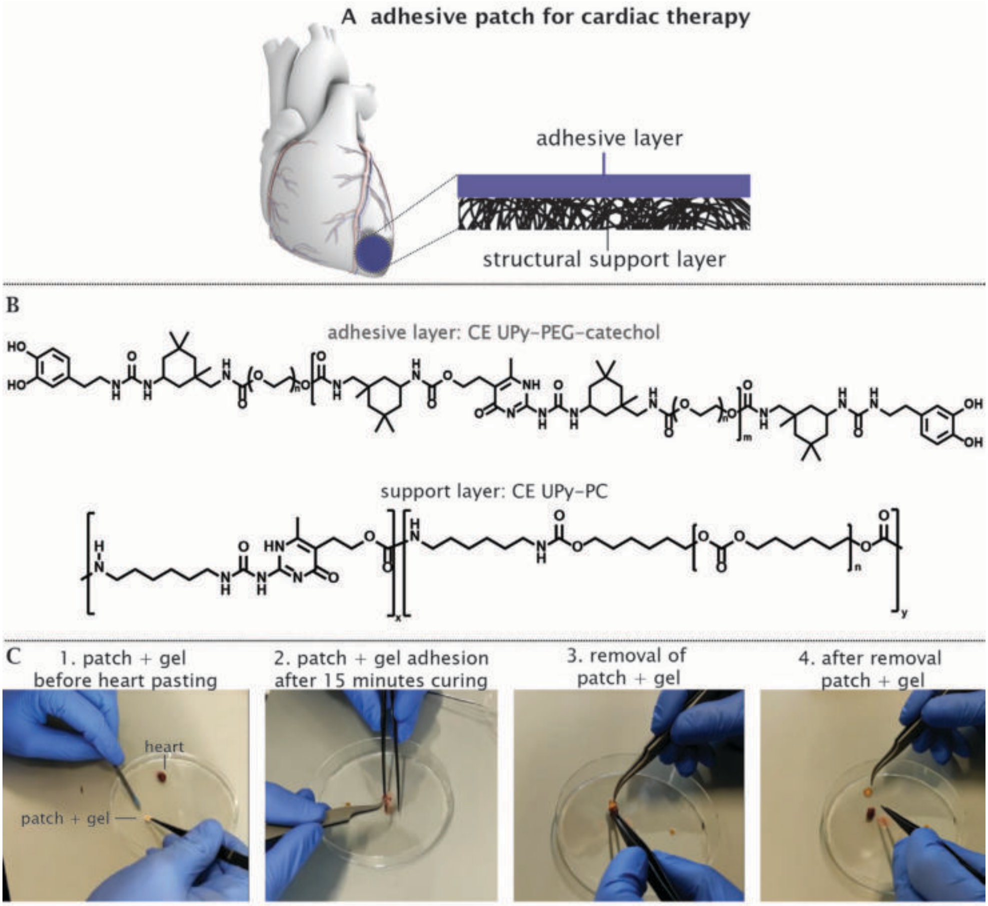

Figure 8.2 A schematic of the adhesive patch for cardiac therapy, containing an adhesive layer and structural supportive layer (A), with the chemical structure of the chain-extended UPy-PEG end-functionalized with catechol-moieties (CE UPy-PEG-catechol) and chain-extended UPy poly(hexamethylene carbonate) (CE UPy-PC) (B). The step-by-step patch + hydrogel adhesion is shown, with the pre-pasting patch + gel and the mouse heart (1), the patch + hydrogel after 15 minutes of curing to the heart (2), the removal of the patch + hydrogel construct from the heart after curing (3), and the patch + hydrogel and heart after the removal of the patch (4) (C).

Previous work by Putti et al. showed the fabrication of a coaxial electrospun UPy-based mesh, with the core consisting of the CE UPy-PC, whilst the shell consists of the hydrophilic CE UPy-poly(ethylene glycol) (CE UPy-PEG).[51] Drug release experiments were performed, in which the drugs were encapsulated in the CE UPy-PEG shell layer during the electrospinning process. A sustained release was observed from encapsulated hydrophobic drugs, whilst highly water soluble drug underwent a burst release. This showed the possible use of this system as a drug-delivery vehicle, for which the CE UPy-PEG-Catechol can function as an adhesive barrier between the mesh and myocardium. Cardiac therapeutics encapsulation in the CE UPy-PEG-Catechol hydrogel can further enhance the therapeutic efficacy of this hybrid mesh.

2.2 Hydrogel-loaded nanoparticles

The BF UPy-PEG hydrogel was able to be encapsulated in a facile manner in giant unilamellar vesicles, as shown in Chapter 5. This further highlighted the applicability of this system as an synthetic cell-like vehicle and drug delivery system. Overall, lipid-based particles are considered promising candidates as cardiac therapeutic delivery systems, as they show similar morphologies compared to cell membranes and can deliver therapeutics such as peptides, protein, and nucleic acids.[52-55]. Polymersomes show an enhanced stability compared to liposomes, with a thicker membrane and the chemical versatility of polymers which allows for a wide range of modification to the polymersomes, tuning the grafting, permeabilty, and stability.[56]

Polymersomes have been previously demonstrated as synthetic organelles, which function as autonomous nanoreactors when encapsulated in synthetic cells[57], as well as be sub-compartmentalized in protocells, from which digestive enzymes were able to be restrained in the lipid bilayer of the polymersome[58]. The applicability of these particles reaches the field of drug delivery, from which the disassembly of the polymersomes can be controlled by tuning the pH.[59] Hydrogel encapsulation in these polymersomes can further lead to a highly tunable release, increasing the retention and sustained release of drugs present this system.

To provide preliminary results, a preparation method to obtain hybrid hydrogel encapsulated polymersomes was conducted. Using the well-established direct hydration methodology, the poly(ethylene glycol)-b-poly(caprolactone-gradient-trimethylene carbonate) (PEG-PCLgPTMC) polymersomes were assembled. The BF UPy-PEG hydrogelator at basic conditions was added during polymersome self-assembly (Figure 8.3A). After neutralization, the particles were analyzed by dynamic light scattering (DLS, Figure 8.3B) and cryogenic transmission electron microscopy (cryo-TEM). Whilst DLS showed an average size of 190 nm, with a polydispersity index of 0.22, cryo-TEM micrographs showed individual particles and high particle clustering, with similar preparation methods at different preparation times showing a large variability in cryo-TEM micrographs (Figure 8.3C). The reproducibility of this system is therefore limited. The individual particles showed no clear sign of hydrogel encapsulation, but a synergistic interaction effect between the PEG-PCLgPTMC and BF UPy-PEG was hypothesized. These results illustrate the crosslinking complexity of two supramolecular polymers, in which further elucidation of the structure and interaction mechanism could lead to an optimized protocol for these hybrid particles. Furthermore, some aggregates observed by cryo-TEM show a similar morphology to organelle structures. A possible combination of these synthetic organelle with the synthetic cell-like system presented in chapter 5 can give rise to further developments regarding synthetic cell-like systems. However, optimization and reproducibility of these polymersome and hydrogel hybrid system is crucial.

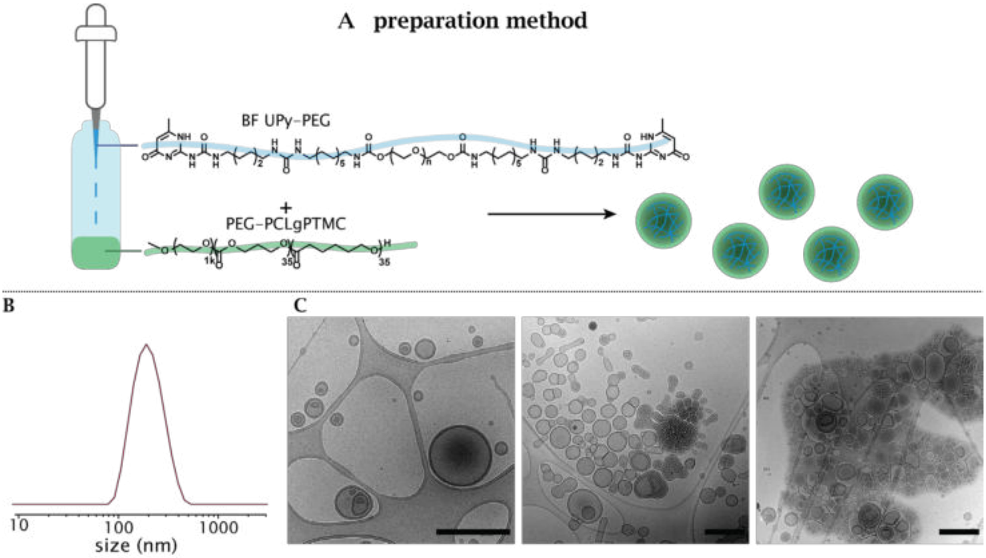

Figure 8.3 Hybrid particles of BF UPy-PEG and PEG-PCLgPTMC, with a schematic overview of the preparation method by the direct hydration method, and chemical structures from which the hybrid polymersome particles were prepared (A), hydrodynamic size distribution by intensity of the particles after preparation, measured by dynamic light scattering (B), and cryogenic transmission electron micrographs of the hybrid BF UPy-PEG and PEG-PCLgPTMC, each micrograph presenting different preparation days, scale bar represents 500 nm (C).

3. Cryogenic transmission electron microscopy as structural elucidation method

"One studies a complex system by dissecting it out physically, chemically, or (...) enzymatically, and then tries to obtain a detailed picture of its parts by X-ray analysis and chemical studies, and an overall picture of the intact assembly by electron microscopy" (Sir Aaron Klug, nobel prize laureate 1982). Klug received his Nobel prize for his development of the crystallographic electron microscopy and structural elucidation of nucleic acid-protein complexes. Even though his work focused on the structural elucidation in the field of molecular biology, this quote is, in my opinion, applicable to the field of supramolecular chemistry as well, with transmission electron microscopy (TEM) playing an important role for clarifying structural compositions. By using cryogenic TEM (Cryo-TEM), the structure of materials can be determined in liquids with a (sub)nanometer resolution and subsecond time resolution.[60] By plunge freezing a thin layer of liquid on a support grid, the chemical assembly and formation process in solution of a reaction can be observed.[61] Furthermore, this can be observed in an unstained frozen-hydrated state, which avoids staining and dehydration artifacts. Besides techniques such as nuclear magnetic resonance, gel permeation chromatography, and dynamic light scattering to obtain a clearer understanding on chemical composition and size, or circular dichroism to elucidate the secondary structure of molecular assemblies, cryo-TEM can give a clear picture on the structural arrangement of molecular assemblies at near atomic resolution. This technique can further elaborate systems with different morphologies, sizes and complex internal structures.[62]

The importance of cryo-TEM is emphasized by Cui et al, who show peptide amphiphiles with identical composition but different sequences of four amino acids displaying differing 1D nano-structural formations.[63] An alkyl spacer functionalized with two glutamic acids and two valines (in different orders) showed to form nanobelts, rigid cylindrical nanofibers, twisted nanoribbons and flexible entangled nanofibers, which was extensively explored by a combination of (cryo-)TEM and x-ray scattering and diffraction. Furthermore, structural elucidation of assembling behavior can be obtained by computer-aided 3D models of polymer structure, as showed by Lafleur et al.[64] They explored the assembling behavior of water-soluble (co)polymers based on benzene-1,3,5-tricarboxamides, forming double helical repeats ranging from 15 to 30 nm. The pitch of these double helical structures could be tuned by mixing various ratios of copolymer compositions. Furthermore, liquid-phase electron microscopy, which is still in an early stage, can be used to directly image material formation and transformation at nanoscale resolution.[65] However, the low amount of experimental data and therefore scarce methodologies present, as well as high radiation damage occurring while imaging soft matters limits the use of this technique.[66] However, this technique can give further insight in the structural rearrangement in soft matter at a nanometer resolution.

An example of this soft matter that can be clearly visualized by cryo-TEM is collagen, the most abundant protein present in humans. The protein is built up by three amino acids chains, consisting of glycine, proline and hydroxyproline, wound together in a triple helix. These tropocollagen molecules form the quaternary structural fibrils, with staggered overlapping arrangement.[67] This quaternary structure can be clearly visualized by cryo-TEM, with alternating light and dark stripes indicating the overlapping and gap zones (Figure 8.4A). By using cryo-TEM, the fibrillar structure can be observed in a frozen-hydrated state, closely mimicking its natural assembling behavior.

Previous work showed fibril formation of UPy-moeities, with monofunctional UPy-PEG displaying long fibril formation, whilst bifunctional UPy-PEG showed relatively short fibrils.[18,68] This was further explored by mixing different molar ratios of BF UPy-PEG to monofunctional (M) UPy-PEG (end-functionalized with a glycine), to observe the assembly effect upon mixing.[9] Long fibril formation was observed when small addition of BF UPy-PEG was added to M UPy-PEG (1 : 84 molar ratio), whilst higher BF UPy-PEG content (1 : 22 ratio) showed to result in shorter fiber formation, similar to only BF UPy-PEG (Figure 8.4B). The high PEG content in the BF UPy-PEG results in high water-shielding, which lowers the contrast of the fibers observed. We hypothesize an increase in exchange dynamics of the BF UPy-PEG due to the higher PEG content in comparison to the M UPy-PEG, resulting in a disruption of the fiber formation due to the destabilization of the packing. The M UPy-PEG, having a lower PEG content and therefore lower exchange dynamics, thereof showed increased bundling formation.

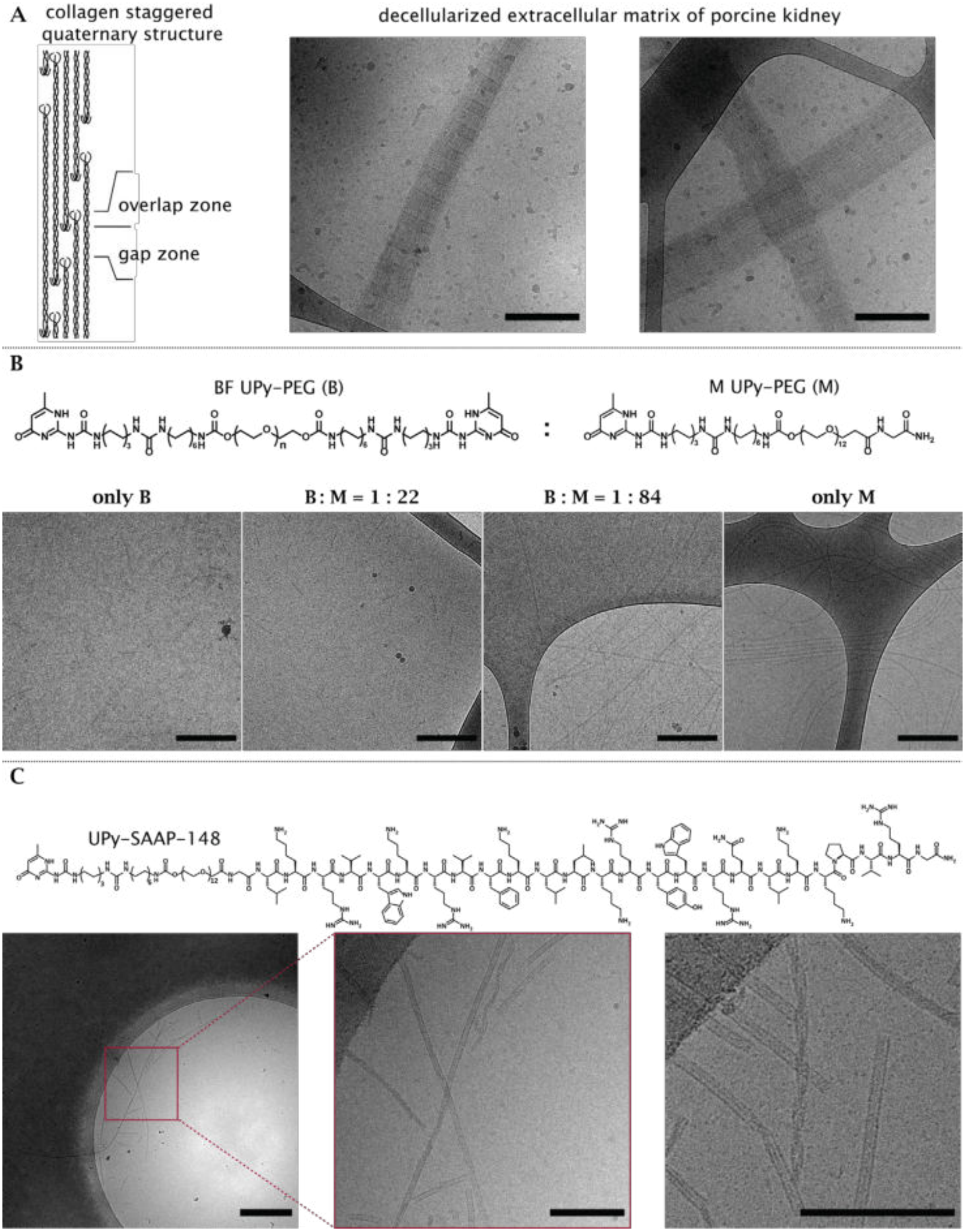

Figure 8.4 An overview of different cryogenic transmission electron micrographs, with a schematic representation of the quaternary structure of collagen, consisting of tropocollagen (image adapted from ref 69), with cryo-TEM micrographs at of decellularized extracellular matrix of porcine kidneys (A), the chemical structures of BF UPy-PEG and M UPy-PEG and micrographs of both compounds as well as mixed at differing ratios (B), and the chemical structure of UPy-SAAP-148 and cryo-TEM micrograph of the compound, scale bar represents 200 nm.

The synthetic peptide with improved antimicrobial and antibiofilm activities (SAAP), specifically SAAP-148 showing prevention of biofilm formation[70], was functionalized to a UPy unit for modular to be implemented into a UPy-based biomaterial (UPy-SAAP-148). Structural elucidation by cryo-TEM showed interesting sheet-like formation of this peptide-functionalized UPy-moiety, as well as ribbon-like formation (Figure 8.4C), whilst the SAAP-148 alone showed random aggregation in solution (results not shown). Interestingly, the sheet observed showed to have clear boundaries present on the sides of the sheet and in the middle, suggesting some overlap of structures. This implies additional interactions present in this molecule, possible of the UPy units and peptide. These results indicate the structural clarification of several organic compounds in solution that can be obtained using cryo-TEM at sub nanometer resolution without the necessity of chemical modifications.

4. Conclusion

The research described in this thesis shows functionalization strategies and applicational purposes of supramolecular UPy-based hydrogels for cardiac regenerative therapies. In a fundamental approach, assembling behavior, mechanical properties, and bioactivity were adapted by introducing modular functionality to the UPy-based system. Moreover, the hydrogel system was used to mimic the viscoadaptable intracellular crowded in a full synthetic cell. In an applicational approach, cardiac retention and redistribution of the UPy-based hydrogels were visualized in vivo, and employing this hydrogel as an RNAi therapeutic delivery for targeting myocardial infarction was further explored. This UPy-based system is envisioned to enable in vivo retention and redistributive visualization, provide a sustained therapeutic release, and thereof increasing the drug efficacy, serving a prominent role in the field of cardiac regenerative therapies.

References

1 B. Peña, M. Laughter, S. Jett, T. J. Rowland, M. R. G. Taylor, L. Mestroni and D. Park, *Macromol. Biosci.*, 2018, **18**, e1800079–e1800079.

2 S. Uman, A. Dhand and J. A. Burdick, *J. Appl. Polym. Sci.*, 2020, **137**, 48668.

3 L. Saludas, S. Pascual-Gil, F. Prósper, E. Garbayo and M. Blanco-Prieto, *Int. J. Pharm.*, 2017, **523**, 454–475.

4 C. Hoeeg, A. Dolatshahi-Pirouz and B. Follin, *Gels (Basel, Switzerland)*, , DOI:10.3390/gels7010007.

5 M. J. Webber and P. Y. W. Dankers, *Macromol. Biosci.*, 2019, **19**, 1800452.

6 M. H. Bakker, E. van Rooij and P. Y. W. Dankers, *Chem. – An Asian J.*, 2018, **13**, 3501–3508.

7 M. H. Bakker, M. Grillaud, D. J. Wu, P.-P. K. H. Fransen, I. H. de Hingh and P. Y. W. Dankers, *Macromol. Rapid Commun.*, 2018, **39**, 1800007.

8 S. Koudstaal, M. M. C. Bastings, D. A. M. Feyen, C. D. Waring, F. J. Van Slochteren, P. Y. W. Dankers, D. Torella, J. P. G. Sluijter, B. Nadal-Ginard, P. A. Doevendans, G. M. Ellison and S. A. J. Chamuleau, *J. Cardiovasc. Transl. Res.*, 2014, **7**, 232–241.

9 M. Diba, S. Spaans, S. I. S. Hendrikse, M. M. C. Bastings, M. J. G. Schotman, J. F. van Sprang, D. J. Wu, F. J. M. Hoeben, H. M. Janssen and P. Y. W. Dankers, *Adv. Mater.*, 2021, **n/a**, 2008111.

10 S. Spaans, P.-P. K. H. Fransen, M. J. G. Schotman, R. van der Wulp, R. P. M. Lafleur, S. G. J. M. Kluijtmans and P. Y. W. Dankers, *Biomacromolecules*, 2019, **20**, 2360–2371.

11 M. H. Bakker, C. C. S. Tseng, H. M. Keizer, P. R. Seevinck, H. M. Janssen, F. J. Van Slochteren, S. A. J. Chamuleau and P. Y. W. Dankers, *Adv. Healthc. Mater.*, 2018, **7**, 1–8.

12 C. B. Sylvester, A. Pugazenthi, K. J. Grande-Allen and R. K. Ghanta, *Cardiovasc. Eng. Technol.*, 2021, **12**, 183–199.

13 J. L. Ifkovits, E. Tous, M. Minakawa, M. Morita, J. D. Robb, K. J. Koomalsingh, J. H. Gorman, R. C. Gorman and J. A. Burdick, *Proc. Natl. Acad. Sci.*, 2010, **107**, 11507 LP – 11512.

14 C. B. Rodell, M. E. Lee, H. Wang, S. Takebayashi, T. Takayama, T. Kawamura, J. S. Arkles, N. N. Dusaj, S. M. Dorsey, W. R. T. Witschey, J. J. Pilla, J. H. Gorman, J. F. Wenk, J. A. Burdick and R. C. Gorman, *Circ. Cardiovasc. Interv.*, , DOI:10.1161/circinterventions.116.004058.

15 H. Wang, C. B. Rodell, M. E. Lee, N. N. Dusaj, J. H. Gorman, J. A. Burdick, R. C. Gorman and J. F. Wenk, *J. Biomech.*, 2017, **64**, 231–235.

16 S. T. Wall, J. C. Walker, K. E. Healy, M. B. Ratcliffe and J. M. Guccione, *Circulation*, 2006, **114**, 2627–2635.

17 M. M. C. Bastings, T. M. Hermans, A. J. H. Spiering, E. W. L. Kemps, L. Albertazzi, E. E. Kurisinkal and P. Y. W. Dankers, *Macromol. Biosci.*, 2019, **19**, 1800296.

18 S. I. S. Hendrikse, S. P. W. Wijnands, R. P. M. Lafleur, M. J. Pouderoijen, H. M. Janssen, P. Y. W. Dankers and E. W. Meijer, *Chem. Commun.*, 2017, **53**, 2279–2282.

19 N. A. Yewdall, B. C. Buddingh, W. J. Altenburg, S. B. P. E. Timmermans, D. F. M. Vervoort, L. K. E. A. Abdelmohsen, A. F. Mason and J. C. M. van Hest, *ChemBioChem*, 2019, **20**, 2643–2652.

20 Y. Zhang, Y. Chen, X. Yang, X. He, M. Li, S. Liu, K. Wang, J. Liu and S. Mann, *J. Am. Chem. Soc.*, , DOI:10.1021/jacs.0c12494.

21 L. L. Wang, Y. Liu, J. J. Chung, T. Wang, A. C. Gaffey, M. Lu, C. A. Cavanaugh, S. Zhou, R. Kanade, P. Atluri, E. E. Morrisey and J. A. Burdick, *Nat. Biomed. Eng.*, 2017, **1**, 983–992.

22 M. J. Hernandez and K. L. Christman, *JACC Basic to Transl. Sci.*, 2017, **2**, 212–226.

23 K. L. Sack, E. Aliotta, J. S. Choy, D. B. Ennis, N. H. Davies, T. Franz, G. S. Kassab and J. M. Guccione, *Acta Biomater.*, 2020, **111**, 170–180.

24 R. Chen, C. Zhu, L. Xu, Y. Gu, S. Ren, H. Bai, Q. Zhou, X. Liu, S. Lu, X. Bi, W. Li, X. Jia and Z. Chen, *Biomaterials*, 2021, **274**, 120855.

25 R. Ross, *Nature*, 1993, **362**, 801–809.

26 M. C. Ciuffreda, G. Malpasso, C. Chokoza, D. Bezuidenhout, K. P. Goetsch, M. Mura, F. Pisano, N. H. Davies and M. Gnecchi, *Acta Biomater.*, 2018, **70**, 71–83.

27 R. Waters, P. Alam, S. Pacelli, A. R. Chakravarti, R. P. H. Ahmed and A. Paul, *Acta Biomater.*, 2018, **69**, 95–106.

28 S. Dobner, D. Bezuidenhout, P. Govender, P. Zilla and N. Davies, *J. Card. Fail.*, 2009, **15**, 629–636.

29 S. T. Wall, J. C. Walker, K. E. Healy, M. B. Ratcliffe and J. M. Guccione, *Circulation*, 2006, **114**, 2627–2635.

30 P. Wise, N. H. Davies, M. S. Sirry, J. Kortsmit, L. Dubuis, C.-K. Chai, F. P. T. Baaijens and T. Franz, *Int. j. numer. method. biomed. eng.*, 2016, **32**, e02772.

31 J. Leor, S. Tuvia, V. Guetta, F. Manczur, D. Castel, U. Willenz, Ö. Petneházy, N. Landa, M. S. Feinberg, E. Konen, O. Goitein, O. Tsur-Gang, M. Shaul, L. Klapper and S. Cohen, *J. Am. Coll. Cardiol.*, 2009, **54**, 1014–1023.

32 D. S. Li, R. Avazmohammadi, C. B. Rodell, E. W. Hsu, J. A. Burdick, J. H. Gorman, R. C. Gorman and M. S. Sacks, *Acta Biomater.*, 2020, **114**, 296–306.

33 H. Lee, N. F. Scherer and P. B. Messersmith, *Proc. Natl. Acad. Sci.*, 2006, **103**, 12999 LP – 13003.

34 E. Faure, C. Falentin-Daudré, C. Jérôme, J. Lyskawa, D. Fournier, P. Woisel and C. Detrembleur, *Prog. Polym. Sci.*, 2013, **38**, 236–270.

35 J. Saiz-Poseu, J. Mancebo-Aracil, F. Nador, F. Busqué and D. Ruiz-Molina, *Angew. Chemie Int. Ed.*, 2019, **58**, 696–714.

36 G. P. Maier, C. M. Bernt and A. Butler, *Biomater. Sci.*, 2018, **6**, 332–339.

37 J. Yang, M. A. Cohen Stuart and M. Kamperman, *Chem. Soc. Rev.*, 2014, **43**, 8271–8298.

38 B. P. Lee, J. L. Dalsin and P. B. Messersmith, *Biomacromolecules*, 2002, **3**, 1038–1047.

39 J. H. Ryu, Y. Lee, W. H. Kong, T. G. Kim, T. G. Park and H. Lee, *Biomacromolecules*, 2011, **12**, 2653–2659.

40 L. Han, X. Lu, K. Liu, K. Wang, L. Fang, L.-T. Weng, H. Zhang, Y. Tang, F. Ren, C. Zhao, G. Sun, R. Liang and Z. Li, *ACS Nano*, 2017, **11**, 2561–2574.

41 Y. Lee, H. J. Chung, S. Yeo, C.-H. Ahn, H. Lee, P. B. Messersmith and T. G. Park, *Soft Matter*, 2010, **6**, 977–983.

42 J. Xu, S. Strandman, J. X. X. Zhu, J. Barralet and M. Cerruti, *Biomaterials*, 2015, **37**, 395–404.

43 L. Han, L. Yan, K. Wang, L. Fang, H. Zhang, Y. Tang, Y. Ding, L.-T. Weng, J. Xu, J. Weng, Y. Liu, F. Ren and X. Lu, *NPG Asia Mater.*, 2017, **9**, e372–e372.

44 J. Shin, J. S. Lee, C. Lee, H.-J. Park, K. Yang, Y. Jin, J. H. Ryu, K. S. Hong, S.-H. Moon, H.-M. Chung, H. S. Yang, S. H. Um, J.-W. Oh, D.-I. Kim, H. Lee and S.-W. Cho, *Adv. Funct. Mater.*, 2015, **25**, 3814–3824.

45 D. Gan, W. Xing, L. Jiang, J. Fang, C. Zhao, F. Ren, L. Fang, K. Wang and X. Lu, *Nat. Commun.*, 2019, **10**, 1487.

46 M. Guo, L. M. Pitet, H. M. Wyss, M. Vos, P. Y. W. Dankers and E. W. Meijer, *J. Am. Chem. Soc.*, 2014, **136**, 6969–6977.

47 L. Ye, W.-H. Zimmermann, D. J. Garry and J. Zhang, *Circ. Res.*, 2013, **113**, 922–932.

48 T. Sugiura, N. Hibino, C. K. Breuer and T. Shinoka, *J. Cardiothorac. Surg.*, 2016, **11**, 163.

49 Y. Matsuzaki, S. Miyamoto, H. Miyachi, T. Sugiura, J. W. Reinhardt, C. Yu-Chun, J. Zbinden, C. K. Breuer and T. Shinoka, *PLoS One*, 2020, **15**, e0234087.

50 M. Morrison, W. Steele and D. J. Danner, *Arch. Biochem. Biophys.*, 1969, **134**, 515–523.

51 M. Putti, T. Mes, J. Huang, A. W. Bosman and P. Y. W. Dankers, *Biomater. Sci.*, 2020, **8**, 163–173.

52 L. E. Paulis, T. Geelen, M. T. Kuhlmann, B. F. Coolen, M. Schäfers, K. Nicolay and G. J. Strijkers, *J. Control. Release*, 2012, **162**, 276–285.

53 I. E. Allijn, B. M. S. Czarny, X. Wang, S. Y. Chong, M. Weiler, A. E. da Silva, J. M. Metselaar, C. S. P. Lam, G. Pastorin, D. P. V de Kleijn, G. Storm, J.-W. Wang and R. M. Schiffelers, *J. Control. Release*, 2017, **247**, 127–133.

54 H. Yang, X. Qin, H. Wang, X. Zhao, Y. Liu, H.-T. Wo, C. Liu, M. Nishiga, H. Chen, J. Ge, N. Sayed, O. J. Abilez, D. Ding, S. C. Heilshorn and K. Li, *ACS Nano*, 2019, **13**, 9880–9894.

55 C. Fan, J. Joshi, F. Li, B. Xu, M. Khan, J. Yang and W. Zhu, *Front. Bioeng. Biotechnol.*, 2020, 8, 687.

56 E. Rideau, R. Dimova, P. Schwille, F. R. Wurm and K. Landfester, *Chem. Soc. Rev.*, 2018, **47**, 8572–8610.

57 L. M. P. E. van Oppen, L. K. E. A. Abdelmohsen, S. E. van Emst-de Vries, P. L. W. Welzen, D. A. Wilson, J. A. M. Smeitink, W. J. H. Koopman, R. Brock, P. H. G. M. Willems, D. S. Williams and J. C. M. van Hest, *ACS Cent. Sci.*, 2018, **4**, 917–928.

58 A. F. Mason, N. A. Yewdall, P. L. W. Welzen, J. Shao, M. van Stevendaal, J. C. M. van Hest, D. S. Williams and L. K. E. A. Abdelmohsen, *ACS Cent. Sci.*, 2019, **5**, 1360–1365.

59 P. L. W. Welzen, S. W. Martinez Ciriano, S. Cao, A. F. Mason, I. A. B. Welzen-Pijpers and J. C. M. van Hest, *J. Polym. Sci.*, 2021, **59**, 1241–1252.

60 P. M. Frederik and N. Sommerdijk, *Curr. Opin. Colloid Interface Sci.*, 2005, **10**, 245–249.

61 J. P. Patterson, Y. Xu, M.-A. Moradi, N. A. J. M. Sommerdijk and H. Friedrich, *Acc. Chem. Res.*, 2017, **50**, 1495–1501.

62 D. Danino, *Curr. Opin. Colloid Interface Sci.*, 2012, **17**, 316–329.

63 H. Cui, A. G. Cheetham, E. T. Pashuck and S. I. Stupp, *J. Am. Chem. Soc.*, 2014, **136**, 12461–12468.

64 R. P. M. Lafleur, S. Herziger, S. M. C. Schoenmakers, A. D. A. Keizer, J. Jahzerah, B. N. S. Thota, L. Su, P. H. H. Bomans, N. A. J. M. Sommerdijk, A. R. A. Palmans, R. Haag, H. Friedrich, C. Böttcher and E. W. Meijer, *J. Am. Chem. Soc.*, 2020, **142**, 17644–17652.

65 H. Wu, H. Su, R. R. M. Joosten, A. D. A. Keizer, L. S. van Hazendonk, M. J. M. Wirix, J. P. Patterson, J. Laven, G. de With and H. Friedrich, *Small Methods*, 2021, **5**, 2001287.

66 H. Wu, H. Friedrich, J. P. Patterson, N. A. J. M. Sommerdijk and N. de Jonge, *Adv. Mater.*, 2020, **32**, 2001582.

67 B. D. Quan and E. D. Sone, in *Research Methods in Biomineralization Science*, ed. J. J. B. T.-M. in E. De Yoreo, Academic Press, 2013, vol. 532, pp. 189–205.

68 M. M. C. Bastings, S. Koudstaal, R. E. Kieltyka, Y. Nakano, A. C. H. Pape, D. A. M. Feyen, F. J. van Slochteren, P. A. Doevendans, J. P. G. Sluijter, E. W. Meijer, S. A. J. Chamuleau and P. Y. W. Dankers, *Adv. Healthc. Mater.*, 2014, **3**, 70–78.

69 D. F. Holmes, C. J. Gilpin, C. Baldock, U. Ziese, A. J. Koster and K. E. Kadler, *Proc. Natl. Acad. Sci.*, 2001, **98**, 7307 LP – 7312.

70 A. de Breij, M. Riool, R. A. Cordfunke, N. Malanovic, L. de Boer, R. I. Koning, E. Ravensbergen, M. Franken, T. van der Heijde, B. K. Boekema, P. H. S. Kwakman, N. Kamp, A. El Ghalbzouri, K. Lohner, S. A. J. Zaat, J. W. Drijfhout and P. H. Nibbering, *Sci. Transl. Med.*, 2018, **10**, eaan4044.

Summary

Heart diseases are one of the main causes of mortality worldwide. The most common heart related disease is myocardial infarction, which occurs when the blood flow to the heart muscle is blocked, causing oxygen depletion. This results a high number of cardiomyocyte perishing, leading to a cascade of cellular processes and eventually the formation of scar tissue. This can severely alter the function of the myocardium and lead to potential heart failure. In attempts to restore the cardiac function, several therapies have been developed, including cell-, drug- and biomaterial-based therapy. Clinical studies have shown modest to low cardiac improvements upon injection of cells in the myocardium, with a high cell death and low retention being the main cause of the low therapeutic efficacy. Injectable hydrogels show to be promising candidates to improve cardiac regeneration, that can reduce the drug toxicity and off-target effects, offer stability, and increase the drug retention and effectiveness at target site with minimal invasive administration. A highly adaptable supramolecular design allow tuneable properties of the hydrogel, such as adaptation of bioactivity, dynamicity, mechanical strength, and implementation of additional functionalization.

In recent years, the therapeutic benefit of hydrogels and patches which can contain either cells, drugs or provide mechanical stability has shown promising results. While the efficacy and retention of cellular therapeutics have been explored extensively in the field of cardiac regeneration, a limited amount of studies show the effect that the amount of retained material has on its efficacy to stimulate cardiac regeneration. Several parameters are of influence when the retention of these materials is considered, such as time of injection, cardiac contraction and properties of the material. These parameters were explored in chapter 2, and we envision that a better understanding of these parameters can lead to an increase in retention and therefore increase in effectiveness for cardiac therapies.

The hydrogelator molecule used in this thesis consists of a supramolecular ureido-pyrimidinone (UPy) moieties, which dimerizes through strong and specific four-fold hydrogen bonds. Hydrogels based on this supramolecular moiety show pH- and temperature responsive behaviour facilitating injection in the liquid state at a $pH > 8.5$, inducing gelation in contact with physiological pH. Due to the non-covalent and modular nature of this system functionalities can be introduced in a simple ‘mix-and-match’ method. Chapter 3 explores this design strategy based on UPy-interactions, in which a recombinant-based hydrogel was developed, functionalized with UPy-moieties to enable control over the structure, assembly behaviour, and gelation. Furthermore, a UPy-based library was introduced, in which monofunctional UPy-units were conjugated to single amino acids. Difference in aggregation, gelation, and cellular adhesiveness were observed when these UPy-amino acids were developed into a hydrogel, displaying the adaptivity of this system. A trend was shown towards higher mechanical strength, an increase of cellular adhesiveness, and spread out cellular morphology when considering the UPy-amino acids with a more polar amino acid functionalization.

Dynamicity and adaptability play a key role in biological systems found in nature. To explore the dynamic properties of guest molecules presented in the UPy-based hydrogel, different guest molecules were synthesized in chapter 4. Three different guest molecules with adaptive affinity towards the hydrogel host network were introduced, being a complementary UPy guest molecule, and two guests based on hydrophobic interactions, i.e. cholesterol and a dodecyl-moiety. Increase in hydrophilicity was obtained by functionalization of an oligo(ethylene glycol) functionalization to the guest-molecules. The highest mobility in the UPy-based hydrogel was displayed by the dodecyl-moiety, whereas the cholesterol-moiety displayed the lowest mobility. Furthermore, large differences in cellular uptake of these guest molecules were shown. This tunability of the host-guest dynamics in transient hydrogels opens the door to various tissue engineering and drug delivery purposes.

The broad applicability of the UPy-based hydrogel was demonstrated in chapter 5, in which the hydrogel was encapsulated in giant unilamellar vesicles (GUVs), serving as a macromolecularly crowded synthetic cell. The hydrogel-loaded GUVs (HL-GUVs) were prepared by the droplet transfer method, a facile one-step procedure, in which the supramolecular pH-responsive hydrogel was encapsulated in the phospholipid microvesicles when in its sol-state at basic conditions. The HL-GUVs displayed increased viscosity at low pH (gel-state) and low viscosity at high pH (sol-state). The HL-GUVs can reversibly switch between low and high viscosity state upon external pH changes. Incorporation of a model enzyme, urease, in the HL-GUVs initiated autonomous switching of its internal state upon addition of urea in the external environment. Furthermore, rate of product formation in the HL-GUVs was shown to be adapted by the viscosity state of the inner lumen. This demonstrated a new artificial cell platform with dynamic stimuli-responsive adaptivity, serving great potential in the field of synthetic biology.

A new method for labelling and tracking a supramolecular hydrogels in vivo is introduced in chapter 6 to obtain a clearer picture on the fate of a material after cardiac injection. A radioactive label was implemented in the hydrogel in a modular fashion, enabling quantitative in vivo tracking of the hydrogel. Furthermore, the bioactive and adhesive properties of the hydrogel were increased by introducing the recombinant-based peptide containing UPy-functionality to the hydrogel. The retention after cardiac injection in a porcine heart was examined over a time span of four hours in a small pilot study, in which a retention of 8% was observed for the UPy-based hydrogel, whereas addition of the recombinant-based peptide displayed a retention of 16% over a time span of four hours. This demonstrates the importance of quantitative retention elucidation, which can greatly affect the efficacy of the injected therapeutics.

The results shown in this thesis have given new insights in different supramolecular functionalization strategies, the versatility of this system, and biological applicability of the UPy-based hydrogel. It is shown that this hydrogel is highly tuneable and versatile, allowing for visualization in vivo, and providing a valuable delivery platform in the field of cardiac regeneration.

Curriculum Vitae

Maaike Schotman was born on December 2nd, 1991 in Vriezenveen. She completed her secondary education in 2011 at ROC van Twente in Almelo. Subsequently, she started her bachelor Biomedical Engineering at the University of Twente in Enschede. During her bachelor's program she expended her knowledge in the biomedical engineering field with a semester abroad at the National Chiao Tung University in Hsinchu, Taiwan. In the faculty of Biomedical Signals and Systems at the University of Twente, she acquired her research experience. This research focused on improving the gait of Parkinson patients by making use of smart glasses providing rhythmic sensory stimulation. After successfully obtaining her bachelor's degree in 2015, Maaike continued with the master Biomedical Engineering at the University of Twente. She performed an internship on the development of poly(β-amino ester)-based transfection agents for skin deficiencies and wound healing at the Charles Institute of Dermatology, under supervision of prof. dr. Wenxin Wang. She received her master's degree in 2017 with her thesis on the development of controlled nanogels as drug delivery vehicles under the supervision of dr. ir. Jos M. J. Paulusse. Thereafter, she started her PhD research in the laboratory of Chemical Biology and Institute of Complex Molecular Systems at the Eindhoven University of Technology under supervision of prof. dr. dr. Patricia Y. W. Dankers. The most important results of this research are presented in this thesis.

List of publications

M. J. G. Schotman, P. Y. W. Dankers, *Factors influencing retention of injected biomaterials to* treat myocardial infarction, in revision at Advanced Materials interfaces

M. J. G. Schotman, P.P.K.H. Fransen, J. Song, P. Y. W. Dankers, *Tuning the affinity of amphiphilic guest molecules in a supramolecular transient network*, submitted to RSC Advances

M. J. G. Schotman‡, A. Llopis Lorente‡, J. C. M. van Hest, L. K. E. A. Abdelmohsen, P. Y. W. Dankers, *Hydrogel-loaded giant unilamellar vesicles as versatile viscoadaptable platforms.* In preparation. ‡Contributed equally

J. E. C. Eding, M. Vigil-Garcia, M. Vink, C. Demkes, D. Versteeg, L. Kooijman, M. H. Bakker, M. J. G. Schotman, P. Y. W. Dankers, E. van Rooij, *Hydrogel-based delivery of antimiR-195 improves cardiac efficacy after ischemic injury*, in preparation

M. Diba, S. Spaans, S. I. S. Hendrikse, M. M. C. Bastings, M. J. G. Schotman, J. F. van Sprang, D. J. Wu, F. J. M. Hoeben, H. M. Janssen, P. Y. W. Dankers, *Engineering the Dynamics of Cell Adhesion Cues in Supramolecular Hydrogels for Facile Control over Cell Encapsulation and Behavior.*, Adv. Mater. **2021**, 33(37), 2008111

A. Nicosia, F. Vento, G. Marletta,G. M. L. Messina, C. Satriano, V. Villari, N. Micali, M. T. De Martino, M. J. G. Schotman, P G. Mineo. *Porphyrin-Based Supramolecular Flags in the Thermal Gradients' Wind: What Breaks the Symmetry, How and Why*. Nanomaterials (Basel). **2021,** 11(7):1673

J. Liu, M. J. G. Schotman, M.M.R.M. Hendrix, X. Lou, P. P. Marín San Román, I. K. Voets, R. P. Sijbesma, *Effects of structural variation on the self-assembly of bis-urea based bolaamphiphiles.*, J Polym Sci., **2021**, 59(12), 1162-1170

M. J. G. Schotman‡, M. M. C. Peters‡, G. C. Krijger, I. van Adrichem, J. L. M. Bemelmans, M. J. Pouderoijen, M. G. T. A. Rutten, K. Neef, S. A. J. Chamuleau, P. Y. W. Dankers*, In Vivo Retention Quantification of Supramolecular Hydrogels Engineered for Cardiac Delivery.* Adv. Healthcare Mater., **2021**, 10(10), 2001987. ‡Contributed equally

S. Spaans, P. P. K. H. Fransen, M. J. G. Schotman, R. van der Wulp, R. P. M. Lafleur, S. G. J. M. Kluijtmans, and P. Y. W. Dankers *Supramolecular Modification of a Sequence-Controlled Collagen-Mimicking Polymer,* Biomacromolecules, **2019**, 20(6), 2360-2371

M. Putti, O. M. J. A. Stassen, M. J. G. Schotman, C. M. Sahlgren, and P. Y. W. Dankers, *Influence of the assembly state on the functionality of a supramolecular jagged1-mimicking peptide additive*, ACS Omega, **2019,** 4(5), 8178-8187

Dankwoord

De afgelopen vier jaren zijn voorbij gevlogen; zo komt er toch een eind aan mijn mooie promotietijd. Ik ben erg dankbaar voor de hulp en bijdragen van vele mensen. Zonder jullie was me dit niet gelukt.

Allereerst wil ik mijn eerste promotor, Patricia, bedanken. Vanaf de eerste dagen tijdens mijn promotie wist ik dat ik de juiste keuze had gemaakt om naar Eindhoven te komen om een promotie te starten in de biomaterialen. Het warme welkom wat ik kreeg van jou en van de groep was erg fijn. Je enthousiasme over mijn project, biomaterialen in het algemeen, en de chemie was aanstekelijk. Met je oneindige ideeën, onophoudelijke optimisme, en fijne begeleiding kijk ik terug op een prettige samenwerking (je hebt me soms in het diepe gegooid, wat ik ook af en toe nodig had). Ik vond het super om mee te gaan naar de MRS meeting in Phoenix, om daar mijn werk te presenteren en meer te proeven van de verdere biomateriaal wereld. Bedankt voor het vertrouwen dat je me de afgelopen jaren hebt gegeven en ik hoop dat Dankersgroep nog veel wetenschappelijke hoogstandjes tegemoet gaat.

Loai, ik wil je bedanken voor je begeleiding aan het einde van mijn PhD, en voor de fijne samenwerking en discussies wat betreft het liposome en hydrogel project. Mooi om de wondere werelden van synthetische cellen en hydrogelen te combineren. Ik vond het leuk om nog een kijkje te kunnen nemen in de Bio-organic chemistry groep, en ik wens je nog veel succes en geluk voor de toekomst. I would also like to include Toni here, thank you for the great collaboration, the advice, experiments, discussions, and just nice talks. I enjoyed working with you and wish you all the best for the future.

Prof. dr. Steven Chamuleau, bedankt voor het deelnemen in mijn commissie en voor het kritisch doorlezen van mijn proefschrift. De samenwerkingsprojecten die we hebben mogen uitvoeren voor MIGRATE en REMAIN waren altijd super leuke projecten waar ik met veel plezier op terug kijk, en waar nog een mooie publicatie uit is voortgekomen.

Prof. dr. Jason Burdick, I had the pleasure of meeting you in Utrecht a couple of years ago. I want to thank you for critically reviewing my thesis, and It is an honour to have you in my defense committee. I wish you all the best at your new research lab at CU Boulder.

Verder wil ik prof. dr. Carlijn Bouten, prof. dr. Rint Sijbesma en dr. Anke Smits bedanken voor het kritisch doorlezen van mijn proefschrift en de deelname aan mijn promotiecommissie. Rint, bedankt voor de fijne samenwerking wat betreft het project van Jie waar ik cryo-TEM plaatjes voor mocht maken, waar nog een mooie publicatie uit voorgekomen is. Anke, ik vond het leuk om mee te denken en mee te experimenteren met het samenwerkingsproject om te zoeken naar een adhesieve gel. Er zijn mooie stappen gezet, en ik hoop dat het vervolg project mooie resultaten zou opleveren. Ook wil ik Esther Dronkers bedanken voor de fijne samenwerking en de altijd gezellige meetings.

Graag wil ik nog een aantal mensen van het UMCU en Hubrecht Instituut bedanken voor de prettige samenwerkingen, discussies en meetingen van de afgelopen jaren. Het was leuk om als de 'UPy-gel' expert langs te komen, en ik wil bedanken: Marijn, Klaus, Aina, Steven Wenker, Frebus, Joep, prof. dr. Eva van Rooij en prof. dr. Joost Sluijter.

Voor de fijne samenwerking met FujiFilm wil ik graag Bas Kluijtmans en Suzan van Dongen bedanken. Mensen van het ICMS, met name Monique, Cindy, en Wendy, wil ik graag bedanken voor de goede sfeer, het managen van ICMS, en het op orde houden van Ceres. Jolanda, bedankt voor het helpen bij en regelen van vele administratieve zaken. Soms kostte het wat moeite (het proefkonijn), maar gelukkig zijn we er uit gekomen. Voor alle animaties ben ik de ICMS animation studio erg dankbaar, met name Koen. Ook wil ik Greet bedanken voor de gezellige praatjes en dat Ceres er altijd zo spik en span uit ziet. SyMO-Chem, met name Henk Janssen, wil ik graag bedanken voor het synthetiseren van vele polymeren, maar ook voor het leveren van advies. De mensen van SupraPolix, met name Tonny Bosman, bedankt voor de discussies en het advies. De gehele vakgroep van SMO wil ik graag bedanken voor de fijne werksfeer en alle faciliteiten. Naast alle groepsleiders, wil ik bij deze ook graag het secretariaat, het analytisch team, Hans en Henk meenemen. Ook wil ik Christien bedanken voor het schoonhouden van Helix. Hans Damen wil ik bedanken voor alle bestellingen, Henk Eding voor het op orde houden van de keuken en veel meer. Joost wil ik bedanken voor zijn adviezen wat betreft de LC-MS metingen, en Ralf en Lou voor de het meten van alle Maldi-TOF samples, evenals de hulp met het meten van mijn GPC samples. Peggy, bedankt voor alle pijn en moeite die je stopt in het op orde houden van het biolab. Ik wens je nog vele mooie weekenden in Zeeland toe. Furthermore, I would like to thank all the members from the Biolab for all the help and the nice atmosphere in the lab. Iris en Sylvia bedankt voor alle Qtof metingen. Sebastiaan, bedankt voor al je hulp bij de triple-quad. Bas Rosier en Bas Bögels, bedankt voor jullie advies over RNAs. Furthermore, I would like to thank all the old and current members of the BMT meeting group for the input, advice, help and fruitful discussions.

In Enschede heb ik voor het eerst mogen proeven van de wetenschapswereld. Jos, Pia en Rachel, jullie gaven me het vertrouwen om de stap te maken voor het uitvoeren van een promotieonderzoek. Bedankt hiervoor.

In het begin van mijn PhD was ik veel te vinden in lab 2, STO4, waar ik advies kreeg maar ook leuke gesprekken had met veel mensen. Ik wil met name Bas de Waal bedanken voor al zijn adviezen wat betreft synthese. Verder wil ik Marcin en Elisabeth bedanken voor het op orde houden van het lab, maar ook de gezeligheid en goede sfeer.

Mijn paranimfen, Moniek en Muhabbat, wil ik bij deze ook bedanken. Moniek, al vanaf het begin van onze PhD konden we goed kletsen over van alles (wetenschappelijk en minder wetenschappelijk). Bedankt voor de wandelingen, drankjes en opbeurende praatjes als ik er even doorheen zat. Nog even volhouden en dan ben jij ook aan de beurt. Muhabbat, we hebben vrijwel dezelfde weg afgelegd, begonnen in Enschede en promoveren in Eindhoven wat onze band bijzonder maakt. Ik bewonder je enthousiasme, je kennis, en je goede smaak in series uiteraard. Ik ben blij dat jij mijn paranimf bent.

Ik heb de eer gehad om veel TEM te meten tijdens mijn PhD, van mij en andere mensen, waardoor ik veel leuke mensen van deze afdeling heb mogen ontmoeten. Ten eerste Anne Spoelstra, bedankt voor je de introductie op de Sphera, maar ook de leuke en gezellige gesprekken van de afgelopen jaren. Het was super dat je altijd klaarstond voor een nieuwe uitdaging, zelfs het embedden van organoids. Paul Bomans, bedankt voor de introductie in de cryo-TEM wereld. De rust en geduld waarmee je de trainingen en ook alle problemen aanpakte achter de TEM heb ik als zeer prettig ervaren. Ook wil ik Rick Joostens bedanken, wie ik veruit het meest heb gebeld tijdens mijn PhD als ik weer tegen een probleem stuitte achter de TITAN. Bedankt voor al je hulp, maar ook voor alle gezellige gesprekken. Furthermore, I would like to thank Hanglong for the nice TEM talks, but also for the help. Mark, jij ook bedankt voor de hulp wanneer Rick afwezig was en veel succes bij ThermoFisher.

I had the pleasure to be part of a group that was full of extremely helpful, skilled and smart people. I would like to thank the entire Dankers group for the great scientific meetings, great feedback and guidance I received throughout the years. Besides the scientific side, the group was also great fun! Thanks for all the nice group outings, drinks, borrels, chats, coffee breaks, walks etc. Thanks to Jasper, Paul, Riccardo, Simone, Laura, Jingyi, Vincent, Oleksandr, Ying, Geert, Marcel, and Jolanda. Maritza, het was leuk dat ik je half mocht begeleiden tijdens je master opdracht, en nog veel succes met je PhD in de groep. Peter-Paul, de synthese goeroe, bedankt voor alle hulp met mijn synthese-, gel-, en alle andere vragen (want het waren er veel). Bedankt dat je altijd de tijd nam om me te helpen! Boris, bedankt voor al je hulp, ook met betrekking tot het electrospinnen, maar ook de goeie gesprekken. Heel veel succes met het afronden van je PhD. Joyce, mijn buurvrouw, ook al mochten we niet in hetzelfde kantoor zitten, toch vond ik het gezellig om altijd even bij binnenkomst te kletsen. Martin, het was een feest om met jou RPK-D te volgen. Bedankt dat je altijd antwoord gaf op mijn (soms een beetje domme) rheologie vragen. Annika, het was een eer om samen met je het UPy-Amino acid project uit te voeren en hopelijk komt er nog een leuke publicatie uit. Dan Jing, het was leuk om samen met je de DPD onveilig te maken. Bedankt voor alle gezellig etentjes en hopelijk zullen er meer volgen. Johnick, bedankt voor alle goede gesprekken met een colaatje on-the-side. Succes met de afronding van je PhD.

I would furthermore like to thank the ‘old guard’ of the Dankers group for the tips and guidance, but also for the fun drinks, game nights and parties. Thanks to Bastiaan, Ronald, Matilde, Sergio, Jiankang, and Mani.

Furthermore, I would like to thank my (old-)office mates for all the scientific and not-so scientific talks: Jinxing, Madita, Federica, Jari, and Yingtong. Jinxing, thanks for the Chinese lessons, the many snacks and chocolates, and all the times you reminded me to take my keys with me when I left. Daarnaast wil ik iedereen van STO3/4 bedanken voor alle gezelligheid tijdens TGIFs, borrels en andere uitjes.

Naast hard werken was de lunch een belangrijk deel van mijn dagbesteding hier. Ik wil graag Suzanne, Wiggert, Rens, Simone, Iris, Femke, Daan, Marleen, en Roy bedanken voor de gezellige lunches. De snackproeverijen, bitterbal avonden, en borreltjes waren altijd gezellig. Pascal en Imke, dank voor jullie nuchterheid en droge humor. Pascal, jammer dat het polymersome en hydrogel project uiteindelijk niet helemaal gelukt is, maar het was leuk om met je samen te werken.

Esther, Gerjan, Belinda en David, jullie ook super bedankt voor alle leuke en gezellige weekendjes weg, etentjes, dagjes uit, en nog veel meer. Ondanks dat we nu allemaal een beetje verspreid wonen, vind ik het super dat we elkaar nog zo vaak zien en spreken. Ik hoop dat er nog vele leuke, gezellige en soms spontane olifanten dagjes/weekenden mogen komen.

Rinske, ook al zien we elkaar wat minder sinds ik in Eindhoven woon, ik geniet des te meer wanneer we weer een borrel of dagje samen hebben. Karen, ik vind het leuk dat we elkaar nog vaak spreken. Ik hoop dat er nog veel gezellige lunches mogen komen en super bedankt voor het helpen met het ontwerpen van zo'n mooie thesis cover!

Bij deze wil ik ook graag mijn schoonfamilie bedanken voor alle gezellige etentjes, weekendjes weg, wandel en fietssessies. Het was even wennen om in zo'n sportieve (kabouter) familie terecht te komen, maar gelukkig merkte ik al snel dat ik het niveau prima aan kon (vooral van jullie, Tim en Kathelijn). Op dat er nog veel etentjes en wandel/fietstochten mogen komen!

Niek, Nardie, Ard, Ankie, en Jochem bedankt voor de vele kopjes koffie, de goeie gesprekken en alle gezelligheid van de afgelopen jaren. De weekendjes weg, of gewoon lekker in Hellendoorn, waren altijd heerlijk ontspannend. Ik hoop dat er nog veel mogen volgen en ik kan niet wachten om mijn kleine nichtje te ontmoeten. Verder wil ik Kufo en Nutsy bedanken, welke altijd in zijn voor een knuffel of speelsessie in de tuin.

Pap en mam, super bedankt voor alle steun de afgelopen jaren, en dat jullie altijd voor me klaar staan. Pap, ik vind de fietstochten die we samen maken altijd fijn. Je nuchtere instelling ('wat is het ergste wat er kan gebeuren?') heeft me er op veel momenten doorheen gesleept. Mam, we hebben dezelfde goede humor en je bent altijd in voor een kort belletje als ik ergens mee zit en weet me vrijwel altijd gerust te stellen. Zonder jullie zou ik dit niet hebben kunnen doen, bedankt daarvoor!

Lenne, jij bent wel het leukste wat ik tijdens mijn PhD ben tegenkomen. Zonder jou was deze hele rit niet zo vlekkeloos gelopen. Je bood ontspanning als ik er aan toe was, gaf me advies als ik het nodig had (ook al wou ik het soms niet horen), en stond altijd klaar voor een knuffel. Je bent de liefste en ik kijk uit naar wat we samen nog allemaal mogen meemaken!

Bedankt iedereen en het ga jullie goed!

Maaike